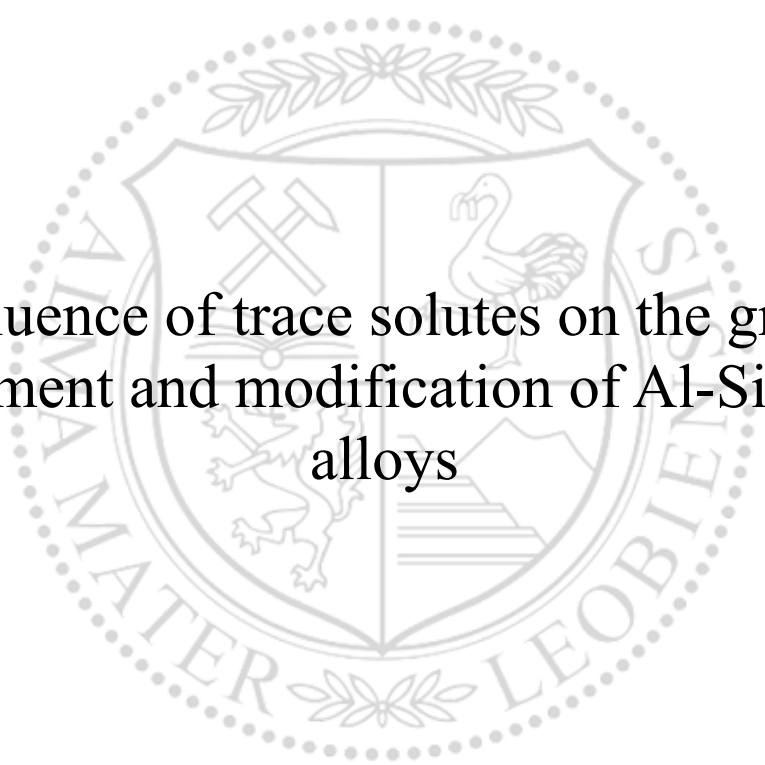Chair of Casting Research
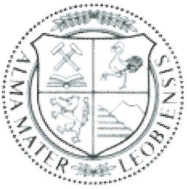
Doctoral Thesis

Influence of trace solutes on the grain refinement and modification of Al-Si based alloys

Ing. Ivo Spáčil

August 2023

MONTANUNIVERSITÄT LEOBEN
www.unileoben.ac.at

AFFIDAVIT

I declare on oath that I wrote this thesis independently, did not use other than the specified sources and aids, and did not otherwise use any unauthorized aids.

I declare that I have read, understood, and complied with the guidelines of the senate of the Montanuniversität Leoben for "Good Scientific Practice".

Furthermore, I declare that the electronic and printed version of the submitted thesis are identical, both, formally and with regard to content.

Date 19.07.2023

Signature Author
Ivo Spacil

Acknowledgements

Contents

Contents

Abstract

Al-Si based alloys are widely used in automotive and aerospace applications as components manufactured from these alloys are significantly lighter than cast iron and steel parts and they possess a good strength-to-weight ratio. The properties are affected by several factors. In this work, the effect of solutes on molten metal treatments is investigated using casting experiments, thermal analysis (TA), multi-scale characterisation methods, density functional theory (DFT), differential scanning calorimetry (DSC) and entrained droplet technique. In terms of grain refinement, the investigated solutes are Ti and Ta. In terms of modification, eutectic grain refinement and heterogeneous nucleation of eutectic Si, the investigated solutes are Eu, P and Sr.

The controlled addition of solute Ta in combination with stoichiometric Al-2.2Ti-1B grain refiner results in a lower grain size than the addition of conventional Al-5Ti-1B grain refiner. The grain size is further decreased with increasing Ta content. Both Ti and Ta-refined alloys exhibit a negligible undercooling. Atomic investigation using transmission electron microscopy (TEM) reveals Ta at the interface of TiB_2 and DFT interface energy shows that Ta is as energetically favourable as Ti at the interface of TiB_2. No interaction of Ta with other elements is observed. Ta is concluded to be a suitable remedy for Si-poisoning.

Modification is achieved via the addition of Sr and Eu. The shape factor increases with increasing the addition of Eu, however, the shape factor decreases with increasing the addition of P. Al_2Si_2Sr and Al_2Si_2Eu intermetallic phases are observed in the microstructure. Lattice mismatch calculation and entrained droplet technique elucidate that Al_2Si_2Eu is nucleated on EuP, which is favourably formed from increasing Eu and P additions. The new nucleation sequence is proposed: $EuP \rightarrow Mg_3P_2 \rightarrow Al_2Si_2Eu$ in the presence of Mg. In terms of growth of eutectic Si, the solute Eu atom is calculated to be preferably located along the twin boundary of eutectic Si. Ta shows no mutual interaction with Eu or Sr.

Combined additions of Eu and P result in a refined eutectic grain size while maintaining the modified eutectic Si. Ta and TiB_2 are found to have no effect on nucleation of eutectic Si. The addition of P into Eu-modified high purity alloy produced using entrained droplet technique shows a decrease in undercooling and displacement of nucleation temperature

to higher temperatures. Entrained eutectic Si droplets are consisting of fine fibrous and randomly oriented Si particles. Addition of P results in a transition to fewer number of single oriented Si plates.

The peak hardness is achieved 1 h later in high Ta alloy compared to conventional alloy refined with Ti. Interface energy of Al and β'' precipitate with Ti and Ta-doped interfaces shows a lower interface energy for Ta-doped interface. DSC revealed a very low activation energy of β precipitate with the addition of Eu, therefore complete precipitation is expected to save economic costs.

The highest elongation of 24 % is observed in high Ta alloy in T4 condition. Ta-refined and/or Eu-modified alloys exhibit a comparable strength and a lower elongation than conventional Ti-refined and Sr-modified alloy, presumably due to formation of Al_2Si_2Eu on the grain boundaries and different porosity distribution in Eu-modified alloys.

The present work demonstrates the strong influence of solutes (in hundreds of ppm) on the nucleation, growth, kinetic and thermodynamic processes and mechanical properties.

Kurzfassung

Legierungen auf Al-Si-Basis sind in der Automobil- und Luftfahrtindustrie weit verbreitet, da die aus diesen Legierungen hergestellten Bauteile wesentlich leichter sind als Gusseisen- und Stahlteile und ein gutes Festigkeits-Gewichts-Verhältnis aufweisen. Die Eigenschaften werden durch verschiedene Faktoren beeinflusst. In dieser Arbeit wird die Auswirkung von gelösten Stoffen auf die Behandlung von Metallschmelzen mit Hilfe von Gießversuchen, thermischer Analyse (TA), Multiskalen-Charakterisierungsmethoden, Dichtefunktionaltheorie (DFT)-Berechnungen, Differenzkalorimetrie (DSC) und der Technik der mitgerissenen Tröpfchen untersucht. Im Hinblick auf die Kornfeinung werden Ti und Ta als gelöste Stoffe untersucht. Hinsichtlich der Modifikation, der eutektischen Kornverfeinerung und der heterogenen Keimbildung von eutektischem Si sind die untersuchten gelösten Stoffe Eu, P und Sr.

Die kontrollierte Zugabe von gelöstem Ta in Kombination mit stöchiometrischem Al-2.2Ti-1B-Kornfeiner führt zu einer geringeren Korngröße als die Zugabe von herkömmlichem Al-5Ti-1B-Kornfeiner. Die Korngröße nimmt mit steigendem Ta-Gehalt weiter ab. Sowohl Ti als auch Ta-veredelte Legierungen weisen eine vernachlässigbare Unterkühlung auf. Atomare Untersuchungen mit Hilfe der Transmissionselektronenmikroskopie (TEM) zeigen Ta an der Grenzfläche von TiB_2, und die DFT-Grenzflächenenergie zeigt, dass Ta an der Grenzfläche von TiB_2 energetisch genauso günstig ist wie Ti. Es wird keine Wechselwirkung von Ta mit anderen Elementen beobachtet. Ta ist somit ein geeignetes Mittel gegen Si-Vergiftungen.

Die Modifizierung wird durch den Zusatz von Sr und Eu erreicht. Der Formfaktor steigt mit zunehmender Zugabe von Eu, jedoch sinkt er mit zunehmender Zugabe von P. Al_2Si_2Sr und Al_2Si_2Eu intermetallische Phasen werden im Gefüge beobachtet. Die Berechnung der Gitterfehlanpassung und die Technik der mitgerissenen Tröpfchen zeigen, dass Al_2Si_2Eu auf EuP gebildet wird, das sich mit zunehmender Eu- und P-Zugabe formiert. Folgende neue Keimbildungssequenz wird vorgeschlagen: $EuP \rightarrow Mg_3P_2 \rightarrow Al_2Si_2Eu$ in Gegenwart von Mg. In Bezug auf das Wachstum von eutektischem Si wird berechnet, dass sich das gelöste Eu-Atom vorzugsweise entlang der Zwillingsgrenze des eutektischen Si befindet. Ta zeigt keine gegenseitige Wechselwirkung mit Eu oder Sr.

Die kombinierte Zugabe von Eu und P führt zu einer verfeinerten eutektischen Korngröße unter Beibehaltung des modifizierten eutektischen Si. Ta und TiB_2 haben keinen Einfluss auf die Keimbildung von eutektischem Si. Die Zugabe von P zu einer Eu-modifizierten hochreinen Legierung, die mit der Technik der mitgerissenen Tröpfchen hergestellt wurde, zeigt einen Rückgang der Unterkühlung und eine Verschiebung der Keimbildungstemperatur zu höheren Temperaturen. Mitgerissene eutektische Si-Tropfen bestehen aus feinen faserigen und zufällig orientierten Si-Teilchen. Die Zugabe von P führt zu einem Übergang zu einer geringeren Anzahl einfach orientierter Si-Plättchen.

Die höchste Härte wird bei einer Legierung mit hohem Ta-Gehalt 1 Stunde später erreicht als bei einer herkömmlichen, mit Ti veredelten Legierung. Die Grenzflächenenergie von Al und β''-Ausscheidungen mit Ti und Ta-dotierten Grenzflächen zeigt eine niedrigere Grenzflächenenergie für Ta-dotierte Grenzflächen. DSC-Untersuchungen ergaben eine sehr niedrige Aktivierungsenergie der β-Ausscheidung mit dem Zusatz von Eu, daher wird erwartet, dass eine vollständige Ausscheidung wirtschaftliche Kosten spart.

Die höchste Dehnung von 24 % wird bei einer Legierung mit hohem Ta-Gehalt im Zustand T4 beobachtet. Ta-raffinierte und/oder Eu-modifizierte Legierungen weisen eine vergleichbare Festigkeit und eine geringere Dehnung auf als herkömmliche Ti-raffinierte und Sr-modifizierte Legierungen, was vermutlich auf die Bildung von Al_2Si_2Eu an den Korngrenzen und eine andere Porositätsverteilung in Eu-modifizierten Legierungen zurückzuführen ist.

Die vorliegende Arbeit zeigt den starken Einfluss der gelösten Stoffe (in Hunderten von ppm) auf die Keimbildung, das Wachstum, die kinetischen und thermodynamischen Prozesse und die mechanischen Eigenschaften.

List of symbols

$\hat{T}_e$	Kinetic energy of the electrons
$\hat{V}_{e-e}$	Electron-electron interaction
$\hat{V}_{ext}$	Interaction of electrons with a positive external potential
$\hat{V}_{n-e}$	Nucleus-electron interaction
$T_{G,\mathrm{eu}}$	Eutectic growth temperature
T_G	Growth temperature
$T_{min,\mathrm{eu}}$	Eutectic minimum temperature
T_{min}	Minimum temperature
$T_{N,\mathrm{eu}}$	Eutectic nucleation temperature
α_J	Jackson alpha factor
β_Q	Growth restriction parameter
δ_c	Thickness of solute rich layer ahead of the solid-liquid
ΔT_{fg}	Free growth undercooling
ΔC	Concentration at the tip of the dendrite
ΔC_0	Concentration difference at the solid-liquid interface
$\Delta E_{\mathrm{site,i}}^{\xi}$	Site preference energy of species i in the phase ξ
ΔE_f^{ξ}	Formation energy difference between phase ξ containing species i and pure phase ξ
$\Delta E_{\mathrm{phase}}$	Phase preference energy
ΔE_{site}	Site preference energy

ΔE_{sub} Substitutional energy

ΔG Change in Gibbs free energy

ΔG^* Energy barrier to form a critical nucleus

ΔG_A Energy required to form a new surface area

ΔG_i Surface free enthalpy

ΔG_v Volume free enthalpy

ΔG_{het} Gibbs free energy required for heterogeneous nucleation

ΔG_{hom} Gibbs free energy required for homogeneous nucleation

Δg_{SL} Free energy between solid and liquid per unit volume

ΔH_F Enthalpy change

ΔK Stress-intensity factor range

ΔS_F Entropy of fusion

Δs_F Entropy of fusion per unit volume

ΔT Undercooling

ΔT_c Constitutional undercooling

ΔT_k Kinetic undercooling

ΔT_N Nucleation undercooling

ΔT_p Pressure undercooling

ΔT_r Curvature undercooling

ΔT_t Thermal undercooling

ΔT_{eu} Eutectic undercooling

δ Lattice mismatch

$\frac{K_r}{K_c}$ Constant

γ_{LP} Surface energy between liquid and particle

γ_{SP} Surface energy between solid and particle

γ Interface energy

γ_{SL}	Solid-liquid interface energy
$\hat{H}$	Hamiltonian operator
$\hat{T}_n$	Kinetic energy of the nuclei
$\hat{V}_{n-n}$	Nucleus-nucleus interaction
λ	Interlamellar spacing
λ_b	Upper limit of interlamellar spacing
λ_e	Extreme of interlamellar spacing
μ_s	Chemical potential of species s
Ω_c	Supersaturation
ϕ	Heating rate
Ψ	Wave function
ρ_{atm}	Density of the sample solidified at atmospheric pressure
$\rho_{\text{H}_2\text{O}}$	Density of water
ρ_{vac}	Density of the sample solidified at reduced pressure
ρ	Number density of inoculant particles
σ_y	Stress in y-direction
θ	Wetting angle
ξ	Phase
A	Area
a, b, c, β	Lattice parameters
a_0	Lattice parameter of nucleating phase
A_5	Elongation
a_c	Conventional cubic lattice parameter
a_n	Lattice parameter of nucleant
a_{ef}	Effective lattice parameter
a_{final}	Final crack length

A_{SF}	Area of a particle
A_{SP}	Surface area of spherical nucleus
B	Thickness
C	Concentration
C^*	Equilibrium concentration difference
C_0	Concentration of solidified alloy
C_l	Concentration in the liquid
C_s	Concentration in the solid
CN_I	Total number of nearest-neighbour sites in the crystal
CN_S	Number of nearest-neighbour sites in a layer parallel to the surface
D	Diffusion coefficient
d	Particle diameter
D_l	Diffusion coefficient in liquid
d_{gs}	Grain size diameter
DI	Density index
E	Total energy of the system
E_a	Activation energy
E_{0X}	Equilibrium energy
E_{Eu}	Energy with an Eu atom
E_f^{ξ}	Formation energy
E_{pure}	Energy with pure structure
E_{strain_x}	Strain energy
$E_{\mathrm{TiB_2}}$	Total energy of TiB$_2$
$E_{\mathrm{TiB_2}/X}$	Total energy of slab containing TiB$_2$ and constituent (X)
E_{tot}^{ξ}	Total energy of a SC representing phase ξ
E_X	Total energy of constituent

f	Jump frequency
$f(\theta)$	Geometrical factor
f_0	Atomic vibration frequency
f_p	Fraction of active particles
f_s	Fraction solid
G	Gibbs free energy
G_T	Temperature gradient
H	Enthalpy
I	Nucleation rate
I^{het}	Heterogeneous nucleation rate
I_0^{het}	Pre-exponential constant
I^{hom}	Homogeneous nucleation rate
I_0^{hom}	Pre-exponential constant
k	Partition coefficient
k_B	Boltzmann constant
K_Q	Provisional fraction toughness
K_{max}	Maximum stress intensity
L	Length of primary dendrite arm
L_m	Latent heat of fusion
m	Liquidus slope
m_{air}	Mass in the air
$m_{\text{H}_2\text{O}}$	Mass in the water
N	Number of secondary arms
n	Number of atoms
n^*	Number of atoms required to form R^* (number of critical clusters)
n_{het}^*	Number of atoms required to form R^* for heterogeneous nucleation

List of symbols

n^*_{hom}	Number of atoms required to form R^* for homogeneous nucleation
n_l	Number of atoms in liquid
n_p	Number of sites for heterogeneous nucleation
N_s	Number of atoms of species in the SC
P	Supercooling parameter
p	Pressure
p_a	Probability of capturing an atom to the surface
P_c	Péclet number
P_{max}	Maximum force
P_{min}	Minimum force
P_Q	Provisional force
P_{SF}	Perimeter of a particle
Q	Growth restriction factor
R	Spherical radius
$R = P_{\mathrm{min}}/P_{\mathrm{max}}$	Compression-compression ratio
R^*	Critical radius
R_g	Grain radius
R_m	Tensile strength
r_m	Atomic radius of the modifier
r_{Si}	Atomic radius of Si
R_{gas}	Gas constant
R_{max}	Maximal radius
$R_{\mathrm{p0.2}}$	Yield strength
R_{tip}	Dendrite tip radius
S	Entropy

S_d — Spacing between the particles

$SDAS$ — Second dendrite arm spacing

SF — Shape factor

T — Temperature

T_l — Liquid temperature

T_m — Melting temperature

T_N — Nucleation temperature

T_s — Solid temperature

T_{eq} — Equilibrium temperature

T_{max} — Maximum peak temperature

U — Internal energy

V — Growth rate

v — Volume

v^* — Velocity

V_s — Volume of a spherical cap

V_{SP} — Volume of a sphere

W — Width

w^* — Width of SSN zone

X — Constant

x_{cs} — Distance a grain need to growth to create constitutional undercooling

z — Distance from the interface

List of acronyms

APT   Atom probe tomography

BF   Bright field

BS   Backscattered electron

C(T)   Compact-tension

CET   Columnar to equiaxed transition

CP   Commerical purity

CT   Computed tomography

DFT   Density functional theory

DF   Dark field

DI   Density index

DSC   Differential scanning calorimetry

EBSD   Electron backscatter diffraction

EDM   Electro discharge machining

EDS SI   Energy dispersive X-ray spectrum imaging

EDS   Energy-dispersive X-ray spectra

FCC   Face centred cubic

FDU   Foundy degassing unit

FFT   Fast Fourier transform

FIB   Focused ion beam

GGA	Generalised gradient approximation
GP-zones	Guinier-Preston zones
HAADF	High-angle annular dark-field
HCP	Hexagonal close packed
HPDC	High pressure die casting
HP	High purity
HRTEM	High resolution transmission electron microscopy
IIT	Impurity induced twinning
IPF	Inverse pole figure
KAM	Kernel average misorientation
LDA	Local density approximation
MIA	Multiple image alignment
MMR	Modified Murakami reagent
OM	Optical microscropy
OR	Orientation relationship
PAW	Projector-augmented wave
PBC	Periodical boundary condition
PBE	Perdew-Burke-Ernzerhof potential
PIPS	Precision ion polishing system
PP	Pseudopotential
RPT	Reduced pressure test
SC	Supercell
SE	Secondary electron
SEM	Scanning electron microscopy
SSN	Solute supression nucleation
SSSS	Supersaturated solid solution

STEM	Scanning transmission electron microscopy
T4	Solution treatment
T6	Solution treatment and artificial ageing
TA	Thermal analysis
TB	Twin boundary
TEM	Transmission electron microscopy
TPRE	Twin plane re-entrant edge
UTS	Ultimate tensile strength
VASP	Vienna ab initio simulation package
VESTA	Visualization for electronic structural analysis
μ-XRF	X-ray fluorescence

Introduction

Al-Si based alloys have been widely used in the automotive and aerospace industries over the decades due to their strength-to-weight ratio. Their applications are increasing as industries search for new ways to save weight, resulting in reducing energy consumption and reduction of CO_2. On the other hand, another important aspect is to achieve a reliable quality of the casting products. In order to produce castings with high mechanical properties and to meet requirements for specified applications, it is necessary to understand the effects of casting technologies, chemical composition, melt treatments and heat treatments on solidification and precipitation microstructure, which is covered in Chapter 2.

A well control of solidification microstructure via melt treatments or casting technology is of great necessity to achieve desired microstructure and hence the mechanical properties. In liquid melt, the melt treatments such as grain refinement of α-Al, modification of eutectic Si, grain refinement of eutectic grains and degassing are often performed. This work aims to study solutes, their effect on microstructure and mechanical properties and their role during commercially used melt treatments such as grain refinement of α-Al, modification of eutectic Si and heat treatment of Al-7Si-0.3Mg based alloys. Methodology used to investigated the effect of solutes is described in Chapter 3.

First, solutes grain refinement of Al-Si alloys faces a so-called Si-poisoning problem. Si-poisoning occurs in Al-Si melts when Si concentration is higher than 3 wt. % [1, 2]. It should be noted that the majority of the casting alloys contain Si concentration in the range of 5-12 wt. %. In practice, grain refinement is performed using Al-5Ti-1B grain refiner. The grain refiner contains inoculant particles (TiB_2) which play a role as a nucleation site for α-Al grains and free Ti [3]. However, the interaction of free Ti with Al-Si melt results in the formation of ternary silicides which block the TiB_2 particle and prevent nucleation of α-Al [4, 5]. The common ways to overcome Si-poisoning are (i) increasing addition of Al-5Ti-1B grain refiner [6–8], which increases economic costs, (ii) addition of other particles such as AlB_2 [9, 10], NbB_2 [11–13], TiC [14, 15], (iii) reducing the Ti concentration in grain refiners

[16] and (iv) replacement of solute Ti. Based on the literature [3, 17], this work investigates the effect of solute Ta on grain refinement and Si-poisoning in Al-Si casting alloys. Chapter 4 is dedicated to effect of Ta in Sr-modified Al-Si based alloys.

Secondly, chemical modification, using a small amount of a certain modifying element is implemented to change the morphology of eutectic Si. In practice, the additions of Na [18, 19] or Sr [20, 21] are applied to obtain modified eutectic Si in as-cast microstructure. However, chemical modification using Na or Sr causes an increase in porosity and eutectic grain size. P is a ubiquitous trace element in all Al alloys. Al and P form the AlP phase which plays a role as a nucleation site for eutectic Si in Al-Si casting alloys [21–23] and therefore small eutectic grain size can be achieved. The addition of modifiers (e.g., Na, Sr) reacts with P [23], removes AlP and forms Na_3P or Sr_3P_2 compounds. Free modifier then provides modification effect of eutectic Si, however, neither Na_3P nor Sr_3P_2 are suitable nucleation sites for eutectic Si, resulting in increasing eutectic grain size. Note that increasing the concentration of P with the recycling process requires increasing additions of modifiers [23]. Although the modification causes pore formation, the benefit of changing the morphology of eutectic Si is still dominant and widely used in foundry practice. Eu as the only element from the rare earth group is known to achieve a fully modified eutectic structure [24]. In Al-Si melt, Eu depletes the AlP (similar to Na or Sr) and forms the EuP phase. Although the EuP is not as efficient nucleant as AlP, the EuP is suggested to nucleate eutectic Si and thereby refine the eutectic grains [25]. The second research focus is to modify eutectic Si via Eu and P additions in combination with solute Ta used as a grain refiner. Chapter 5 is dedicated to effect of Eu and P in Ta-refined Al-Si based alloys.

Thirdly, the modification effect of Eu is reduced with increasing P [25]. As mentioned, above the addition of modifying elements changes not only the growth morphology but also the nucleation behaviour of eutectic Si. Nucleation studies are very challenging due to possible impurity effects on nucleation, short nucleation time, very small size and overall reproducibility of experimental measurements. In the present work, the influence of solute elements (Eu, P and Ta) on nucleation and growth of eutectic Si is studied using entrained droplet technique [26, 27] in high-purity (HP) Al-5Si alloys (wt. %, used here after unless stated otherwise). The goal is to elucidate the effect of Eu, P and Ta on the shape, size, size distribution of eutectic droplets. Chapter 6 describes the effect of Eu, P and Ta on microstructure and nucleation kinetics of rapidly solidified Al-Si based alloys.

Lastly, casting defects (e.g., gas porosity and shrinkage porosity) negatively influence mechanical properties. Most of the casting defects are formed in the later stage of solidification [28]. Therefore, the effect of solutes is investigated to achieve fine solidification microstructure to reduce the amount of casting defects or at least to achieve fine distribution of casting defects compared with conventional melt treatments. Behaviour of solutes on the distribu-

tion of casting defects is summarised in Chapter 7.

Theoretical background

This chapter briefly covers the theoretical description of the basic thermodynamics of solidification, nucleation and growth. The special focus is on grain refinement and modification of eutectic Si in Al-Si based alloys.

2.1   Basic thermodynamics

Any phase transformation (e.g., solidification) is driven by the change in Gibbs free energy (G) and expressed as [29–31]:

$$G = U + p \cdot v - T \cdot S \tag{2.1}$$

where U is the internal energy (amount of work required to change a system from a standard state to a present state), p is the pressure, v is the volume, T is the absolute temperature and S is entropy. In terms of entropy, the liquid has a larger disorder than the solid, thus the entropy is higher in liquid and this disorder leads to an increase in the volume of most materials during melting [29].

During melting the metal or solidification of the metal, we need to get through the equilibrium point. This equilibrium is attained at the minimum of Gibbs free energy. The melting process operates at the constant pressure, therefore the equation 2.1 can be written as [29, 31–33]:

$$G = H - T \cdot S \tag{2.2}$$

where H is the enthalpy ($H = U + p \cdot v$) [29, 31–33]. At the melting temperature (T_m), two phases coexist and its change in free energy ($\Delta G = G_L - G_S$) is zero [29, 31, 33]:

$$\Delta G = \Delta H_F - T_m \cdot \Delta S_F = 0 \tag{2.3}$$

where $\Delta H_F = H_L - H_S$ is the enthalpy change during melting (latent heat) and $\Delta S_F = S_L - S_S$ is the entropy of fusion (melting) [29, 31, 33]. ΔH_F and ΔS_F can be obtained from

the following equations:

$$\Delta H_F = T_m \cdot \Delta S_F \tag{2.4}$$

$$\Delta S_F = \frac{\Delta H_F}{T_m} \tag{2.5}$$

At temperature T, which is lower than T_m, and inserting equation 2.5 to equation 2.3 we get [29, 32]:

$$\Delta G = \Delta H_F - T \cdot \frac{\Delta H_F}{T_m} = \Delta H_F \cdot \frac{T_m - T}{T_m} = \Delta S_F \cdot \Delta T \tag{2.6}$$

where ΔT is the undercooling. ΔT drives the transformation from liquid to solid. The equation for undercooling can be defined as [29, 32]:

$$\Delta T = \frac{\Delta G}{\Delta S_F} \tag{2.7}$$

No transformation occurs when ΔT is zero, because the system is in equilibrium. However, this is only a thermodynamic classification of undercooling, representing that undercooling is required for solidification. Local undercooling at the interface can be affected by several influences and therefore this local undercooling (undercooling, used here after unless stated otherwise) can be described as [29]:

$$\Delta T = \Delta T_k + \Delta T_p + \Delta T_r + \Delta T_t + \Delta T_c \tag{2.8}$$

where ΔT_k is the kinetic undercooling, ΔT_p is the pressure undercooling, ΔT_r is the curvature undercooling, ΔT_t is the thermal undercooling and ΔT_c is the constitutional undercooling [29, 34]. ΔT_k describes the net difference in atoms transported from liquid to solid. For metals, the ΔT_k is 0.01-0.05 K and therefore is neglected. ΔT_p represents the increase in undercooling via increasing pressure at the solid-liquid interface or at the whole volume, however, for metals the ΔT_p is negligible. Only the ΔT_r, ΔT_t, ΔT_c are relevant [29] for the purposes of this work. ΔT_r describes the increase in energy via a newly formed interface. The small radius (=high curvature) of the formed solid possesses a high surface to volume ratio and therefore undercooling increases with increasing curvature [35]. For pure undercooled metal, ΔT_t describes the temperature difference between the equilibrium of solid-liquid temperature (T_{eq}) and actual liquid temperature (T_l) [29]. ΔT_c is the contribution due to the presence of solutes rejected by solid during solidification of an alloy [35]. Alloys transform gradually from liquid to solid in temperature interval (freezing range), while the pure metals solidify at one temperature [36]. More detail about undercooling is shown in section 2.3.

2.2   Nucleation

Nucleation of a new phase is the first step to transform a solid from a liquid [37] and is referred as the formation of cluster atoms with crystalline structure [32]. Nucleation is also

very hard to observe since only atomic clusters are involved, therefore only theoretical models and experiments are used to verify this very early stage of solidification [38]. Clusters large enough to be stable are called nuclei, while smaller clusters are called embryos [29, 31, 32, 38]. Whether the cluster is viable or not with decreasing temperature below the freezing point is described by thermodynamics. Nucleation also applies in broader contexts such as defects (gas porosity). The theory of nucleation is divided into homogeneous nucleation and heterogeneous nucleation, respectively and are described below [29, 31, 32]. The third way that the crystals are formed is called crystal multiplication [29, 39].

2.2.1 Homogeneous nucleation

The mobility of atoms is high at temperatures higher than the melting point. Even though the number of atoms required to form a cluster according to homogeneous nucleation is very high, with increasing undercooling (ΔT), the size of the cluster (thus the number of atoms) is decreasing. Required undercooling in order to achieve homogeneous nucleation is usually large (e.g., larger than 100 K) [29, 32]. The nucleation of crystal from the melt depends on two processes. Firstly, thermal fluctuations lead to the formation of crystal clusters. Secondly, the creation of a solid-liquid interface [38]. The number of atoms required to form a critical nucleus is described by [29, 38]:

$$n \cong \frac{4\pi R^3}{3v} \tag{2.9}$$

where n is the number of atoms to form a critical radius, R is the spherical radius, and v is the volume of the number of atoms. The sum of interface and volume terms of Gibbs free energy describes the critical condition for nucleation and is given by [38]:

$$\Delta G = \Delta G_i + \Delta G_v = \gamma_{SL} \cdot A_{\mathrm{SP}} - \Delta g_{SL} \cdot V_{\mathrm{SP}} \tag{2.10}$$

where ΔG is Gibbs free energy, ΔG_i is surface free enthalpy, ΔG_v is volume free enthalpy, γ_{SL} is solid-liquid interface energy, A_{SP} is the surface area of spherical nucleus, Δg_{SL} is free energy between solid and liquid per unit volume, V_{SP} is the volume of a sphere.

Fig. 2.1 shows the free enthalpy change as a function of cluster radius, including ΔG_i and ΔG_v. The homogeneous nucleation of the spherical cup, including geometry, equation 2.10 can be simplified as follows assuming pure Al and $\Delta T > 0$ [29–33, 38]:

$$\Delta G_{\mathrm{hom}} = \gamma_{SL} \cdot 4\pi R^2 - \frac{4\pi R^3}{3} \cdot \Delta s_F \cdot \Delta T \tag{2.11}$$

where Δs_F is the entropy of fusion per unit volume, ΔT is undercooling. The first term on the right-hand side of the equation is R^2 and positive, which represents the energy barrier or penalty by creating a surface. The second term is proportional to R^3 and negative, indicating the release of energy when $\Delta T > 0$. In other words, if R is small, the penalty will exceed
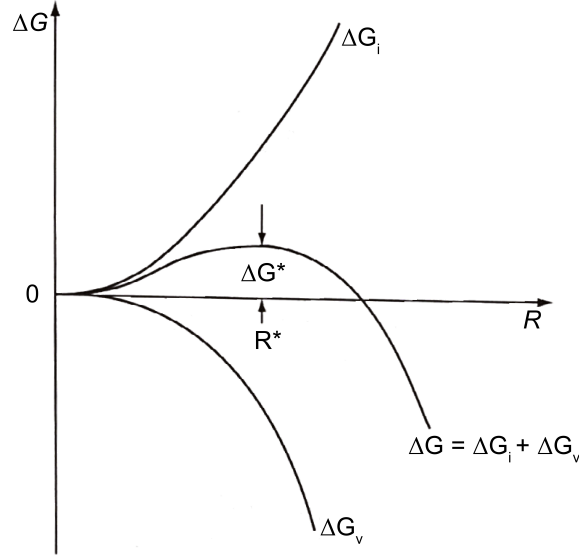
Figure 2.1: Free enthalpy change of a sphere crystal cluster with radius R [33].

the liberation of energy of the volume. Whereas, if R is large, the volumetric contribution is dominant. The critical radius (R^*) at which this contribution creates maximum ΔG_{hom} is called a homogeneous nucleation barrier that needs to be exceeded in order to form and grow the nuclei.

Work required to form a critical nucleus

Free enthalpy change referred as undercooling of the melt (ΔT) shows the maximum ΔG, its maximum value can be interpreted as a work of formation to exceed in order to form a nucleus that grows. This maximum value is given by [38]:

$$\frac{d(\Delta G)}{dR} = 0 \tag{2.12}$$

Size of critical spherical nucleus (R^*) for homogeneous nucleation is obtained by applying equation 2.12 on equation 2.11 [30–33, 40]:

$$R^* = \frac{2\gamma_{SL}}{\Delta s_F \cdot \Delta T} \tag{2.13}$$

Additionally, number of atoms required to form R^* is described by [30, 32, 38]:

$$n^* = \left(\frac{32\pi}{3v}\right) \cdot \left(\frac{\gamma_{SL}}{\Delta s_F \cdot \Delta T}\right)^3 \tag{2.14}$$

Variation of cluster radius R with undercooling ΔT is illustrated in Fig. 2.2. The $R_{\max}$ increases with decreasing temperature [36]. When $R_{\max}$ reaches R^* the crystal cluster is
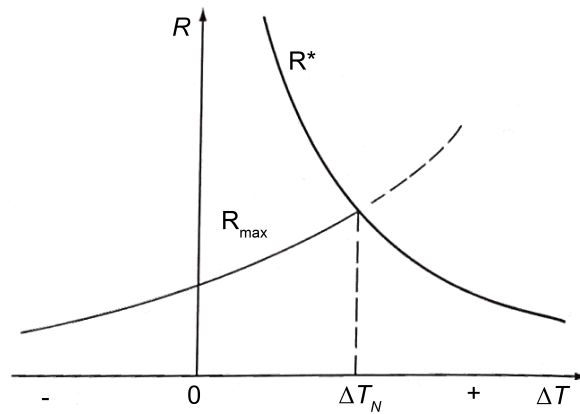
Figure 2.2: Effect of undercooling on the critical size of a nucleus [33].

formed at nucleation undercooling of ΔT_N. The work of formation of homogeneous nucleation energy barrier to form a critical nucleus (ΔG^*) is obtained by introducing equation 2.13 into equation 2.11 [29–31, 33, 38, 40]:

$$\Delta G^* = (\frac{16\pi}{3}) \cdot (\frac{\gamma_{SL}^3}{(\Delta s_F \cdot \Delta T)^2}) \tag{2.15}$$

Nucleation rate of homogeneous nucleation

The nucleation rate describes the number of grains nucleated within a melt volume and time [38]. The amount of energy required to form a new surface area of a new structure is described as ΔG_A [36]. If the liquid contains the number of atoms in liquid n_l, then the number of atomic clusters n^* that reached the size of the critical radius R^* can be obtained [29–33, 38, 41]:

$$n^* = n_l \cdot exp(-\frac{\Delta G_A}{k_B T}) \tag{2.16}$$

where ΔG_A is activation energy to overcome the energy barrier to transfer atoms from liquid to a crystal, k_B is Boltzmann constant and T is the temperature. A critical nucleus of R^* grows in case one more atoms are added from liquid to nucleus [31–33, 38]. These atoms have to overcome the activation Gibbs free energy barrier (ΔG_A) for the transfer of atoms from liquid to nucleus [29, 31]. Therefore, to estimate the nucleation rate, the size of the cluster and free energy are required [32]. The nucleation rate (I) of atoms being attached (equation 2.17) is proportional to the number of critical clusters (n^*) and the rate of incorporation of new atoms in nuclei f, sometimes called 'jump frequency' (equation 2.18). Here one question arises: "How fast do the solid nuclei appear in the liquid at a given undercooling?". The answer to the question is covered in the following equations [29, 31–33, 38]:

$$I = n^* \cdot f \tag{2.17}$$

$$f = f_0 \cdot p_a \cdot exp(-\frac{\Delta G_A}{k_B T}) \tag{2.18}$$

where f_0 is the atomic vibration frequency and p_a is the probability of capturing an atom to the surface. Inserting equation 2.16 and 2.18 into equation 2.17 we obtain the nucleation rate equation:

$$I^{\text{hom}} = f_0 \cdot p_0 \cdot n^* = f_0 \cdot p_0 \cdot n_l \cdot exp(-\frac{\Delta G^*}{k_B T}) \cdot exp(-\frac{\Delta G_A}{k_B T}) \tag{2.19}$$

where $f_0 \cdot p_0 \cdot n_l = I_0^{\text{hom}}$ is the pre-exponential constant. For metals, the constant has the value $I_0 = 10^{42}$ [m$^{-3}\cdot$ s^{-1}] [29]. Therefore, the equation 2.19 can be rewritten as:

$$I^{\text{hom}} = I_0^{\text{hom}} \cdot exp(-\frac{16\pi \cdot \gamma_{SL}^3}{3 \cdot (\Delta s_F \cdot \Delta T)^2 \cdot k_B T}) \cdot exp(-\frac{\Delta G_A}{k_B T}) \tag{2.20}$$

As mentioned before, nucleation is a thermally activated process that strongly depends on temperature [32, 42]. The nucleation rate greatly increases with increasing ΔT. Pure melt with no impurities and large undercooling is required for homogeneous nucleation. However, this rarely occurs in practice as the impurities contribute to the nucleation process. How impurities can affect the nucleation is described by heterogeneous nucleation [32].

2.2.2 Heterogeneous nucleation

In the theory of heterogeneous nucleation of solids, the nucleation is initiated on a foreign surface such as a surface of a mould or crucible, oxide layer or foreign particle suspended in the melt [32, 43]. Foreign particles are unintentional impurities or intentionally added substrates to control the microstructure. The latter is referred as inoculation. Heterogeneous nucleation takes place at a higher temperature than homogeneous nucleation, otherwise, the particles would have no effect [32, 33]. Particles of various sizes do not nucleate above a particular single nucleation temperature (T_N), however, below that temperature, the nucleation is nearly instant [32]. Nucleation potency is characterised by the nucleation temperature of each foreign particle [32]. The heterogeneous nucleation process is facilitated due to foreign surface, thus the number of atoms and the work of formation are significantly lower compared to homogeneous nucleation [32, 38]. Fig. 2.3 demonstrates the nucleation on a particle (foreign substrate). The forces applied to a particle are described in the equation 2.21, where γ_{SL} is solid-liquid interface, γ_{LP} is surface energy between liquid and particle, γ_{SP} is surface energy between solid and particle and θ is wetting angle [29–33, 38, 44, 45]. It should be noted that the structure and chemistry of the substrate should match well with those of the solid in order to be energetically favourable to form a solid nucleus on the substrate [32]. This and other conditions of potent substrates are discussed more in detail at the end of this section.

$$\gamma_{LP} = \gamma_{SP} + \gamma_{SL} \cdot cos\theta \tag{2.21}$$
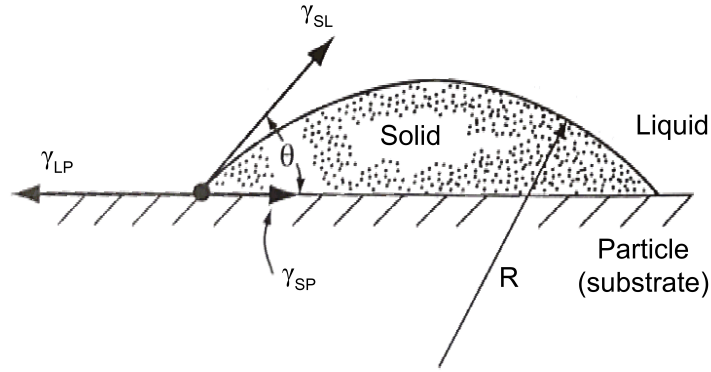
Figure 2.3: Heterogeneous nucleation of the spherical cap at liquid-substrate interface [33, 40]. Note that surface energies are all isotropic and gravity is neglected.

The geometric factor $(f(\theta))$ reducing the nucleation barrier can be expressed as the ratio of the volume of a spherical cap (V_s) and the volume of a full sphere with the identical radius $(4\pi R^3/3)$ [29, 32, 33, 38].

$$f(\theta) = \frac{V_s}{4\pi R^3/3} = \frac{(2 + cos\theta) \cdot (1 - cos\theta)^2}{4} \tag{2.22}$$

In terms of heterogeneous nucleation, the numerical value of equation 2.22 is $f(\theta) < 1$. In case that $f(\theta) = 0$, there is no nucleation barrier and thus immediate growth can occur, whereas if $f(\theta) = 1$, the homogeneous nucleation occurs [29, 32, 33, 38]. Except for parameters required to describe homogeneous nucleation, the only single parameter (θ) can be used to describe heterogeneous nucleation [42] .

Work required to form a nucleus

The number of atoms required to form a nucleus (n^*) and the work required to form a nucleus $(\Delta G^* = \Delta G_{\mathrm{hom}})$ is decreased due to the geometric factor of wetting angle $f(\theta)$. Thus, the number of atoms required to form a nucleus n^*_{het} from equation 2.16 equals to $n^*_{\mathrm{hom}} \cdot f(\theta)$ [32]. The critical radius of a spherical nucleus (R^*) is constant for both heterogeneous and homogeneous nucleation [32, 38]. The effect of wetting on the work required to form a solid nucleus for homogeneous and heterogeneous nucleation is illustrated in Fig. 2.4 and described in the following equation [29, 30, 32, 33, 38, 40, 46].

$$\Delta G_{\mathrm{het}} = \Delta G_{\mathrm{hom}} \cdot f(\theta) = (\frac{16\pi}{3}) \cdot (\frac{\gamma_{SL}^3}{(\Delta s_F \cdot \Delta T)^2}) \cdot f(\theta) \tag{2.23}$$

Due to the geometric factor of wetting angle $f(\theta)$ only a small undercooling ΔT is required to form a stable heterogeneous nuclei [32]. To obtain a good wetting (small θ), the γ_{SL} interface energy (Fig. 2.3) should be small [47].

27
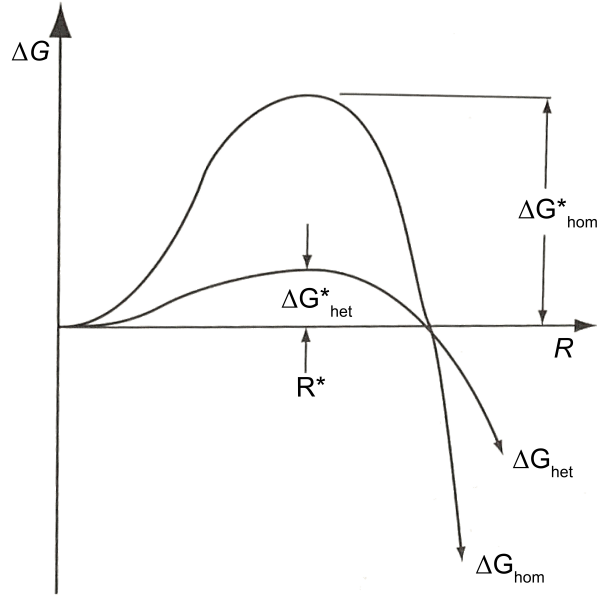
Figure 2.4: Gibbs free energy of homogeneous (no wetting) and heterogeneous (wetting) nucleation [33].

The nucleation rate of heterogeneous nucleation

The number of sites for heterogeneous nucleation is determined by the amount (n_p) and the type of the particles [29]. This is in contrast to homogeneous nucleation, where every atom in liquid (n_l) is a potential nucleation site. Therefore, the amount of n_p is significantly lower than n_l [29, 32]. The equation for heterogeneous nucleation rate is then written as [29, 32]:

$$I^{\text{het}} = f_0 \cdot p_0 \cdot n_p \cdot exp(-\frac{\Delta G_{\text{het}}}{k_B T}) \cdot exp(-\frac{\Delta G_A}{k_B T}) \tag{2.24}$$

The $I_0^{\text{het}} = f_0 \cdot p_0 \cdot n_p$ is the pre-exponential constant [32]. Therefore, the equation 2.24 can be rewritten as:

$$I^{\text{het}} = I_0^{\text{het}} \cdot exp(-\frac{16\pi \cdot \gamma_{SL}^3 \cdot f(\theta)}{3 \cdot (\Delta s_F \cdot \Delta T)^2 \cdot k_B T}) \cdot exp(-\frac{\Delta G_A}{k_B T}) \tag{2.25}$$

It should be noted that I_0^{het} is smaller compared to I_0^{hom}, however the $f(\theta)$, depending on the value of θ, can be much more important [32]. The heterogeneous nucleation rate increases with increasing the number of nucleation sites since I^{het} is proportional to n_p [29].

Properties of a potent foreign substrate (inoculant)

Nucleus lattice parameters are strained in order to achieve a minimum free energy [42]. During nucleation, atoms are attached from liquid to the solid nucleant, therefore the closer the nucleant lattice is to the forming (nucleating) phase, the easier nucleation should be

[29, 42]. This phenomenon is described as lattice mismatch δ and is calculated as [29, 42]:

$$\delta = \frac{a_n - a_0}{a_0} \cdot 100\% \tag{2.26}$$

a_n and a_0 are lattice parameters of nucleant (e.g., particle) and nucleating phase (e.g., primary phase) at the interface, respectively [29, 42]. It is reported that the significant grain refinement is observed for $\delta < 10$ % (equation 2.26) [42]. The nucleation process is sensitive to interface energy changes with regard to the nucleus surface, therefore, any contamination may result in a change of the contact angle and hence the nucleation properties [48]. It is generally accepted that if the symmetry of surface planes, spacing and bonding forces of nuclei are close to those of embryo, the low contact angles and good nucleation properties can be expected [48].

Author [29] claims that the crystal structure of the nucleant and nucleating phase may differ. Nevertheless, the atomic spacing and distribution of atoms of the nucleating phase 'must' have one or more planes similar to that of the nucleant. Besides that, the nucleant should exhibit: a low contact angle (θ) or high surface energy (γ_{LP}), expose a large area to the liquid via increasing number density (n_p) or have a rough surface of nucleant, solid nucleant should have a high thermal stability in the liquid to avoid depletion, a melting point must be higher than liquid temperature to avoid dissolution, the particle should be larger than a critical size R^* and lastly, the ability to nucleate at a very low undercooling (ΔT) [29, 44].

Overall, very good nucleating properties are achieved when the inoculant and nucleating phases are identical. For example, inoculation of Al melt by Al dendrites exhibits no wetting angle and therefore requires no undercooling [38]. However the stability of Al dendrites above the melting point of Al alloys is problematic, therefore, inoculation via Al dendrites is achieved by mechanical forces during solidification.

2.3 Growth

The growth is described as the moving (growing) of an interface between liquid and nucleus towards liquid. After the embryo reaches R^*, spontaneous growth occurs [29]. The atoms are added to the crystal to continue the growth. Growth is limited by the kinetics of atom attachment to the interface, capillarity and diffusion of heat and mass [38]. One would expect that after reaching the critical radius R^*, the sphere would grow until reaching macroscopic dimensions. However, spherical morphology becomes unstable by perturbations in shape. Then the solid growths in preferred growth directions, the preference is derived from anisotropy [32]. The growth mechanism mainly depends on the nature of the solid-liquid interface [29]. On the atomic scale, there are two different types of interface: atomically rough (non-faceted) and atomically smooth (faceted) [29, 33, 38]. On the micro scale, the
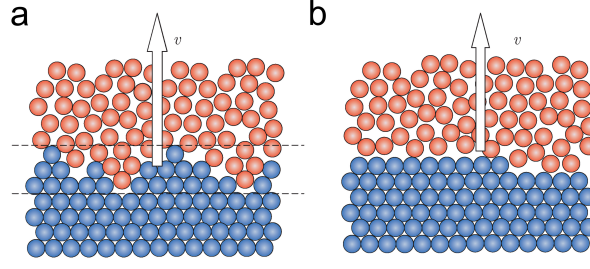
Figure 2.5: (a) Atomically rough interface and (b) atomically smooth interface [32].

atomically rough interface advances through continuous growth and the atomically smooth interface advances through lateral growth [29, 33, 38]. Continuous growth is significantly faster than lateral growth. The calculated undercooling required for continuous growth is 0.01-0.05 ºC, while for lateral growth it is 1-2 ºC [29].

Materials with a high value of surface energy anisotropy tend to have a large entropy of fusion (ΔS_F) [32]. Dimensionless Jackson alpha factor α_J can conveniently predict the crystallisation behaviour [32, 38, 49]. Calculation of α_J is shown in equation 2.27 [32, 38]:

$$\alpha_J = \frac{\Delta S_F}{R_{\text{gas}}} \tag{2.27}$$

where the R_{gas}= 8.314 [J· mol^{-1}· K^{-1}] is gas constant. It is proposed that if $\alpha_J < 2$ the non-faceted crystal is formed and if $\alpha_J > 2$ the faceted crystal is formed [32, 38]. α_J for Al and Si are 1.30 [32] and 3.59 [32] ($\sim$5 [49]), respectively. In other words, a material with energetically difficult atom attachment to the surface of a growing solid exhibits higher ΔS_F [38] and therefore, the faceted growth can be expected.

2.3.1 Continuous growth

Continuous growth involves the random incorporation of atoms on the surface via diffusion. This interface is atomically rough and each step corresponds to an atomic distance (Fig. 2.5) [29]. Continuous type of growth results in a non-faceted interface and is associated with metals (Al) [29, 33, 38]. Atoms can be attached to any site of a solid surface from a liquid [38]. The interface is disordered and atoms can arrive at random positions with insignificant effect on the equilibrium of the interface [33].

2.3.2 Lateral growth

Lateral growth progresses through liquid across a single atomic layer [29]. Such a smooth interface provides low accommodation sites for attaching atoms from liquid [33]. Lateral type of growth results in a faceted and is associated with non-metals (Si) [29, 33, 38]. A more complex situation occurs when an equilibrium interface is atomically smooth. As mentioned
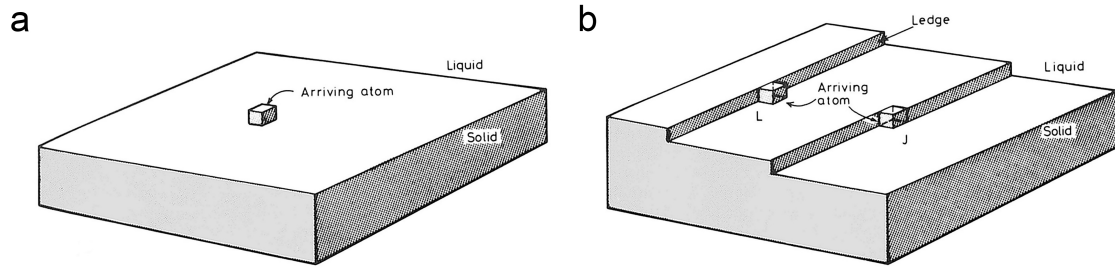
Figure 2.6: (a) Atomically smooth surface with one attached atom and (b) lateral growth of faceted morphology [33]. L corresponds to ledge and J corresponds to jog. Note that squares represent the atoms.

above, atomically smooth close-packed interfaces are preferably formed for materials with a high entropy of melting (ΔS_F). Therefore, the interface minimum free energy corresponds to the internal minimum energy. In the case of the atomically smooth surface, there is a high probability that the atom will not be attached and jumps dissolve back to liquid (Fig. 2.6a), however, if the ledges or jogs are present the atoms willingly join the surface. Therefore growth depends on ledges and jogs, as non-equilibrium features, on the interface (Fig. 2.5b and Fig. 2.6b) [33]. According to author [33], there are different ways to supply the ledges and jogs at the interface: by repeated surface nucleation, by spiral growth and from twin boundaries. In this work, the main focus is the growth of eutectic Si, therefore only the support of ledges and jogs from twin boundaries is further discussed.

Growth from twin intersections

Eutectic Si grows with twinning plane {111} growing to liquid in <211> as germanium [50] and the angle at the twin planes at the twin boundary is 70.5º (141º). When the two crystals in different orientations are in contact, that contact point plays a role as a permanent source of steps for the growth of eutectic Si. This point is the intercept of interfacial facets at the twin boundary, therefore providing a new source of steps. It is similar to spiral growth as shown in Fig. 2.7 [33].

2.3.3   Interface stability

During growth, the solid-liquid interface is subjected to random disturbances by thermal fluctuations, grain boundaries or insoluble particles. Then the stable or unstable interface is distinguished based on the response to disturbances [38].

Casting a pure metal to a mould results in the initiation of solidification on the wall of the mould. The heat flow direction is from hotter liquid to colder solid and the solid-liquid interface grows in the direction opposite to heat flow. The temperature ahead of the growing interface is higher, therefore the temperature gradient ($G_T = dT/dz$, where z is distance) is
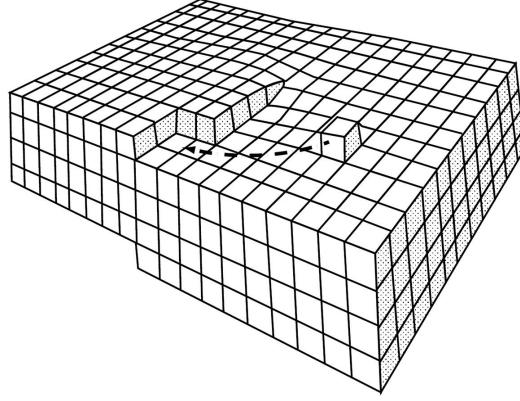
Figure 2.7: Spiral growth of a screw dislocation providing a new steps [33].

positive. A stable interface is observed if $G_T > 0$ [38, 51] and the growth is then controlled by heat flow [31, 33]. If perturbation is formed, the tip of perturbation is located further in the hotter liquid, leading to remelting the tip and stabilising the interface [38, 52].

In an undercooled melt of pure metal, the crystal formed in the volume of liquid and the heat flow direction is from hotter solid to cooler liquid, the temperature gradient is therefore negative ($G_T < 0$). As a result of $G_T < 0$, the solid-liquid interface is unstable. Thus, if the perturbation occurs, the perturbation tip is located in a cooler liquid and more latent heat from a hotter solid can be transferred to the liquid. [38, 52, 53].

Alloy solidification is controlled by heat conduction and solute diffusion [29, 33]. In the alloy, the solutes are piled up ahead of the solid-liquid interface due to the solubility difference in solid and liquid [54]. Then the differences in composition at the solid-liquid interface are described using partition coefficient [32, 36, 38, 55]:

$$k = \frac{C_s}{C_l} \tag{2.28}$$

where C_s is the concentration in the solid and C_l is the concentration in the liquid. Solute atoms are rejected because their solubility in the solid is less than in liquid ($k < 1$), therefore the concentration of solute in the remaining liquid increases [54]. The concentration difference at the solid-liquid interface (ΔC_0) can be calculated as [35, 38]:

$$\Delta C_0 = \frac{C_0}{k} - C_0 = \frac{C_0 \cdot (1 - k)}{k} \tag{2.29}$$

where C_0 is the concentration of solidified alloy. The solute rich layer ahead of the solid-liquid interface is formed with a thickness (δ_c) and calculated as [29, 38]:

$$\delta_c = \frac{2D}{V} \tag{2.30}$$

where D is the diffusion coefficient in liquid and V is the growth rate. Due to the accumulation of solutes, the liquidus temperature (T_l) is decreased [35]. As seen in the upper left part
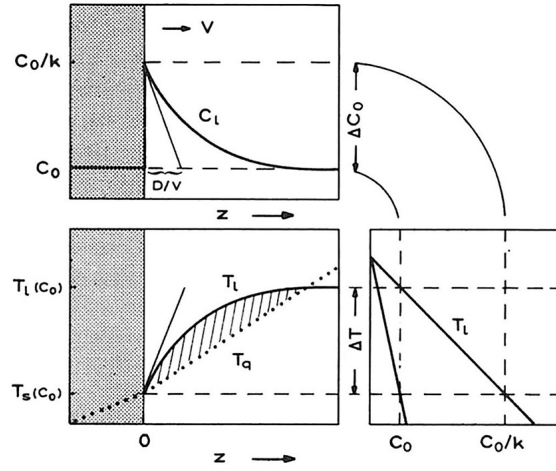
Figure 2.8: Constitutional undercooling (cross-hatched) region at the planar interface [38].

of Fig. 2.8, with increasing distance (z) from the interface, the C_l decreases exponentially, according to equation 2.31, until the C_l is equal to the (alloy concentration) composition of a solid (C_0) [38]:

$$C_l = C_0 + \Delta C_0 \cdot exp^{\frac{-V \cdot z}{D}} \qquad (2.31)$$

It is also evident from Fig. 2.8 that with increasing distance from the interface z, the T_l increases with further reducing C_l [38]. The solidus temperature (T_s) of an alloy is equal to T_l at the solid-liquid interface [32, 38]. Undercooling of an alloy at the composition C_0 is varying with ΔC_0 and can be described as follows [32, 35, 38, 51]:

$$\Delta T = T_l - T_s = -m \cdot \Delta C_0 \qquad (2.32)$$

where ΔT is the undercooling and m is the liquidus slope ($m = dT_l/dC$, where C is concentration). Thus, constitutional undercooling ΔT_c arises from the change of composition rather than temperature [36, 38, 53]. Undercooling depends on the cooling rate, growth rate, concentration of the alloying elements in the melt and the type of alloying element [31]. The thickness of the boundary film is described in equation 2.30. Involving the solutes in interface stability, the criterion to determine the stable solid-liquid interface can be written as [29, 32, 35, 38, 51, 53–56]:

$$\frac{G_T}{V} \geq \frac{\Delta T}{D} = \frac{-m \cdot \Delta C_0}{D} \qquad (2.33)$$

A stable planar interface is maintained only if $\frac{G_T}{V}$ is larger than $\frac{\Delta T}{D}$. Increasing $\frac{G_T}{V}$ forces the cells to become shorter until the interface becomes planar [39]. Solidification of unstable interface leads to columnar, columnar dendrite or equiaxed dendrite morphology of grains [38, 53, 57], as demonstrated in Fig. 2.9. It is evident that with increasing undercooling, the solid-liquid interface changes its morphology (Fig. 2.9). However, as seen in equation 2.33, besides the undercooling, the growth velocity is also an important parameter influencing
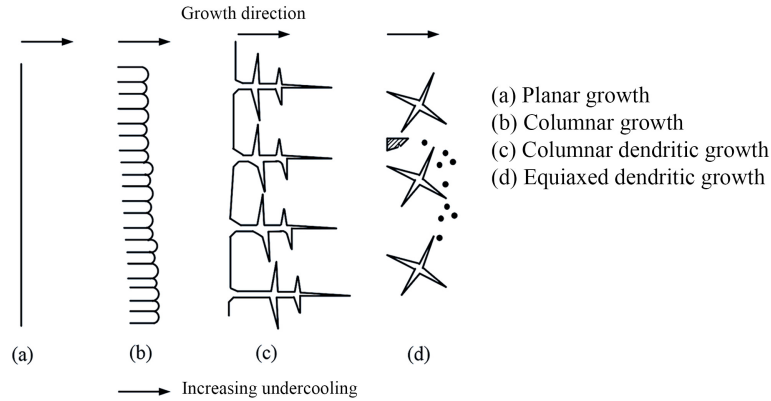
Figure 2.9: Growth morphology change with increasing undercooling [58].

the interface stability and therefore the morphology [32]. Since columnar and columnar dendritic solidification are not the main topic of this work, they are described very briefly. More attentions have been paid on equiaxed dendritic growth.

Columnar

Columnar growth applies when $G_T > 0$ [32, 38, 53, 57] and with increasing undercooling the interface depressions become interconnected, resulting in an elongated cell [29]. Cells usually grow perpendicular to the solid-liquid interface regardless of crystal orientations. However, with increasing growth rate, the cell deviates towards the preferred crystallographic growth direction (<100> in FCC) [29, 58, 59]. Usually, the growth orientation is close to the heat flow direction [38]. In alloys, solutes also can be rejected at the lateral direction and that reduces the solute concentration at the cell tip which leads to an increase in the temperature of the cell tip. Depressed areas (behind the tip) are accumulating an excess of rejected solutes [38, 60].

Columnar dendritic

With further increasing undercooling [29, 58] or increasing growth rate [53, 60] the cells are changed to dendrites. Directional solidification or constrained growth is ensured only if $G_T > 0$ [51]. Dendrite orientation is close to the heat flow [38]. Due to crystallographic effects, the cross section of the cell is not circular (round) but it forms the so-called 'maltese cross', in cubic materials [59]. Dendrites grow at a rate determined by the constitutional undercooling of the melt at their tips [53]. With further increasing undercooling, the tips grow into the liquid and develop side branches referred as tree-like morphology [53]. A transition from columnar to equiaxed (CET) occurs when equiaxed grains are nucleated in liquid ahead of the columnar zone. CET involves both nucleation and growth [57].

Equiaxed dendritic

In pure metal, during equiaxed growth the heat flows from the randomly oriented crystal into the undercooled melt ($G_T < 0$) and energetic contribution is only from ΔT_t and ΔT_r [52, 53, 59]. Pure metals cannot form equiaxed crystals because of the fact that absence of alloying elements hinders the driving force contribution from constitutional undercooling [53]. Large undercooling forces the initiation of growth ahead of solid-liquid interface [38, 59]. The driving force for the growth of the dendrite is expressed as undercooling of the melt in contact with the tip below T_l [29, 53]:

$$\Delta T = \Delta T_c + \Delta T_r + \Delta T_t \tag{2.34}$$

The preferred orientation of equiaxed dendrites is in all available directions [001] because only then the heat extraction is isotropic [38, 53, 59]. Equiaxed grains in pure metal are always observed with dendritic morphology due to thermal fluctuations [38, 52, 53].

The fully equiaxed structure is observed in alloys [51, 59]. In the case of Al alloys, the equiaxed growth can be induced in castings via the addition of efficient nucleant substrates [53]. The intention of adding nucleation substrates to achieve equiaxed solidification is called grain refinement. Dendrite morphology is finer with increasing cooling rate (heat extraction) [59]. Equiaxed growth in alloys, in addition to equiaxed growth of pure metal, is driven also by ΔT_c [38]. ΔT_c can be derived from Fig. 2.10.

The dendrite tip rejects the solutes more effectively than the planar interface, therefore the V of the dendrite tip is higher. The temperature of the tip is therefore also changed due to solute rejection. However, according to equation 2.30, with increasing V, the δ_c is decreasing [38]. In the dendritic solid-liquid interface (Fig. 2.10), the composition of the solid is not the same as C_0 in the planar interface. During equiaxed dendritic growth both the temperature and concentration decrease away from the interface [61].

V of the tip is driven by supersaturation Ω_c, constitutional undercooling ΔT_c and thermal undercooling ΔT_t. Supersaturation (Ω_c) is the driving force for the solute to diffuse at the dendrite tip [29, 38, 53]:

$$\Omega_c = \frac{\Delta C}{\Delta C^*} = \frac{C_l - C_0}{C_l \cdot (1 - k)} \tag{2.35}$$

where $\Delta C = C_l - C_0$ is concentration at the tip, and $\Delta C^* = C_l - C_s$ is the equilibrium concentration difference, depicted in Fig. 2.10. It should be noted that supersaturation is just a concentration ratio, meaning the degree of supersaturation is in the range of 0-1.

The relationship between supersaturation, growth rate and dendrite tip radius (R_{tip}) is described as $\Omega_c = P_c$ where $P_c = \frac{V \cdot R_{\text{tip}}}{2D}$ is the Péclet number for solute diffusion [38] and this relationship can be simplified as [29]:

$$V = \frac{2D \cdot \Omega_c}{R_{\text{tip}}} \tag{2.36}$$
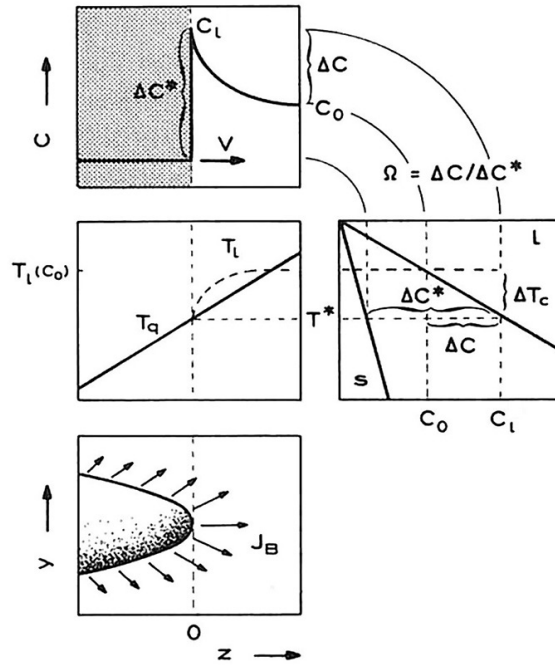
Figure 2.10: Concentration profile ahead of the dendrite tip [38].

With increasing supersaturation, the growth rate increases. The smaller dendrite tip radius is possessed with the high rejection rate of solutes and therefore the velocity of the growing tip is higher. Equiaxed dendrites in casting alloys grow under similar conditions to free growth model [61].

As the primary trunk of Al dendrite proceeds the growth, the second dendrite arms are formed. The secondary arms are formed because the paraboloidal interface of the cell tip becomes unstable [59]. With decreasing $\frac{G_T}{V}$ ratio, the cellular structure is changed to dendritic and secondary arms appear [36, 60]. These second arms determine the microstructure of Al alloys and are quantified as second dendrite arm spacing ($SDAS$), which measures the perpendicular distances between secondary arms of a dendrite [59, 62]. Secondary dendrite arms are coarser with increasing solidification time [53, 60]. $SDAS$ is controlled by cooling rate only [55]. Mechanical properties (namely strength and toughness) are improved with a lower $SDAS$ [62, 63]. $SDAS$ can be calculated using following equation [64]:

$$SDAS = \frac{L}{N-1} \tag{2.37}$$

where L is the entire length of the primary dendrite arm and N is the number of secondary arms. $SDAS$ within the microstructure can be measured as denoted in Fig. 2.11.
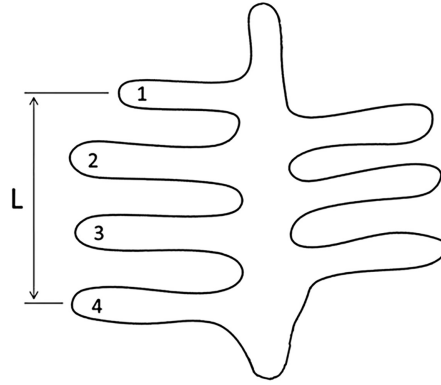
Figure 2.11: Schematic representation of $SDAS$ [64].

2.4 Role of solute in grain refinement of primary Al

Efficient grain refinement depends on both, nucleation and growth restriction [65, 66]. This chapter highlights the important role of solutes on the growth of equiaxed dendritic structure in Al alloys.

2.4.1 Growth restriction factor

Constitutional supercooling was first termed by Tiller [54] and later the supercooling parameter P (equation 2.38) was described as [67]:

$$P = \frac{m \cdot C_0 \cdot (k - 1)}{k} \tag{2.38}$$

It was reported that with increasing P the fine equiaxed structure is obtained [67]. Considering the planar interface, the P can be derived from Fig. 2.8. Assuming that solidus and liquidus lines are straight, P is equal to the freezing range ΔT [68]. The effect of increasing P on grain size in Al alloys was studied using TP-1 testing by Spittle and Sadli [68]. After reaching $P = 15$-20 the grain size remained constant, however, the amount of solutes was below 5 wt. % [68].

Solutes restrict grain growth, causing slow latent heat extraction. This results in the increase of undercooling to activate also the smaller particles and therefore small grain size is achieved. The effect of solutes on growth is summarised using the growth restriction factor (Q) [69]:

$$Q = m \cdot C_0 \cdot (k - 1) \tag{2.39}$$

where m is the liquidus slope, C_0 is the concentration of solute in the alloy and k is the partition coefficient. Table 2.1 summarises the effect of solutes in a binary system. Ti is generally accepted to be the strongest segregant in Al alloys [1, 40, 65]. High growth restriction elements are usually those that exhibit peritectic reactions with Al. However, to

Table 2.1: Phase diagram parameters for certain binary alloying elements with Al [1].

Element	k_i	m_i	$(k_i - 1) \cdot m_i$	Binary system
Ti	~9	30.7	245.6	Peritectic
Ta	2.5	70	105	Peritectic
V	4.0	10.0	60.0	Peritectic
Hf	2.4	8.0	11.2	Peritectic
Mo	2.5	5.0	7.5	Peritectic
Zr	2.5	4.5	6.8	Peritectic
Nb	1.5	13.3	6.6	Peritectic
Fe	0.02	-3.0	2.9	Peritectic
Si	0.11	-6.6	5.9	Eutectic
Mg	0.51	-6.2	3.0	Eutectic

calculate Q, the m and k are linear to the solute concentration [70] and it should be noted that only free solutes are assumed to play a role as growth restricting elements. Interaction of solutes is not involved and therefore the Q is suitable only for binary systems. However, 7 wt. % Si has the Q value of 41.3 and 0.01 wt. % Ti has the Q value 24.5 [65]. Si was reported to refine the α-Al grain size up to ~2 wt. %, where the solidification interval is the largest according to the equilibrium Al-Si phase diagram (Fig. 2.21 in section 2.7) [2]. It is evident then, that the main growth restriction effect in casting Al-Si based alloys is led by Si concentration, although the Ti is the strongest segregant. In multicomponent system, the Q is approximated as a sum of all solutes: $\sum Q = m_i \cdot C_0 \cdot (k_i - 1)$ [71].

It is evident from Fig. 2.12 that grain size decreases with increasing growth restriction till a certain limit. Above this limit, the grain size starts to increase with increasing solute concentration in the alloys.

In real systems where the solidus and liquidus are non-linear, the Q is calculated as follows [70, 72]:

$$Q = \frac{d\Delta T_c}{df_s} \tag{2.40}$$

where T is the temperature and f_s is the fraction solid. Solutes cause the initial rate of development of the constitutionally undercooled zone. This determines how quickly the undercooling is achieved. Q describes how quick the development of the constitutionally undercooled zone is at the beginning of the growth ($f_s=0$) [73]. The sum of Q is used as an approximation in alloys with high solute contents [73]. The study on multicomponent alloy systems by Schmid-Fetzer [70] highlighted the importance of thermodynamic software to determine Q. In summary, P describes the constitutional undercooling ahead of a planar interface, while Q describes how rapidly the constitutionally undercooled zone is achieved [73].
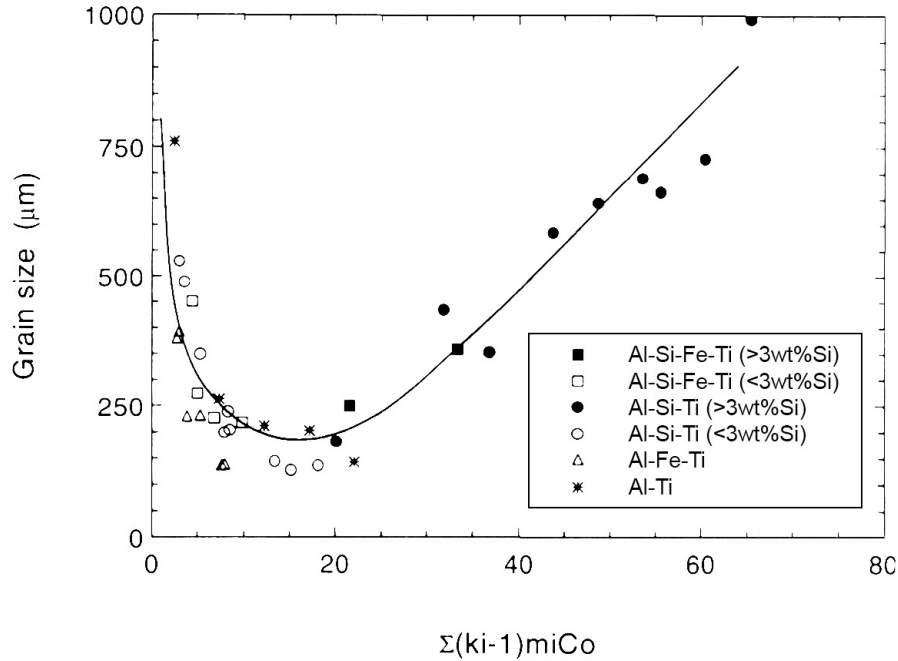
Figure 2.12: Effect of growth restriction on grain size in different alloys [1].

2.4.2 Free growth model

The free growth model links the nucleation and growth of the grains to growth restriction via solutes [52, 71]. The model is based on the model of Maxwell [69], where the classical steady state heterogeneous nucleation on dispersed substrates, followed by spherical growth was numerically modelled. The concept of Maxwell [69] model is that the growth of nucleated grains hinders the nucleation of other nuclei due to an increase in temperature via the release of latent heat. The model assumes (i) spatially isothermal melt, (ii) heterogeneous nucleation rate according to the classical nucleation theory, and (iii) spherical diffusion controlled growth. This model assumed one nucleation event per particle, while the particle size and contact angle (θ) are single values. It should be noted that the θ is considered as the indication of nucleation potency.

In the free growth model [71], the size distribution of nucleation sites (TiB$_2$) via the addition of commercial Al-5Ti-1B is considered. Particles are simplified to be discs with a diameter of d. The nucleus is formed on the face of the TiB$_2$ particle at very low undercooling via adsorption or the spherical cup. Nucleus grows laterally to fully cover the face of the particle and then the curvature radius of the interface needs to be reduced for subsequent growth to occur. The condition is that the curvature radius cannot be smaller than R^* for nucleation, from equation 2.13. If $d < 2 \cdot R^*$, then free growth is prohibited. However, with increasing ΔT, the R^* is reduced (Fig. 2.2). For a particle diameter d, the required free growth

39
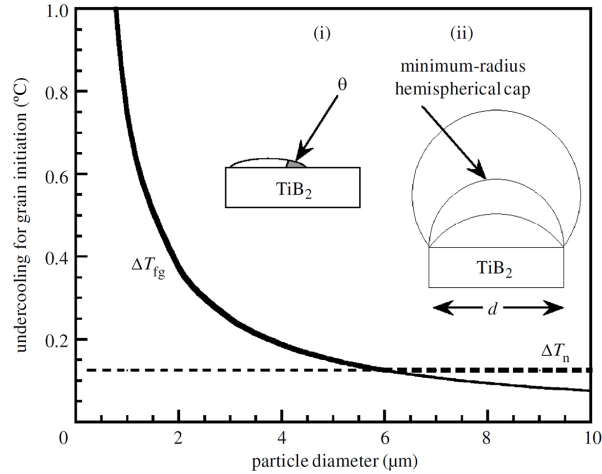
Figure 2.13: Undercooling is necessary for grain initiation according to the free-growth model plotted as a function of particle diameter [75].

undercooling (ΔT_{fg}) is defined as [71, 74]:

$$\Delta T_{\text{fg}} = \frac{4\gamma_{SL}}{\Delta s_f \cdot d} \tag{2.41}$$

In summary, equation 2.41 and $d < 2 \cdot R^*$ condition, describes that firstly, the nucleation occurs on the largest particles and then with increasing undercooling the smaller particles are activated until recalescence occurs due to latent heat release from the growth of nucleated grains and stops the nucleation. With increasing temperature from latent heat release, the nucleation events are remelted. The role of solutes is to restrict the growth, therefore to decrease the rate of latent heat release, which keeps the nucleation possible in the undercooled zone until recalescence [71]. ΔT_{fg} as a function of d is shown in Fig. 2.13, where (i) represents the classical spherical cap model for heterogeneous nucleation and (ii) shows a minimum-radius hemispherical cap on a TiB$_2$ particle [72]. Free growth model suites well for application in equiaxed growth in real situations. The amount of active particles to initiate grain growth in the grain refiner is only about 1 % [37, 71, 76]. Fig. 2.14 shows the amount of active TiB$_2$ (shaded) within the commercial Al-5Ti-1B grain refiner.

2.4.3 Interdependence theory

Interdependence theory links nucleant selection and growth and their interdependent outcomes with the presence of nucleants [37]. The concept of interdependence theory is developed from an analytical model predicting grain size based on constitutional undercooling [77, 78]. The vast majority of particles ($\leq$ 96 %) are not active inoculants in the melt [37]. Only 1-2 % of particles are reported to be active [37, 71]. With increasing cooling rate, the number of active nucleants is increases and the rate of development of undercooling for further nucleation increases [79].
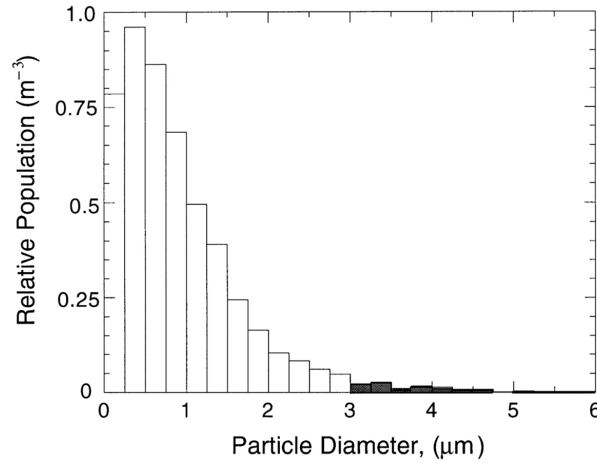
Figure 2.14: TiB$_2$ particle distribution in Al-5Ti-1B (wt. %) grain refiner. Distribution is determined from scanning electron microscopy (SEM) analysis [71]. Active particles under typical conditions are shaded.

In interdependence theory, the assumption that nucleation depends on the growth of a previously nucleated grain provides an indication of why only a small fraction of nucleants are active in grain refiners. It is reasonable then to describe the growth first and then the nucleation. The model links grain size diameter (d_{gs}) to be inverse of growth restriction factor (Q) [37]:

$$d_{gs} = \frac{1}{\sqrt[3]{\rho \cdot f_p}} + \frac{D \cdot \Delta T_N}{V \cdot Q} = \frac{1}{\sqrt[3]{\rho \cdot f_p}} + x_{cs} \qquad (2.42)$$

where ρ is the number density of inoculant particles added to the melt, f_p is a fraction of active particles, D is diffusion, ΔT_N is the undercooling required to cause nucleation (nucleation undercooling), V is growth rate and x_{cs} is the distance that grain needs to grow to create constitutional undercooling sufficient to trigger nucleation of a next grain [37].

To establish the spacing between the previously nucleated (and continuously growing) grains and subsequent nucleation events, the particle distribution needs to be established [37]. As shown in the free growth model (section 2.4.2), the undercooling required to initiate the grain growth decreases with increasing particle size, which is the same as in Fig. 2.15b. Fig. 2.15c shows that average spacing between the particles (S_d) increases with increasing particle size, clearly demonstrating that smaller particles exhibit smaller spacing and therefore more numerous grains can grow closer to each other. Undercooling required for growth initiation (T_N) decreases with increasing S_d, indicating that grain initiation is not likely to occur close to the grain (Fig. 2.15d) [37, 52].

The zone between the growing grain and another point, where the critical T_N is reached to initiate the growth is called the nucleation-free zone, as shown in Fig. 2.16 [37]. The amount of constitutional undercooling is reduced when the growth of new grain grows towards the

41
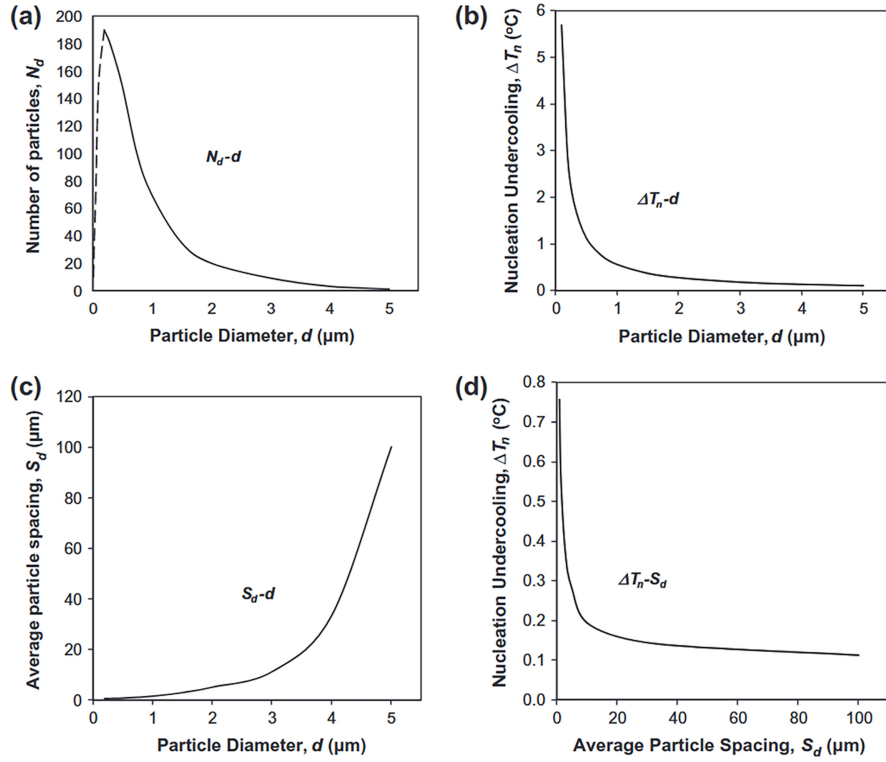
Figure 2.15: (a) The distribution of the number of nucleant particles for each diameter. The dashed line represents the smallest particles that are excluded in further images (b-d). (b) Influence of particle diameter on nucleation undercooling (T_N). (c) Particle spacing based on the particle diameter. (d) Nucleation undercooling plotted against particle spacing [37].

previous one. Initiation of a further grain between the two growing grains is improbable and therefore this distance between the two grains is assumed to be the final grain size [37].

In summary, the interdependence theory provides analytical expression to predict final grain size in inoculated melts and elucidates the low efficiency of Al-Ti-B based grain refiners [37].

2.5 Eutectic solidification

The fact that eutectic composes of more than one phase gives a wide variety of eutectic arrangements [38]. For simplicity, only eutectics consisting of two phases are considered. Author [38] stated that if the volume fraction of the minor phase is lower than 0.28, the fibrous morphology can be expected, while if the minor phase is 0.28-0.50, the lamellar morphology can be expected. The eutectic is formed via eutectic reaction when two solids are precipitated simultaneously and cooperatively from the liquid [47, 55]. The eutectic reaction can be written as Liquid $\rightarrow \alpha_{eut} + \beta_{eut}$ and occurs at the eutectic temperature [32, 33, 38, 47, 59].
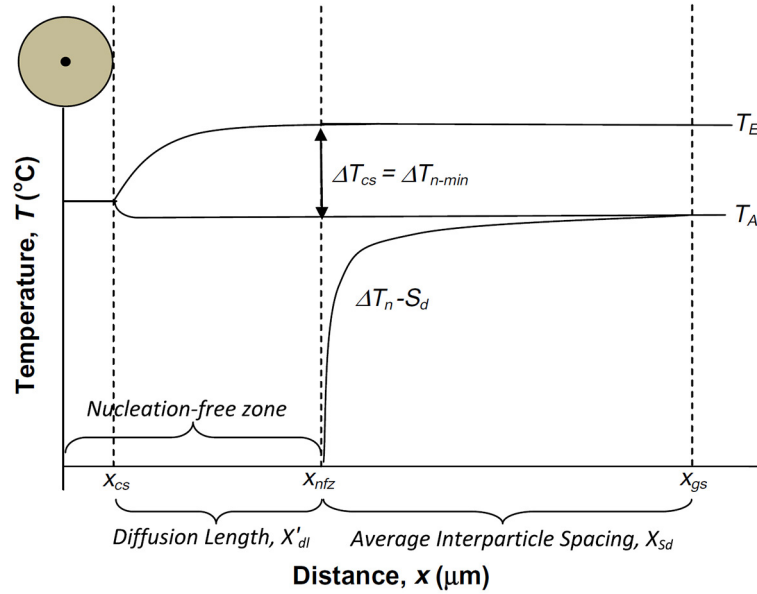
Figure 2.16: Scheme of interdependence theory. Sum of three regions (x_{cs}, diffusion length and average interparticle spacing) equals to grain size (d_{gs}) [37].

2.5.1 Regular and irregular eutectic

The α_{eut} and β_{eut} grow side by side and are parallel to the growth direction and perpendicular to the solid-liquid interface (Fig. 2.17a) [38]. Eutectic can be divided into coupled and degenerated eutectic based on their cooperation during their growth [33, 38]. Whether the growth proceeds regularly or irregularly is dependent on the nature of the atom's attachment to a particular phase [28]. The rate of detachment depends on the number of nearest neighbours, which binds the atom to the interface. However, the rate of attachment is based on the diffusion in liquid [38].

Coupled eutectic growth such as regular and irregular proceeds growth of α_{eut} and β_{eut} phase by lateral diffusion of solute in liquid. The α_{eut} phase rejects B atoms and β_{eut} phase rejects A atoms (termed as periodic diffusion field) [32, 33, 38]. Coupled growth provides lateral diffusion at the planar interface of each phase in the liquid (Fig. 2.17b), which maintains a low solute build-up ahead of both phases. Therefore the temperature of the growing interface is close to equilibrium [38]. Speed of lateral diffusion increases with decreasing interlamellar spacing (λ) [32], which leads to a faster growth [38]. However, with decreasing λ the curvature of lamellae at the interface increases. The effect of curvature is expressed as ΔT_r [38].

In order to maintain positive curvature of the interface (Fig. 2.17a), the interface undercooling (ΔT) has to be equal to the sum of ΔT_c and ΔT_r, otherwise, depression (negative curvature) at the centre of a lamella can occur at large λ to compensate large solute build-up.

43
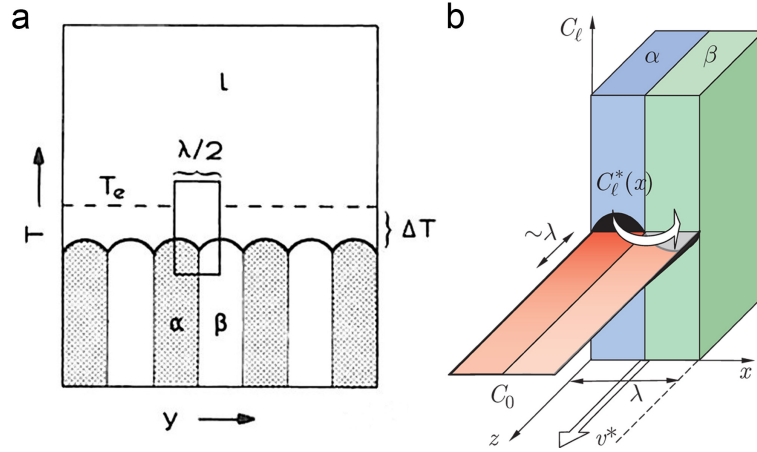
Figure 2.17: (a) Regular lamellar two phase eutectic morphology [38] and (b) two lamellae α_{eut} and β_{eut} growing in a coupled manner [32].

ΔT_c increases with increasing λ, while ΔT_r decreases with increasing λ [38].

Steady-state eutectic growth theory for lamellar and rod-like eutectic was established by Jackson and Hunt [80]. The steady-state solute field ahead of the planar solid-liquid interface of lamellar eutectic moving in z direction at a constant velocity v^* is described as [56, 80, 81]:

$$\frac{\partial^2 C_l}{\partial x^2} + \frac{\partial^2 C_l}{\partial z^2} + \frac{v^*}{D_l}\frac{\partial C_l}{\partial z} = 0 \tag{2.43}$$

where C_l is the solute concentration in the liquid, D_l is the diffusion coefficient in the liquid and v^* is the constant velocity of the eutectic solidifying with a spacing λ. Note that the simplified model for lamellar eutectic is two-dimensional, therefore independent of y-coordinate [81].

Regular eutectic (Fig. 2.17a) is achieved if both phases have a low entropy of melting (ΔS_F) [38]. Regular eutectic is typical for both non-faceted metals [32, 82] because they grow with a comparable growth rate and therefore they form a planar front [28]. Regular eutectic is highly ordered and predictable since it is controlled by diffusion [55].

Irregular eutectic is typically observed in metal-non-metal systems such as Al-Si and Fe-C alloys. α_{eut} is non-faceted (Al) and β_{eut} is faceted (Si) [28, 82]. If one phase grows faceted (high ΔS_F), then the eutectic exhibits an irregular structure such as in Al-Si [38]. Irregular eutectics are branching in order to adapt the growth according to local conditions. Larger λ is typical for irregular eutectic [38, 83]. The faceted phase of eutectic (Si in Al-Si eutectic) grows in a highly anisotropic manner until one lamellae can branch [38]. Faceted Si cannot promptly change or adjust the spacing based on the growth conditions. The spacing varies between the upper limit (λ_b) and extreme (λ_e), as denoted in Fig. 2.18. After meeting one of these limitations, the new branch is formed and spacing is therefore reduced. When two faceted β_{eut} phases diverges, the spacing increases (up to λ_b), therefore solute pile-up ahead
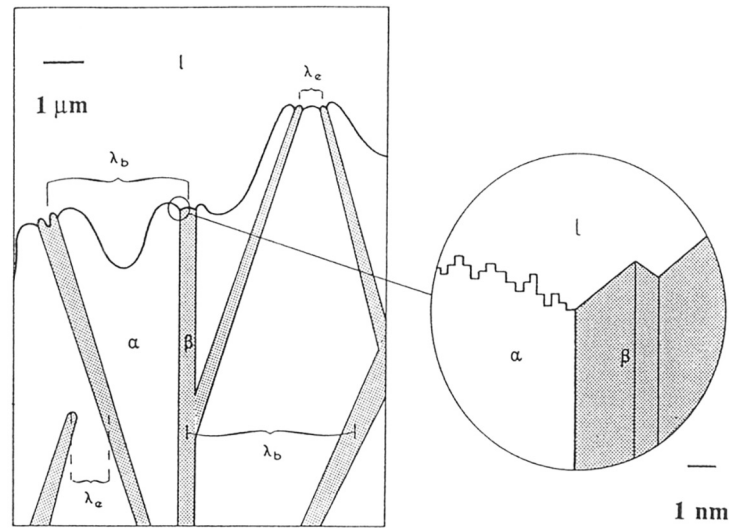
Figure 2.18: Irregular eutectic growth at micro and atomic scale [38].

of both phases increases. This results in the depression of solid-liquid interface and hence single lamella can split into two branches. When two faceted β_{eut} phases converges, the spacing decreases (up to λ_e), while the solute pile-up decreases with increasing curvature. At this point the interface undercooling is minimum and the growth is terminated. As so-called zig-zag growth occurs between λ_b and λ_e [38]. Lamellar spacing (λ) versus growth rate (V) is described as [38]:

$$\lambda^2 = \frac{1}{V} \cdot \frac{K_r}{K_c} \tag{2.44}$$

where V is the growth velocity, and $\frac{K_r}{K_c}$ is constant. The relationship (equation 2.44) shows that the lamellar spacing (λ), which depends on the diffusion rate, decreases with increasing growth velocity (cooling rate) [33, 38].

Recalled the equation 2.27 from section 2.3 is expanded to:

$$\alpha_J = \frac{\Delta S_F}{R_{\text{gas}}} \cdot \frac{CN_S}{CN_I} \tag{2.45}$$

where CN_S is the number of nearest-neighbour sites in a layer parallel to the surface and CN_I is the total number of nearest-neighbour sites in the crystal [84, 85]. Note that α_J only indicates, whether the phase grows faceted or non-faceted, while the volume fraction of the eutectic phase indicates, whether the second (minor) phase grows fibrous or lamellar.

2.5.2 Other eutectics

This section demonstrates that during the growth of these eutectics, the two phases do not cooperate.
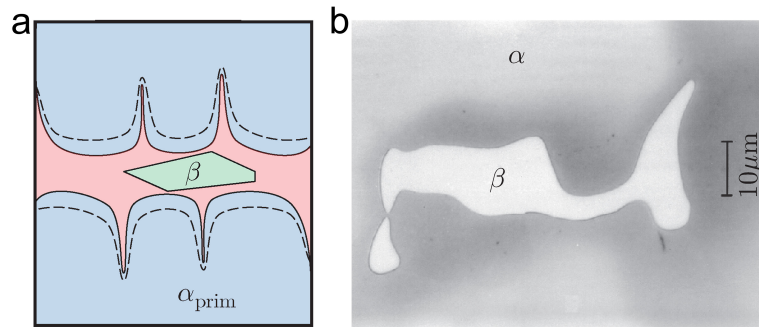
Figure 2.19: (a) Outline of divorced eutectic and (b) divorced eutectic in Mg-9Al-1Zn alloy [32].

Faceted-faceted eutectic grows simultaneously with both faceted phases. However, these phases grow independently from each other, while maintaining solute exchange through the liquid, therefore inhibiting coupled growth [32].

Divorced eutectic can be observed in hypoeutectic alloys with a high fraction of the primary phase at the eutectic point (Fig. 2.19a). The nucleation of the second phase requires a large undercooling, while the primary phase keeps advancing, hence provides less available space for the secondary phase. Therefore the secondary phase is formed independently in isolation [32]. Binary Mg-Al alloys are alloys with a low solute concentration. By having a high fraction of primary phase (Mg) at the eutectic point, the so-called liquid pockets (thin films) are formed. In these pockets, the other phase is nucleated individually at a large undercooling (Fig. 2.19b) [28].

2.6 Entrained droplet technique

Experimental study of heterogeneous nucleation is challenging due to the presence of impurities which have a catalytic effect on nucleation and ensure irreproducible results. This difficulty can be overcome using entrained droplet technique, which produces low melting point particles embedded in a higher melting point matrix [86, 87] by rapid solidification (melt spinning section 3.9), as shown in Fig. 2.20a. A large number of small droplets contain fewer impurities, as reported in the study of homogeneous nucleation by Turnbull [88]. With subsequent controlled heating using DSC, the nucleation kinetics can be monitored. In DSC the alloy is heated above the melting point of the low melting phase (eutectic Si) and cooled at a constant rate. Firstly, the eutectic at grain boundaries solidify, where most of the impurities are pushed. Secondly, eutectic droplets are heterogeneously nucleated by the surrounding matrix (Al), as shown in Fig. 2.20b. Study of heterogeneous nucleation using entrained droplet technique was suggested by Wang [89] and the potential of this technique was further developed by Cantor and co-workers [26, 27, 86, 87, 90–93].
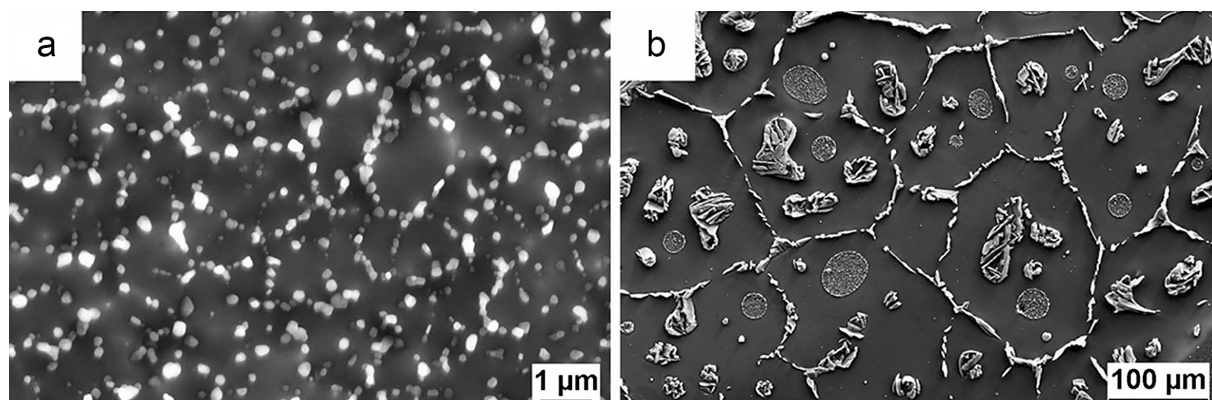
Figure 2.20: Al-5Si alloy in (a) melt-spun condition and (b) after DSC heating [94].

The main advantages of producing fine scale liquid droplets dispersed in the solid matrix are: (i) reproducible liquid undercooling (from DSC) for a detailed investigation of the droplet solidification kinetics as a function of cooling rate, (ii) independent nucleation of each droplet and fine dispersion of droplets enlarge the contribution to nucleation rather than growth in DSC signal, (iii) detailed examination (microstructure and crystallography) of fine scale droplets is possible using TEM (section 3.4.6), (iv) surrounding matrix catalytically enhances the droplet solidification, therefore the heterogeneous nucleation is investigated under a controlled conditions, and (v) influence of trace alloying elements on heterogeneous nucleation and droplet-matrix interface structure can be investigated [86].

Method to investigate the solidification of entrained eutectic droplets embedded in a solid matrix of different alloy systems [87, 95] was developed by Kim [93]. The model shows that solidification onset, peak and end temperatures and height of exothermic peak all increase with increasing droplet size. Therefore, the sharper exotherm corresponds to an increase in the number of potential catalytic nucleation sites per droplet. With increasing number of potential catalytic nucleation sites the similar behaviour of exotherm is observed as the effect of increasing droplet radius. Total integrated peak area and the exothermic peak height increase with increasing cooling rate. The solidification onset temperature is independent of cooling rate but the peak and end temperature decreases with increasing cooling rate [93].

2.7 Al-Si Alloy phase diagram

85 % to 90 % of total Al cast parts are produced from Al-Si alloys [96]. Si is the main alloying element in Al alloys. Al-Si is a eutectic system, where Al is a non-faceted cubic phase, while Si is a faceted diamond phase [29, 33, 38, 97]. Si in Al ensures high fluidity, good feeding and low shrinkage, while the density of Si (2.3 g·cm^{-3}) is lower than that of Al (2.7 g·cm^{-3}), therefore adding the Si improves the properties without loss of weight

47

Figure 2.21: Al-Si phase diagram [97].

advantage [96]. When two metals with no complete solubility in each other are alloyed, eutectic composition with a lower freezing point than that of constituents is achieved [98]. A three-dimensional (3D) network of interconnected eutectic Si platelets improves the strength of soft Al-matrix. The maximum solubility of Si in Al is 1.5 at. % at eutectic temperature 577 ⁰C. Eutectic concentration is 12.2 at. % at the eutectic temperature, therefore hypoeutectic Al-Si based alloys are those having concentration of Si below eutectic concentration and different microstructures are formed. Alloys having a concentration of Si above eutectic concentration are called hypereutectic alloys. Fig. 2.21 shows Al-Si phase diagram [97, 99]. The volume change of liquid and solid are usually 3-8 % based on the differences in packing of liquid and solid. The forces between the liquid atoms are weaker than those of solid, however, attraction in liquid is still strong enough to keep the melt together [31]. Therefore, the solidification of hypoeutectic Al-Si based alloys is initiated by the nucleation of α-Al. α-Al grows with further cooling until the point of dendrite coherency. Then the dendritic network just coarsens. The remaining liquid becomes Si-rich due to consumed primary phase to form Al dendrites and then the eutectic reaction is initiated.

Most of the casting defects are formed in the later stage of solidification, hence the eutectic reaction and the volume of eutectic can influence the properties of a casting [28]. Al-Si based alloys have good resistance to corrosion and good casting properties [99] and wear resistance. Si in combination with other elements plays an important role in heat treatment (section 2.10) to further improve strength.

2.7.1   Effect of cooling rate on microstructure

The quality and structure of Al alloys are highly influenced by melt temperature and cooling rate. The structure is refined by high heat extraction using a high cooling rate [96]. Usually in Al alloys, the microstructure of α-Al grains is evaluated based on the grain size and $SDAS$ [36]. Increasing the cooling rate is beneficial to grain refinement of Al-Si based alloys [100]. The higher cooling rate maintains small and uniformly distributed α-Al grains throughout the microstructure and retains more segregation of the solutes in the Al matrix, which is beneficial to suppress the formation of hydrogen gas pores [101] and to form a strengthening phase during heat treatment (section 2.10). Furthermore, increasing the cooling rate decreases $SDAS$ and refines the eutectic Si and intermetallic phases which are uniformly distributed around more grain boundaries which improve elongation and ultimate tensile strength (UTS) [96, 98, 102]. Finer grain size, greater strength and elongation are achieved at the higher cooling rate of the Al alloy [96, 98, 100, 103].

2.8   Grain refinement of Al-Si based alloy

Hypoeutectic Al-Si alloys contain a large fraction of the α-Al phase. The quality of the casting increases with decreasing grain size of α-Al grains. With grain refinement, the morphology of grains is changed from coarse columnar to fine equiaxed structure [104]. Grain refinement of α-Al grains reduces hot tearing, evenly distributing shrinkage porosity, provides uniform microstructure, improves mechanical properties e.g., fatigue and strength, improves surface finish, second phases are finely distributed (therefore better machining), improves feeding eliminating shrinkage through feeding through the mushy zone and better pressure tightness [8, 40, 55, 62, 69, 74, 77, 104–106].

The mechanism of grain refinement requires numerous potent heterogeneous nuclei that are dispersed in the melt. Those nuclei become active during solidification and nucleate the primary α-Al phase. Commonly it is achieved via the addition of master alloys where the Al matrix is dissolved and intermetallic particles are released into the melt to subsequently act as nucleation sites [107]. In terms of nucleation, the grain initiation was not clear in the past, it was well established that nucleation is initiated by the peritectic reaction of the Al_3Ti phase, which has been found in the centre of Al grains and believed to heterogeneously nucleate Al grains [108]. Later study [109] supported that TiB_2 particle can be nucleant for Al. A review of grain refinement was well summarised by Easton [65, 66] and the following introduction to grain refinement of Al alloys is dedicated to this review.

Theories regarding nucleation such as nucleant-particle theory, phase diagram theory, peritectic hulk theory, duplex nucleation theory were proposed. The particle theory proposes that nucleation occurs on the borides (TiB_2, AlB_2, $(Ti,Al)B_2$) [110]. As reported [111],
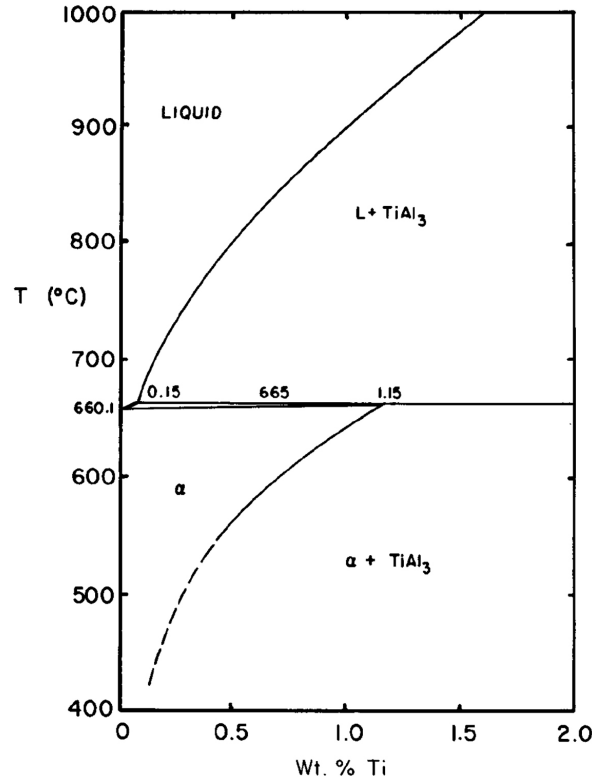
Figure 2.22: Al-rich corner of Al-Ti phase diagram [114].

B is slightly more expensive than Ti, however, its solubility in solid Al is less. Phase diagram theory proposes that grain refinement is achieved via the nucleation of Al on the Al_3Ti phase. It is generally accepted that Al_3Ti is a better nucleant for α-Al than TiB_2 [3, 17, 40, 112, 113]. B was believed to force precipitation of Al_3Ti as a pre-peritectic phase, however, this hypothesis failed thermodynamically [110, 114] and also experimentally [109].

So-called fading occurs because the Al_3Ti particle is unstable in hypoperitectic concentrations, thus Al_3Ti phase dissolves and the grain size increases. For those reasons, the phase diagram theory would be possible only at hyperperitectic concentrations. Also, the peritectic reaction in Al-Ti system (Fig. 2.22) occurs at the concentration above 0.15 wt. % Ti [62], that concentration is too high for casting alloys.

The peritectic hulk theory proposes that borides form a shell around Al_3Ti and slow down its dissolution in Al melt. However, Al-Ti-B master alloy exposed to long holding times (in hours) showed no effect on nucleation temperature (T_N) [109]. Therefore, no dissolution of Al_3Ti was observed and the grain refining effect was maintained.

The duplex-nucleation theory was first proposed by Mohanty [107], when the TiB_2 was found effective only in the presence of Ti. The Ti-rich layer (concluded as Al_3Ti) was formed between the surface of TiB_2 and α-Al at hypoperitectic concentrations. The duplex theory
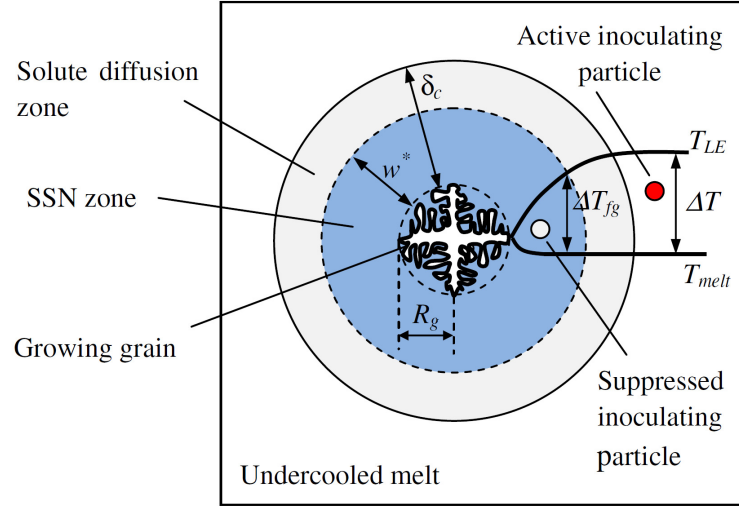
Figure 2.23: Schematic description of solute suppression nucleation (SSN) due to solute diffusion zone [120]. Note that $T_{LE} = T_{\text{eq}}$

was further confirmed on the atomic scale by establishing an orientation relationship (OR) between $TiB_2(0001)$, $Al_3Ti(112)$ and $Al(111)$ observed in embedded Al-Ti-B grain refiner in Al-rich metallic glass [17, 115]. The Al_3Ti phase on the TiB_2 basal plane is so-called a two-dimensional compound (2DC Al_3Ti). Subsequent annealing showed that the size of 2DC Al_3Ti remains the same, while α-Al crystals grow significantly.

Theories such as the free growth model [71, 116–119] and the interdependence theory [37] were described in section 2.4.

A modified free growth theory modelled by Shu [120] includes the effect of the solute field on free growth. In the distance w^* from growing equiaxed grain with radius R_g in an undercooled melt, the solute suppression nucleation (SSN) zone is established in which no further nucleation occurs (Fig. 2.23). The width of w^* is determined by:

$$w^* = \frac{\Delta T_{\text{fg}} - \Delta T_c - \Delta T}{\Delta T_c} \cdot \delta_c \tag{2.46}$$

The solute diffusion field around the dendrite tip is described in equation 2.30, where the V is the growth rate of the dendrite tip. Undercooling in the diffusion field zone is lower than in SSN, therefore the growth of new grains in the diffusion field zone is possible only after the undercooling reaches ΔT_{fg} or the particle with different inoculating particle diameters d is located in the solute diffusion zone. With increasing Q the model shows a slower grain growth and a wider solute diffusion zone resulting in a larger grain size. The model predicts that grain refinement of the alloys with high concentrations of solutes is controlled by SNN. An epitaxial model for heterogeneous nucleation on a potent substrate was introduced by Fan [121]. The model proposes that beyond critical undercooling the nucleation takes place by epitaxial growth on the surface of a potent substrate.

Later, Fan [122] proposed a new concept for growth restriction during solidification, where he derives a new parameter to quantify growth restriction in multicomponent systems including the nature of the solutes (m and k) as well as their concentration (C_0). The growth restriction parameter β_Q is defined as:

$$\beta_Q = \frac{m \cdot C_0 \cdot (k-1)}{\Delta T} - k \qquad (2.47)$$

In addition, β_Q parameter of a multicomponent system can also be calculated through the ratio of the liquid fraction to the solid fraction. The concept does not take into account the potential interaction of solutes. It should be noted that only solutes not bounded to other phases (e.g., intermetallic) are assumed to play a role as growth restricting elements [1, 65].

As discussed above, the nucleation sites are important in grain refinement. Understanding of nucleation site in Al alloys was problematic due to the treatment of the nucleation site in the isolation from melt chemistry [66]. It is well-known, that solutes play a vital role in grain refining of aluminium alloys as well as nucleant particles [66, 123]. Wrought alloys show a better response to grain refinement than foundry alloys. Al-Ti-B grain refiner with an excess of Ti shows poor performance in foundry alloys [66, 111]. The B-rich grain refiners were found more effective in the refinement of casting alloys than Ti-rich grain refiners [16, 66, 104, 124]. The discrepancy in grain refining behaviour of wrought and cast alloys using the same grain refiner is believed to be due to the effect of solutes on nucleation and growth [65]. Therefore, Spittle [68] observed the grain size changes in binary alloys with a fixed concentration of Al-5Ti-1B grain refiner. It was found, that after a certain level of growth restriction, further solute additions were found to have a minor effect on the refinement of α-Al grains. However, the effect of solutes was not studied for high solutes concentration such as in casting alloys. Further experiment [1] was performed in Al-Si casting alloys and it was revealed, that increasing solute content, thus increasing growth restriction factor (Q), was not beneficial to the refinement of α-Al grains. On the other hand, after a certain value, the grain size starts to increase with further increasing solute content.

2.8.1 Si-poisoning

In Al-Si based alloys, the grain size value of effective grain refinement was established to be ∼200 μm [3, 7, 76]. The grain size decreases with increasing Si content up to 2-3 wt. % (Fig. 2.24) with [1, 125] and also without Al-5Ti-1B grain refiner [2]. Above this level, increasing Si concentration resulted in an increased grain size for Ti-rich grain refiners [125]. For Ti, it was not possible to compensate the increase in grain size even via higher addition of grain refiner [125], while other studies show that increasing the addition of Al-5Ti-1B grain refiner can counteract the Si-poisoning [7, 8]. So-called Si-poisoning is accepted to be responsible for the reduced efficiency of Ti-rich grain refiners. Above 3 wt. % Si a coating of bulk ternary silicides is formed on the surface of TiB_2, for example, $TiSi_2$ [72, 126, 127], Ti_5Si_3 [128], τ_1
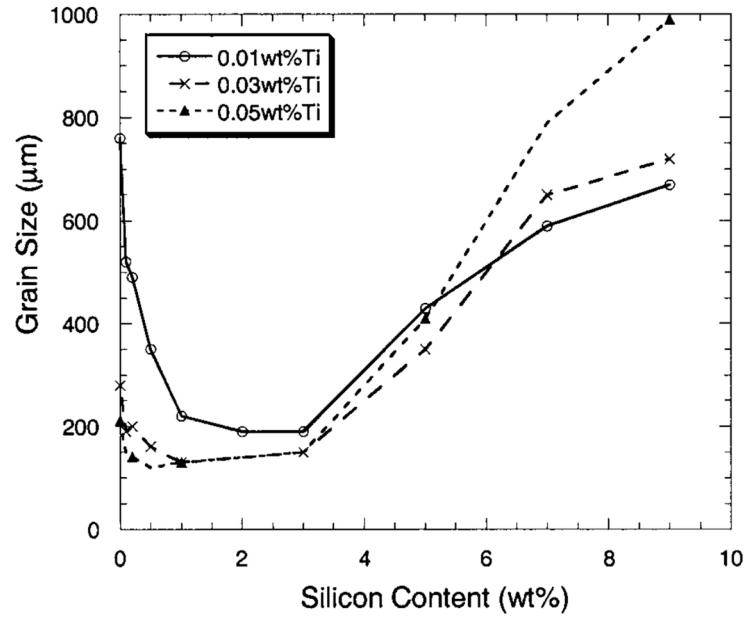
Figure 2.24: Influence of Si on the grain size at various additions of Al-5Ti-1B grain refiner. Legend represents the concentration of solute Ti [1].

phase ($Al_{1.5}Si_{14.5}Ti_4$) [4, 5] and τ_2 phase ($Al_{1.3}Si_{6.7}Ti_4$) [5]. Li [5] concluded that τ_1 and τ_2 phases reduce grain refinement efficiency. On the other hand, Gröbner [4] calculated that τ_2 is formed via peritectic reaction at 704 °C (Liquid+TiSi+τ_1=τ_2). Therefore the τ_2 can be present in the microstructure as an intermetallic phase but not the phase inhibiting the TiB_2 particle. However, it was concluded [129], based on thermodynamic calculation, that reaction (Liquid+TiSi+τ_1=τ_2) takes place at high Si additions (10.6 wt. %) before nucleation of α-Al. Although, the reaction is believed to be suppressed due to the high cooling rate during die casting into permanent mould. The formation of silicides is detrimental not only to nucleation via blocking potent 2DC Al_3Ti and therefore the surface of nucleation sites (TiB_2), but also via reducing the amount of solutes that can contribute to growth restriction [2]. Although, the growth restriction factor (Q) in Al-7Si alloys is 41.3 [65], which is significantly higher than in wrought alloys, therefore the reduced amount of solutes is not a critical point in this case, but it is definitely an undesired effect. First-principle calculation [129] elucidates the strong Si-Ti covalent bond, therefore weakening the Ti-Ti bond of 2DC Al_3Ti and TiB_2. Therefore, Si-poisoning of Al-5Ti-1B grain refiner is caused by Si-doped 2DC Al_3Ti [129]. The Si-poisoning is thus caused by the Si concentration rather than the Ti concentration. Si-poisoning is not a problem in other binary Al based alloys e.g., Al-Cu, [47, 130]. However, hypoeutectic Al-Si based alloys contain more than 5 wt. % of Si. It is therefore of great necessity to find a remedy for Si poisoning.

B was found to effectively reduce the grain size with increasing Si content [2]. AlB_2 alone cannot refine α-Al, but the AlB_2 was concluded to be more effective in the presence of Si

(above 4 wt. %) [2, 131]. This effective combination of AlB_2 and Si was attributed to the formation of the layer of SiB_6 at the interface of AlB_2, however, this enhancing layer at the interface is not believed to be stable [131]. Another subsequent study did not succeed in the observation of the Si-B layer at the interface of AlB_2, strongly supporting the previous proposal that layer SiB_6 is metastable [9].

B was found not only to form AlB_2, but also to interact with Sr, which is commonly used as a modifier in Al-Si based alloys, to form SrB_6 compound [23]. Actually, no interaction of Sr and Ti-rich grain refiner was observed in Al-7Si-0.4Mg alloy. Interestingly, no Sr-B interaction was observed with the addition of 0.1 wt. % B in the same alloy. Further increasing B content up to 0.5 wt. % resulted in the formation of SrB_6 particle [132]. Formation of SrB_6 reduces the amount of free B and also free Sr, which is the most widely used element for modification [133]. It is evident from the formation energies of TiB_2 (-1.06 eV/at. [134]), SrB_6 (-0.45 eV/at. [134]) and AlB_2 (-0.043 eV/at. [134]), that TiB_2 is more stable than AlB_2, therefore it is reasonable to assume that free B tends to form TiB_2 firstly. Then, free B is consumed by the formation SrB_6 rather than AlB_2 [132]. This is why no interaction of Sr and Al-5Ti-1B grain refiner was observed [133, 135], however, no modification effect was observed using sub-stochiometric grain refiner (Al-1.5Ti-1B) in combination with Sr [133]. It was also reported that the size of SrB_6 particle is more than 5 µm and tends to settle down due to its high density [132].

In practice, several methods are implemented to overcome Si-poisoning, such as: (i) increasing addition of grain refiner, (ii) addition of nucleation sites with different chemistry (NbB_2 [11, 136, 137], AlB_2 [2, 9, 16, 104] or TiC [14, 15]) or (iii) to remove solute Ti from the melt. All of the mentioned methods increases the economic cost of the final product. Especially removing solute Ti can be very challenging. It is suggested [129] to retard the dissolution of Si into 2DC Al_3Ti using elements that possess a lower affinity to Si than Ti. We propose that introducing solute Ta to the melt may provide a good grain refining effect, while avoiding Si-poisoning. The reasons for that are described in the following section.

2.8.2   Effect of Ta in Al-Si based alloys

Nowadays, Ti has been widely applied in Al-Si based alloys due to its highest growth restriction effect in Al binary alloys (Table 2.1) and the Al-Ti solidifies according to the peritectic phase diagram (Fig. 2.22) at peritectic equilibrium temperature of 665 ºC. So-called 2DC Al_3Ti is formed on TiB_2 basal plane even below the hypoperitectic concentration [17, 115, 130].

Ta was unintentionally introduced to metallic glass experiments from a master alloy [17, 115]. Table 2.1 shows that Ta has the highest growth restriction effect right after the Ti, while also forming peritectic with Al. Furthermore, Al_3Ta (similar to that of 2DC Al_3Ti) was found at
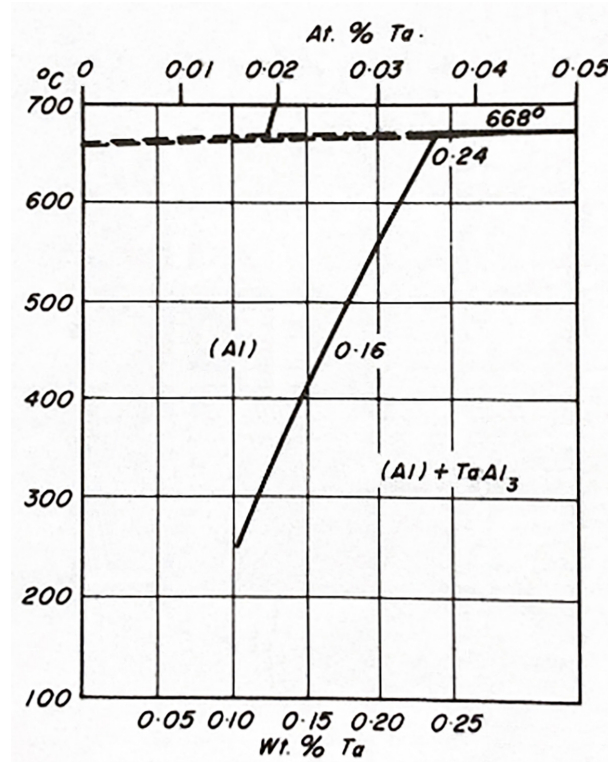
Figure 2.25: Al-rich corner of Al-Ta diagram [139].

the basal plane (0001) of TiB_2 [17, 115]. Lattice parameters of Al_3Ta (DO_{22}, $a = 3.84$ Å, $c = 8.55$ Å) and Al_3Ti (DO_{22}, $a = 3.85$ Å, $c = 8.60$ Å) are very close. The peritectic temperature of Al-Ta diagram is ~ 3 °C higher than that of Al-Ti diagram (Fig. 2.25) [3, 17, 138], which indicates that if both Ta and Ti are present, 2DC Al_3Ta is formed prior to 2DC Al_3Ti on (0001) plane. This assumption gives a strong argument to overcome Si poisoning. Based on the phase diagram and segregation behaviour, Ta is eligible to play a role as nucleant and growth restrictor in Al-Si alloys.

Ta was reported [140] to increase the grain size of α-Al in Al-4Ti and Al-5Ti-1B alloys up to hypoperitectic concentration. The grain size decreases with the addition of Ta above the peritectic concentration, which is attributed to the presence of the Al_3Ta phase. However, data confirming the effect of Ta in Al-Si based alloys is still missing.

2.9 Modification of Al-Si based alloy

Modification in hypoeutectic Al-Si alloys is referred as a morphology change of the eutectic Si from large brittle plates to a fine fibrous coral-like morphology (Fig. 2.26) [141]. The coarse needle-like form of eutectic Si gives a low strength and poor ductility [23, 99, 105] since the plates with sharp edges are assumed to act as crack initiators [62]. Unmodified
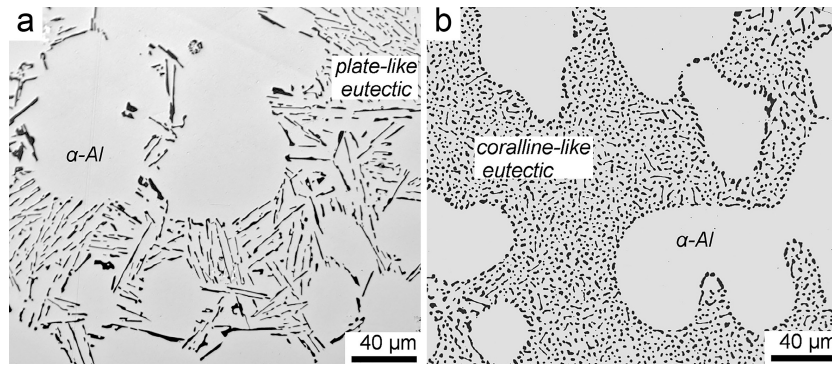
Figure 2.26: (a) Al-Si plate-like eutectic in an unmodified alloy and (b) coral-like eutectic in Sr-modified alloy [145].

alloys often exhibit elongations no more than a few percent and the fracture surface is primarily brittle [23], while modified alloys exhibit a higher elongation and UTS [16, 142]. Mechanical properties of Al-Si are changed by the shape and size distribution of eutectic Si [55, 99]. Significant improvement in mechanical properties was discovered in 1921 [18] by the addition of sodium fluoride flux into Al-Si alloy which is today well-known as a modification of Al-Si eutectic. Modification improves mechanical properties, especially for ductility [143]. The modification of eutectic Si can be achieved by chemical modification or quench modification. Addition of modification elements (e.g., Na, Sr), sometimes called modifying agents, corresponds to chemical modification, while applying high cooling rates during solidification corresponds to quench modification. Both methods displace the eutectic point to lower temperatures and a higher Si concentration [28, 144]. It should be noted that chemical modification influences the nucleation as well as the growth mechanism of eutectic Si.

Chemical modification is required in castings, where the quenching modification cannot be achieved throughout the whole casting due to large volumes, such as sand casting, gravity die casting and low pressure die casting. While no modification is applied for thin walled casting parts produced by high pressure die casting (HPDC), due to a design of a part and rapid cooling effect [99].

2.9.1 Nucleation of eutectic Si

Quenched microstructure of eutectic Si in the work of Nogita [22] revealed the nuclei particle at the centre of eutectic Si. TEM (section 3.4.6) identified AlP to be the nucleation site for eutectic Si. Investigation [26] on the effect of 0.25-35 ppm P in high purity (HP) Al-3Si based alloy using entrained droplet technique (section 2.6) revealed a lower undercooling required to form eutectic droplets embedded in the Al matrix with the presence of AlP. It was concluded that Si particles heterogeneously nucleate on pre-existing AlP [23, 26, 27]. In

Al-Si casting alloys, the increasing P increases the nucleation temperature and decreases the undercooling of eutectic Si [146–149]. Thermodynamic calculation of Liang [150] revealed that the AlP in Al-Si based alloys can be stable at different stages of solidification for various P and Si additions. In Al-7Si based alloys, the AlP can precipitate before α-Al and eutectic Si when the P exceeds the concentration of ~15 ppm and ~4 ppm, respectively. The solubility of P in Al is low (0.07 ppm at 660.3 $^{\circ}$C [150]) and it decreases with decreasing temperature [26]. P is usually in Al-Si based alloys in small concentrations [55], such as ~10 ppm [23] in commercial purity (CP), however, its content can increase with recycling or from refractory materials [151]. In casting alloys, the AlP is pushed by solidification in front of α-Al dendrites and segregates at the dendrite-liquid interface. Although Al and Si possess cube-to-cube orientation, Al ($a = 4.05$ Å) is not believed to be a good nucleation site for Si ($a = 5.42$ Å) due to their large differences in lattice parameters [27, 141]. The eutectic Al is believed to nucleate on the α-Al dendrites. On the other hand, lattice parameter a of cubic AlP equals to 5.43 Å [141], which gives a lattice mismatch δ with Si (equation 2.26) lower than 1 % [22]. The addition of P produces finer primary Si in hypereutectic Al-Si alloys [23, 152]. Nucleation of Fe-rich intermetallics was proposed by Shankar [153], who suggests that β-(AlFeSi) particles are nucleated in the solute field ahead of α-Al dendrites and eutectic Si nucleate on these particles. Cho [154] concluded that pre-eutectic β-(Al$_5$FeSi) intermetallic is nucleated on AlP.

Eutectic grain size

Refinement is termed as the decrease in the size of eutectic Si from coarse to fine platelets and is related to the nucleation of eutectic Si. While the modification is referred as a morphology change of the eutectic Si from large plate-like to fine fibrous and is related to the growth of eutectic Si [94, 141]. Quench experiments [21, 22, 24, 142, 146, 147, 149, 155–157] of unmodified Al-Si alloys revealed very fine eutectic grains. Authors [146–148] concluded that eutectic Si exhibit finer eutectic grain size with increasing addition of P or decreasing purity of Al-Si alloys. Refinement of eutectic grains is of great necessity as the porosity is mainly formed around eutectic grain boundaries [23, 158]. Although eutectic grain size is finer in unmodified alloys, the morphology of eutectic still remains plate-like (Fig. 2.26a).

2.9.2   TPRE mechanism

Atoms of faceted crystal are attached to close-packed planes, which requires larger undercooling, as shown in section 2.3. Twin Plane Re-entrant Edge (TPRE) growth mechanism was proposed based on the observation in Ge dendrites [50, 159], which was later applied to describe crystal growth of Si. Angle 141 $^{\circ}$ in re-entrant edge is maintained between two {111} planes and rapidly progresses in <211> directions, while ridge is developed at the
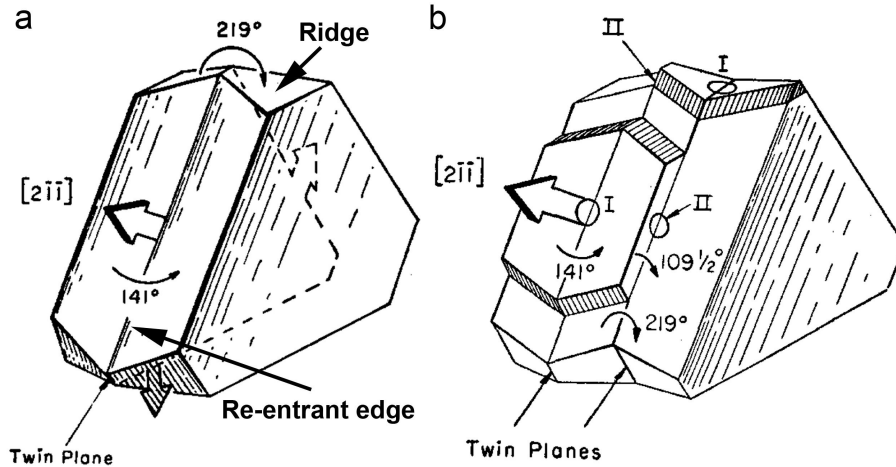
Figure 2.27: (a) Twin plane emerges from re-entrant edges, which interchange with ridge structures. (b) Nucleation at re-entrant corners (I) and development of new re-entrant corners (II) [50].

angle of 219 º (Fig. 2.27). Si forms flat plate-like crystals with no branching, referred as unmodified Si eutectic, which requires a low undercooling.

Attachment of atoms to the interface is adequate for pure binary materials [160]. Based on TPRE concept, poisoning of TPRE by adsorbed impurities (i.e, Na or Sr) was proposed to retard the growth at TPRE growth step and therefore provide heavily twinned modified eutectic Si [160–162].

2.9.3 IIT mechanism

The branching of Si is achieved via the addition of impurities at the re-entrant edge at the solid-liquid interface [28]. Impurity Induced Twinning (IIT) was proposed by Lu [163] via the addition of impurity atoms (Na, Sr) with a suitable size on the solid-liquid interface of growing Si. The criterion was described as:

$$\frac{r_m}{r_{\text{Si}}} = 1.646 \tag{2.48}$$

where r_m is the atomic radius of the modifier (impurity) and r_{Si} is the atomic radius of Si. Atoms close to the value of 1.646 are adsorbed at the growth step, the new twin is created and the growth is altered. This results in multiply twinned Si producing fine fibrous eutectic Si. The ratio of atomic radii of common modifiers is listed in Table 2.2.

Fig. 2.28a shows impurity atom inducing branching of Si crystal at the angle of 70.53 º and Fig. 2.28b shows growth of solid-liquid interface containing adsorbed impurity atom. For example, Yb is proposed to fit ideally to the IIT criterion, however, the experimental investigation revealed only refinement of eutectic using Yb, while maintaining plate-like

Table 2.2: Proposed modifying elements based on IIT criterion [163].

Element	Atomic radius [Å]	r_m/r_{Si} [-]
Si	1.1755	1.00
Ba	2.18	1.85
Ca	1.97	1.68
Na	1.86	1.58
Sr	2.16	1.84
Sb	1.40	1.19
Y	1.81	1.54
Yb	1.93	1.65
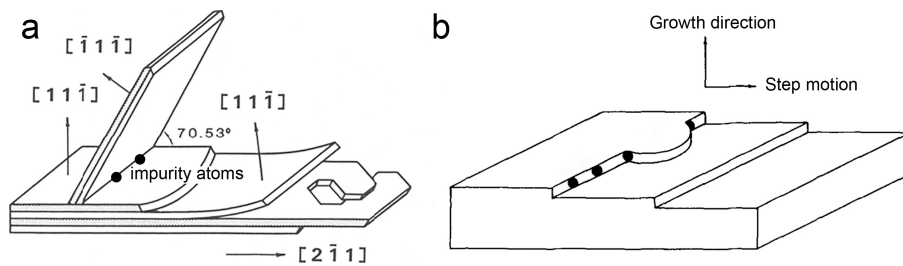
Figure 2.28: (a) Branching in silicon flake due to impurity atoms and (b) adsorption of impurity atoms on the growing interfaces [163].

morphology [141, 164–167]. Therefore, the ratio of atomic radius alone seems not to be the main parameter in the transition from plate-like to fine fibrous morphology.

2.9.4 Chemical modification

The intentional addition of impurities to liquid metal [55, 62, 99] to induce modification in Al-Si alloys was investigated for various modifying agents: Na [27, 55, 91, 96, 99, 142, 144, 163, 165, 168, 169], Sr [16, 20, 21, 23, 55, 96, 99, 100, 103, 135, 144, 147, 148, 154, 156–158, 165, 168, 170], Sb [21], Ca [149, 165], Ba [164], Yb [141, 164–167, 170] and rare-earth elements (Sc [171], Y [164] and lanthanides [24, 55, 99, 172, 173]). The addition of the excessive amount of modifier exerts overmodification, which is related to a detrimental coarsening of the eutectic Si, resulting in the decrease of mechanical properties [55, 99, 100]. It was reported [100] that overmodification is better than undermodification and overmodification is also recommended for alloys with unknown composition.

Refinement and modification of eutectic Si are phenomena proceeding simultaneously. Hence, the effect of the modifier on the refinement and modification of eutectic Si is also described simultaneously in the following section.

Effect of Na

The addition of metallic Na exhibit a modified structure [49]. Quenching experiments of un-modified and Na-modified Al-Si alloys of Flood and Hunt [142] revealed that Na modification not only alters the growth morphology but also inhibits nucleation of eutectic Si ahead of the solidification front. Therefore, a larger undercooling and finer eutectic lamellar spacing was observed in Na-modified alloys. Investigations of Ho and Cantor [26, 27] assumed that the addition of Na results in the formation of the Na_3P phase. Although the formation energy of Na_3P (-0.332 eV/at.) is higher compared to AlP (-0.610 eV/at.) [134], Na is believed to deplete the AlP which is not a good nucleation site for eutectic Si [26] and to form Na_3P [19, 27], which is not good nucleant for eutectic Si due to its large lattice parameter [25]. Thus Na poisons the AlP which results in an increase in the eutectic grain size [23]. It is generally excepted that Na reacts with AlP in the melt and the excess amount of Na changes the growth morphology from coarse plates to fine fibrous eutectic Si [91, 142]. The addition of Na decreases the nucleation temperature and shifts the nucleation of eutectic Si to a higher undercooling [91, 143, 144]. On the atomic scale, particle-like Na-rich clusters were detected at the intersection of Si twins and elongated rod-like Na-rich clusters along the <112> growth directions of eutectic Si using atom probe tomography (APT) [19]. Both of these observations provide an experimental support for IIT and TPRE growth mechanism, respectively. A further APT investigation by Barrirero [168] showed a non-conclusive result, whether a single atom or AlSiNa clusters includes the twinning in eutectic Si.

In terms of application, Na is known to be the strongest modifier [102], which dissolves very fast, does not oxidise [163] and provides a perfect modification at very low cooling rates [169]. Fully modified eutectic Si was observed with the addition of only 19 ppm Na in HP Al-5Si [19]. TEM observation by Li [165] showed that the addition of 50 ppm Na promoted a significant increase of Si twinning compare to 200 ppm Sr addition in the same alloy. However, application of Na in Al-Si alloys faces some difficulties, especially its low yield (as pure metal varies from 20-40 % [99]) due to its low solubility in Al (0.197 ppm Na at 659.25 °C [174]), evaporation of Na and no recovery after remelting [23, 55, 99].

Effect of Sr

Sr is introduced to Al-Si melt as a pure metal or in the form of a master alloy. Quench experiment [21, 147, 154, 156, 157] of unmodified and Sr-modified alloy with the addition of Sr showed a similar result to that of Na [142], that Sr poisons AlP [23, 148, 157]. Sr as well as Na, decreases the nucleation temperature [21] and shifts the nucleation of eutectic Si to a higher undercooling [175–177]. SEM (section 3.4.3) investigation of Cho [154] revealed a P-rich region in Sr-rich intermetallic, presumably Sr_3P_2. Al_2Si_2Sr was detected in DSC traces of HP Al-5Si [175–177] with 100 ppm Sr addition, however, microscopy data confirming the

absence of Al_2Si_2Sr. Timpel [20] found two types of Sr-Al-Si co-segregation in Al-10Si alloy using APT. The first type of co-segregation promotes the formation of new twins during growth (IIT mechanism), while the second type of co-segregation is assumed to be adsorbed at the solid-liquid interface, therefore contributing to the branching of Si fibres (TPRE mechanism). Sr poisons the growth directions of Si [96]. It was suggested that Al_2Si_2Sr is nucleated on AlP which leads to even less active AlP for the nucleation of eutectic Si [154]. Lee [135] found Al_2Si_2Sr around the AlP phase and proposed orientation relationship: $AlP\{111\}||Al_2Si_2Sr\{0001\}$.

Yield up to 90 %, long modification effect, no environmental issues and high recovery after remelting are the main reasons for its widespread use of Sr in the industry compared to Na [23, 55, 99, 102, 133, 163]. Discrepancies regarding the dissolution of Sr are found in the literature. Earlier literature [99] stated that Sr needs longer times to be active (probably compared to Na addition), which is in contrast to a later study by Kori [16], where the Sr modification was fully achieved already after 2 min. Therefore, the addition of Sr is recommended at higher temperatures to enhance dissolution [102] and to reduce oxidation. Sr was reported to improve elongation in Al-Si alloys [16, 55] and to have a consistent performance in terms of mechanical properties than Na-modified alloys [23]. Sand casting shows a worse response to modification in Sr-modified alloys [96], however, impact properties were improved in Sr-modified alloys produced by sand casting and die casting [178]. Joenoes [179] found that Mg forms a complex Mg-Sr-Al-Si phase in Sr-modified alloy, which resulted in only partial modification.

However, Sr is more susceptible to H pick up compared to Na [180]. It should be noted that H can be already in solution in Al-Sr master alloy [55, 62]. In foundry practice, it is well-known that disturbing melt surfaces should be avoided. Sr modification is used for low pressure die casting, where the melt disturbances are low and the enclosed furnace inhibits the exposure to the environment (i.e., moisture) [55, 62]. Porosity induced by modification can negate the benefits in mechanical properties [96], if, as mentioned, the melt is not treated carefully. The author's experience [23] suggests avoiding high Sr addition and high melting temperature (above 760 ºC). No significant loss of Sr is reported during degassing [23].

With increasing Sr addition or increasing purity of Al-Si alloy, only a few eutectic grains are nucleated [21, 156], hence the eutectic grain size increases [148], which results in a higher eutectic growth rate [147]. Eutectic grain size is usually up to 2 mm in Sr-modified alloys [147, 148, 157, 158]. Nucleation sites such as AlP, AlB_x, CrB_x were proposed to reduce eutectic grain size [151]. However, the reaction of AlP and AlB_2 with a modifier (namely Sr) was discussed in this section and section 2.8.1, respectively. A study of Li [158] showed that the eutectic grains can be refined using CrB_2 particles in Sr-modified alloys, which underlines the importance of refinement of eutectic grains.

Effect of Eu

As shown for Na and Sr, the modifier affects both the nucleation and growth of the eutectic Si [142]. The behaviour of Eu in Al-Si alloys is similar to that of Na and Sr, while other rare-earth elements (i.e., La, Ce, Pr, Nd, Sm, Gd, Tb, Dy, Ho, Er, Tm, Yb and Lu) produce only refined plate-like eutectic structure [24, 167]. Eu as the only one element from the rare earth group is known to achieve a fully modified eutectic structure [24, 25, 167, 181–185]. Thermal analysis investigation confirmed that increasing Eu addition increases the eutectic undercooling (ΔT_{eu}), while the eutectic decreasing nucleation temperature ($T_{N,eu}$) and the minimum eutectic temperature ($T_{min,eu}$) [181, 183, 184]. Die casting experiment of HP Al-5Si with the addition of Eu up to 200 ppm and P up to 10 ppm showed increasing undercooling with increasing Eu [25]. The same result was observed in CP Al-Si based alloys [25]. DSC traces of melt-spun HP Al-5Si based alloy with additions of 500 ppm Eu and 44 ppm P showed undercooling of $\sim$52 ^{o}C [181]. A quenching experiment of HP Al-5Si [25] revealed a large number of eutectic grains while maintaining modification effect for controlled addition of Eu and P. Another quenching experiment of CP Al-7Si revealed fine eutectic grain size for all addition of Eu, however fully modified eutectic Si structure was achieved with Eu additions above 1600 ppm [183]. Al-10Si exhibit a fully modified structure at 600 ppm Eu [24]. Hypoeutectic Al-7Si-0.3Mg alloy shows modified structure above 800 ppm Eu addition [184]. Eu was found to refine and modify primary Si in Al-40Zn-6Si alloy [186]. Therefore, not only Si concentration but also the concentration of trace elements influence the modification of eutectic Si.

The μ-XRF (X-ray fluorescence) [167] elucidated that Eu segregates to the Si phase rather than to the Al phase. Ab initio calculation indicates that Eu prefers to bond with P rather than with Al [25], therefore no Eu-Al interaction is expected. Eu is absorbed at TPRE, which fits well with segregation energies obtained from ab initio calculation [182]. Eu-rich clusters were observed along {112} and the at intersection of {111} twins, which support IIT and poisoning of TPRE [181]. Al_2Si_2Eu phase was observed in the vicinity of eutectic Si [25, 181, 182]. AlP or EuP phase is usually surrounded by Al_2Si_2Eu [25, 183]. Li [181] revealed that Al_2Si_2Eu is formed during the pre-eutectic stage using DSC. The APT experiment showed that Al and Eu atoms are always found in the defects of eutectic Si and never as single atoms. Eu co-segregates with Al in eutectic Si and forms ternary Al_2Si_2Eu compound [166].

The addition of Na or Sr poisons AlP and result in the formation of Na_3P and Sr_3P_2, respectively. Hence no nucleation sites are present in the liquid melt. The predicted formation energies of EuP and AlP are -1.04 eV/at. and -0.610 eV/at., respectively [134], therefore it indicates that Eu can deplete AlP and forms EuP. Lattice parameters of EuP 5.75 Å and Si 5.42 Å are similar and it is reasonable to assume that EuP can nucleate primary and/or
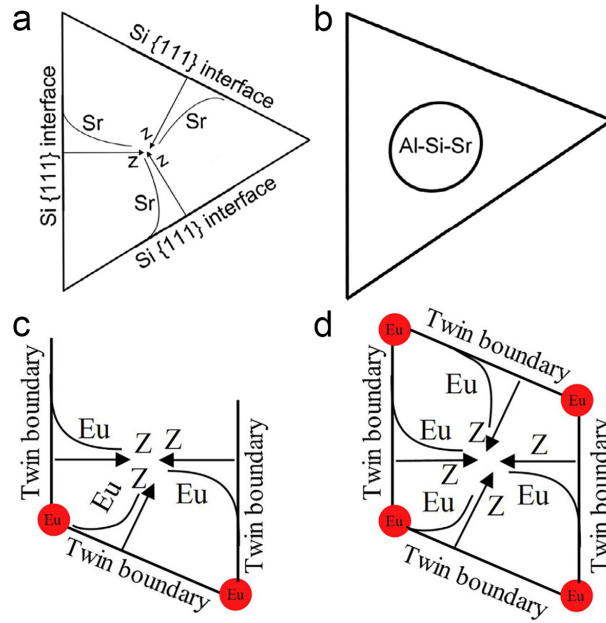
Figure 2.29: (a, b) solute entrainment occurs forming Sr-rich clusters with finally formed Al_2Si_2Sr particle within eutectic Si [187]. (c, d) the formation of numerous Si twin boundaries and the interconnection of twin boundaries resulting in the formation of entrained Al_2Si_2Eu compound [186].

eutectic Si. Note that EuP is not believed to be as good nucleant as AlP with a lattice parameter of 5.43 Å [25]. A later study [25] showed that eutectic grains can be refined with the combined addition of Eu and P. The aim of this work is to achieve simultaneous modification and refinement of eutectic Si in Al-Si based alloys.

2.9.5 Solute entrainment

Solute entrainment is used to describe the formation of Al_2Si_2M phases or M-rich clusters within Si crystals, where M=Na, Sr, Eu, Yb. It is important to distinguish between solute entrainment and solute trapping. Solute entrainment, as demonstrated in Fig. 2.29, is formed by solute segregation of overlapping Si crystal planes. Solute trapping is freezing the solutes within crystal during rapid solidification [165, 186, 187].

The Al_2Si_2M phases or M-rich clusters are proposed to be an artefact caused by solute entrainment during Si growth rather than a real factor affecting modification. All the elements with partition coefficients less than 1 will segregate into liquid ahead of the solidification front during Si growth [165, 187].

2.10 Heat treatment of Al-Si-Mg based alloy

The mechanical properties of Al-Si based alloys are influenced by composition, defects, melt treatments, cooling rate and heat treatment [96, 102]. The effect of casting defects such as gas porosity (section 2.7.1) and melt treatments (section 2.8 and section 2.9) were discussed. This chapter briefly describes the overview of the heat treatment of Al-Si based alloys and its alloying effect on the mechanical properties of a final product.

The right choice of heat treatment (different combinations of temperatures and times) depends on the desired properties, casting process and chemical composition [99, 188, 189]. Heat treatment improves the hardness and strength by inhibiting the movement of dislocations through the formation of finely distributed precipitates [188, 190]. In Al alloys, Si, Cu and Mg are the main alloying elements to increase strength [191–193]. Mg is often added to increase strength via heat treatment, while Cu is used for higher strength of alloys produced by HPDC [194]. Small precipitates of Cu and Mg contribute to strength but reduce the ductility [105, 191]. Ag can be used to strengthen the Al, while Zn and Si have a hardening effect in combination with Mg [55, 99, 195]. These alloys are referred as heat-treatable [179, 193, 196].

In this work, investigated alloy system (Al-7Si-0.3Mg) contains only Si and Mg, hence Mg-Si type precipitates are discussed. It is generally accepted that precipitation sequence follows: Supersaturated solid solution (SSSS) $\rightarrow$ Mg-Si clusters $\rightarrow$ Guinier–Preston (GP) zones $\rightarrow$ $\beta'' \rightarrow \beta' \rightarrow \beta$ [197]. The section 2.10.3 is dedicated to the precipitation sequence of β-MgSi precipitates. There are several types of heat treatment of Al alloys depending on the chemical composition and final properties. The heat treatment of Al-7Si-0.3Mg alloys is referred as T6 treatment and it consists of solution treatment, quenching and ageing treatment in order to obtain the highest combinations of strength, ductility, and toughness [96, 178, 196]. T6-treated alloys are exhibiting the highest strength without sacrificing other properties [196].

2.10.1 Solution treatment

During solidification, the formed crystals do not have the same composition as that of the melt. The rest of the metal which solidifies around the first crystal is more concentrated [190]. The purposes of the solution treatment are: (i) to spheroidize the eutectic Si particles, (ii) to get soluble hardening elements into a solid solution (homogenisation), and (iii) to dissolve soluble phases formed during solidification [188, 196]. The rate of processes increases with temperature [188]. The alloy is held at a temperature close to the eutectic point (540-550 ºC) for 0.5-12 h and then is quenched to water [100, 114, 196, 198].

Eutectic Si particles undergo breaking and spheroidization in unmodified alloys as shown in Fig. 2.30. As the particles spheroidize, they get coarser and increase the interparticle spacing
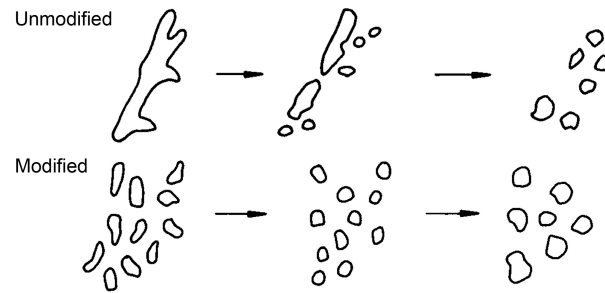
Figure 2.30: Spheroidization of unmodified and modified alloy [96].

which applies for both, unmodified and modified alloys [82, 96, 178, 184]. Modification produces finer eutectic Si and therefore the rate of breaking and spheroidization of eutectic Si is increased compared to unmodified alloys [96, 196]. When Al-Si alloys are chemically modified with Na [23] or Sr [23, 188], the solution heat treatment time may be reduced, which is an important economical aspect in the industry [23, 188]. However, Paray [96] reported a minimal beneficial effect of modification on the heat treatment of Al-7Si-0.3Mg alloy. It was stated that after 1 h of solution treatment, the difference between unmodified and modified alloy was diminished but the eutectic Si particles in unmodified alloy are coarser. Ductility and impact properties are reported to increase in modified and unmodified alloys with increasing solution treatment time [96, 178]. This can be attributed to spheroidization and an increase in interparticle spacing of eutectic Si, therefore the crack initiation and propagation are decreased [188, 198].

During the homogenisation phase of solution treatment, the atoms of intermetallic phases produced during solidification are detached and diffuse through the matrix. The diffusion rate depends on the diffusion distance and solution treatment temperature. Lower $SDAS$ can enhance diffusion by providing a shorter diffusion distance [188].

Increasing Mg produced larger Si particles in both, unmodified and Sr-modified alloys [179, 199]. Increasing Mg decreased ductility and increased yield strength [99, 100, 193, 199, 200]. The optimum Mg level to provide the hardening effect is in the range of 0.30-0.50 wt. %. No further benefits are obtained at levels up to 0.7 wt. % Mg [193]. Mg concentration in α-Al dendrites in the vicinity of the Fe-rich phase increased up to nominal bulk concentration after 1 h solution treatment at 540 ºC in Al-7Si-(0.3-0.7)Mg based alloy. The maximum Mg in the matrix was measured $\sim$0.5 wt. % [200]. Note that Mg and Si atoms that are partitioning in intermetallics provides no strengthening effect via precipitation [99, 105, 188, 193]. The time and temperature of solution treated alloy is therefore a function of as-cast microstructure [196].

As-cast alloys contain less than 5 % volume of intermetallic phases in the whole volume, despite the low volume of intermetallic, their negative effect on mechanical properties is

significant [201]. It was reported that with increasing Mg concentration, the Mg_2Si and π-AlFeMgSi phase have increased in number and size [200]. Increasing Mg decreases ductility, presumably due to large π-AlFeMgSi [199]. Fe-rich phases such as π-$Al_8FeMg_3Si_6$, α-Al_{15}(Fe, Mn)$_3Si_2$ and β-Al_5FeSi have commonly been observed in the microstructure of Al-Si-Mg based alloys. The exact stoichiometry of Fe-rich intermetallic is varies throughout the literature, therefore intermetallic phases are referred as π-AlFeMgSi, α-AlFeMnSi and β-AlFeSi in the following text.

Fe is ubiquitous in Al alloys, Fe is even deliberately added to Al alloys in order to minimise die soldering in high pressure die casting. Reduction in the sticking tendencies may achieve with Fe content above 0.5 wt. % [105, 154]. Fe reduces elongation [100, 154], presumably due to the formation of Fe-rich intermetallic phases. β-AlFeSi plates were observed in the microstructure of Al-7Si-0.4Mg alloy with 0.1-0.2 wt. % Fe [199]. With increasing Fe in the alloy, the formation of β-AlFeSi needles is observed in the microstructure [100]. However, the addition of Mg up to 0.7 wt % resulted in the formation of large π-AlFeMgSi and small β-AlFeSi [188, 199]. Wang [200] observed π-AlFeMgSi and β-AlFeSi in the microstructure after T4 treatment. π-AlFeMgSi is reported to dissolve if the Fe and Mg concentration is low [100, 199], however, as demonstrated [199], the π-AlFeMgSi is formed at the presence of high Mg, therefore the dissolution of π-AlFeMgSi is unlikely when the Mg and Fe concentration are high enough to form the π-AlFeMgSi. Short solution treatment time of Al-7Si-0.3Mg alloys was reported to have no significant effect on Fe-rich intermetallic[198]. A high cooling rate was reported to refine the π-AlFeMgSi phase [199]. Earlier literature stated [100] that β-AlFeSi is not dissolved by heat treatment. In contrast, it was reported [188] that β-AlFeSi platelets do fragment and are gradually dissolved after exposure to high temperature for a long time.

The formation of needle-like β-AlFeSi is usually treated with controlled addition of Mn to form a compact α-AlFeMnSi phase, referred as Chinese script. Fe-rich phases are shown in Fig. 2.31. The addition of Mn should not exceed 50 % of Fe concentration [105, 154, 191, 201]. β-AlFeSi is formed at high cooling rates, while α-AlFeMnSi is formed at low cooling rates in Al-Si alloys [105]. α-AlFeMnSi phase is hard to dissolve and is reported to be unaffected via solution treatment [188].

At high Fe additions (>1.1 wt. %) which are common Fe concentrations for HPDC alloy, the β-AlFeSi phase was reported to form prior to eutectic reaction and with the size of $\sim$100 µm [154]. The addition of modifier (Sr) was reported to decrease the nucleation temperature of β-AlFeSi [154]. Heat treatment showed no effect on Al-Si-Sr intermetallic [100], therefore it is very unlikely, that solution treatment would decrease the amount of Al-Si-M (where M=Na, Sr, Eu, Yb) in the microstructure.
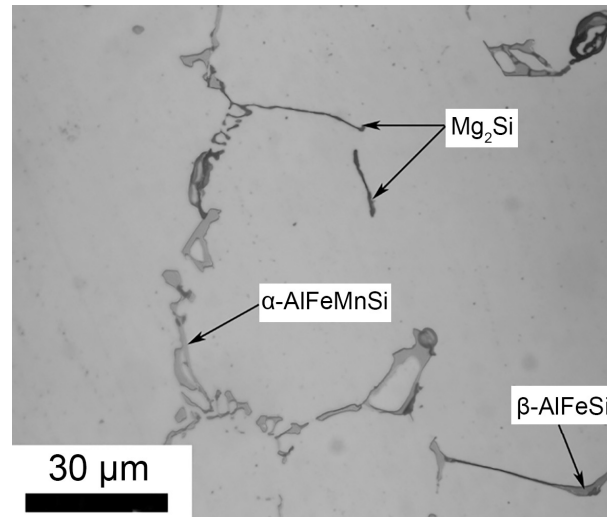
Figure 2.31: Optical micrograph of intermetallic phases in Al-0.9Mg-0.6Si-0.2Fe-0.45Mn alloy [202].

2.10.2 Quenching

The goal of quenching is to preserve high number of vacancies in the material. Quenching the alloy from high solution treatment temperature to room temperature ensures a high vacancy concentration [33, 188]. If cooled slowly, the precipitation at dislocation or along grain boundaries may occur [188]. The vacancies suite as heterogeneous nucleation sites [33]. The quenching from solution treatment temperature to room temperature must be rapid enough to produce a supersaturated solid solution [196]. The best combination of strength and ductility is associated with the most rapid quenching rates [196]. Water provides a cooling rate of up to 200 $^{\circ}$C/s, but it decreases with increasing water temperature [196]. In order to maintain an intensive cooling throughout the quenching, it is recommended to ensure fluid flow during immersion [196]. For lower cooling rates, the boiling water or polymer quenching medium is applied [196]. However, elongation decreases with decreasing quench rates [188].

2.10.3 Ageing treatment

Ageing achieved at room and elevated temperature is called natural ageing and artificial ageing, respectively. In this work, only artificial ageing is discussed and investigated. [188]. The goal is to achieve optimum size and distribution of precipitates [188, 196]. Typical temperatures for artificial ageing are in the range of 150-210 $^{\circ}$C. Atoms can move over longer distances at elevated temperatures [188]. Precipitation starts with the formation of GP-zones and is followed by metastable precipitates that nucleate heterogeneously on GP-zones or lattice defects (i.e., dislocation) [188].

In Al-Si-Mg based alloys, the precipitation starts with the formation of Mg and Si enriched
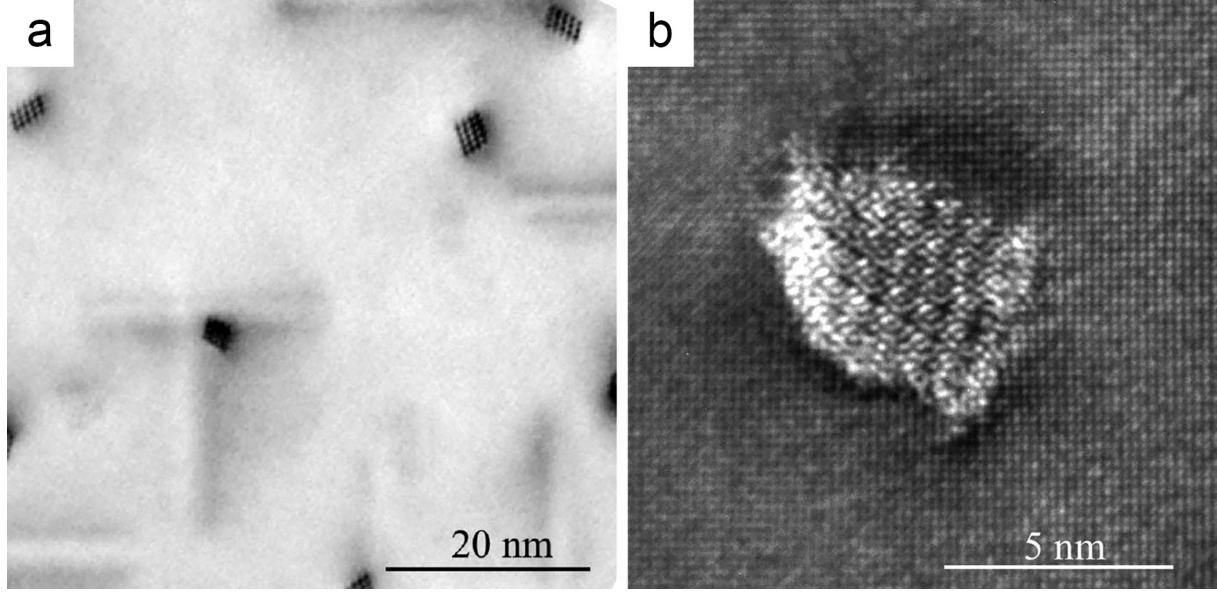
Figure 2.32: TEM of β'' needles at <100>Al zone axis in Al-0.72Si-0.58Mg alloy [203].

Table 2.3: Stoichiometry of β-type precipitate observed during precipitation of Al-Mg-Si [197].

Phase	Formula	Lattice parameters
GP-zones	Mg_x-Al_{5-x}-Si_6	Primarily monoclinic
β''	Mg_5Si_6	Monoclinic; a=15.16 Å, b=4.05 Å, c=6.74 Å; β=105.3º
β'	Mg_9Si_5	Hexagonal; a=7.15 Å, c=12.15 Å
β	Mg_2Si	FCC; a=6.39 Å

GP-zones which further elongate and form β'' precipitate [188]. The peak hardness [189, 203–205] and strength [195, 198] are attributed to a high density of needle or rod of β'' precipitate. The β'' precipitates are aligned along three equivalent <001>Al directions [189, 206] with a mean diameter of ∼4 nm and an average length of ∼50 nm [195, 206]. TEM image (Fig. 2.32) shows β'' precipitate in Al-0.72Si-0.58Mg alloy [203].

The β'' precipitate was reported to be fully coherent with Al matrix with OR: Al(001)$||\beta''$(010), Al[310]$||\beta''$[100] [206, 207]. The growth of the needle progresses until it becomes a semi-coherent rod-shaped β' precipitate. Lastly, the non-coherent equilibrium β phase is formed with the composition of Mg_2Si [188, 197]. The chemical composition and crystal structure of β-MgSi precipitates are listed in Table 2.3.

2.11   Ab initio method

The spatial distribution of atoms determines the properties of the material. Therefore computing on an electron level, requiring no empirically fitted inputs, can provide an enhance-

ment in the development of new materials. The many-body problem is the electromagnetic interaction of nuclei with other particles [208]. Schrödinger equation yields wave function which describes the position and energy of the electron in time and space. Behavior of electrons around atomic nuclei is described using Schrödinger equation simplified for time-independent solutions as:

$$\hat{H}\Psi = E\Psi \tag{2.49}$$

where $\hat{H}$ is the Hamiltonian operator (total energy of the particles), Ψ is the wave function and E is the total energy of the system. Hamiltonian can be written as the sum of kinetic energies and electrostatic interactions occurring in the simulation box:

$$\hat{H} = \hat{T}_n + \hat{T}_e + \hat{V}_{n-n} + \hat{V}_{e-e} + \hat{V}_{n-e} \tag{2.50}$$

where $\hat{T}_n$ is the kinetic energy of the nuclei, $\hat{T}_e$ is the kinetic energy of the electrons, $\hat{V}_{n-n}$ nucleus-nucleus interaction, $\hat{V}_{e-e}$ is the electron-electron interaction, $\hat{V}_{n-e}$ is the nucleus-electron interaction. Despite the fact that this Hamiltonian works only with electrostatic Coulombic interactions, it is impossible to solve it exactly and therefore certain approximations are needed [209].

2.11.1 The Born-Oppenheimer approximation

Note that electrons are much lighter compared to nuclei ($\sim$1000x), thus when nuclei move, the electrons adopt to the new nuclear distribution basically instantly [210]. Therefore nuclei can be fixed and assumed that electrons are in equilibrium. Hence only electrons are playing a role in many body problem [208] and nuclei are fixed as positive charged background [209], meaning the positive charge is now sort of 'external' to the electron cloud [208]. As a result of this approximation, equation 2.50 can be simplified so that $\hat{T}_n$ equals to 0, the term $\hat{V}_{n-n}$ is changed to constant, and the $\hat{V}_{n-e}$ is changed to the interaction of electrons with a positive external potential ($\hat{V}_{ext}$), which represents the material-specific information. Therefore, the electronic Hamiltonian becomes [208, 209]:

$$\hat{H} = \hat{T}_e + \hat{V}_{e-e} + \hat{V}_{ext} \tag{2.51}$$

Thus the ground state of electrons and exclusion of gravity simplify the problem of the exact solution since the interaction of all particles leads to a reduced complexity of the solution. However, the solution using the Born-Oppenheimer approximation is still too complex to be solved [209].

2.11.2 Density functional theory

Density functional theory (DFT) is an ab initio computational quantum mechanical modelling method which solves the many-body electronic problem. DFT provides a solution by

replacing the wave function with the electron charge density. The advantage here is that the electron density is independent of the number of electrons.

Kohn-Sham approach

A system of many interacting electrons (represented by coupled partial differential equations) can be solved using Schrödinger equation for non-interacting particles. This is known as the Kohn-Sham approach [211]. The method guarantees that the resulting particle density of the non-interacting particles represents the true electronic ground-state density. The initial density is guessed and subsequently, the potentials are constructed based on this density. The resulting Kohn-Sham equations are solved and a new electron density is constructed based on the this solution [209]. The process continues until self-consistent density is obtained.

Exchange-Correlation potentials

The most widely used representations of the exchange and correlation energies are local density approximation (LDA) and the generalised gradient approximation (GGA). The LDA is the more simple of those two and assumes the exchange-correlation potential depending on electron density at the particular location of the electron system. However, LDA treats the system as a homogeneous electron cloud. The GGA is a more accurate model considering the electron density gradient, therefore inhomogeneities of the charge density are taken into account and real systems can be described more precisely. Perdew-Burke-Ernzerhof (PBE or GGA-PBE) is a commonly applied parametrisation in solid states materials science [210, 212], and has been also used in this thesis.

2.11.3 VASP

The Vienna Ab initio Simulation Package (VASP) [213] is a software package for modelling materials at the atomic scale, which computes the ground-state properties based on the DFT approach. VASP uses the projector-augmented wave (PAW) pseudopotentials, which describe electron-nucleus interactions. The PAW method splits the wave function into core electrons and valence electrons, therefore higher accuracy can be achieved. Calculation is limited to ∼100 atoms, therefore initial setup for calculation needs to be tailor-made for each case. VASP uses periodical boundary conditions (PBC) for representation calculation of 'macroscopical' crystal. The geometry is therefore infinitely multiplied by its copies. It is therefore necessary to maintain coherent configurations. Large enough configurations have to be considered to avoid unwanted effects of PBC image. Convergence tests are performed before running the new crystal structure in order to control accuracy. Full relaxation is performed in order to obtain an equilibrium structure. To do so, the cell is put under compressive and tensile loads ranging from 95-105 % of its original volume. In this way,

computation of elastic constants can be performed in VASP using Hooke's law via the *strain-stress method*. Elastic constants are required in cases that the interface of two phases is constructed. Usually, the lattice parameters of two phases in a particular OR are not equally large, therefore one structure needs to be stretched and/or the other compressed in order to obtain a coherent interface. In case of surface slab calculations 'empty' sites in the supercell (SC) are treated as a vacuum in VASP. The atomic configurations are calculated at 0 K, therefore the thermal movement atoms is frozen, hence the atomic movement is based purely on energetic minimisation.

To run a VASP, the four different input files with the same designation for each particular calculation are required:

INCAR: File containing tags with specific descriptions of the calculation run. Importantly, the tag for cut-off energy, denoted as ENCUT [eV], defines the size of plane-wave basis set to be used in the DFT. The higher ENCUT, the higher accuracy and the calculation time. Calculations with different cut-off energies are generally not comparable. A balance between computational power and accuracy should be always kept in mind.

KPOINTS: Describes the mesh in the reciprocal k-space. VASP can generate automatic k-points based on the cell geometry. It generates the Γ-centered mesh along all reciprocal axes. The accuracy of calculation goes in hand with the number of k-points.

POSCAR: Lattice geometry and species occupying the lattice are described. The atomic positions, the allocation of elements to the particular positions and the lattice vectors are involved.

POTCAR: Definition of pseudopotentials (PPs) of each element. PPs describe the interaction of the 'non-frozen' valence electrons with the pseudo-atom, thereby the number of electrons is reduced and the efficiency of calculations is increased. The compatible order of elements in POTCAR and POSCAR must be ensured.

Visualization of structures before and after calculation, as used further in the thesis, was done using Visualization for Electronic Structural Analysis (VESTA) software.

Experimental and simulation methods

3.1 Melting and casting

Middle laboratory scale (50kg) casting of Al-7Si-0.3Mg based alloys were prepared using an electrical resistance furnace. Crucible has been manufactured from SiC and coated with BN to avoid any interaction of molten metal and crucible. Firstly, the commercial purity CP-Al was heated overnight to 350 $^{\text{o}}$C and 550 $^{\text{o}}$C, respectively. The next day the programmed temperature was set to 800 $^{\text{o}}$C. The furnace is equipped with an automatic temperature controller to record the furnace temperature. Secondly, the commercial purity CP-Si together with Al-3.3Mg or Al-8Mg master alloy was added. After each alloying the furnace was held on the temperature for 30 min to ensure the chemical homogenisation and to stabilise temperature. The degassing is then performed with degassing parameters: 5 l/min gas flow (Ar) for 20 minutes. The impeller (Fig. 3.1) was preheated for 5 min on the lid of the furnace before immersing into the melt. Degassed melts have been covered for an extra 10 minutes under the Ar atmosphere to reduce H reabsorption. Products of degassing have been skimmed and a reduced pressure test (RPT) has been performed. H content in Al-Si-Mg melt was quantified using the density index (DI) formula [214]:

$$DI = \frac{\rho_{\text{atm}} - \rho_{\text{vac}}}{\rho_{\text{atm}}} \cdot 100\% \tag{3.1}$$

where ρ_{atm} is the density of a sample solidified at the atmospheric pressure and ρ_{vac} is the density of a sample solidified at a reduced pressure of 80 mbar. The density of a sample is calculated as [63]:

$$\rho = \frac{m_{\text{air}}}{m_{\text{H}_2\text{O}}} \cdot \rho_{\text{H}_2\text{O}} \tag{3.2}$$

where m_{air} is the mass of the sample measured in the air, $m_{\text{H}_2\text{O}}$ is the mass of the sample measured in the water and $\rho_{\text{H}_2\text{O}}$ is the density of water. Note that DI does not measure the H content but the tendency of the alloy to form gas porosity. Samples before and after degassing are shown in Fig. 3.2. If the final value of density index (DI) was measured below

Figure 3.1: FDU (Foundry Degassing Unit) degassing using impeller at the Chair of Casting Research, Leoben.
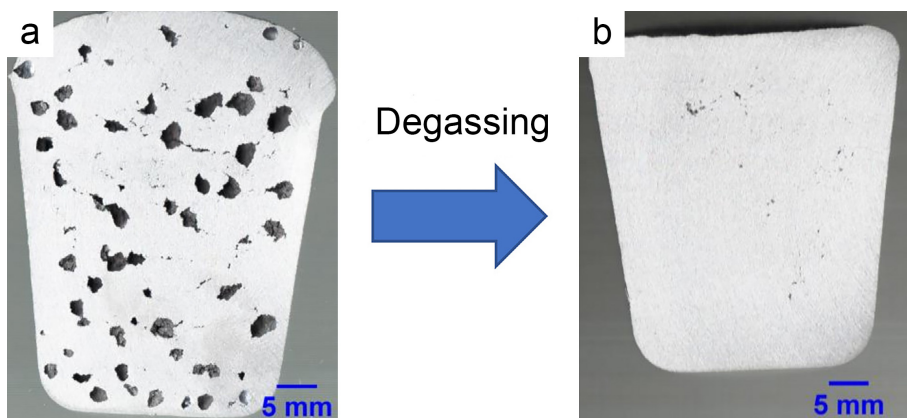

Figure 3.2: Cross-sectional images of the samples cast (a) before and (b) after degassing [215].

Figure 3.3: As-cast sample for microstructure evaluation sectioned from Diez mould.

1.5, the solutes in the form of master alloys (Al-10Ta, Al-2.2Ti-1B, Al-10Sr, Al-5Eu, Al-3P) were added to the melt. It should be noted that the melt temperature was increased to 740 ºC in order to facilitate the dissolution of Al-3P master alloy. Stirring was performed prior to casting with BN-coated and preheated tools. A molten metal temperature of 720 ºC was manually cast into a preheated Diez mould at 220 ºC made of cast iron coated with BN (Fig. 3.3). A ceramic filter of 20 ppi (pores per inch) was applied to limit the entrapment of bifilms. After the solidification, the sample for microstructure investigation was cut, as shown in Fig. 3.3.

3.2 Thermal analysis

Development of the microstructure during solidification was studied and recorded using the thermal analysis (TA) technique, namely the Quick cup method. A croning sand cup (Fig. 3.4) equipped with a single K-type Chromel-Alumel thermocouple position in the centre was implemented. The shape of the croning is rectangular (44 mm at the bottom and 50 mm at the top, height is 65 mm). Cup was placed on a stand (Pylet) and connected to the measurement device. Thermocouple was connected to software (PicoLog) installed in the operating laptop. The casting temperature of thermal analysis samples was 720 ºC. Obtained cooling curve from temperature recording was further evaluated using Origin(2020) software. In TA the undercooling was used to indirectly quantify the effectiveness of grain refinement of α-Al and modification of eutectic Si [55].

3.3 Heat treatment

Heat treatment was performed in a quenching furnace (Fig. 3.5). The rod samples were inserted into steel baskets and placed in the furnace. The furnace temperature was recorded by thermocouple build-in in the furnace. To verify and adjust the temperature inside the furnace the Al reference rod sample with a drilled hole in the middle and inserted K-type thermocouple was also placed in the basket with treated samples. Usually, the temperature deviation between the furnace thermocouple and the thermocouple in the sample was about 12 ºC at temperatures higher than 500 ºC and 3 ºC at temperatures lower than 200 ºC. The

Figure 3.4: Rectangular Croning sand cup including K-type thermocouple on the stand at the Chair of Casting Research, Leoben.

treatments applied in this work were solution treatment and artificial ageing, respectively.

Solution treatment: The samples inserted into the furnace were heated up to 530 $^\circ$C and held for 1 hour. The temperature was then increased to 540 $^\circ$C for 15 hours. The treated samples were quenched into water ($\sim$20 $^\circ$C) within 5 seconds.

Artificial ageing: Samples were inserted into the furnace at room temperature and heated up to 180 $^\circ$C and held for 4 hours as soon as the ageing temperature was reached in the Al reference rod. The samples were cooled down in the air.

3.4 Microstructure characterisation

This section provides an overview of multiple-characterisation techniques that were implemented in the present work. Sample preparation for each particular technique is described.

3.4.1 Metallography

Metallography samples were prepared using a standard metallography process consisting of grinding and polishing, respectively (Fig. 3.6a). Grinding was performed using SiC paper with 80, 220, 600, 800 and 1000 grades by hand for 3-5 mins for each step. Polishing was performed using 3 µm diamond suspension and 50 nm colloidal silica suspension. Polishing was performed on ATM Saphir 350 E instrument (Fig. 3.6b) Ethanol was used for cleaning the polished surface. To remove the remaining polishing suspension the ultrasonic cleaning (Fig. 3.7) was implemented for 30 minutes. Barker's etching was implemented in order to
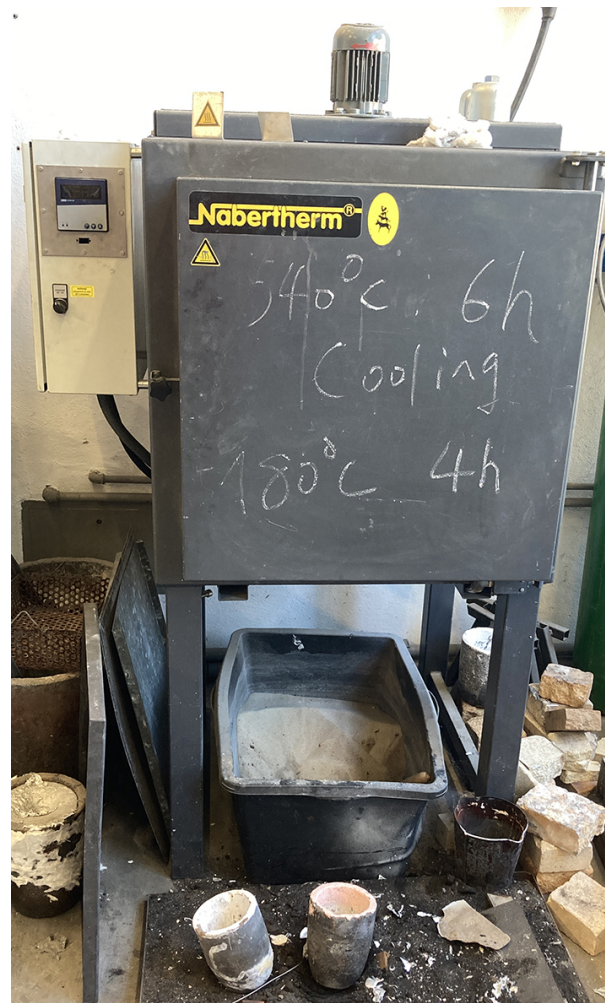
Figure 3.5: Heat treatment furnace at the Chair of Casting Research, Leoben.

easily detect the α-Al grains by using a polarized filter on Zeiss AXIO optical microscope (Fig. 3.8). Modified Murakami reagent (MMR) was implemented in as-cast samples for 90 seconds to facilitate the observation of eutectic grain boundaries. MMR is a mixture of 240 ml H_2O, 40 g NaOH and 20 g $K_3[Fe(CN)_6]$. MMR reacts with segregated phases at the grain boundaries and then the eutectic grain size can be investigated using OM. Deep etching was performed using 15 % HCl for 30 mins to remove α-Al and reveal the 3D morphology of eutectic Si.

3.4.2 Optical microscopy

The α-Al grain size and eutectic grain size were investigated using an (A1m AXIO) ZEISS Imager (Fig. 3.8). The digital images were taken using a Nikon Digital Sight DS-Fi1 camera and stored in TIFF format for further image analysis using ImageJ software. Samples were investigated at magnifications of 50-1000x. The large images for grain size evaluation and eutectic grain boundaries analysis were constructed in a total of 16 images at a magnification

Figure 3.6: (a) Grinding and polishing equipment and (b) grinding and polishing machine at the Chair of Casting Research, Leoben.

Figure 3.7: Ultrasonic cleaner at the Chair of Casting Research, Leoben.

Figure 3.8: Optical microscope (OM) at the Chair of Casting Research, Leoben.

of 50x from the centre of the sample via multiple image alignment (MIA). The grain size was measured according to ASTM E112 standard [216].

The dimensionless shape factor (SF) parameter is defined as follows [96, 217]:

$$SF = \frac{4\pi A_{\mathrm{SF}}}{P_{SF}^2} \tag{3.3}$$

where A_{SF} is the area and P_{SF} is the perimeter. SF value can vary from 0 to 1, where 1 represents the perfect circle and 0 represents the line of investigated particle.

3.4.3 SEM

Scanning Electron Microscopy (SEM) was implemented to investigate eutectic morphology and intermetallic phases in as-cast and heat treated samples and entrained eutectic droplets within melt-spun ribbons after DSC heating. SEM JOEL in (Fig. 3.9) is equipped with electron backscatter diffraction (EBSD) detector (Oxford) and energy-dispersive X-ray spectra (EDS) (Oxford). EBSD was applied to investigate the grain size of α-Al and the orientation of eutectic Si in melt-spun samples. Evaluation of SEM and EBSD data was performed using AZtec and AZtec Crystal software. The grain size of melt-spun samples is usually too small ($\sim$5 µm) to be analysed using Barker's etching and polarised filter in OM, therefore the EBSD was mainly applied to quantify grain size. EBSD of as-cast alloys was performed using an acceleration voltage of 20 kV with a probe current 16 nA, working distance of 16 mm and step size of 0.5 µm (section 4.4 and 5.4), while step size of 1 µm is used for EBSD in melt-spun samples (section 6).

3.4.4 Dimple grinding and PIPS

The sample was sectioned from the Diez mould rod and then manually grounded using SiC grinding paper in various grades based on the thickness of the sample: 220 grade (up to 500

Figure 3.9: SEM JOEL at the Chair of Ferrous Metallurgy, Leoben.
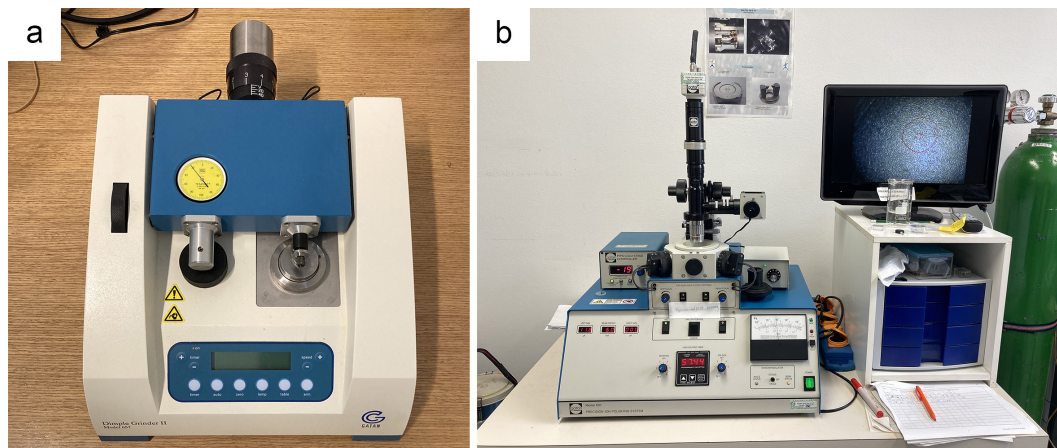
Figure 3.10: (a) Dimple grinder at the Chair of Casting Research, Leoben and (b) PIPS machine at Erich Schmid Institute of Materials Science, Leoben.

µm), 800 grade (up to 300 µm), 1200 (up to 150 µm), 2500 (up to 100 µm) and 4000 (up to 70 µm). The thickness of the sample was controlled via a micrometre. The sample with a thickness of 70 µm was punched out into a 3 mm disc and dimpled using Gatan model 691 (Fig. 3.10a) with a final thickness of 15-20 µm in the centre of the disc.

The last step is the Precision Ion Polishing System (PIPS), which is shown in Fig. 3.10b. PIPS is implemented for thinning and/or polishing of the samples. Samples can be PIPS at a very low operation temperatures (below 0 $^\text{o}$C). The rotation of the sample was set to 2-3 rpm and the ion gun was set to 6 keV. The angle of ion gas flow was set to $\pm 8^\text{o}$ from the bottom and top, respectively. If the sample was dimple grounded below 25 µm, PIPS takes 2-3 hours for Al-Si alloy.
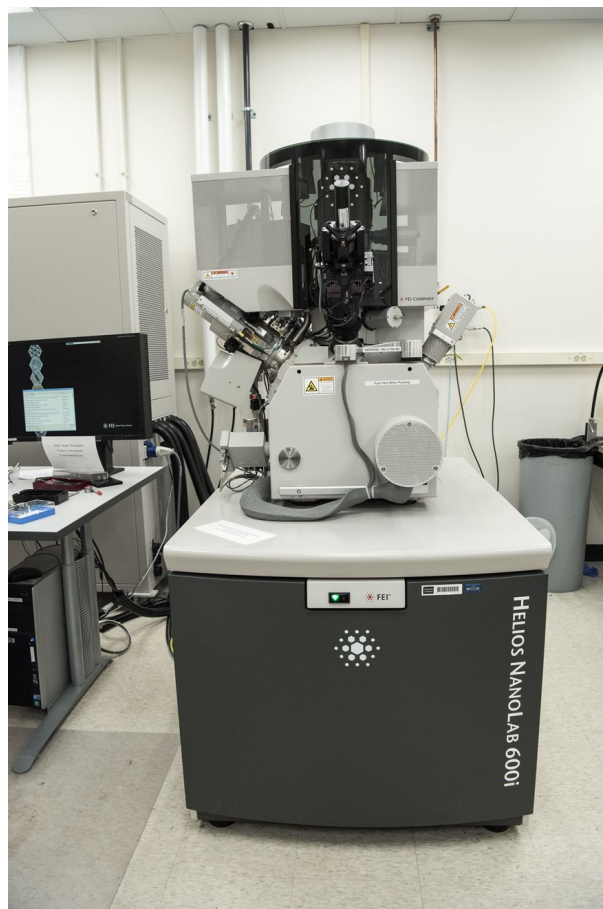
Figure 3.11: FEI Helios Dual Beam SEM/FIB 600/600i instrument [220].

3.4.5 FIB

The focused ion beam (FIB) technique was used to produce very thin samples suited for TEM, where a thickness of about ∼100 nm is required. Specimens from specific regions can be cut out and studied, which is an advantage compared to dimple grinding, where the investigated area is given by the creation of random hole based on the sample thickness. FEI Helios Dual Beam SEM/FIB 600/600i instrument (Fig. 3.11) is used to produce TEM samples from bulk material using standard lift-out method [218, 219]. FIB is equipped with SEM. SEM uses a beam of electrons, while FIB applies a focused beam of ions, typically gallium.

3.4.6 TEM

Transmission Electron Microscopy (TEM) was implemented for atomic examination of as-cast and heat treated samples and ribbons to reveal the intermetallic phases, stable or metastable phases (precipitates) formed during solidification and evolved after heat treatment and grain boundaries of eutectic droplets. High resolution TEM (HRTEM) and EDS

Figure 3.12: (a) TEM JEM 2100F machine at Erich Schmid Institute of Materials Science, Leoben and (b) STEM FEI Titan^{3TM} G2 60–300 at the Austrian Centre for Electron Microscopy and Nanoanalysis in Graz [222].
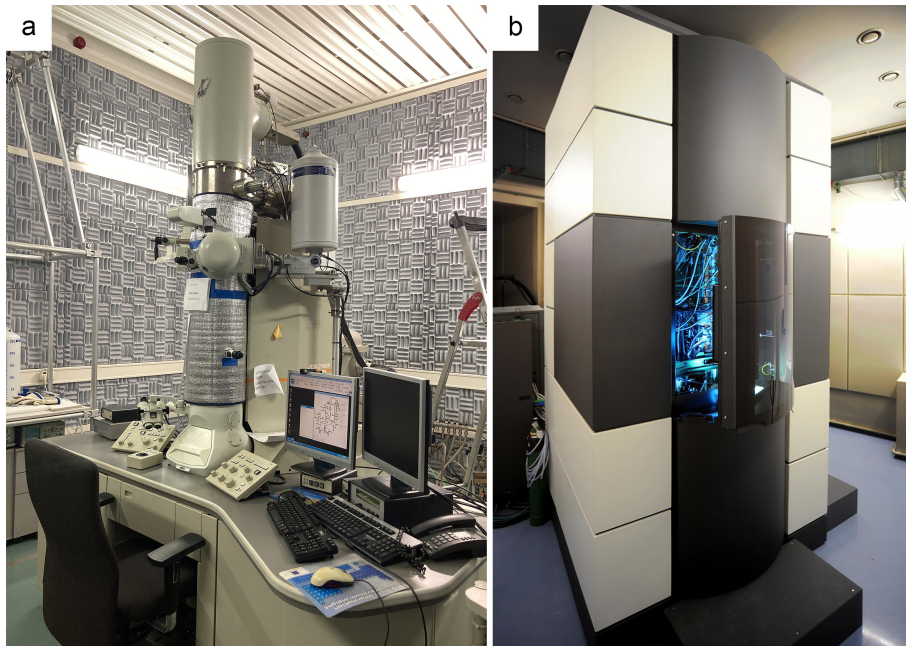
investigations were performed using a Cs-corrected JEOL-2100F microscope operated at 200 kV. Access to the TEM facility (Fig. 3.12a) is provided by the Erich Schmid Institute of Materials Science of the Austrian Academy of Sciences in Leoben.

The high resolution (HR) scanning transmission electron microscopy (STEM) micrographs and EDS investigations were performed using a monochromated and probe corrected FEI Titan^{3TM} G2 60–300 (S/TEM) microscope operated at 300 kV with an X-FEG high brightness emission gun. Access to FEI Titan^{3TM} G2 60–300 microscope (Fig. 3.12b) is provided by Austrian Centre for Electron Microscopy and Nanoanalysis in Graz. The HR images in STEM mode were recorded with a beam diameter of 0.1 nm and a current of 0.04 nA using the high-angle annular dark-field (HAADF) and dark field (DF) detectors. Energy dispersive X-ray spectrum imaging (EDS SI) was acquired by the SuperX detection system (Chemi-STEM technology, VELOX software) with a 120 mm acquisition area, which reduces significantly the acquisition times. Relative elemental quantification of the EDS was performed using the k-factor method. The images were recorded by a Gatan Digiscan unit and Digital Micrograph software and were corrected for dark current and gain variations. Elemental quantification of the EDS was performed using the Zeta factor method [221].

Figure 3.13: Vickers hardness testing machine at the Chair of Metal Forming, Leoben.

3.5   Hardness testing

Solution treated rod samples were sectioned. Samples were placed into a heat treatment furnace (Fig. 3.5) and heated up to 180 °C. Each investigated alloy was removed and cooled down in air at a total of 11 different ageing times (0 h, 0.5 h, 1 h, 2 h, 3 h, 4 h, 6 h, 8 h, 10 h, 20 h and 30 h). After cooling down, the samples were mechanically ground (SiC up to 2500 grade). Hardness was measured using a Vickers hardness testing machine (EMCO-TEST M1C 010) with a load of 1 kg and a dwelling time of 10 s (Fig. 3.13). Testing was repeated at least 5 times. Measurements were kept at a minimum mutual distance of 1 mm.

3.6   Tensile property testing

The rod sample produced by casting to Diez mould are machined to a defined specimens geometry for tensile properties according to DIN 50125. The measurement is performed on Zwick Z250 materials testing machine (Fig. 3.14) at the room temperature according to EN ISO 6892-1. The measurement is destructive and the main tensile properties such as yield strength ($R_{p0.2}$), tensile strength (R_m) and elongation (A_5) are recorded.
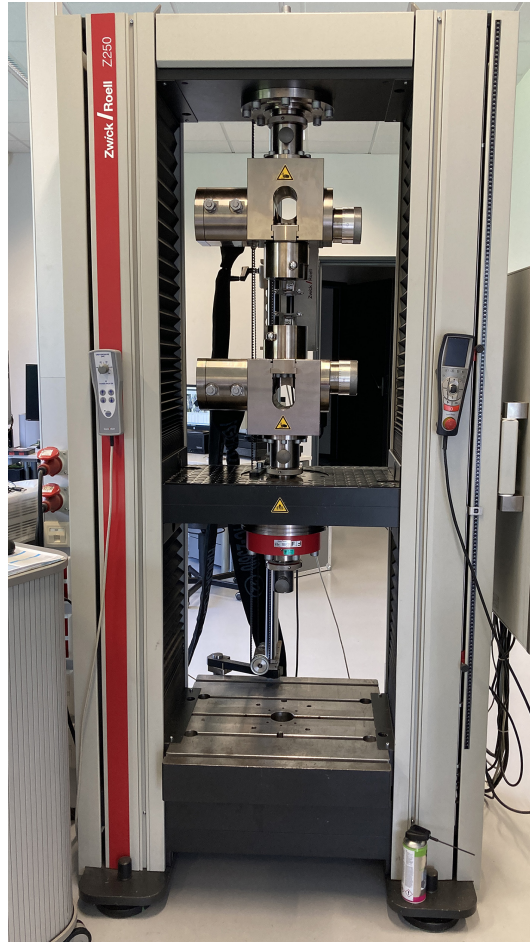
Figure 3.14: Tensile properties testing instrument at the Austrian Foundry Research Institute, Leoben.

3.7 Fracture toughness testing

For the fracture toughness testing, the compact-tension C(T) samples according to the ASTM standards (ASTM E399 and E1820) were machined by electro discharge machining (EDM). The geometry of the samples is shown in Fig. 3.15. The access to fracture toughness testing facilities is granted to Erich Schmid Institute of Materials Science in Leoben.

Firstly, the sample has a nominal width (W) of 18 mm, a thickness (B) of 9 mm and a final crack length including an introduced fatigue pre-crack of approximately 10 mm. A fatigue pre-crack is introduced by compression-compression loading using a load ratio ($R=P_{min}/P_{max}$) of 10 and a stress-intensity factor range, ΔK, of ΔK=10 for approximately 30000 cycles. Secondly, this sharp crack was then extended under cyclic tensile loading using an R of 0.1 and ΔK of 6 for approximately 10000 cycles. Thirdly, after the introduction of the fatigue pre-crack side-grooves were also introduced into the sample with a depth of 0.75 mm per side.
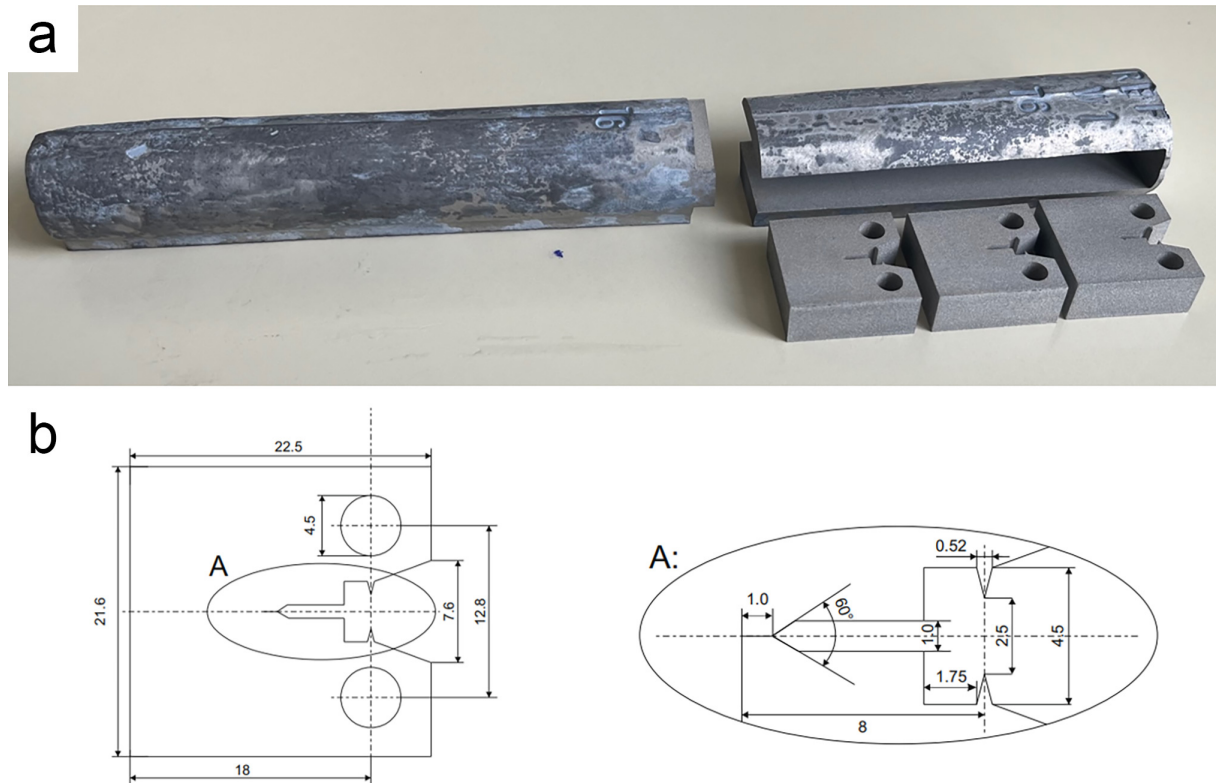
Figure 3.15: (a) Orientation of the samples and (b) specimen geometry. The magnified view of (b) shows only the notch length, not the final crack length.

The experiments were performed with a universal testing machine from Zwick (Z100) employing a constant displacement speed of 0.1 mm/min. The displacement of the sample was measured in the load line with a HBM (DD1) displacement gauge.

3.8   Arc melting

In this chapter, melting of HP alloys is described. Solutes were added in the form of CP master alloys. HP 5N (99.999 wt. %) aluminium ingots (Hydro Aluminium High Purity GmbH, Germany) and HP 5N (99.999 wt. %) silicon (Siltronic AG, Germany) were purchased. Additions of Ta, Eu and TiB_2 were made using CP Al-10Ta, Al-5Eu, Al-2.2Ti-1B master alloys, respectively. Prior to melting in an arc melter (Fig. 3.16a), the material was sectioned using a hacksaw without any oil or lubricant and cleaned with ethanol. This process was implemented in order to keep the contributions of impurities to a minimum. Aluminium pieces (5-10 mm) were then grounded using 800 SiC paper to remove possible impurities. A large piece of Si was rolled into fibre-free paper and sectioned into smaller pieces using a hammer. Al and Si pieces were thoroughly cleaned with ethanol. Lastly, the pieces were cleaned using ultrasonic cleaner (Fig. 3.7). Due to very low additions of
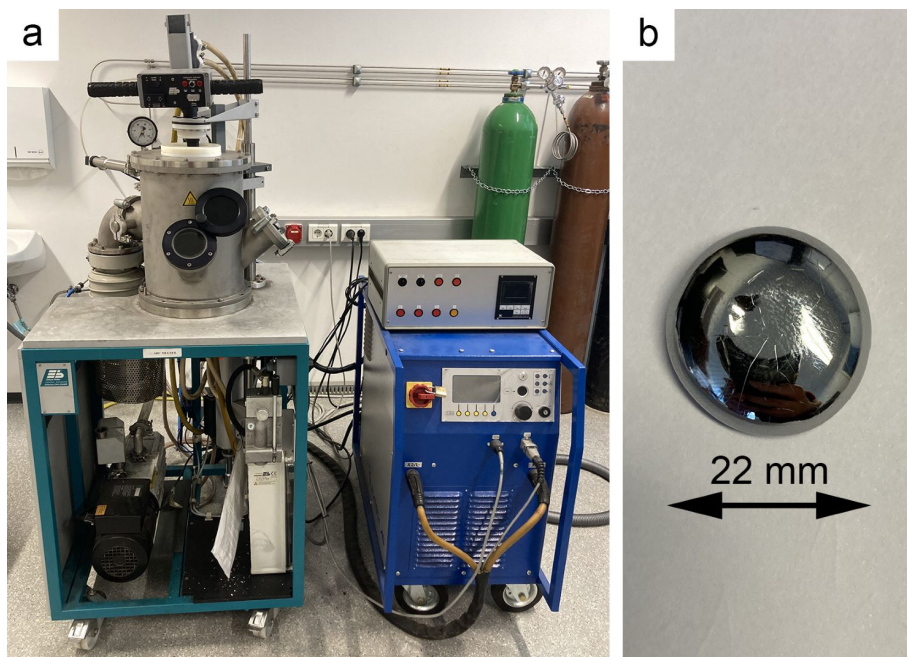
Figure 3.16: (a) Arc melter at the Chair of Casting Research, Leoben. (b) Alloy after arc melting.

solutes in the form of master alloys, the small pieces of master alloys were cleaned using only ultrasonic cleaner for 30 min.

Small Al-Si ingots in the form of disks ($\sim$10 g) with controlled additions of Ta, Eu and TiB$_2$ were manufactured in an arc melter (Fig. 3.16b). Weighted material was placed into water cooled Cu heart grooves in the form of a disk. The arc melter further consisted of a Ti gettler, a water cooled chamber and a W electrode. The free movement of the electrode under a reduced atmosphere was ensured via a pressure compensating mechanism. Prior to melting, the vacuum of 10^{-5} mbar was achieved using a combination of rotary and diffusion pumps. Then the chamber was filled with 800 mbar of Ar. The Ti gettler was used to stabilise the arc during the start and to remove oxygen from the atmosphere in order to reduce possible oxidation before melting. The alloys in the form of 10 g disks were remelted at least two times using a higher current of 250 A in order to ensure full dissolution and homogenisation of alloying elements.

3.9 Melt spinning

The goal of this method was to obtain rapidly solidified ribbons. Melt spinner as a laboratory technique provides a high cooling rate (in the order of 10^6 K/s [47]) necessary to produce fine rapid quenched microstructure. Melt spinning instrument is shown in Fig. 3.17a. An induction coil, quartz crucible and Cu wheel were placed within a chamber. Disks produced

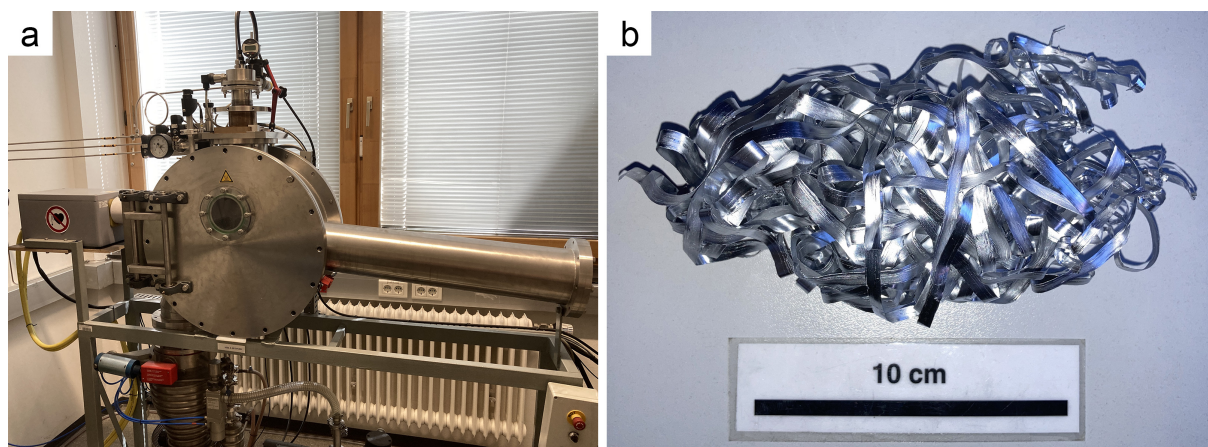Figure 3.17: (a) Melt spinning instrument at the Chair of Casting Research, Leoben and (b) Al-5Si ribbons produced by melt spinning.

from arc melting were cut and cleaned with ethanol and subsequently loaded into a quartz crucible having a length of 100 mm and diameter of 16mm. At the bottom of the crucible there is a hole with $\sim$0.8 mm in diameter. The distance between the quartz crucible and the Cu wheel was set to 0.5 mm. A similar vacuum system to arc melter was implemented to achieve a vacuum of 10^{-5} mbar. Then the chamber was filled with He up to 200 mbar.

Cheltenham induction heating unit melted the loaded crucible. The samples were heated at $\sim$800 ºC. The significantly higher temperatures than the liquidus temperature of Al-Si alloys were implemented in order to reduce the viscosity for subsequent ejection. The melt was ejected using 200 mbar Ar overpressure onto the Cu wheel rotating with a tangential wheel speed of 20 m·s^{-1}. Produced ribbons (Fig. 3.17b) had usually 3 mm in width and 80-120 µm in thickness.

3.10 DSC

The precipitation kinetics of solid-solid reactions (e.g., precipitation, dissolution, etc) in Al alloys can be studied using DSC [223]. It mainly depends on the supersaturation of the solid solution, concentration of vacancies, solute atoms and diffusion and bonding energy of vacancy.

Solidification and precipitation during artificial ageing were investigated using Perkin Elmer Diamond DSC calorimetry equipped with Pyris7 software, as shown in Fig. 3.18. All the DSC runs were measured using graphite crucibles. The DSC heating and cooling thermographs were recorded in Ar protective atmosphere. Prior to each DSC run, cleaning up to 600 ºC was performed by the software to remove the dirt and volatiles from the preceding experiment. Cast samples were manually ground using 220 SiC paper in a mass range of

Figure 3.18: DSC instrument at the Chair of Casting Research, Leoben

20-50 mg and cleaned with ethanol. Ribbons were cut, cleaned with ethanol and weighted $\sim$10 mg. As-cast samples were investigated for solidification behaviour. The samples were heated from 50 ºC to 700 ºC and cooled from 700 ºC to 50 ºC with a heating/cooling rate of 10 ºC/min. The initial and final temperatures were always held for one minute to ensure equilibrium. Quenched samples (after solution treatment) were investigated for precipitation of β-type precipitates. The samples were heated from 200 ºC to 350 ºC with a various heating rates, namely 1, 2, 5, 10 and 20 ºC/min with also one minute equilibrium before the heating/cooling stage. The baseline was subtracted, onset temperature, endset temperature, peak temperature and total enthalpy change were extracted using Pyris7 software. Data were further processed using Origin software or Python. The baseline of all heating rates was obtained by running the empty runs with an identical heating and cooling and within an identical temperature range. It should be noted that at lower heating rates such as 1 and 2 ºC/min, the peaks are smaller and thus the peak temperatures are not significant. Moreover, to determine all the possible peaks, namely β-(Mg_2Si), the heating rate of 10 ºC was performed in the temperature range from 200 ºC to 450 ºC.

3.10.1 Activation energy analysis

It is generally accepted that non-isothermal experiments are more complicated than isothermal experiments. Mostly, the non-isothermal data are interpreted by activation energy (E_a). In this work, the Kissinger method [224–226] is implemented to determine the activation energy. This technique is straightforward and is popular among researchers due to its high

accuracy. The Kissinger method can be also applied when the exact reaction mechanism is not known [224–226]. The original form of Kissinger method of calculating activation energy is as follows:

$$\frac{\phi}{T_{\max}{}^2} = X - \frac{E_a}{R_{\text{gas}} \cdot T_{\max}} \tag{3.4}$$

where ϕ is the heating rate, $T_{\max}$ is the maximum peak temperature, X is the constant and R_{gas} is the gas constant. From the DSC run, the only parameter that needs to be extracted is the maximum peak temperature ($T_{\max}$), which makes this technique very convenient especially for unknown reaction mechanisms. Therefore the evolution, nucleation stage and thermal history of the investigated material are not involved in this method. It should be noted that Kissinger method is also applicable to isothermal runs.

The position of $T_{\max}$ is shifted to a higher temperature with increasing heating rate (ϕ). After extracting the ($T_{\max}$) from DSC non-isothermal curves with various heating rates the $ln(\frac{\phi}{T_{\max}{}^2})$ vs. $\frac{1}{T_{\max}}$ plot shows a straight line of the slope equals to $-E_a/R_{\text{gas}}$ [224, 227, 228]. In the following pages, this plot is referred as a Kissinger plot and the plot is rearranged to $ln(\frac{\phi}{T_{\max}{}^2})$ vs. $\frac{1}{-R_{\text{gas}} \cdot T_{\max}}$, then the slope of the plot equals directly to E_a.

3.11 Simulation set up

Four types of calculations were performed within the framework of this thesis: (i) interface energy calculation of TiB_2 particle with aluminides, (ii) interface energy of Al with β'' precipitate, (iii) the effect of alloying on the thermodynamic stability of β-type precipitates, and (iv) substitution energy of an alloying element at the twin boundary (TB) of Si, respectively. In this section, methods and parameters used for DFT calculation are described.

3.11.1 Interface energy of TiB_2 and aluminides

For the interface of a TiB_2 particle with aluminides, in total, five different interface structures were calculated with ten specific configurations. The configurations of SCs are shown in Fig. 3.19 and the calculation of interface energy (γ) is as follows:

$$\gamma = \frac{E_{\text{TiB}_2/X} - (E_{\text{TiB}_2} + E_X)}{2 \cdot A} \tag{3.5}$$

where $E_{\text{TiB}_2/X}$ is the total energy of the slab, E_{TiB_2} is the total energy of TiB_2. E_X is the total energy of the constituent, where X=Al, Al_3Ti or Al_3Ta, and A is the interface area. The total energy of E_X can be calculated using the following equation:
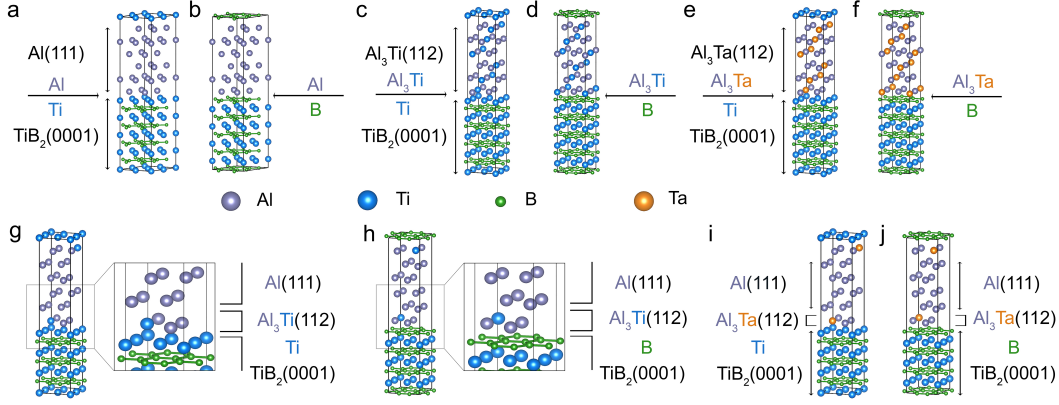
$$E_X = E_{0X} + E_{\text{strain}_X} \tag{3.6}$$

Figure 3.19: Side view of three $TiB_2(0001)$ Ti-terminated slabs with: (a) Al(111), (c) $Al_3Ti(112)$ and (e) $Al_3Ta(112)$ and B-terminated (b),(d),(f), respectively. The sandwich structures (g-j) contain (g,h) Al_3Ti and (i,j) Al_3Ta layer in between Al(111) and $TiB_2(0001)$ with Ti and B-termination, respectively [229].

Table 3.1: Initial lattice parameters from the literature (marked with *) and calculated lattice parameters.

		Lattice parameters [Å]			
Phase	Structure	a^*	c^*	a	c
Al	FCC	4.051 [230]	-	4.037	-
TiB_2	HCP	3.0314 [230]	3.2228 [230]	3.030	3.228
Al_3Ti	Tetragonal	3.8537 [231]	8.5839 [231]	3.846	8.618
Al_3Ta	Tetragonal	-	-	3.859	8.582

where E_{0X} is the equilibrium energy and E_{strain_X} is the strain energy calculated as described in section 2.11.3. The atomic planes of TiB_2 that are facing the aluminides (Al, Al_3Ti or Al_3Ta) at the interface are Ti or B-terminated (Fig. 3.19). OR between $TiB_2(0001)$, $Al_3Ti(112)$, $Al_3Ta(112)$ and Al(111) planes were considered according to reference [17, 115]. Slabs with OR of $TiB_2(0001)||Al_3Ti(112)$ or $Al_3Ta(112)$ and/or Al(111) is shown in Fig. 3.19a-f. Sandwich structures with OR: $TiB_2(0001)||Al_3Ti(112)$ or $Al_3Ta(112)$ monolayer$||Al(111)$ is shown in Fig. 3.19g-j. An overview of used lattice parameters is listed in Table 3.1. The reciprocal space was sampled with Γ-centred k-mesh with a k-points spacing of maximum ~0.17 Å^{-1} (corresponding to, e.g. 12x12x11 mesh for TiB_2 unit cell). The plane-wave cut-off energy was set to 500 eV.

3.11.2 Interface energy of Al and β''

Doping of Ti or Ta at the interface of $Al(001)||\beta''(010)$ [206] was studied in order to elucidate the effect of solutes at the interface energy. The equation for the calculation of interface energy is the same as in equation 3.5. The model of the interface is shown in Fig. 3.20. The $Al(001)||\beta''(010)$ SC have reached equilibrium, then a single Ti or Ta atom was placed at the
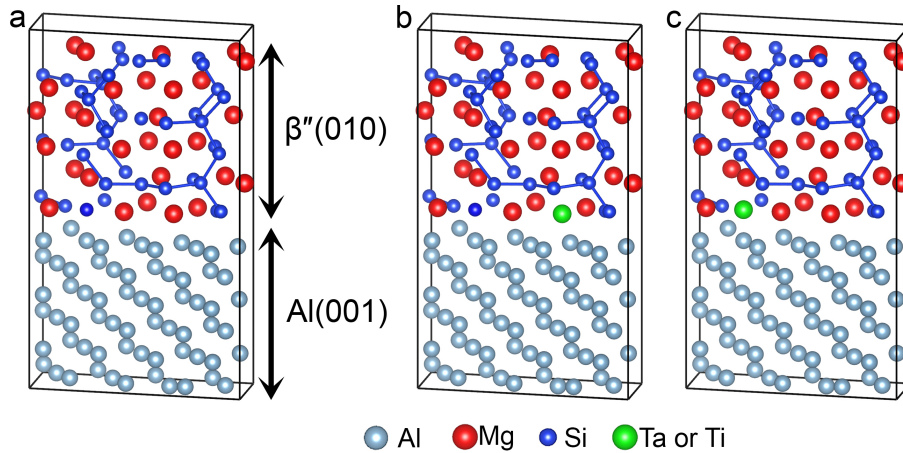
Figure 3.20: Side view of three used slabs: (a) Initial configuration of Al(001)$||\beta''$(010) interface, alloyed interface by Ta or Ti on (b) Mg sublattice and (c) Si sublattice. Note that Ta and Ti atoms were also placed instead of Al [232].

Table 3.2: Calculated lattice parameters and reference lattice parameters from the literature. The last column denotes the used SC and corresponding values from the number of atoms in a SC.

Phase	Structure	Lattice parameters				Number of at.
		a [Å]	b [Å]	c [Å]	β [º]	[-]
Al	FCC	4.03	-	-	-	108
		4.05 [230]				3x3x3
β''-Mg$_5$Si$_6$	Monoclinic, C2/m	15.08	4.09	6.93	110.46	132
		15.16 [206]	4.05 [206]	6.74 [206]	105.3 [206]	1x3x2
β'-Mg$_9$Si$_5$	HCP, P6$_3$/m	7.13	-	12.22	-	112
		7.15 [197]		12.15 [197]		2x2x1
β-Mg$_2$Si	FCC, CaF$_2$-type	6.36	-	-	-	96
		6.39 [233]				2x2x2

interface instead of Al atoms for all interface positions. The same procedure was applied to Mg and Si positions from β'' interface. The lattice parameters of the interface were set the same, thereby bi-axial strain was applied by the coherency of the interface. The plane-wave cut-off energy was set to 500 eV. The reciprocal space was sampled with Γ-centred k-mesh with k-points (7x4x2).

3.11.3   Thermodynamic stability

The stability of pure Al and β-MgSi precipitates from the precipitation sequence of SSSS $\rightarrow$ GP zones $\rightarrow \beta'' \rightarrow \beta' \rightarrow \beta$ has been verified by ab initio calculation. Calculated lattice parameters of precipitates are shown in Table 3.2. Each unit cell was multiplied to obtain a similar size and number of atoms in all SCs due to large differences in lattice parameters of precipitates. The size of the SC and number of atoms are also listed in Table 3.2.
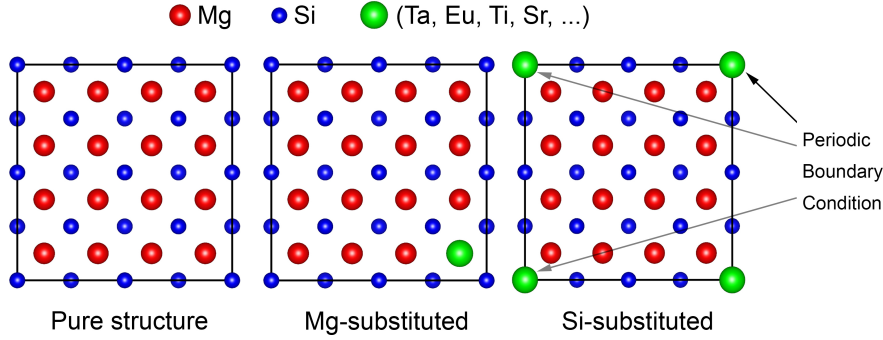
Figure 3.21: Reconstructed pure FCC β-Mg$_2$Si precipitate with substituted Mg or Si atoms by alloying elements. It should be noted that the Si-substituted atom is multiplied in each corner of the Mg$_2$Si cell due to periodic boundary conditions. Thus, only one atom is substituted for each calculation [232].

In total, 20 cases were considered for each phase, one pure structure and 19 structures with 1 alloying atom. In total, 19 elements (Ag, Ce, Cr, Cu, Er, Eu, Fe, Hf, La, Mn, Sc, Sn, Sr, Ta, Ti, V, Yb, Zn and Zr [234]) were considered to be substituted for one Mg, Si atom (green atom in Fig. 3.21). For the β-type precipitates, two configurations with each sublattice were calculated. The formation energy per atom (E_f^ξ) of a phase ξ is calculated in order to compare non-equally sized SCs.

$$E_f^\xi = \frac{E_{\text{tot}}^\xi - \sum_s N_s \cdot \mu_s}{\sum_s N_s} \tag{3.7}$$

where E_{tot}^ξ is the total energy of a supercell representing phase ξ and containing species s, N_s is the number of atoms of species s in the supercell, μ_s is the chemical potential of species s in standard structure (FCC-Al, HCP-Mg, diamond-Si, bcc-Ta, ...). E_{tot}^ξ and μ_s were obtained from VASP. To calculate the preference for Mg or Si sublattice substitution, the site preference energy (ΔE_{site}) of species i in the phase ξ is calculated as follows:

$$\Delta E_{\text{site},i}^\xi = E_{\text{tot},i\to\text{Mg}}^\xi - E_{\text{tot},i\to\text{Si}}^\xi + \mu_{\text{Mg}} - \mu_{\text{Si}} \tag{3.8}$$

where $i\to$Mg ($i\to$Si) means a species i replaces a Mg (Si) atom. In order to determine in which phase the alloying atom is preferred, the phase preference energy (ΔE_{phase}) is calculated as follows:

$$\Delta E_{\text{phase}} = \Delta E_f^{Al(\beta'',\beta')} - \Delta E_f^{\beta''(,\beta',\beta)} \tag{3.9}$$

where ΔE_f^ξ is the formation energy difference between phase ξ containing species i and pure phase ξ.

3.11.4 Twin boundary

Symmetric $\sum$3 <110> {111} twin boundary (TB) was constructed as a representative model of TB in Si. Two identical TBs are obtained due to PBC but only one is situated at the

middle of the simulation box. Atoms on the one side of the {111} plane were. Thereby, a SC consisting of 224 Si atoms and two {111} free surfaces meeting at the TBs was constructed (Fig. 3.22a). Relaxation of the free surface was performed (Fig. 3.22b). Subsequently, one Si atom was replaced by a solute atom (Eu) at every position at the free surface simulating a growing Si twin (shadowed box in Fig. 3.22b). Positions at the TB simulate the IIT mechanism, while those further away correspond to the TPRE mechanism. The atoms at the vertical edge of the SC (left side in the Fig. 3.22a) as well as those at the top (bottom) side of the simulation box were fixed in their initial positions corresponding to an ideal Si bulk (with the TB), whereas all other atoms were relaxed. The SC shape and volume were kept constant during the structural relaxation (with the initial Si-Si spacings corresponding to that in the bulk Si, $b = 2.375$ Å). The calculations were performed using plane-wave code VASP [213], PAW pseudopotentials [234] and GGA-PBE approximation for the exchange and correlation interactions [212]. The plane-wave cut-off energy was set to $\sim$520 eV. The Brillouin zone of the reciprocal space was sampled with Γ-centred k-mesh with k-points spacing of maximum $\sim$0.10 Å^{-1}.

Substitutional energy (ΔE_{sub}) is calculated according to the following equation:

$$\Delta E_{\mathrm{sub}} = E_{\mathrm{Eu}} - E_{\mathrm{pure}} \tag{3.10}$$

where E_{pure} is the energy with pure structure and E_{Eu} is the energy of a SC with an Eu atom replacing one by one the Si atoms at the {111} surface.

3.12 Sand casting

To verify the modification effect in real-size casting, the casting parts were produced by sand casting. The melt preparation is identical as described above (section 3.1). The cores were manufactured using corebox and water glass mixture hardened by CO_2 (Fig. 3.23), while the mould was prepared using cast iron flasks and green sand (Fig. 3.24). The graphite and talc powder to facilitate the demoulding of corebox and to reduce the sticking of the cope and drag to the model plate, respectively. Venting system was carved out manually to avoid gas entrapment during the casting process. The casting temperature for sand casting was 720 ºC. The mould cooled down for 1 h prior demoulding. Green sand was easily removed using moulding tools. Water glass cores were removed using drill due to its high hardness. The samples for microstructure investigation was taken from the area denoted in Fig. 3.24d. Sample preparation for optical microscopy is shown in section 3.4.1.
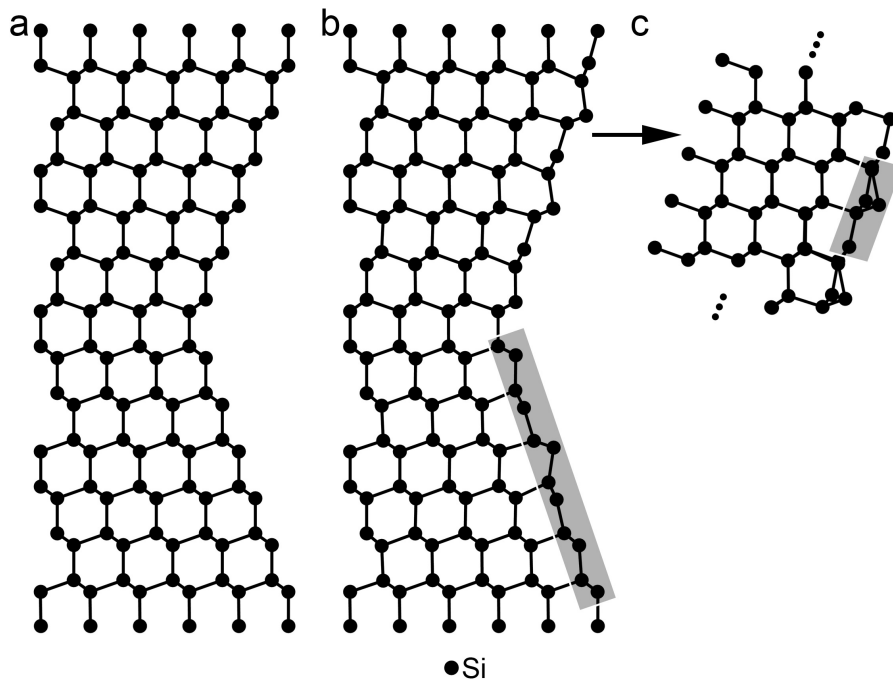
Figure 3.22: Si twin boundary (TB) models of (a) pure Si twin with free surfaces, (b) pure Si twin with free surfaces after relaxation with denoted 12 sites considered for the substitution (shadowed box) and (c) modelled free surface of Si{111} with denoted 8 substituted atoms (shadowed box). Model (c) represents a free surface located far from the TB.
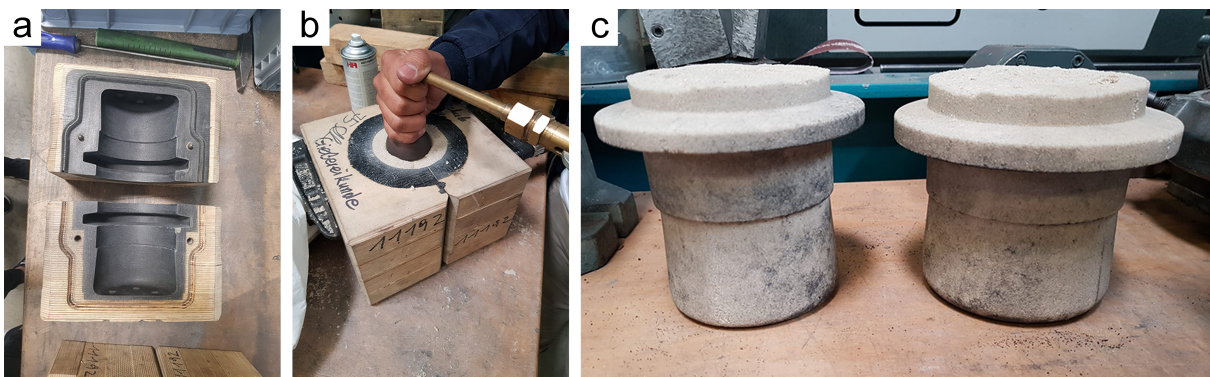
Figure 3.23: (a) core box, (b) CO_2 hardening of the core box filled with a mixture of SiO_2 sand and water glass and (c) demoulded water glass sand cores.
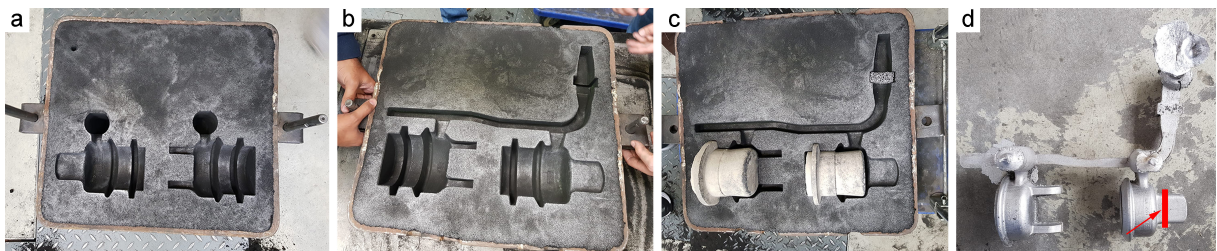
Figure 3.24: (a) cope, (b) drag, (c) water glass cores and filter placed into drag prior to mould assembling and (d) casting part after demoulding with denoted position for microstructure analysis.

Ta grain refinement in Sr-modified Al-Si based alloys

This chapter is based on two publications [229, 232].

The chemical composition of investigated alloys is listed in Table 4.1. Ref alloy is without the addition of grain refiner and modifier. 0.01Ti alloy is grain refined with Al-5Ti-1B grain refiner. 0.07Ta and 0.12Ta alloy are grain refined with Al-2.2Ti-1B grain refiner in combination with 0.07 wt. % Ta and 0.12 wt. % Ta, respectively. All alloys are modified with Sr. Note that only 0.01Ti alloy contains solute Ti from conventional Al-5Ti-1B grain refiner. In Al-2.2Ti-1B grain refiner, all the Ti is bounded with B into TiB_2.

4.1 Thermal analysis

Thermal analysis cooling curves are shown in Fig. A.1 and the extracted values are listed in Table 4.2. Ref alloy shows a significant undercooling (ΔT) of 2 $^\text{o}$C, which is the highest undercooling measured. 0.01Ti, 0.07Ta and 0.12Ta alloys show an increase in minimum temperature (T_{min}). It should be noted that T_{min} increases with increasing Ta and that the T_{min} of 614.9 $^\text{o}$C is very close to the nucleation temperature (T_N) of α-Al in Al-7Si-0.3Mg alloy. Growth temperature (T_G) increases in 0.01Ti compared to Ref alloy, however, T_G was not detected in Ta-refined alloys in the thermal analysis curve. Limited undercooling of 0.1 $^\text{o}$C was detected in 0.01Ti alloy. Overall, high T_{min} and low ΔT are indirect indicators of well-refined α-Al grains. However, thermal analysis results indicate an easy nucleation of α-Al grain at high temperatures with a very limited undercooling, therefore fine grain sizes are expected within the microstructure. T_N is very challenging to detect using thermal analysis due to the impurity effect and therefore is not involved in the measurement.

Solidification of eutectic is referred in Table 4.2 with subscript "$_{eu}$". The equilibrium eutectic

Table 4.1: Measured chemical composition of CP Al-7Si-0.3Mg based alloys with the addition of grain refiner (Ti or Ta) and modifier (Sr). Note that the composition is listed in wt. % [232].

Alloy	Si	Mg	Sr	Ti	B	Fe	Ta	Eu	P	Al
Ref	7.1	0.39	-	-	0.0010	0.06	-	-	0.0028	Bal.
0.01Ti	7.2	0.36	0.0225	0.0136	0.0033	0.06	-	-	0.0028	Bal.
0.07Ta	7.6	0.35	0.0192	0.0144	0.0031	0.10	0.07	-	0.0027	Bal.
0.12Ta	7.4	0.38	0.0194	0.0218	0.0042	0.11	0.12	-	0.0024	Bal.

Table 4.2: Thermal analysis of alloys grain refined by Al-5Ti-1B or Al-10Ta in combination with Al-2.2Ti-1B grain refiner. Measured temperatures are in ºC [232].

Alloys	T_N	T_{min}	T_G	ΔT	$T_{N,\text{eu}}$	$T_{min,\text{eu}}$	$T_{G,\text{eu}}$	$T_{\text{eq}} - T_{N,\text{eu}}$	ΔT_{eu}
Ref	-	610.3	612.3	2.0	576.2	573.3	573.8	0.8	0.5
0.01Ti	-	613.4	613.5	0.1	566.5	563.9	570.0	10.5	6.1
0.07Ta	-	613.5	-	-	568.6	562.5	565.8	8.4	3.3
0.12Ta	-	614.9	-	-	565.5	561.5	565.0	11.5	3.5

temperature (T_{eq}) is 577 ºC as shown in Al-Si diagram (Fig. 2.21). $T_{N,\text{eu}}$ is the largest in Ref alloy (576.2 ºC), which is very close to T_{eq}. Nucleation undercooling ($T_{\text{eq}} - T_{N,\text{eu}}$) is the highest in 0.12Ta alloy and 0.01Ti alloy, respectively. These alloys are undercooled more than 10 ºC before the nucleation of eutectic Si. $T_{N,\text{eu}}$, $T_{min,\text{eu}}$ and $T_{G,\text{eu}}$ are depressed to lower temperatures in the presence of Sr. The highest ΔT_{eu} of 6.1 ºC is measured in 0.01Ti alloy. In 0.07Ta and 0.12Ta the ΔT_{eu} are ∼3.4 ºC, which is not as high as in the 0.01Ti, but significantly larger than in Ref alloy. A small undercooling is attributed to an easy nucleation due to the presence of the AlP phase in Al-Si alloys. Sr reduces the amount of AlP via the formation of the Sr_3P_2 phase. Therefore the amount of nucleation sites is reduced and undercooling is higher. However, microstructure investigations are required to verify thermal analysis results.

4.2   Optical microscopy

Fig. 4.1 shows the solidification microstructure with denoted α-Al grain size of investigated alloys. The grain size of Ref alloy is close to 1 mm. Significant refinement is observed with the addition of a grain refiner. In 0.01Ti and 0.07Ta alloys, the grain size is comparable (∼220 µm). With the addition of 0.12 wt. % Ta, the grain size is lower than ∼150 µm. It was reported that efficient refinement is achieved below 200 µm [3, 7, 76].

It should be noted that although the concentration of solutes can vary, the amount of grain refiner and therefore the amount of TiB_2 particles remained unchanged in 0.01Ti, 0.07Ta and 0.12Ta alloys. Table 4.1 shows nearly identical 0.014 wt. % Ti concentration in 0.01Ti
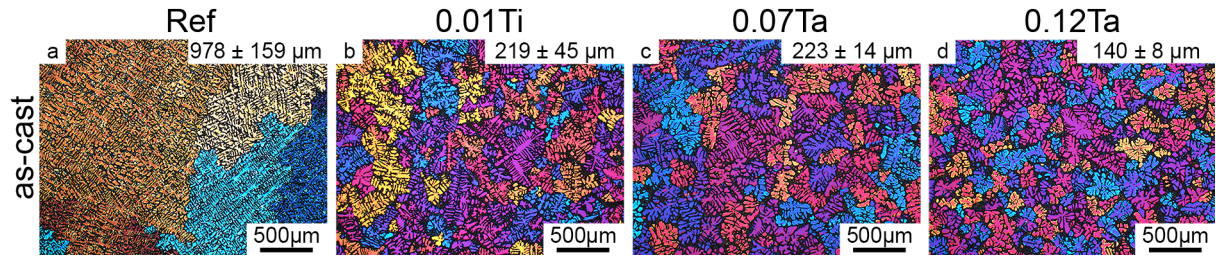
Figure 4.1: As-cast microstructure after Barker's etching (a) Ref, (b) 0.01Ti, (c) 0.07Ta and (d) 0.12Ta [232].
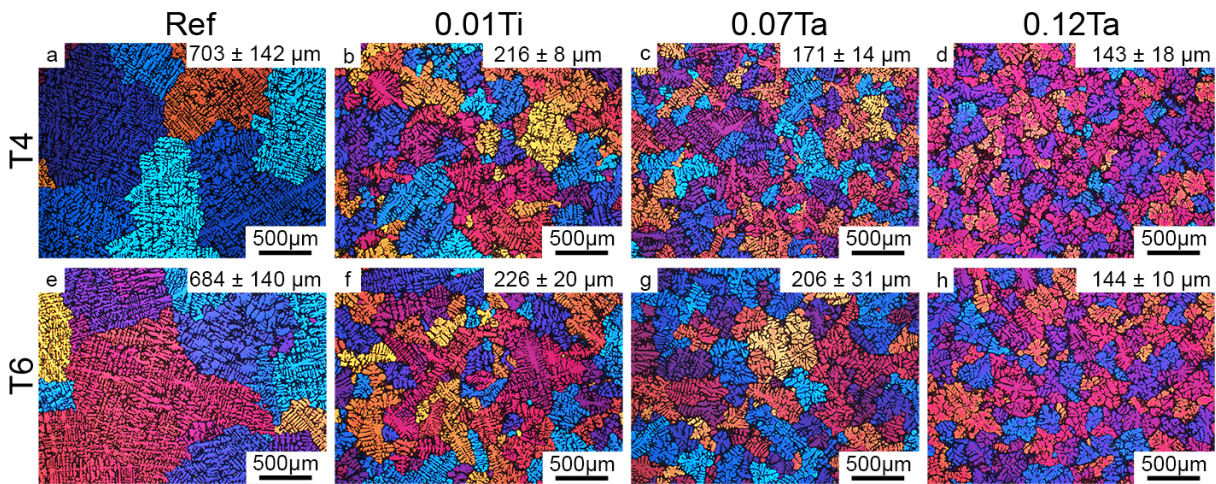

Figure 4.2: Microstructure after (a-d) T4 and (e-h) T6 of alloys; (a,e) Ref, (b-f) 0.01Ti, (c-g) 0.07Ta and (d-h) 0.12Ta [232].

and 0.07Ta alloys, however in 0.07Ta all Ti is bounded to TiB_2, while 0.01Ti contains free Ti from Al-5Ti-1B grain refiner. This indicates, there is a smaller amount of TiB_2 particles in 0.07Ta and 0.12Ta alloys with the addition of Al-2.2Ti-1B grain refiner. Nevertheless, 0.01Ti and 0.07Ta alloys show a comparable grain size (~220 µm), indicating the same efficiency of Al-5Ti-1B grain refiner as Al-2.2Ti-1B in combination with 0.07 wt. % Ta. The grain size can be further refined with increasing solute Ta up to 0.12 wt. %.

Microstructure after T4 and T6 is shown in Fig. 4.2. It is generally accepted that no α-Al grain growth occurs at temperatures below eutectic equilibrium temperature, which is usually applied for T4 treatment. Therefore, the trend of decreasing α-Al grain size with grain refiner is maintained after heat treatment. Slight differences in grain size measurement are believed to be caused due to measurement errors.

The eutectic grain size of the as-cast microstructure after MMR etching is shown in Fig. 4.3. The graph shows that eutectic grain size is very low (~500 µm) in Ref alloy without modification, which indicates enough AlP is present to nucleate eutectic grains. After the addition of Sr (0.01Ti, 0.07Ta, 0.12Ta alloys), the interaction of AlP and Sr reduces the
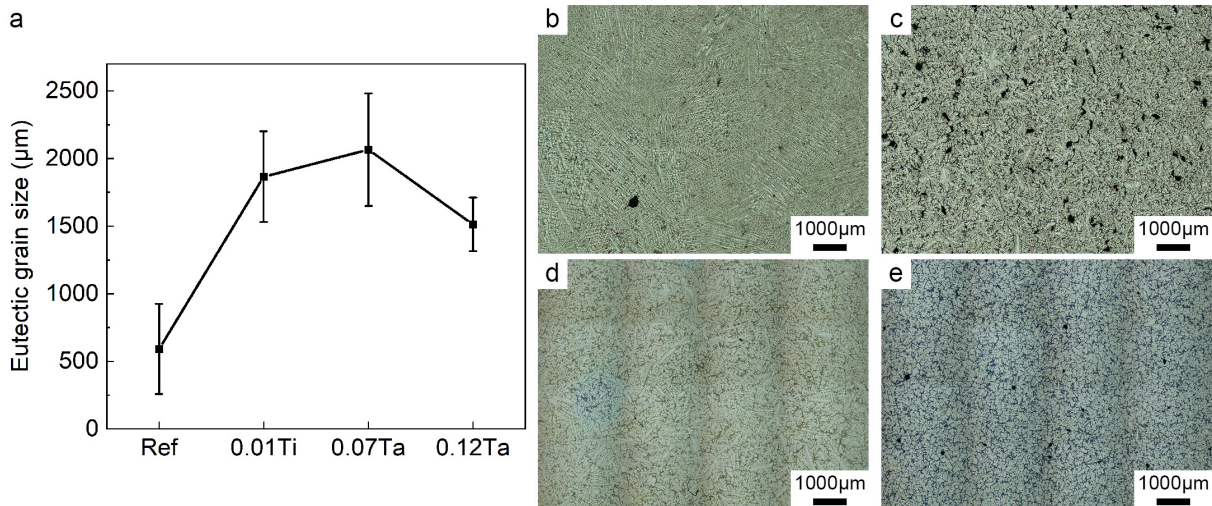
Figure 4.3: (a) As-cast eutectic grain size measured after MMR etching of alloys; (b) Ref, (c) 0.01Ti, (d) 0.07Ta and (e) 0.12Ta [232].

number of nucleation sites and the eutectic grain size increases significantly. Among Sr-modified alloys, 0.12Ta shows the smallest eutectic grain size (∼1500 µm), which indicates that the high Ta addition can refine eutectic grains. Note that the detection of eutectic grain boundaries is very challenging due to low Mg (0.3 wt. %) and therefore low Fe-phase (π-AlFeMgSi) along the grain boundaries.

The shape factor (SF) of eutectic Si is demonstrated in Fig. 4.4a and the corresponding eutectic Si particles in as-cast and after T4 and T6 are shown in Fig. 4.4b-e and Fig. 4.4f-i, respectively. SF values of eutectic Si in as-cast and T6 condition are listed in Table 4.3. Eutectic Si grows in the form of a large plate-like structure in Ref alloy and its shape factor is low (0.41±0.22). After the addition of Sr, the largest SF in 0.12Ta alloy was observed (0.75±0.19). Eutectic Si particles in Sr-modified alloys are finer compared to Ref alloy. Microstructure after heat treatment shows significantly coarser eutectic Si particles due to spheroidization. Compared to as-cast eutectic Si, the interparticle spacing increases with heat treatment. Ref alloy shows a coarser plate-like structure, however, the edges of Si particles are significantly less sharp after T6. This is due to spheroidization during heat treatment which is also the reason for increasing interparticle spacing. SF increased in all investigated alloys after heat treatment. A change of SF from 0.41 in the as-cast condition to 0.69 in the T6 condition is detected in the Ref alloy. Importantly, SF of 0.01Ti and 0.07Ta slightly increases, however, the increase is close to the standard deviation (∼0.05-0.09). 0.12Ta alloy shows only a slight increase in SF after heat treatment. Note that the standard deviation decreased by ∼38 % after T6, therefore the microstructure is much more uniform after T6. This result is attributed to the long T4 treatment (15 h) and the high T4 temperature (540 ºC).
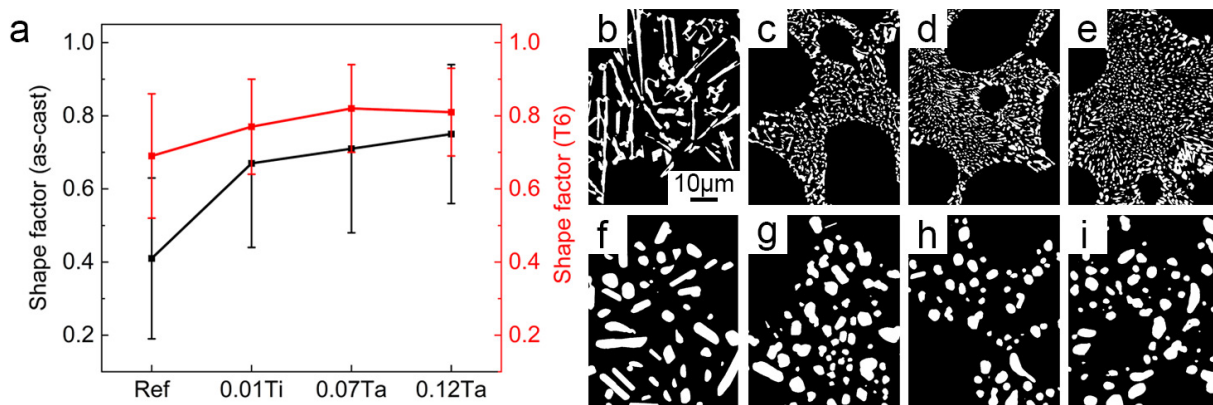
Figure 4.4: (a) Shape factor of eutectic Si in as-cast (black) and T6 (red) condition. Morphology of eutectic Si in as-cast (b-e) and T6 (f-i) in alloys; (b,f) Ref, (c,g) 0.01Ti, (d,h) 0.07Ta and (e,i) 0.12Ta [232].

Table 4.3: Shape factor of eutectic Si in as-cast and T6 condition [232].

Alloy	As-cast [-]	T6 [-]
Ref	0.41±0.22	0.69±0.17
0.01Ti	0.67±0.23	0.77±0.13
0.07Ta	0.71±0.23	0.82±0.12
0.12Ta	0.75±0.19	0.81±0.12

4.3 SEM

The effect of heat treatment is also investigated using SEM (Fig. 4.5). SEM backscattered electron (BS) image is used to clearly distinguish Fe-rich intermetallic particles (bright) in as-cast (Fig. 4.5a-d) and T6 (Fig. 4.5e-h) microstructure. Fe-rich particles are found decorating grain boundaries and are identified as Al-Si-Fe phase by EDS, as shown in Fig. A.2. The distribution of Fe-phases is relatively uniform after heat treatment, they appear also to be fragmented and finely dispersed. Ref alloy exhibits sharp plate-like eutectic Si, while Sr-modified alloys show very fine eutectic structure. The shape of Si particles is spheroidized, as shown in Fig. 4.4.

The Sr_3P_2 is detected along the grain boundaries using EDS maps in as-cast 0.12Ta alloy (Fig. 4.6). At the centre, there is a pore and the Sr and P signal indicates that this phase could be the Sr_3P_2 phase. Although the Sr_3P_2 was reported not to nucleate eutectic Si [25], the Al_2Si_2Sr phase around the Sr_3P_2 indicates possible nucleation of Al_2Si_2Sr on Sr_3P_2. Mg and O signals are observed overlapping with P. However, this is attributed to oxidation during sample preparation, as reported in [154].

Fig. 4.7 and Fig. 4.8 show TiB_2 particles together with the Ta-rich phase at the interface. The thick Ta layer is presumably identified as Al_3Ta and is mainly observed on the basal
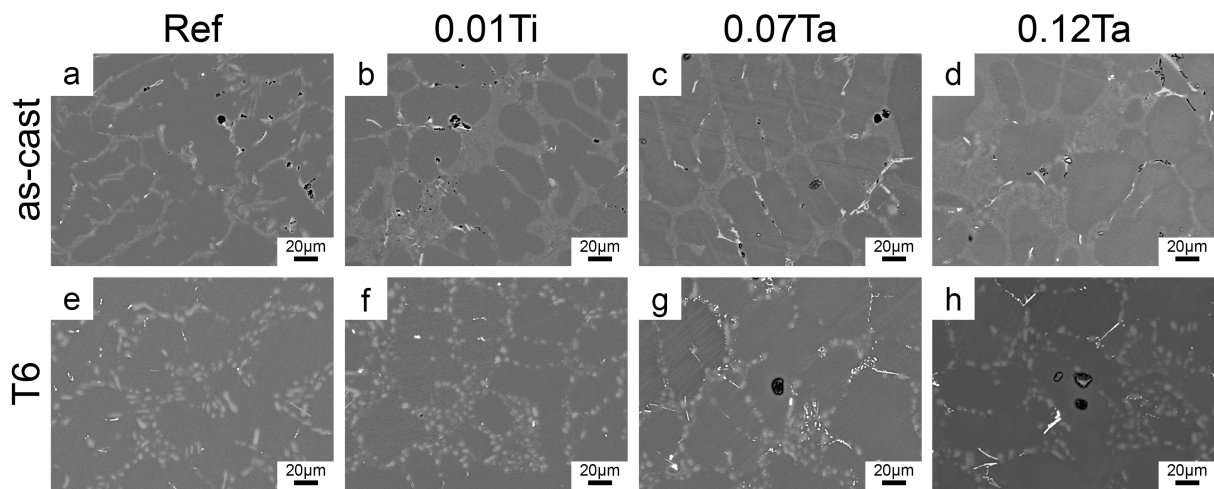
Figure 4.5: SEM BS image of alloys; (a,e) Ref, (b,f) 0.01Ti, (c,g) 0.07Ta and (d,h) 0.12Ta in as-cast (a-d) and T6 (e-h) condition [232].
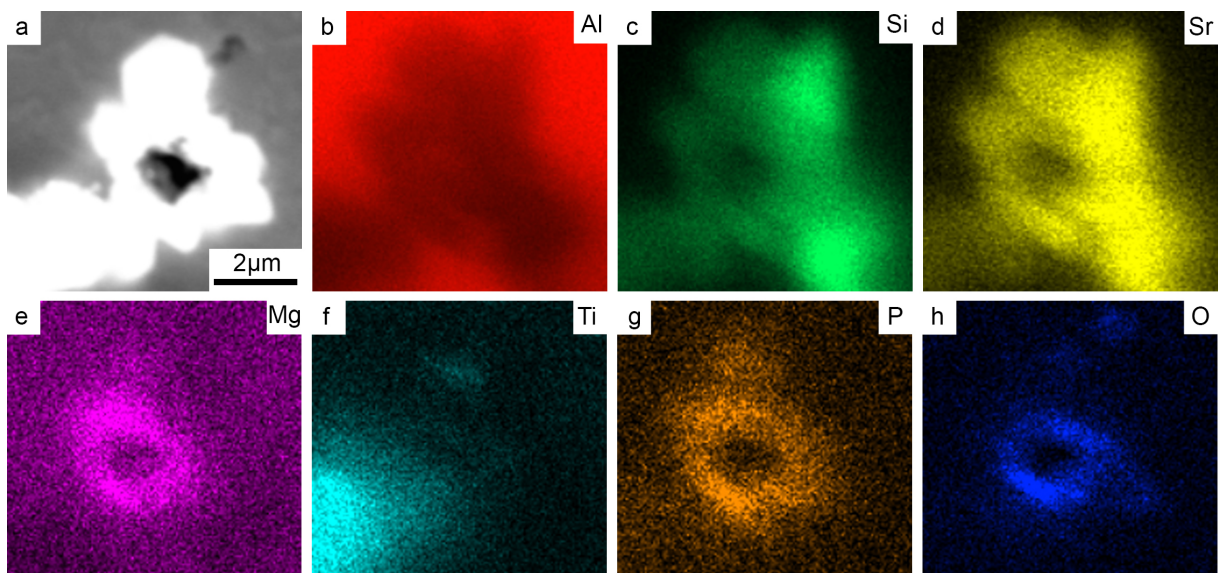

Figure 4.6: (a) SEM BS image of Al_2Si_2Sr and Sr_3P_2 intermetallic phases in the vicinity of porosity in 0.12Ta alloy. (b-h) EDS maps for (b) Al,(c) Si, (d) Sr, (e) Mg, (f) Ti, (g) P, (h) O [232].
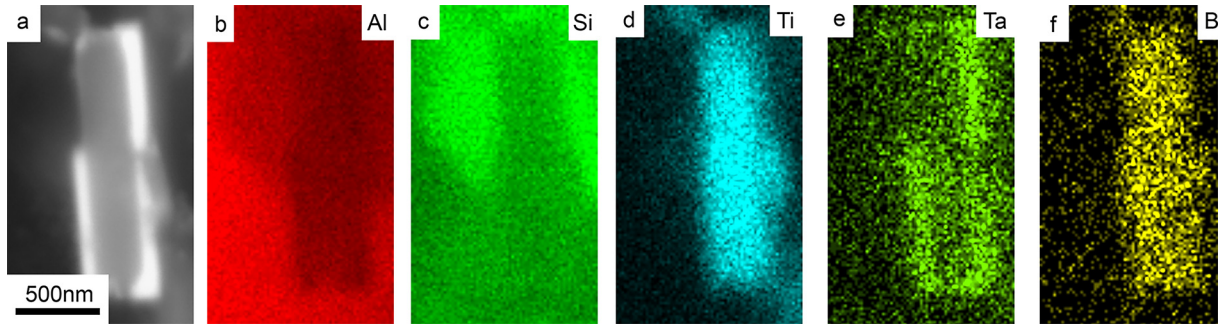
Figure 4.7: (a) SEM BS image of TiB_2 particle covered by Ta-rich layer in 0.12 alloy. (b-f) EDS maps for (b) Al, (c) Si, (d) Ti, (e) Ta and (f) B [229].

plane of TiB_2 particle. Note that within the resolution of the SEM image, there is no Ti overlap at the interface of TiB_2. Since the alloy does not contain solute Ti due to the addition of solute Ta in combination with stoichiometric Al-2.2Ti-1B grain refiner, the Ti signal is only from the TiB_2 particle. Further, no Si and Ti overlap is observed on the basal plane of the TiB_2 particle.

On the other hand, Fig. 4.8 shows TiB_2 particle with the overlap of Si and Ta at the interface. The TiB_2 is fully covered (basal and prism plane) by a thick Ta-Si layer which indicates Si-poisoning. Note that the measured grain size in Fig. 4.1 shows no increase in grain size in 0.12Ta alloy, but the grain size even decreased with increasing solute Ta up to 0.12 wt. %. Hence, the partition of Si at the Ta-rich layer appears to have no negative result on grain size, which is not the case for alloy grain refiner with Ti causing the formation of the AlSiTi phase. EDS point analysis Fig. 4.8i shows a larger Ti concentration (11.05 at. %) at the interface than that of Ta (4.64 at. %). It should be noted that the particles are investigated in solidification microstructure, therefore none of the detected particles can be clearly stated to be potent nucleation site for α-Al.

4.4   EBSD of 0.12Ta alloy

To further confirm the grain size measurement from OM (Fig. 4.1) the grain size measurement of 0.12Ta alloy using EBSD is also implemented. EBSD with Inverse Pole Figure (IPF) and frequency of grain diameter are shown in Fig. 4.9. EBSD shows a lot of small grains at the grain boundaries, which are defined as eutectic Si particles, rather than Al. Note here that a separate index of Si and Al is not established due to the fact that the signal of Si and Al is very close. To overcome this issue, grains smaller than 20 µm were excluded from grain size measurement.

The grain size of 76±44 µm measured by EBSD (Fig. 4.9) is lower than measured after Barkers etching using OM (Fig. 4.1) in 0.12Ta alloy. Such a discrepancy can occur due to
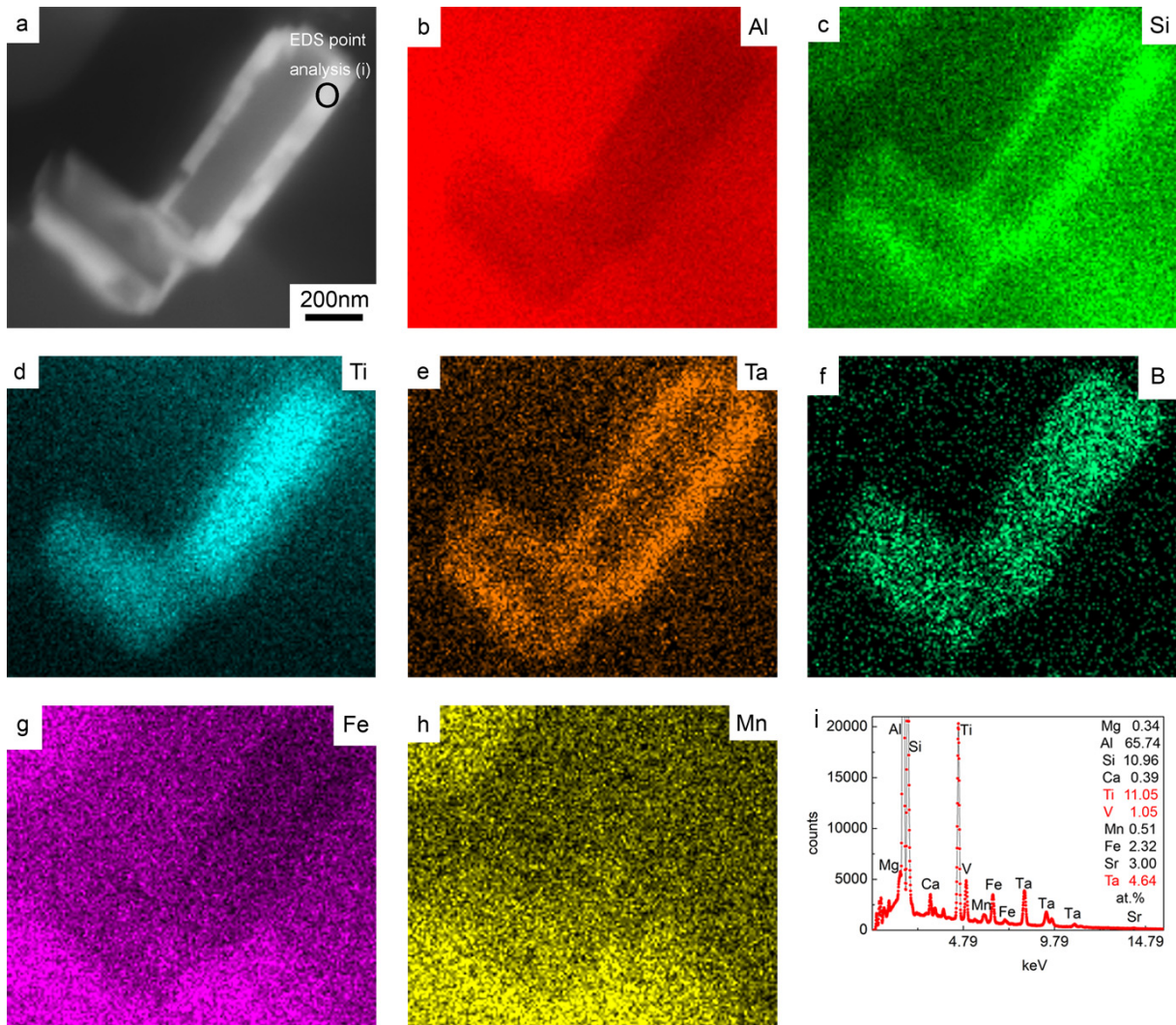
Figure 4.8: (a) SEM BS image of TiB$_2$ particle covered by Al$_3$Ta-rich layer in 0.12Ta alloy. (b-h) EDS maps for (b) Al, (c) Si, (d) Ti, (e) Ta, (f) B, (g) Fe, (h) Mn, and (i) EDS point analysis [232].

involving grains only larger than 20 µm, which occurs at a high frequency for grains below 80 µm.

4.5 TEM-The interface between TiB$_2$ particle and aluminides

To investigate the structure and composition at the interface of TiB$_2$, a TiB$_2$ particle is lift-out using FIB (section 3.4.5). The TiB$_2$ particle is studied using HAADF-STEM in low magnification (Fig. 4.10) and high magnification (Fig. 4.11). EDS maps and EDS line scans were also done. At either basal or prism plane, the Ta-rich layer was observed at the interface of the TiB$_2$ particle. The Ta-rich layer is also observed in the vicinity of the V-rich layer (Fig. A.3) which is consistent with the Ti-rich layer on the basal plane of TiB$_2$ particle. A
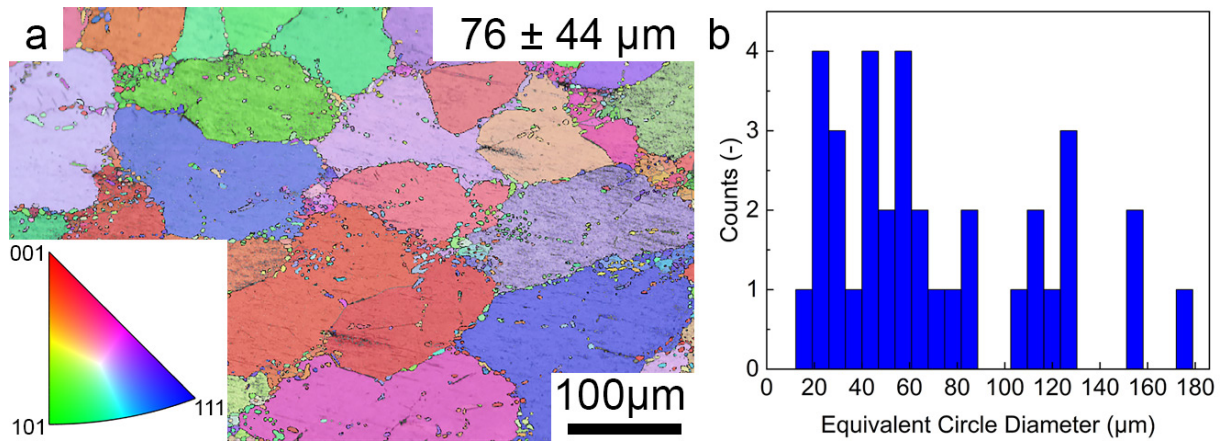
Figure 4.9: (a) EBSD IPF image of as-cast 0.12Ta alloy, (b) grain diameter frequency within the microstructure [232].

significant V detected at the TiB_2 interface (Fig. 4.10e, h and Fig. 4.11e, h) is attributed to the impurity from the preparation of CP Al-2.2Ti-1B grain refiner. V is also present in CP Al alloys. Another Ta-rich layer is observed in the vicinity of the V-rich layer. Ti observed at the interface of TiB_2 particle can be due to overlap with TiB_2 during EDS measurement (Fig. 4.11d, h). The Ta-rich layer on the basal plane is identified as $(Ta, Ti)B_2$ using EDS line scan (Fig. 4.11h) and Fast Fourier Transforms (FFTs) of the structure (Fig. 4.12).

4.6 DSC of as-cast alloys

DSC cooling curves of Ta-refined and Sr-modified alloys are shown in Fig. 4.13. In total four exothermic peaks (1, 2, 3a, 3b) are denoted and correspond to α-Al, eutectic Si, Ti-rich intermetallic phase and Al_2Si_2Sr phase, respectively. The onset and peak temperatures are listed in Table 4.4. Peak 1 shows a lower onset temperature in Ref alloy compared to other alloys (Fig. 4.13a). This result is in good agreement with thermal analysis result (Table 4.2), where a lack of nucleation sites (TiB_2) caused the decrease of T_N and increase of ΔT.

In terms of peak 2, the highest peak temperature of Ref alloy indicates an earlier nucleation of eutectic Si, compared to Sr-modified alloys. Note that the nucleation of eutectic Si is easier with high P additions, however, all investigated alloys in this section contain the same amount of P ($\sim$30 ppm), as shown in Table 4.1. Ref alloy contains no Sr, hence more AlP can play a role as a nucleation site. On the other hand, the interaction of Sr and P in Sr-modified alloys causes the removal of AlP and subsequent formation of the Sr_3P_2 phase. Therefore, less AlP for the nucleation of eutectic Si requires higher undercooling below equilibrium temperature and the nucleation temperature is then shifted to lower temperatures. The onset temperature of peak 2 is excluded from the measurement due to the peak overlap. The peak does not decline to the baseline and cannot clearly state, where the peak is initiated.
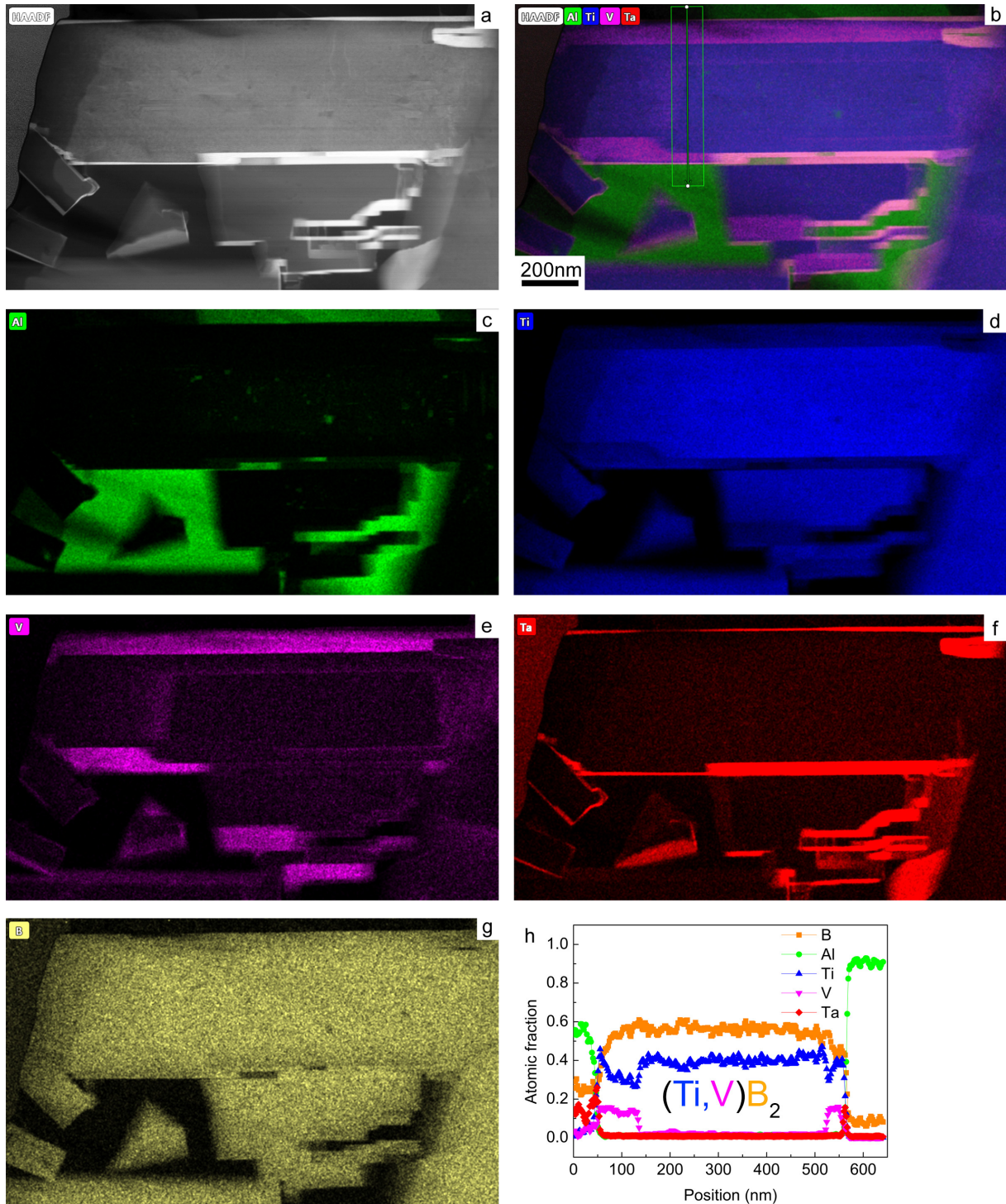
Figure 4.10: (a) Low magnification HAADF-STEM image, (b) mixed EDS maps, (c) Al map, (d) Ti map, (e) V map, (f) Ta map and (g) B map of TiB_2 particle covered by Ta-rich layer in 0.12Ta alloy. (h) EDS line scan across the region as denoted in (b) [232].

Figure 4.11: (a) High magnification HAADF-STEM image, (b) mixed EDS maps, (c) Al map, (d) Ti map, (e) V map, (f) Ta map and (g) B map of TiB_2 particle covered by Ta-rich layer in 0.12Ta alloy. (h) EDS line scan across the region as denoted in (b) [232].
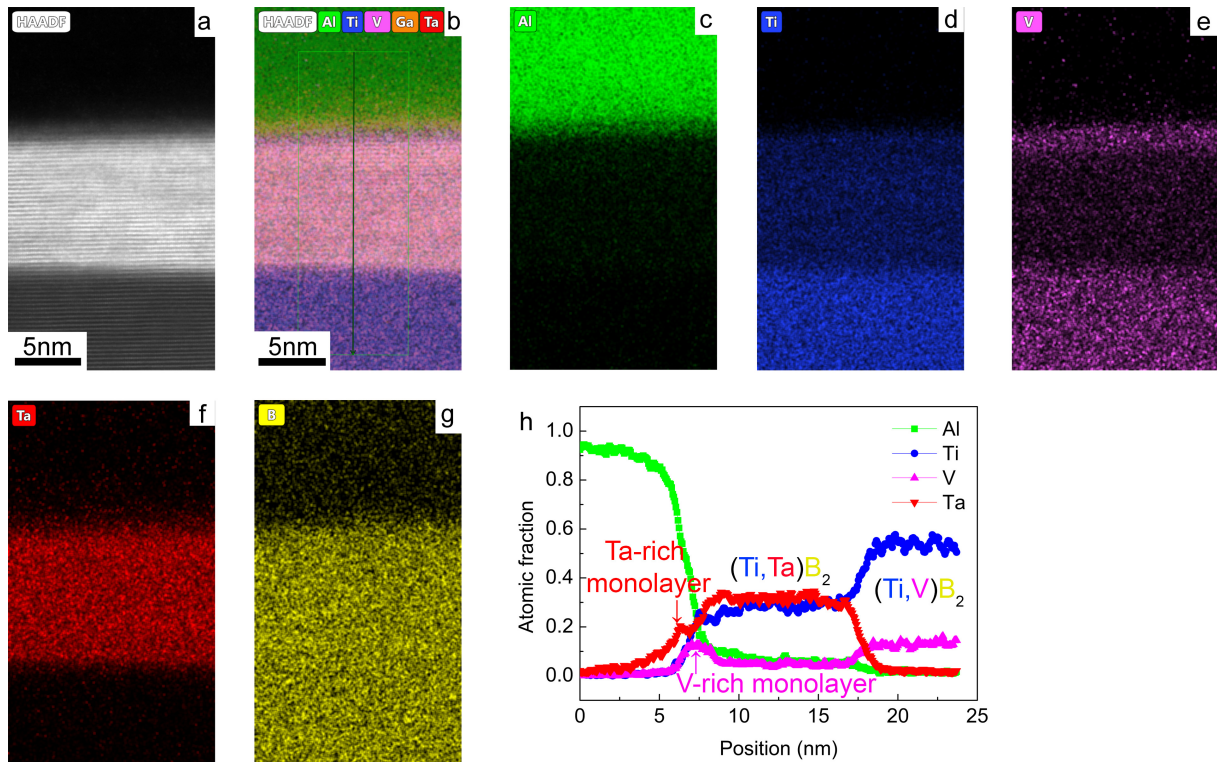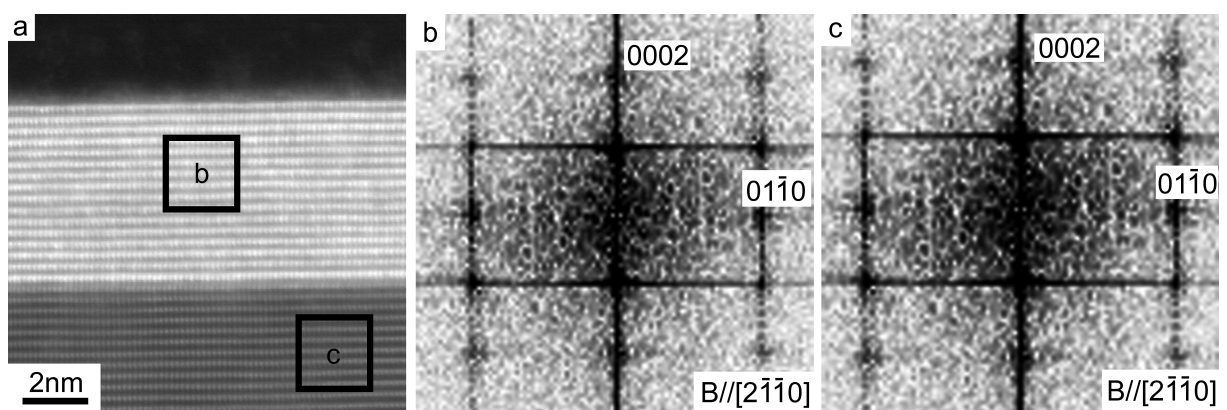

Figure 4.12: (a) High resolution HAADF-STEM image of the interface, (b) FFT from the region $((Ti,Ta)B_2)$, as marked in (a) and (c) FFT from the region (TiB_2), as marked in (a) [232].
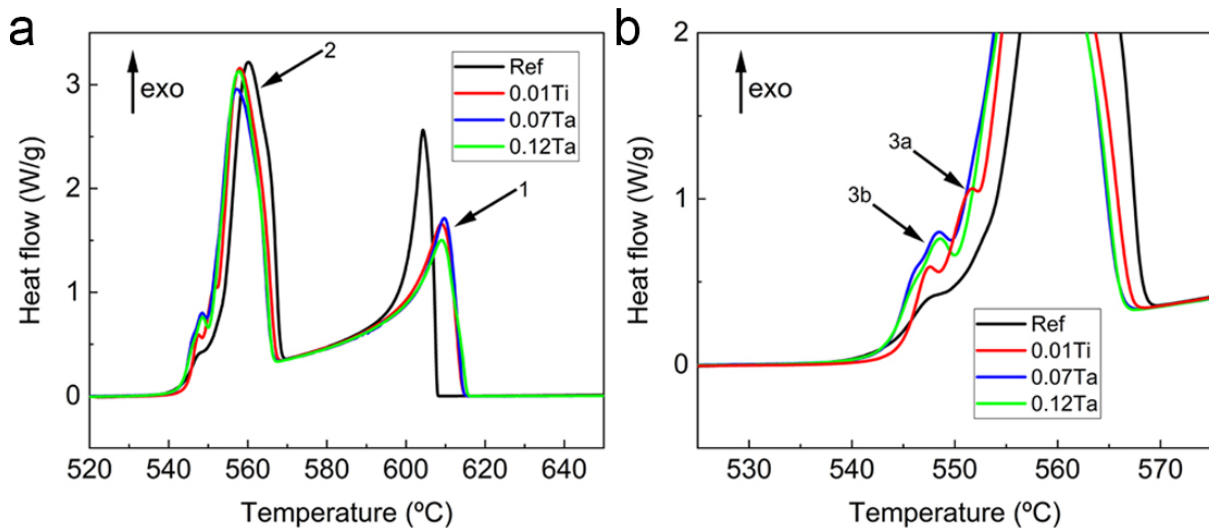
Figure 4.13: DSC thermographs of as-cast alloys including denoted α-Al (peak 1) and eutectic Si (peak 2), (b) enlarged eutectic region (peak 2) showing the Ti-rich intermetallic phase (peak 3a) and the Al_2Si_2Sr phase (peak 3b) [232].

The peak temperature of peak 2 is therefore used to compare the nucleation condition of investigated alloys, where a higher peak temperature indicates an easier nucleation.

In the region after the solidification of eutectic Si, two peaks (3a and 3b) are detected. The peak 3a is observed only in 0.01Ti alloy (Fig. 4.13b) and is attributed to the formation of the Ti-rich intermetallic phase. The formation of the Al_2Si_2Sr phase corresponds to peak 3b in Sr-modified alloys. SEM (Fig. 4.6) is in good agreement with DSC data reported here and elsewhere [176]. Peaks 3a and 3b are not detected in Ref alloy due to a lack of Ti and Sr to form intermetallic phases.

4.7 Hardness curve

Investigated alloys are exposed to 180 $^{\circ}$C up to 30 h. Hardness curve is plotted in Fig. 4.14. The initial drop of hardness after 0.5 h is believed to be caused due to dissolution of GP-zones, which are fully coherent with Al matrix [188]. GP-zones are dissolved due to a limited stability at elevated temperatures and therefore a decrease in hardness is observed (Fig. 4.14b). With increasing ageing time, the increase of hardness is observed due to the growth of coherent β'' precipitate [203–205]. The peak hardness of 0.07Ta alloy was observed after 3 h (122 HV). Slightly lower peak hardness of Ref (121 HV) and 0.01Ti (120 HV) was observed after ageing for 3 h. Interestingly, Ref alloy shows overall higher hardness than 0.01Ti alloy, which is Ti-refined and Sr-modified. In Ref, 0.01Ti and 0.07Ta alloys, the hardness decreases with increasing ageing time. Surprisingly, 0.12Ta alloy shows a peak hardness of 124 HV after ageing for 4 h (Fig. 4.14c). The differences in the hardness

Table 4.4: Onset and peak temperatures of as-cast Ta-refined and Sr-modified alloys extracted from the DSC cooling curve [232].

	Alloy	Onset temperature [^{o}C]	Peak temperature [^{o}C]
Peak 1	Ref	607.87	604.36
	0.01Ti	614.15	608.91
	0.07Ta	614.35	609.69
	0.12Ta	615.41	609.01
Peak 2	Ref	-	560.2
	0.01Ti	-	557.99
	0.07Ta	-	557.23
	0.12Ta	-	557.73
Peak 3a	Ref	-	-
	0.01Ti	-	551.75
	0.07Ta	-	-
	0.12Ta	-	-
Peak 3b	Ref	-	-
	0.01Ti	-	547.55
	0.07Ta	-	548.46
	0.12Ta	-	548.57
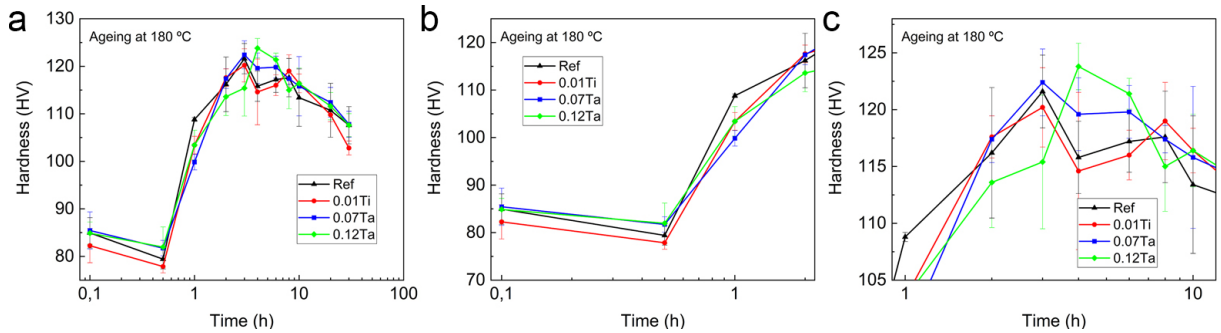
Figure 4.14: Hardness evolution of investigated alloys after ageing at 180 ^{o}C up to 30 h: (a) overview, (b) early stage and (c) peak hardness [232].

of investigated alloys are insignificant. However, the time to achieve the peak hardness is shifted up to 4 h with increasing solute Ta. This result indicates that the solutes can influence the precipitation kinetics of β'' precipitate. The maximum peak hardness is overall attributed to the size and number density of β'' precipitate. After 4 h of ageing at 180 ^{o}C, the hardness further decreases with increasing the ageing time.

4.8 Evolution of β'' -type precipitates

The formation of β-type precipitates is crucial for strengthening effect. The strengthening of Al-Si-Mg alloys is given by the number and size distribution of precipitates. The grain
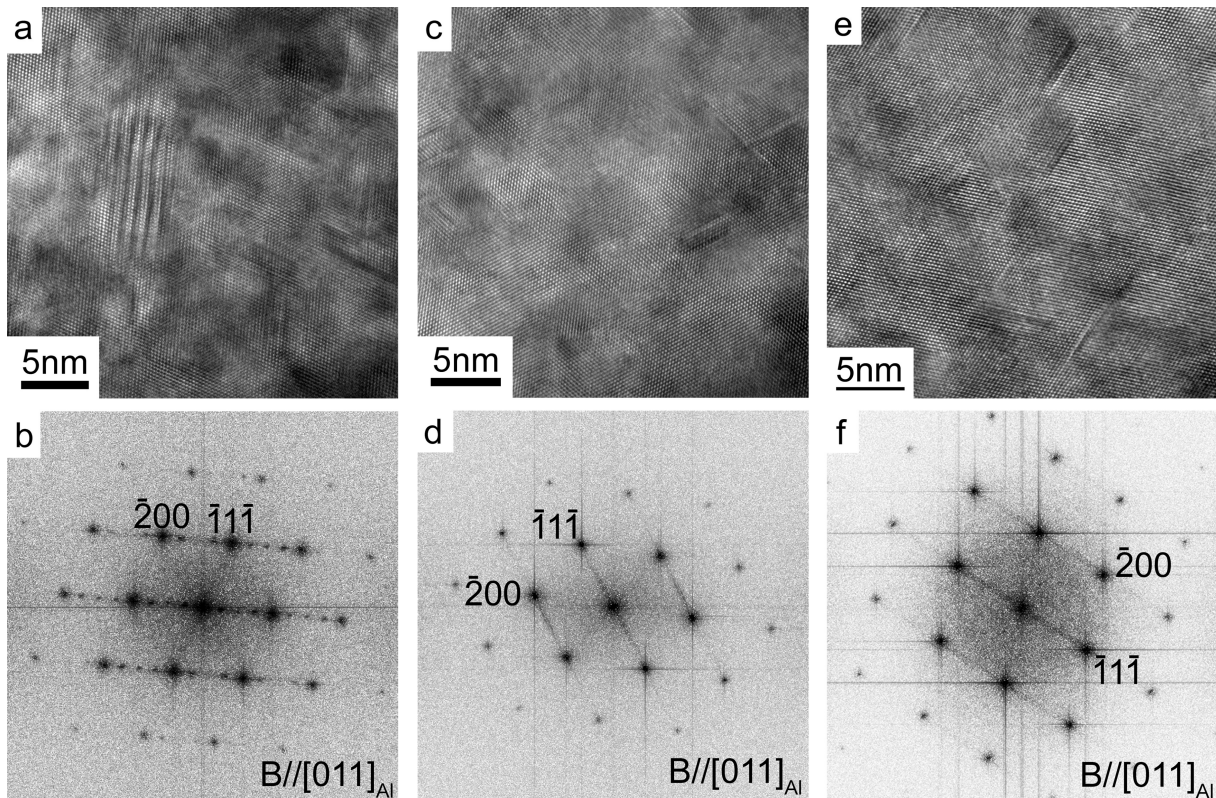
Figure 4.15: (a, c, e) High resolution TEM images and (b, d, f) FFTs of β-series precipitates in 0.12Ta alloy after ageing at 180 °C for (a, b) 0 h (T4), (c, d) 2 h and (e, f) 4 h. B//[011]Al [232].

size and eutectic Si morphology can improve as-cast microstructure, however, the main strengthening effect is developed by heat treatment. The presence of β'' precipitate was investigated with ageing at 180 $^{\text{o}}$C after 0 h, 2 h, 4 h (Fig. 4.15). The presence of main strengthening β'' precipitate was observed in all investigated alloys, however only 0.12Ta is shown here due to their similarity. The rod shape β'' is coherent with the Al matrix viewed from the [011] zone axis with a size of about 5 nm in length and 1 nm in width. The rod shape is clearly seen from the [001] zone axis (Fig. 4.16). With increasing ageing time up to 4 h, the number density of precipitates increases, but a quantitative analysis is still required.

4.9 DSC after solution treatment

Solution treated samples are exposed to a non-isothermal heating rate using DSC. DSC thermographs of alloys investigated using heating rates of 20 $^{\text{o}}$C/min and 10 $^{\text{o}}$C/min are shown in Fig. 4.17a and b. β'', β' and β precipitates are denoted in the thermographs. The peak temperatures of β-type precipitates are listed in Table 4.5. The formation or dissolution of GP-zones was not detected, therefore it is assumed that β'' precipitate was initially formed before the DSC investigation. That assumption is consistent with TEM investigation at 0 h
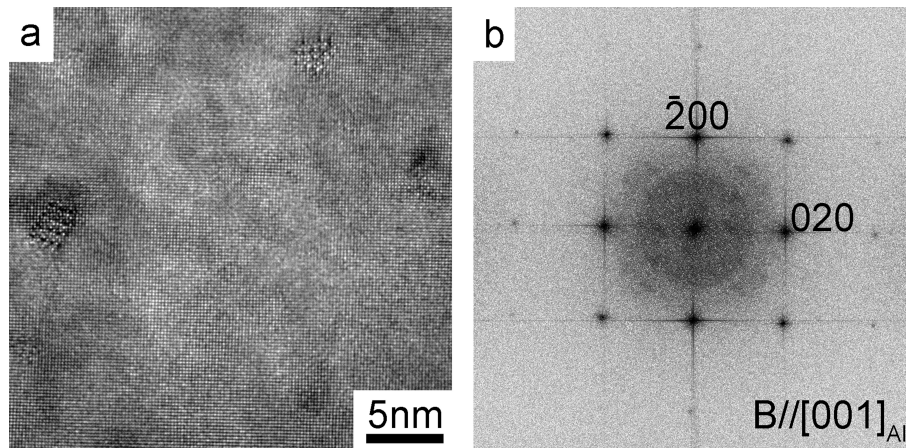
Figure 4.16: (a) High resolution TEM and (b) FFT of β-series precipitates in 0.12Ta alloy aged at 180 °C for 2 h. B//[001]Al [232].

(Fig 4.15), where the β'' precipitates are observed prior ageing.

The maximum peak temperatures to calculate activation energies according to Kissinger method (equation 3.4) are listed in Table 4.5. The detection of the β is very challenging for 1 ℃/min and 20 ℃/min heating rates (Fig. 4.17a). The temperature range of DSC thermograph with a heating rate 10 ℃/min was extended up to 450 ℃ in order to detect the β peak (Fig. 4.17b), therefore only heating rates of 2 ℃/min, 5 ℃/min and 10 ℃/min detected the β peak, as shown in Table 4.5. Plots where the slope equals activation energy are shown in Fig. 4.17c-f.

In terms of β'' precipitate, the maximum peak temperatures are detected in 0.07Ta and 0.12Ta alloys. This may indicate that with increasing Ta addition, the time to achieve the maximum peak temperature is postponed. Conversely, the lowest maximum peak temperature in 0.01Ti for all investigated heating rates indicates an easier precipitation of β'' precipitate. Ref alloy exhibits the lowest maximum peak temperature of β' precipitate. The highest peak temperatures of all β-type precipitates in 0.12Ta alloy (Table 4.5) give a strong experimental support for enhancing the precipitation kinetics.

Table 4.6 shows activation energies of β-type precipitates according to Kissinger method. The values are extracted from Kissinger plots (Fig. 4.17c-f) using Python scripts developed for this purpose. There are no significant changes in activation energies. The range of values of activation energies varies from 116-134, 113-130 and 135-162 kJ/mol for β'', β' and β, respectively. Overall, the lowest activation energy is observed in 0.07Ta alloy, which is lower than that in the Ref alloy. The highest activation energy of β'' and β is calculated for 0.01Ti. On the other hand, the highest activation energy of β' is calculated in 0.12Ta alloy. Solute Ti seems to increase activation energy, while solute Ta (up to 0.07 wt. %) decreases activation energy, which indicates that Ti increases the driving force.

Figure 4.17: (a b) DSC thermographs Ta-refined and Sr-modified alloys. Kissinger plots of alloys :(a) Ref, (b) 0.01Ti, (c) 0.07Ta and (d) 0.12Ta [232].
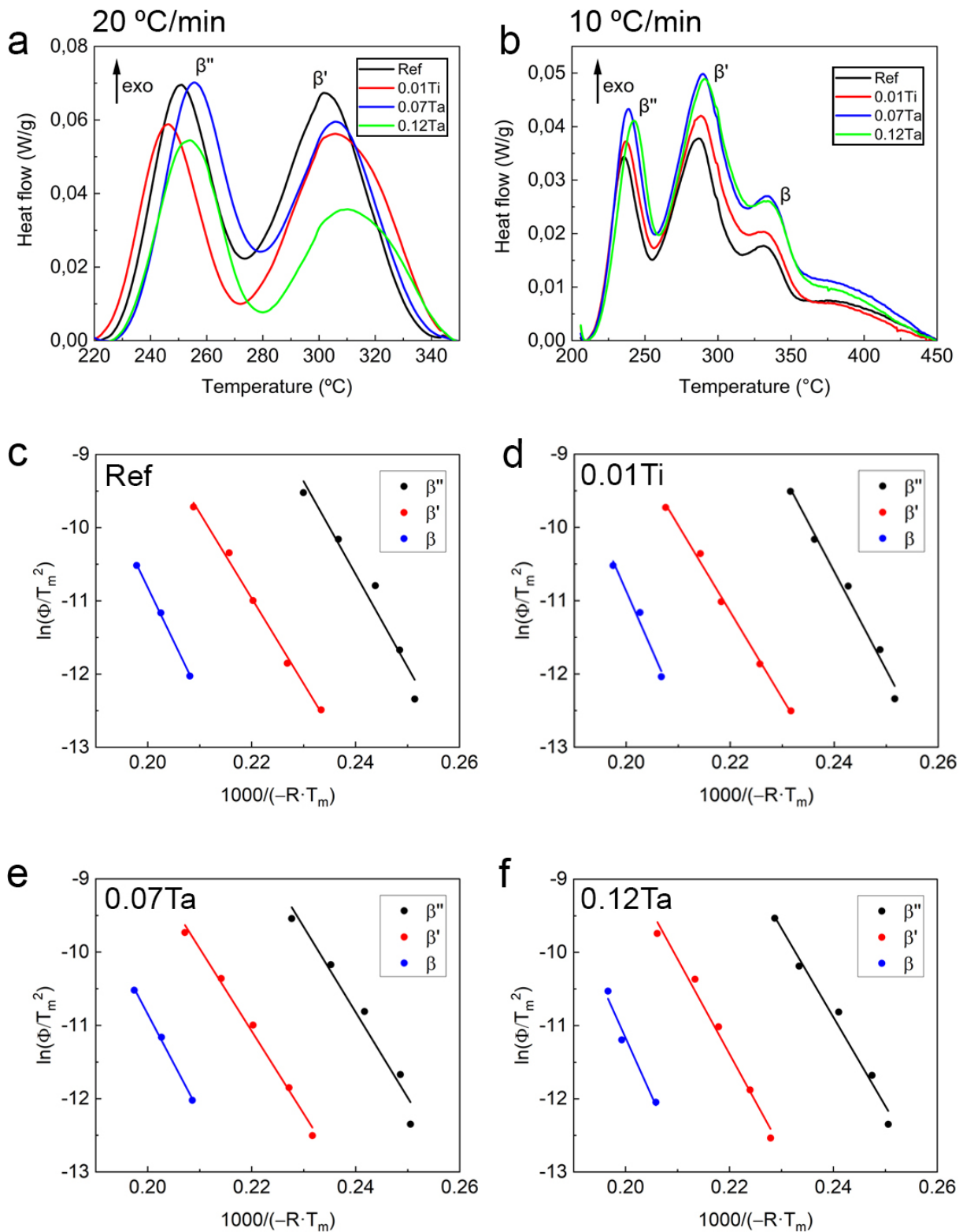
Table 4.5: Peak temperatures of Ta-refined and Sr-modified alloys extracted from the DSC cooling curves after T4 [232].

		Heating rate				
		1 [ºC/min]	2 [ºC/min]	5 [ºC/min]	10 [ºC/min]	20 [ºC/min]
	Alloy	Maximum peak temperature [ºC]				
β''	Ref	205.31	210.86	220.22	235.04	249.86
	0.01Ti	204.82	210.26	222.49	236.04	246.20
	0.07Ta	206.91	210.69	224.49	238.21	255.12
	0.12Ta	206.88	212.96	225.87	242.20	252.76
β'	Ref	242.25	257.05	272.94	284.54	302.88
	0.01Ti	246.04	259.71	277.88	288.20	306.20
	0.07Ta	245.99	256.29	272.88	288.54	307.47
	0.12Ta	254.61	263.91	278.84	290.54	310.40
β	Ref	-	304.80	320.71	334.74	-
	0.01Ti	-	210.26	222.49	335.91	-
	0.07Ta	-	210.36	224.49	336.08	-
	0.12Ta	-	311.21	330.46	338.58	-

Note that the activation energy is only calculated from the peak temperatures. Kissinger method does not involve any thermal history of the sample into measurement. In terms of a driving force, the ascending order of activation energies of precipitates ($\beta'' < \beta' < \beta$) states that higher activation energies are required to obtain β precipitate compared to β'' and β' precipitates (Table 4.6). Ref, 0.01Ti and 0.07Ta show slightly a lower activation energy of β' precipitate compared to β'' precipitate, which is not expectable. However, the precipitation of β'' may require more activation energy to (i) overcome the increased interface energy or (ii) less activation energy is needed for semi-coherent β' to grow once the coherent β'' is formed. For example, during natural ageing at room temperatures, the maximum peak hardness is not achieved due to a lack of precipitation of β''. On the other hand, the elevated temperature during artificial ageing (180-210 ºC [188]) provides a driving force for precipitation due to a higher atom movement and a higher diffusion length. It should be noted that the activation energies of the investigated alloy system cannot be directly compared with literature due to different composition (mainly Si and Mg concentration) and solution treatment [139, 227, 228].

4.10   DFT-interface energy of TiB_2 with aluminides

All configurations from Fig. 3.19 are calculated and plotted with respect to the slab size (Fig. 4.18). TiB_2(Ti) interface energies are lower than TiB_2(B). (Ti) and (B) correspond to Ti- and B-terminated surfaces of the TiB_2 particle, respectively. This result strongly indicates that TiB_2(Ti) is energetically more favourable than TiB_2(B). No significant difference was

Table 4.6: Calculated activation energies according to Kissinger method [232].

	Activation energy		
	β'' [kJ/mol]	β' [kJ/mol]	β [kJ/mol]
Ref	127	117	147
0.01Ti	134	118	162
0.07Ta	116	113	135
0.12Ta	121	130	158
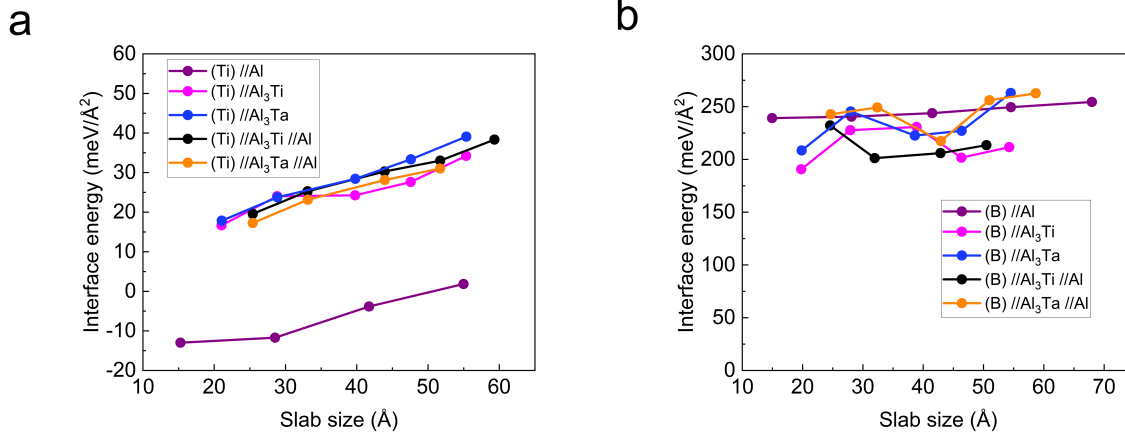
Figure 4.18: (a) Ti and (b) B-terminated TiB$_2$ interface energies with respect to the slab size. Note the different y-axis scaling [229].

obtained for TiB$_2$(Ti)(0001)||Al$_3$Ta(112). The similar result is calculated for sandwich configuration of TiB$_2$(Ti)(0001)||Al$_3$Ta(112)||Al(111) and TiB$_2$(Ti)(0001)||Al$_3$Ti(112)||Al(111). Interestingly, the interface energies of Ta or Ti doped interfaces are close to identical, showing no energetic preference for Al$_3$Ta or Al$_3$Ti. With increasing slab size, no energetic preference for Al$_3$Ta or Al$_3$Ti is obtained. Identical interface energies of Ti-containing and Ta-containing configurations support that Ta exhibits the same behaviour as Ti and therefore Ta can replace Ti. Surprisingly, TiB$_2$(Ti)(0001)||Al(111) configuration exhibits the lowest interface energy of all models. There are two possible explanations: (a) Ti-terminated TiB$_2$ in contact with Al can be seen as a Ti-rich layer and Al-rich layer, therefore the 2DC layer consisting of Al-rich and Ti-rich layer can be formed. The presence of 2DC is believed to be unstable and may dissolve after the nucleation. (b) In terms of thermodynamics, the negative energy represents the driving force to form a new phase. However, more experimental and theoretical support is required to verify both hypotheses.
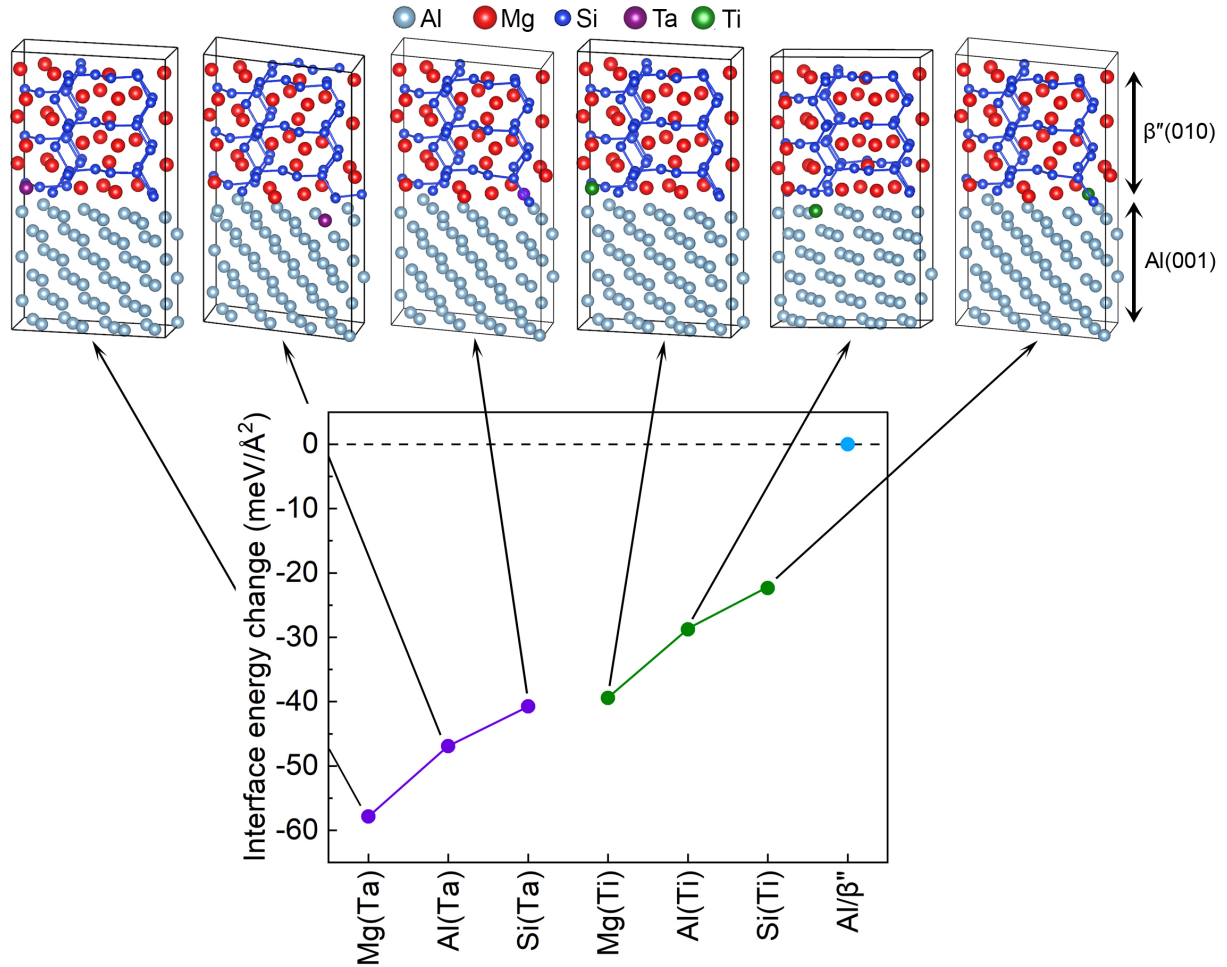
Figure 4.19: Interface energy of Al(001)$||\beta''$(010) interface alloyed by Ta or Ti atom on the Mg, Si or Al site. The lowest interface energy for particular sublattice is shown in SC image in the top of the image [232].

4.11 DFT-interface energy of Al with β''

Based on the configuration from Fig. 3.20, the interface energies of Al(001)$||\beta''$(010) are calculated. The interface is alloyed with a single Ti or Ta atom at all Al, Mg and Si positions. Only the lowest energy configurations are shown in Fig. 4.19. The pure Al in contact with β'' with no alloying element shows the highest interface energy. Ta alloyed interface shows a lower interface energy compared with Ti alloyed interface. These results clearly indicate that Ta is energetically more favourable at the Al$||\beta''$ interface. The lowest interface energies are obtained by the substitution of Mg for both Ta and Ti alloyed interfaces. Ta and Ti prefer to substitute for Mg, Al and Si (in descending order). A very low difference between Si(Ta) and Mg(Ti) further highlights that Ta is a more favourable solute to reduce interface energy rather than Ti.
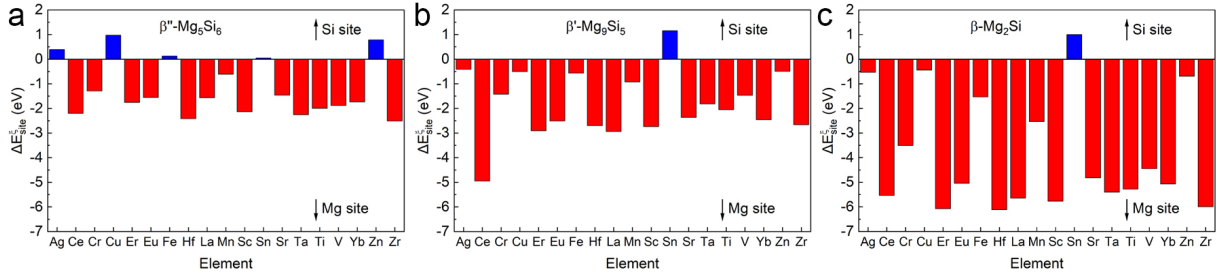
Figure 4.20: Site preference of (a) β'', (b) β' and (c) β precipitates after substitution of Si or Mg atom by an alloying element [232].

4.12 DFT-thermodynamic stability of β-type precipitates

Fig. 4.20 shows site preference energy of β-type precipitates. Even though Ta is the main research focus, other solutes are included in the calculation. Only Ag, Cu, Fe, Sn and Zn prefer the Si sublattice of β'' precipitate, while all the other solutes prefer the Mg sublattice (Fig. 4.20). Overall the site preference energies in the Si sublattice are very low. The investigated solutes present in this work are preferably occupying the Mg sublattice. Apart from Sn, the preference of all solutes is in Mg sublattice of β' and β. Ag, Cu and Zn change the preference from β'' to β' and β, respectively. Energetically, all other solutes prefer to replace Mg rather than Si atoms. Therefore further investigations are focused mainly on stabilising precipitates on the Mg sublattice.

The solubility preference of solute elements in β-type precipitates is shown in Fig. 4.21. Fig. 4.21a shows that solutes such as Cr, Cu, Fe, Mn, Ta, Ti, V and Zn are favourable to stay in SSSS of Al. These results indicate that these solutes may delay the precipitation of β'' phase. More common alloying elements such as Ce, Er, Eu, Hf, La, Sc, Sn, Sr, Yb and Zr are favourable to partition in the β'' (Fig. 4.21a). Interestingly, Fig. 4.21b shows that their placement on Mg sublattice is energetically more favourable in β'' rather than β'. This indicates that solutes may postpone the precipitation of β' and therefore extend the stability of β'' precipitate. Cr, Fe, Mn, Ta and V are expected to exhibit such a behaviour. The hardness curve (Fig. 4.14) provides an experimental support showing that precipitation of β'' is postponed with increasing Ta concentration. Further, the investigated solutes prefer to stay in the β' precipitate and therefore postpone the final precipitation of the β phase. Note that the precipitation sequence is not expected to change based on the formation energies sequence calculation but the dynamics of the precipitation (kinetics, thermodynamic forces) are modified, namely for Ti and Ta.
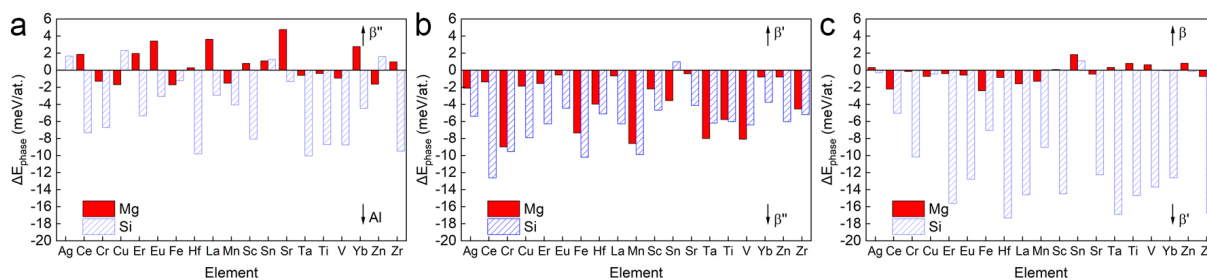
Figure 4.21: Phase preference energies for co-existence of two phases (a) Al and β'', (b) β'' and β', (c) β' and β phases. Phase preference energy of value 0 represents no preference in investigated phases [232].
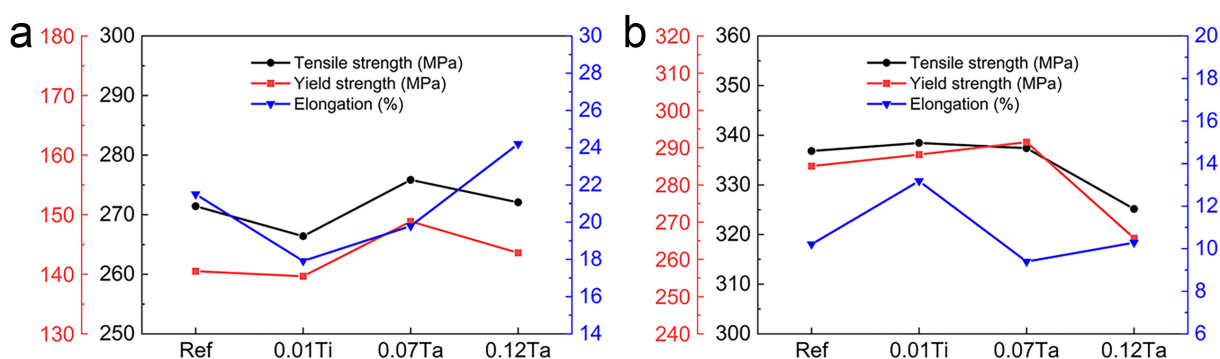
Figure 4.22: The tensile properties of Ta-refined and Sr-modified alloys in (a) T4 and (b) T6 condition.

4.13 Mechanical properties of Ta-refined and Sr-modified alloys

The mechanical properties after solution treatment (T4) are shown in Fig. 4.22a. Tensile and yield strength are lower in 0.01Ti alloy than in Ref alloy. The lowest elongation is measured in 0.01Ti alloy. Addition of 0.07 wt. % Ta result in a slight increase of tensile and yield strength, however, the elongation is still lower than that of Ref alloy. Further increase of solute Ta up to 0.12 wt. % shows a slight decrease in tensile and yield strength. On the other hand, the elongation increases with increasing solute Ta. The highest elongation in T4 condition is measured to be ~24 % in 0.12Ta alloy.

The tensile properties in T6 condition are plotted in Fig. 4.22b. Interestingly, the tensile and yield strength are comparable in Ref, 0.01Ti and 0.07Ta alloy. A slight increase in yield strength is observed in 0.07Ta alloy. Further addition of Ta (0.12Ta alloy) shows a significant decrease in the tensile and yield strength. The highest elongation of ~13 % is measured in 0.01Ti alloy. Ta-refined alloy show a lower elongation than 0.01Ti alloy, however, increasing solute Ta up to 0.12 wt. % improves the elongation approximately ~2 %. Nevertheless, the Ref alloy exhibits a higher elongation than Ta-refined and Sr-modified alloys.

117

Figure 4.23: Test-records (black) of 0.01Ti alloy including the 95 % secant line (red) in conjunction with the provisional force, P_Q and the maximum force P_{max}.

Table 4.7: Summary of important parameters and measures extracted from the fracture toughness testing of 0.01Ti alloy.

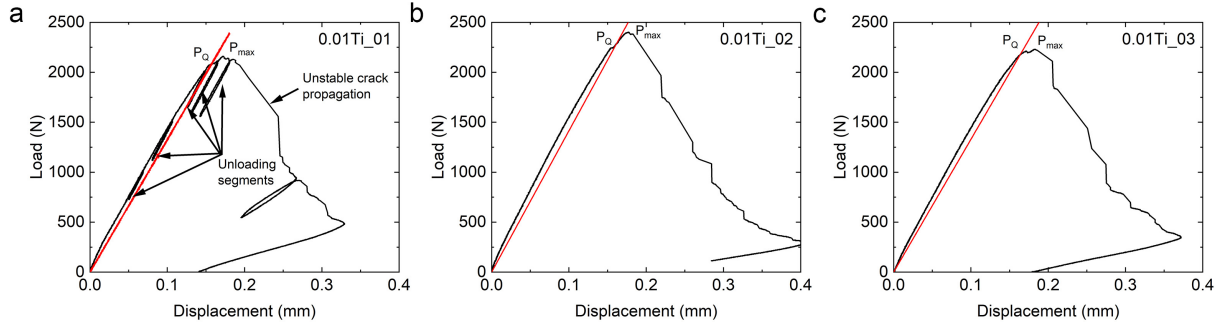| Alloy designation	B [mm]	a_{final} [mm]	$(W - a_{final})$ [mm]	P_{max}/P_Q [-]	K_Q [MPa·m$^{1/2}$]	K_{max} [MPa·m$^{1/2}$]	$2.5 \cdot (K_Q/\sigma_y)^2$ [MPa·m$^{1/2}$]
0.01Ti_01	8.9	9.73	8.27	1.04	21.5	22.3	10.1
0.01Ti_02	8.9	9.43	8.57	1.07	21.3	22.7	9.9
0.01Ti_03	8.9	9.87	8.13	1.02	22.7	23.2	11.2

4.14 Fracture toughness of Ti-refined and Sr-modified alloy

In this section, the fracture tougness assessment is performed in 0.01Ti alloy (Table 4.1) in T6 condition. In total, three specimens of 0.01Ti alloy are measured (Fig. 4.23).

In the first series of experiments, the unloading sequences are applied (Fig. 4.23a) in the case that a J-Integral approach would be needed to assess the material's behaviour. This would allow to measure the crack extension from the change of the sample's compliance. However, the investigated sample does not exhibit a continuous deformation behaviour, as shown in Fig. 4.23a. The crack advances in an unstable crack growth. Subsequent experiments revealed that the samples are only monotonically deformed. The fracture toughness is assessed according to ASTM E399.

Summary of measured parameters including the ratio of the measure maximum force (P_{max}), the provisional force (P_Q), the provisional fracture toughness (K_Q), the maximum stress intensity, K_{max} and the quantity $2.5 \cdot (K_Q/\sigma_y)^2$ are listed in Table 4.7. The K_Q can be referred as the stress intensity for the unstable crack growth. The table further includes the thickness of the sample (B), the final crack length (a_{final}), the remaining ligament ($W - a_{final}$) and the ratio of maximum and provisional load (P_{max}/P_Q).

It is evident that the validity criteria (P_{max}/P_Q) is always fulfilled as the ratio is always

smaller than 1.1. To qualify a plain strain fracture toughness the dimensions of the samples B, a_{final} and $(W - a_{\text{final}})$ must be larger than $2.5 \cdot (K_Q/\sigma_y)^2$. As the table and the nominal dimension show, this criterion could not be fulfilled. Nevertheless, the comparison of the obtained K_Q-values can be used to interpret the fracture resistance because the sample dimensions are identical. The average K_Q of 0.01Ti alloy is 21.8±0.7 MPa·m$^{1/2}$.

4.15 Discussion about effect of Ta on grain size and precipitation

4.15.1 Effect of Ta on grain refinement in Sr-modified alloys

Grain size decreases with increasing solute Ta (Fig. 4.1). The grain refinement is mainly affected by heterogeneous nucleation and growth restriction. The heterogeneous nucleation is influenced by characteristics of nucleation sites inside the grain refiner (such as size and size distribution, number density and other factors discussed in section 2.2.2). Because of the same addition of Al-2.2Ti-1B, the number of particles is assumed to be equal in 0.07Ta and 0.12Ta. Only the largest particles (∼1 %) are activated within the grain refiner and therefore can refine the α-Al grains [71]. However, the number of particles is not considered as a dominant factor for grain refinement.

Growth restriction effect $m \cdot (k - 1)$ of Ti and Ta are 245.6 K and 105 K, respectively [1, 65, 66]. Hence Ti has a stronger growth restriction effect than Ta, as shown in Table 2.1. High Si concentration (7 wt. %) significantly increases the growth restriction in Al-Si based alloys. Note that only solutes, therefore not bounded elements, can play a role as growth restrictor. The peritectic temperature of Al-Ta (Fig. 2.25) is higher than that of Al-Ti (Fig. 2.22) [139]. In metallic glass experiments by Schumacher [3, 17], the Ta was detected on the basal plane of TiB$_2$ and was specified as Al$_3$Ta layer, even though the Al$_3$Ta is not stable below peritectic concentration. Equation 2.39 is used to compare the effect of Ta and Ti within the investigated alloy system. Q values of 0.01Ti, 0.07Ta and 0.12Ta alloys equal to 2.46, 7.35 and 12.6, respectively. Therefore the increasing amount of solutes can enhance the growth restriction. Further refinement of Ta up to 0.12 wt. % is not caused by the formation of additional Al$_3$Ta phase but by increasing the growth restriction effect. Therefore, the pre-peritectic Al$_3$Ta is not believed to be responsible for grain refinement. The maximal solubility of Ta in Al is 0.24 wt. % at 668 $^\text{o}$C at the peritectic temperature [139]. Other literature [235, 236] reported the maximal solubility of Ta in Al is 0.105 wt. % at 700 $^\text{o}$C. This indicates that the Al$_3$Ta phase can be found in 0.12Ta alloy, however, microscopical studies did not reveal any Al$_3$Ta phase. It was reported [108] that Al$_3$Ti was found in the centre of α-Al grains. Although this behaviour can be expected for Al$_3$Ta, a direct experimental support was not observed within the solidification microstructure.

The formation of AlSiTi phase occurs above 3 wt. % Si when Ti is present [1, 125]. Investigated alloy system contains Ti only in the form of TiB_2 due to the addition of stochiometric Al-2.2Ti-1B grain refiner. Therefore no free Ti is available to form a poisoning AlSiTi phase. Overlap of Si and Ta is detected in SEM EDS maps (Fig. 4.8), however the peaks of Si and Ta are very close, therefore the possible overlap cannot be avoided. Fig. 4.10 and Fig. 4.11 show that the Si is not present at the interface of TiB_2. EDS analysis (Fig. 4.11h) and FFTs of the interface layer (Fig. 4.12) indicates the composition of the Ta-rich layer on the basal plane is $(Ti, Ta)B_2$. Grain size measurement with Ta additions gives a strong experimental support for the substitution of Ta as a remedy to Si-poisoning.

V detected in Fig. 4.11 is believed to be an impurity from the production of primary Al or CP Al-2.2Ti-1B grain refiner. Practical and theoretical verification of V as grain refiner in Al alloys was studied, however, the trend is not clearly established in both casting alloys [237] and wrought alloys [238]. Note that none of these studies investigated the effect of V in combination with Al-Ti-B grain refiner, therefore are not further discussed.

4.15.2   Sr, P and Ta interaction

Fig. 4.4 shows Sr-modified alloys exhibit a well modification effect in hypoeutectic Al-7Si-0.3Mg based alloys. P impurity forms AlP which promotes the nucleation of eutectic Si [21, 22, 25, 26]. $T_{N,\text{eu}}$, $T_{min,\text{eu}}$ and $T_{G,\text{eu}}$ are depressed with the addition of Sr (Table 4.2), which indicates that the nucleation potency of AlP is reduced. It is well-accepted that Sr interacts with AlP and forms a stable Sr_3P_2 phase, therefore the nucleation is decreased and ΔT_{eu} is increased. ΔT_{eu} represents the driving force (undercooling) required for nucleation and to hinder the growth of eutectic Si. Increasing eutectic grain size in Sr-modified alloys compared to Ref alloy (Fig. 4.3) is in good agreement with literature [148, 158]. Intermetallic Al_2Si_2Sr is observed with the addition of 0.02 wt. % Sr (Fig. 4.6). A similar result was reported in HP Al-5Si alloys with the addition of 100 ppm Sr [176]. The large lattice mismatch of Al_2Si_2Sr with eutectic Si indicates that the Al_2Si_2Sr is unlikely to nucleate the eutectic Si [177, 187]. Al_2Si_2Sr phase is observed in the vicinity of P, presumably the Sr_3P_2 phase, which indicates that Sr_3P_2 can possibly nucleate Al_2Si_2Sr. This assumption is further discussed in section 5.11.

Compared to Ref alloy, the ΔT_{eu} increases in 0.01Ti alloy with the addition of free Ti from Al-5Ti-1B grain refiner. Grain refinement and modification are well-known to have no mutual effect. On the contrary, their combined effect improves the properties of alloys more than using them in a separate manner [16, 104]. However, no interaction is well-known only in the case of Ti as a grain refiner and Sr as a modifier. Sr and P concentrations are the same in investigated alloys (Table 4.1). In Ta-refined and Sr-modified alloys (0.07Ta, 0.12Ta), the lower ΔT_{eu} are detected. With increasing Ta the $T_{min,\text{eu}}$ and $T_{G,\text{eu}}$ is depressed compared

to 0.01Ti alloy. Interestingly, the SF increases with increasing Ta concentration (Fig. 4.4). The eutectic grain size decreases with increasing Ta, as shown in Fig. 4.3. $T_{N,eu}$ of 0.01Ti and 0.12Ta are close, nonetheless, the $T_{min,\text{eu}}$, $T_{G,\text{eu}}$ and ΔT_{eu} are $\sim$2 $^{\text{o}}$C, $\sim$5 $^{\text{o}}$C and $\sim$3 $^{\text{o}}$C lower in 0.12Ta alloy compared to 0.01Ti alloy. One possible explanation may be that Ta narrows the solidification interval of the eutectic reaction via depression of $T_{min,\text{eu}}$, $T_{G,\text{eu}}$ and ΔT_{eu} and thus refine the eutectic Si. However, the thermodynamic data for Ta are not available to verify this assumption.

4.15.3 Effect of Ta on precipitation kinetics of β-type precipitates

Increasing activation energy of β'' precipitate with increasing Ti concentration is shown in Table 4.6. The highest activation energy of β' precipitate is calculated in 0.12Ta alloy. Low additions of Ta (0.07 wt. %) decrease the activation energy and high addition of Ta (up to 0.12 wt. %) increases the activation energy of investigated β-type precipitates.

In the hardness curve (Fig. 4.14) the 0.07Ta reaches the peak hardness after 3 h, while 0.12Ta reaches the peak hardness after 4 h. 0.12Ta alloy is aged at 180 $^{\text{o}}$C for 1 h longer to achieve the peak hardness. Because of the identical ageing condition in investigated alloys, the chemical composition is the only parameter to alter the precipitation. It should be noted that the Kissinger method does not involve any thermal history, nucleation or evolution of the studied samples. DFT shows the thermodynamic stability of precipitates with solutes (Fig. 4.21). Bearing in mind that kinetic processes (DSC) and thermodynamic stability (DFT) are two different phenomena which cannot be directly compared. Regardless, DFT provides a useful insight into phase stability and is in good agreement with the hardness curve.

Ta reduces the interface energy of Al(001)$||\beta''$(010) as shown in Fig. 4.19, while the presence of Ti at the interface exhibits higher interface energies. Thermodynamic stability calculation indicates where the Ta is energetically preferred to stay. On the other hand, the interface energy indicates whether the interface is energetically preferred with the Ta at the interface to become more stable. Based on these ab initio calculations we assume that Ta is retained in SSSS within α-Al dendrite. The distribution of solutes (namely Mg) was studied by Wang and Davidson [200] and is therefore reasonable to assume that the same phenomena apply to any other element which forms a solid solution with Al matrix (i.e., Ti or Ta). When the Ta is present at the interface, the interface energy decreases and therefore it should be energetically easier to initiate the growth of β'' precipitate from the Al matrix. More experimental support for the distribution of solute Ta in the matrix as well as at the interface of β'' is required.

Ta grain refinement in Eu-modified Al-Si based alloys

This chapter is based on one publication [239] and a publication submitted to *Journal of Alloys and Compounds* with the title: *Elucidating effects of Eu and P on solidification and precipitation of Al-7Si-0.3Mg based alloys refined by Ta and TiB$_2$.*

The chemical composition of investigated alloys is listed in Table 5.1. Ref alloy is without the addition of grain refiner and modifier. 0.02Eu, 0.05Eu, 0.02Eu40P and 0.05Eu40P alloys are modified with Eu and P, respectively. Except for Ref alloy, all alloys are grain refined with Al-2.2Ti-1B grain refiner and solute Ta with an addition of 0.12 wt. %. The concentration of Ta is different from Table 4.1 due to measurement error. It should be noted that the nominal composition of Ta is the same in investigated alloys.

5.1 Thermal analysis

In total five thermal analysis cooling curves are shown in Fig. B.1 and the temperatures are listed in Table 5.2. In terms of α-Al, the highest ΔT is measured in Ref alloy (2 ºC). No ΔT is measured in Ta-refined alloys (200Eu, 200Eu40P, 500Eu40P) except 500Eu alloy, where the ΔT of 0.5 ºC is recorded. A low ΔT indicates an easy heterogeneous nucleation of α-Al grains using solute Ta in combination with stoichiometric Al-2.2Ti-1B grain refiner. T_N is not included due to the possible effect of impurities and the very short time of nucleation.

In terms of eutectic Si, the lowest $T_{N,\text{eu}}$ is measured in 500Eu40P alloy. Comparable $T_{min,\text{eu}}$ and $T_{G,\text{eu}}$ are detected in 200Eu, 500Eu and 500Eu40P alloys. The highest ΔT_{eu} (3.9 ºC) is measured in 200Eu alloy. The lowest ΔT_{eu} is observed in Ref and 200Eu40P alloys. Usually, a high $T_{N,\text{eu}}$ and a low ΔT_{eu} indicate an easy heterogeneous nucleation and subsequent growth, presumably enhanced via the presence of AlP. Therefore, a modified eutectic Si structure

Table 5.1: Chemical composition of CP Al-7Si-0.3Mg based alloys with additions of Eu and P. Note that the composition is listed in wt. %.

Alloy	Si	Mg	Sr	Ti	B	Fe	Ta	Eu	P	Al
Ref	7.1	0.39	-	-	0.001	0.06	-	-	0.0028	Bal.
200Eu	7.3	0.38	-	0.0079	0.002	0.07	0.086	0.024	0.0022	Bal.
500Eu	7.2	0.34	-	0.0076	0.002	0.07	0.086	0.06	0.0023	Bal.
200Eu40P	7.4	0.39	-	0.0095	0.002	0.08	0.086	0.024	0.0043	Bal.
500Eu40P	8.0	0.35	-	0.0082	0.002	0.07	0.086	0.06	0.0042	Bal.

Table 5.2: Thermal analysis of Eu-modified alloys. Measured temperatures are listed in $^{\mathrm{o}}$C.

Alloy	T_N	T_{min}	T_G	ΔT	$T_{N,\mathrm{eu}}$	$T_{min,\mathrm{eu}}$	$T_{G,\mathrm{eu}}$	$T_{\mathrm{eq}} - T_{N,\mathrm{eu}}$	ΔT_{eu}
Ref	-	610.3	612.3	2.0	576.2	573.3	573.8	0.8	0.5
200Eu	-	612.5	-	-	571.4	564.9	568.8	5.6	3.9
500Eu	-	612.9	613.5	0.5	572.0	565.0	566.2	5	1.2
200Eu40P	-	613.1	-	-	579.9	571.8	572.3	-	0.5
500Eu40P	-	612.5	-	-	570.7	567.4	569.7	6.3	2.3

can be expected in all alloys except Ref and 200Eu40P alloys, where an unmodified structure is expected. A higher $T_{N,\mathrm{eu}}$ is observed in Eu-modified alloys compared to that of Ref alloy. Surprisingly, the $T_{N,\mathrm{eu}}$ of 200Eu40P is even higher than the equilibrium temperature (T_{eq}) in the Al-Si phase diagram (577 $^{\mathrm{o}}$C) as shown in Fig. 2.21. This result indicates that the nucleation may occur above T_{eq}.

5.2   Optical microscopy

Grain refinement of α-Al below 200 μm is achieved using solute Ta in combination with Al-2.2Ti-1B grain refiner (Fig. 4.1). The same result is observed in Eu-modified alloys grain refined with Ta (Fig. 5.1). It was reported [3, 7, 76] that an effective grain refinement is achieved when the grain size is below 200 μm. The amount of the TiB$_2$ particles is assumed to be the same as the addition of Al-2.2Ti-1B grain refiner is equal in all Eu-modified alloys.

Note that the Al-2.2Ti-1B grain refiner with solute Ta in Eu-modified alloys exhibits a lower grain size than the conventional Al-5Ti-1B grain refiner (Fig. 4.1). A slight increase in grain size is observed with increasing Eu and P. Grain size after T4 and T6 are shown in Fig. B.2. Despite the slight decrease of grain size in the T6 condition, the heat treatment is well-known to have no effect on α-Al grain size, as shown previously in Fig. 4.2. The grain size is not affected by Eu and/or P addition and therefore the addition of Al-2.2Ti-1B grain refiner with solute Ta promotes grain refinement in both, Sr-modified (Fig. 4.1) and Eu-modified alloys (Fig. 5.1).

The eutectic grain size of as-cast microstructure in Eu-modified alloys is shown in Fig. 5.2.
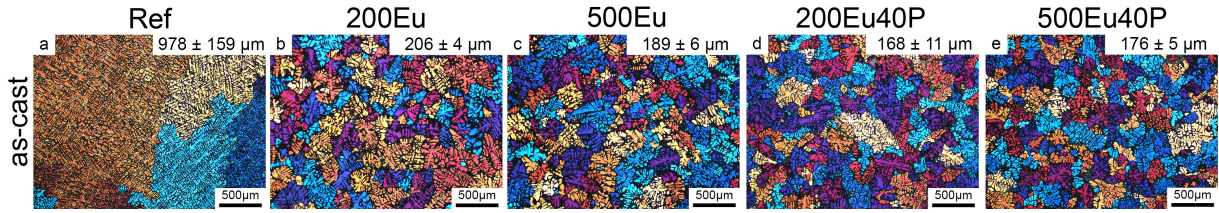
Figure 5.1: As-cast microstructure after Barker's etching (a) Ref, (b) 200Eu, (c) 500Eu, (d) 200Eu40P and (e) 500Eu40P.
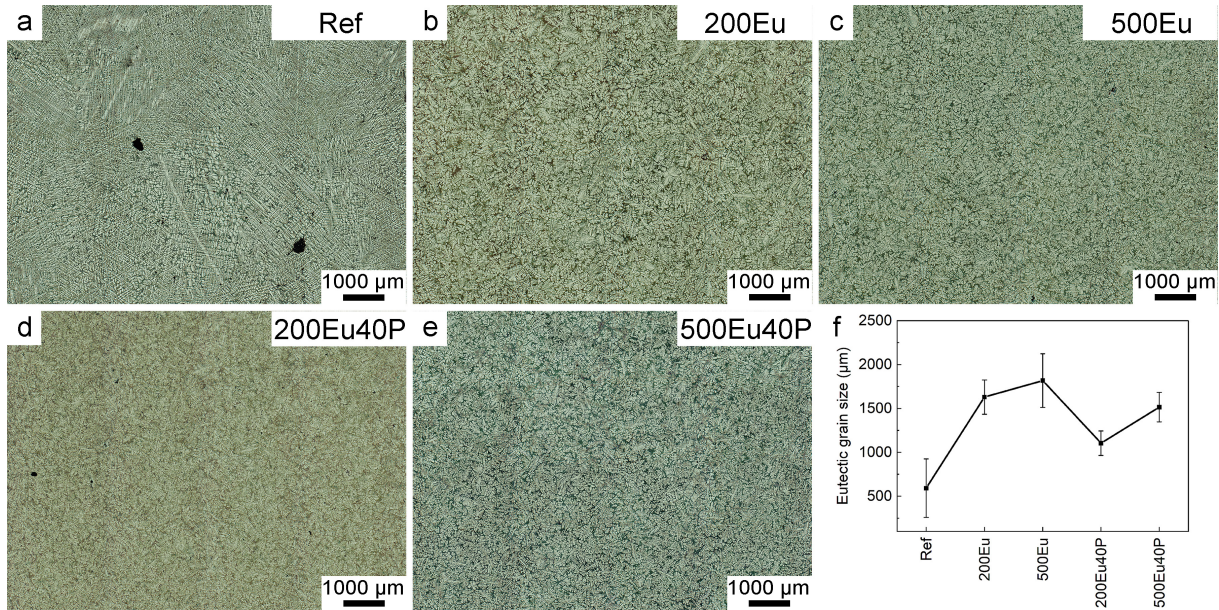

Figure 5.2: Eutectic grain size after MMR etching: optical microscopy images of as-cast (a) Ref, (b) 200Eu, (c) 500Eu, (d) 200Eu40P, (e) 500Eu40P and (f) measured eutectic grain size of five alloys.

Ref alloy exhibits the lowest eutectic grain size ($\sim$600 µm). The eutectic grain size increases with increasing Eu, therefore 500Eu alloy exhibits the highest eutectic grain size ($\sim$1800 µm). With increasing P addition, the eutectic grain size and modification effect of Eu decreases. Among Eu-modified alloys, the 200Eu40P exhibits the lowest eutectic grain size, which indicates an unmodified structure. The eutectic grain size of 1865 µm is obtained in Sr-modified alloy refined with Ti (Fig. 4.3) while the eutectic grain size in Eu-modified alloys ranges between 1500-1800 µm which is lower than that of Sr-modified.

SF of eutectic Si in as-cast and T6 condition in Eu-modified alloys is shown in Fig. 5.3. Large plates of eutectic Si with the lowest SF value are observed in Ref alloy. The highest SF ($\sim$0.87) is observed in 500Eu alloy. The values of SF are summarised in Table 5.3. Similarly to Ref alloy, 200Eu40P alloy exhibits a low SF, however, the standard deviation is largest in investigated alloys. This result indicates a high heterogeneity of Si particles in the solidification microstructure. Except for 200Eu40P alloy, the Eu-modified alloys exhibit
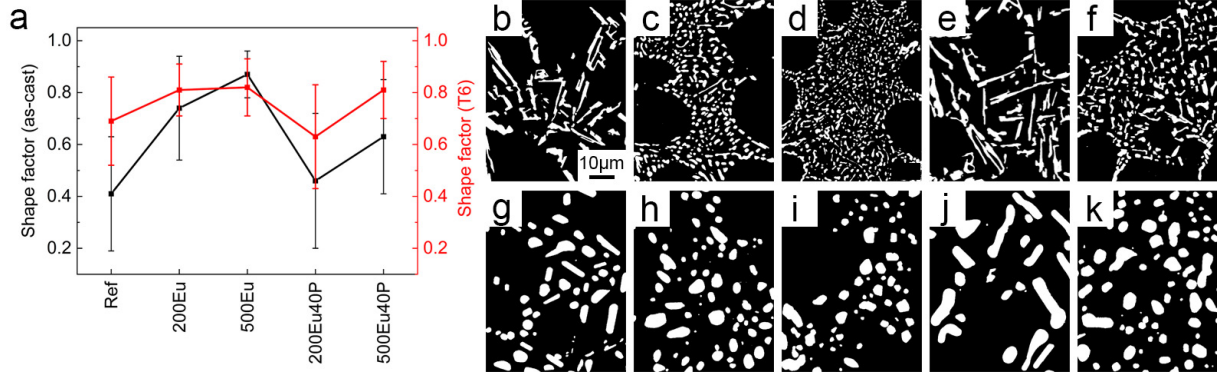
Figure 5.3: Shape factor of eutectic Si (a) in as-cast (black) and T6 (red) condition. Morphology of eutectic Si in (b-f) as-cast and (g-k) T6 in alloys (b, g) Ref, (c, h) 200Eu, (d, i) 500Eu, (e, j) 200Eu40P, and (f, k) 500Eu40P.

Table 5.3: Shape factor of eutectic Si in as-cast and T6 condition in Eu-modified alloys.

Alloy	As-cast [-]	T6 [-]
Ref	0.41±0.22	0.69±0.17
200Eu	0.73±0.20	0.81±0.10
500Eu	0.87±0.09	0.82±0.11
200Eu40P	0.46±0.26	0.63±0.20
500Eu40P	0.63±0.22	0.81±0.11

fine fibrous eutectic Si particles. With increasing P addition up to 40 ppm (500Eu40P), significantly coarser eutectic Si particles with low SF values are observed.

After T4 and T6, similar to Sr-modified alloys (Fig 4.4), the eutectic Si undergoes spheroidization accompanied by increasing interparticle spacing between Si particles compared to as-cast microstructure in Eu-modified alloys (Fig 5.3). Table 5.3 shows that SF is increased and the standard deviation is decreased after T6 treatment. The standard deviation decreased in average by ~25 %, which confirms that the microstructure after T6 is more homogeneous compared to the as-cast microstructure, which is attributed to the long solution treatment time and high temperature.

With increasing P concentration, the eutectic grain size and shape factor decrease while the eutectic grain size and shape factor increase with increasing Eu concentration. Note that the shape factor can be improved by implementing the heat treatment, however, the eutectic grain size is controlled by the solidification process alone.

5.3 SEM

Comparison of unmodified and modified structures of eutectic Si is further investigated using SEM backscattered electron (BS) images (Fig. 5.4). 3D morphology of eutectic Si is shown
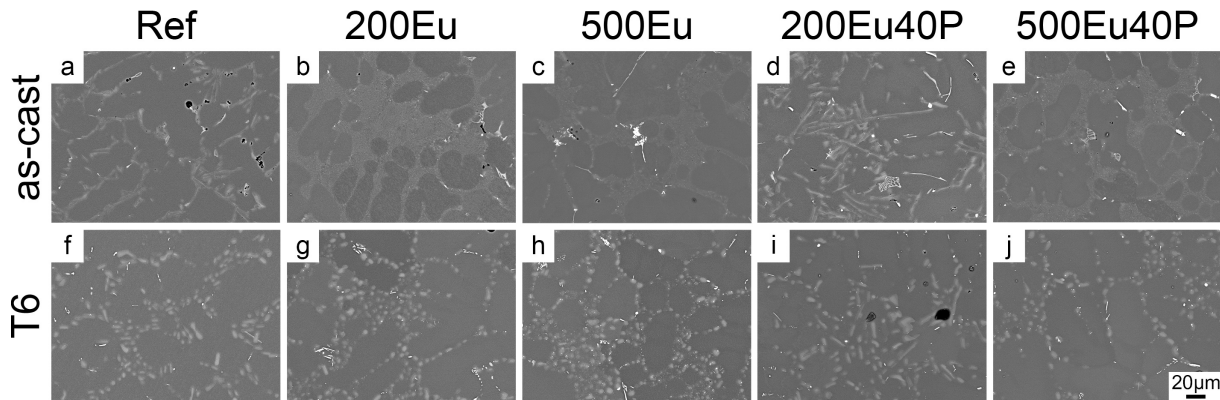
Figure 5.4: SEM BS images of (a-e) as-cast and (f-j) T6 microstructure of alloy (a,f) Ref, (b,g) 200Eu, (c,h) 500Eu, (d,i) 200Eu40P, and (e,j) 500Eu40P.
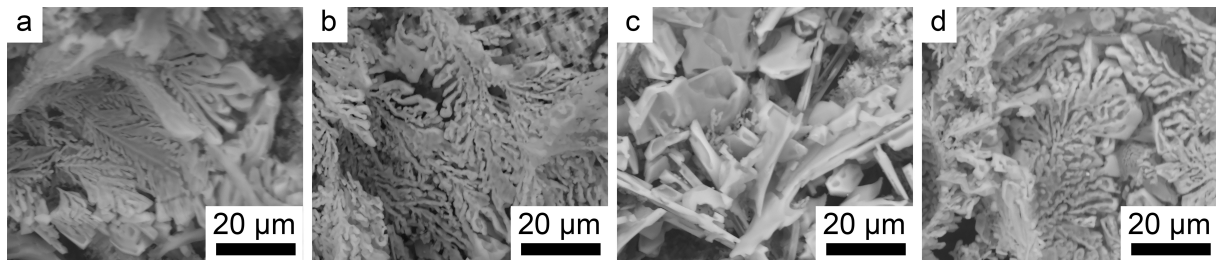

Figure 5.5: SEM SE image demonstrating the 3D morphology of eutectic Si at a high magnification in (a) 200Eu, (b) 500Eu, (c) 200Eu40P, and (d) 500Eu40P after deep etching [239].

in Fig. 5.5 and Fig 5.6 using SEM secondary electron (SE) images. Eutectic Si is observed in the form of long plates with sharp edges in Ref and 200Eu40P alloys (Fig. 5.4). The modified structure is observed in 200Eu, 500Eu and 500Eu40P alloys which is fully consistent with Fig. 5.3. Eutectic Si undergoes spheroidization, as shown in Fig. 5.4.

Fe intermetallic phases (bright) are distributed along the grain boundaries. Smaller Fe-phases are observed in Ref alloy. The relative size of Fe-phases is significantly larger in Eu-modified alloys, indicating that the distribution of intermetallic phases along the grain boundaries can be influenced by modification.

Fig. 5.7 show EDS maps of presumably EuP phase surrounded by Eu-rich phase, presumably identified as Al_2Si_2Eu intermetallic phase. The EDS point analysis (Fig. 5.7h) of Eu and P indicates that the EuP phase is located at the centre. The distribution of O well-correspond to the P distribution, which is believed to be caused due to oxidation of P during sample preparation as reported in literature [154]. EuP was reported to be a good nucleation site for eutectic Si due to its small lattice mismatch [25] and cube-to-cube orientation, although the efficiency of EuP is believed to be less than that of AlP. Mg signal is detected in the centre of the intermetallic phase (Fig. 5.7d), which indicates the possibility of Mg-rich phases to

127
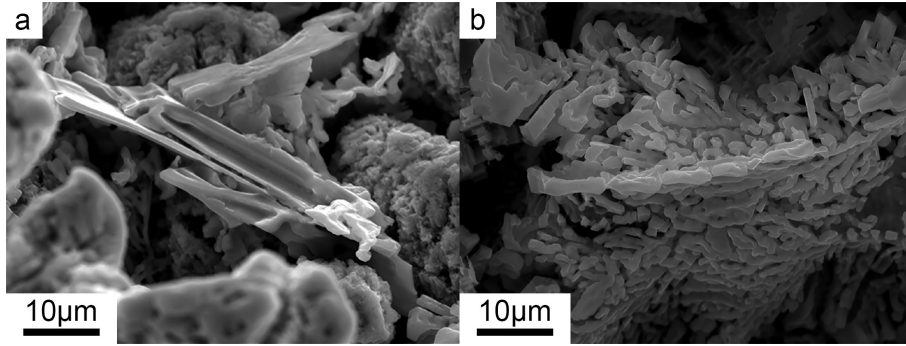
Figure 5.6: SEM SE images showing 3D morphology of eutectic Si at high magnification in (a) 200Eu40P and (b) 500Eu40P after deep etching.
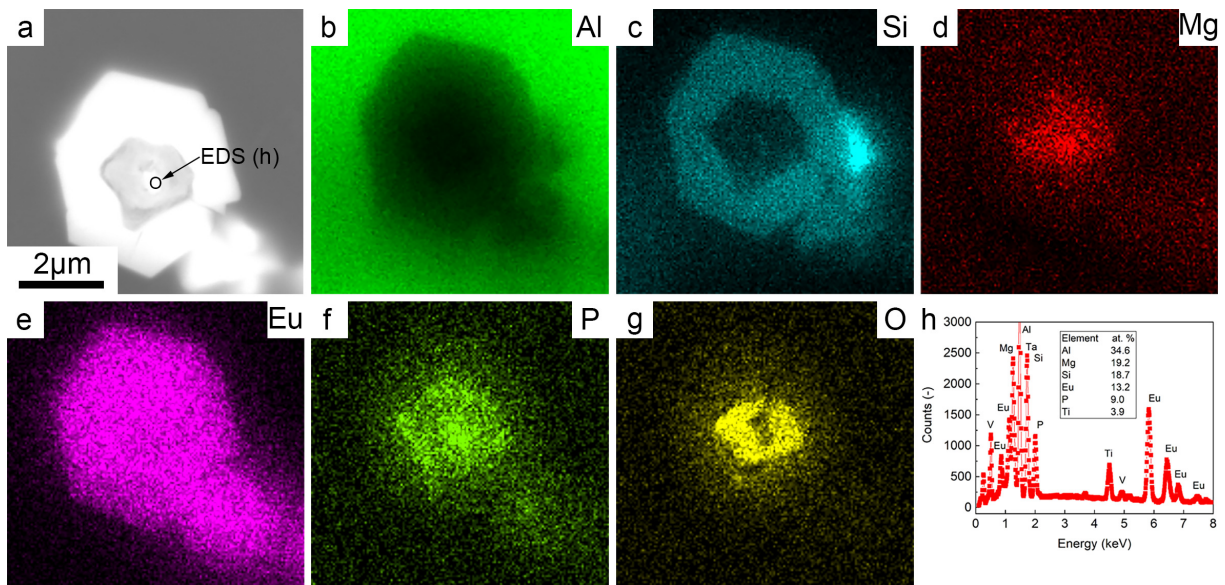
Figure 5.7: SEM BS image of (a) Al$_2$Si$_2$Eu intermetallic phase in 500Eu40P alloy and EDS maps of (b) Al, (c) Si, (d) Mg, (e) Eu, (f) P, (g) O and (h) EDS point analysis as marked in (a).

nucleate P-rich or Al-Si-Eu (section 5.11).

5.4   EBSD of 500Eu40P alloy

The grain size of the as-cast 500Eu40P alloy is investigated using EBSD (Fig. 5.8). Small grains are detected at the grain boundaries in the IPF, as shown in Fig. 5.8a. Since the Al and Si signals are very close, the grains smaller than 20 μm were excluded from the measurement of grain size. The frequency of measured α-Al grains is shown in Fig. 5.8b. The grain size measured using EBDS is much less than that measured using OM, as shown in Fig. 5.1e. Furthermore, due to the high frequency of grain size less than 30 μm, the standard deviation is very high (more than ∼50 %).
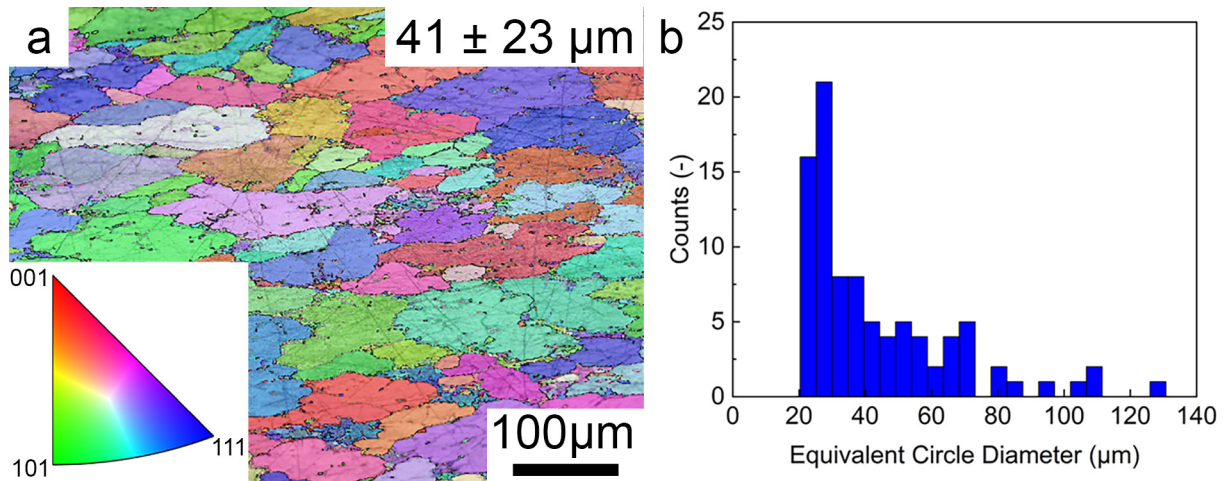
Figure 5.8: (a) EBSD IPF map of 500Eu40P alloy and (b) grain size frequency within the as-cast microstructure.
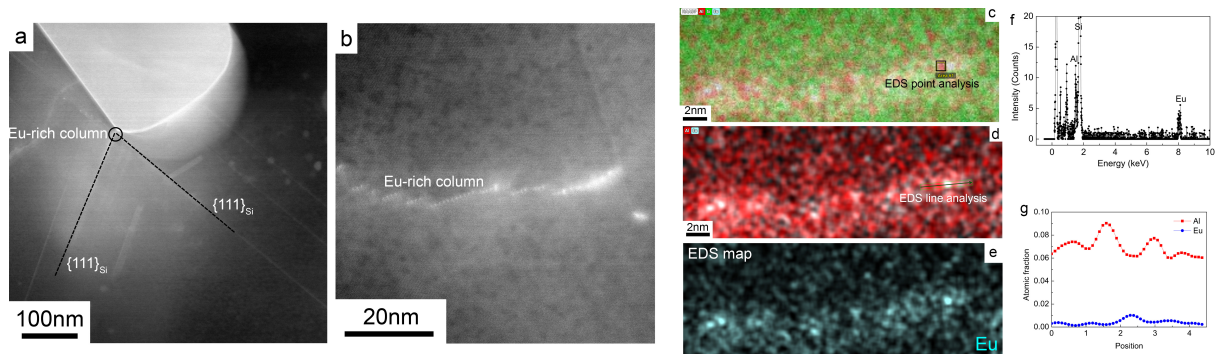
Figure 5.9: (a, b) High resolution STEM image of Eu-rich column with twinned Si, (c, f) EDS point analysis, (d, g) line measurement and (e) map of Eu-rich column in 500Eu40P alloy.

5.5 TEM-distribution of Eu within eutectic Si

The distribution of Eu within eutectic Si is shown in Fig. 5.9a. The Fe-containing phase within eutectic Si is attributed to the overlap between the Fe-containing phase and Si. However, another possibility that the Fe-containing phase is indeed formed within eutectic Si cannot be rulled out. Eu-rich columns are observed at the intersection of two {111} twins in the vicinity of the Fe-containing phase (Fig. 5.9). Furthermore, the Eu-rich columns are observed to continuously along the growth step of faceted eutectic Si (Fig. 5.9b). EDS map, EDS point analysis and EDS line scanning are shown in Fig. 5.9c-d, Fig. 5.9f and Fig. 5.9g, respectively. EDS investigations confirm the presence of Eu-rich columns. These results are fully consistent with those reported in the literature [181].

129

Figure 5.10: DSC thermographs of as-cast alloys including denoted α-Al (peak 1) and eutectic Si (peak 2), (b) enlarged eutectic region (peak 2) showing the Al$_2$Si$_2$Eu phase (peak 3).

5.6 DSC of as-cast alloys

Non-isothermal DSC cooling curves of as-cast samples are shown in Fig. 5.10. The onset and peak temperatures extracted from DSC are listed in Table 5.4. In total, three exothermic peaks are denoted: α-Al (peak 1), eutectic Si (peak 2), and the Al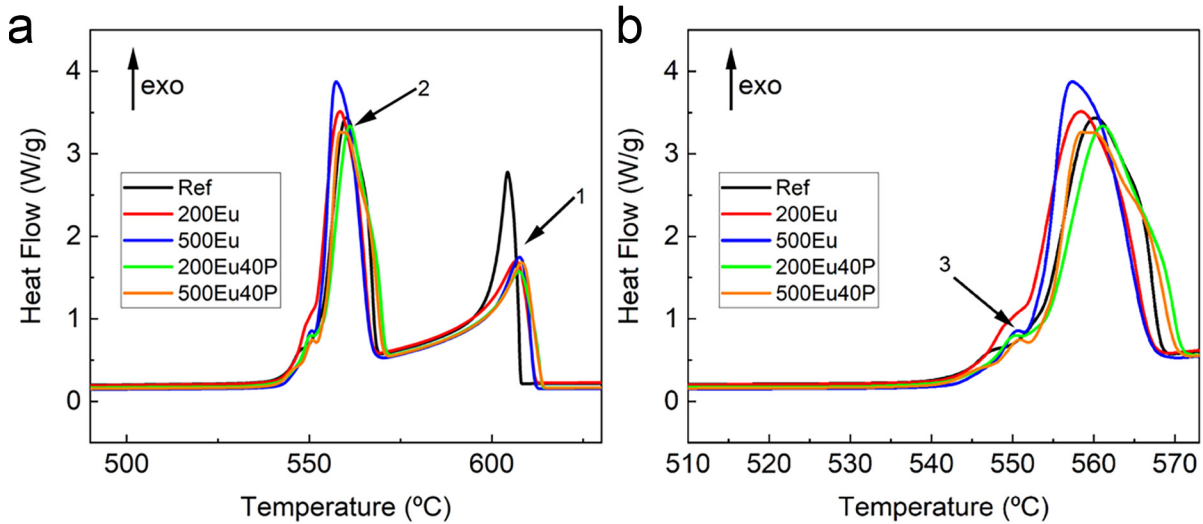$_2$Si$_2$Eu (peak 3), respectively. The lowest onset temperature of peak 1 is detected in Ref alloy. This result is consistent with thermal analysis results (Table 5.2), indicating a low number of nucleation sites for the nucleation of α-Al.

In terms of eutectic Si, 200Eu40P alloy exhibits the highest peak temperature of peak 2, which indicates the easy nucleation of eutectic Si. Without P (200Eu and 500Eu alloys), maximum peak temperatures of peak 2 are 1-2 $^\circ$C below those of the Ref alloy and alloys with P (200Eu40P and 500Eu40P alloys). Note that it is very challenging to determine the onset temperature of eutectic Si in DSC curves. The peak does not decline to the baseline and it is impossible to clearly state where the peak is initiated, therefore only the peak temperature is used to evaluate quantitatively the nucleation of investigated alloys. We assume that a shift to a higher peak temperature results in an easier nucleation of eutectic Si compared to a lower peak temperature.

Lastly, at the last stage of solidification of eutectic Si, peak 3 is detected and is attributed to the formation of the Al$_2$Si$_2$Eu phase (Fig. 5.10). Al$_2$Si$_2$Eu phase was reported to be present in the DSC thermograph in Eu-modified alloy produced by melt spinning [181]. Interestingly, Ref and 200Eu alloys exhibit a very low peak 3. This feature is further discussed in section 5.11.

Table 5.4: Onset and peak temperatures of as-cast Ta-refined and Eu-modified alloys extracted from the DSC cooling curve.

	Alloy	Onset temperature [^{o}C]	Peak temperature [^{o}C]
Peak 1	Ref	608.25	604.36
	200Eu	612.78	606.5
	500Eu	612.95	607.52
	200Eu40P	614.98	607.35
	500Eu40P	614.47	608.19
Peak 2	Ref	-	560.2
	200Eu	-	558.28
	500Eu	-	557.27
	200Eu40P	-	560.99
	500Eu40P	-	559.13
Peak 3	Ref	-	-
	200Eu	-	-
	500Eu	-	550.68
	200Eu40P	-	550.35
	500Eu40P	-	550.85

5.7 DSC after solution treatment

DSC thermographs of alloys investigated using heating rates of 20 ^{o}C/min and 10 ^{o}C/min are shown in Fig. 5.11a and b. β'', β' and β precipitates are denoted in the thermographs. The peak temperatures of β-type precipitates are listed in Table 5.5. Neither the formation nor the dissolution of GP-zones is detected, therefore it is assumed that β'' precipitate is initially formed before the DSC investigation. This assumption is based on TEM results in Sr-modified alloy where the β'' precipitates are observed prior to ageing (Fig 4.15).

The maximum peak temperatures are listed in Table 5.5. The peak temperatures are used to calculate activation energy according to Kissinger method (equation 3.4). With increasing heating rate the peak is shifted to higher temperatures. Kissinger plots (Fig. 5.11c-g) are used to extract the activation energy of β-type precipitates. Activation energies of Eu-modified alloys are shown in Table 5.6. The slope of Kissinger plot equals the activation energy. The slopes and the activation energies of both β'' and β' are comparable. The highest activation energy is calculated in 500Eu40P alloy for β'' precipitate. In terms of β'' precipitate, the activation energy is lower in 500Eu40P alloy than those in Ref alloy. The highest activation energy of β' precipitates are calculated in 200Eu40P and 500Eu40P alloys. In terms of β precipitate, significant changes are observed. Eu-modified alloys exhibit significantly lower activation energies compared to Ref alloy, indicating that Eu in combination with P significantly affects the precipitation kinetics of β precipitate. Precipitation kinetics of β'' and β' precipitates exhibit only slight differences.
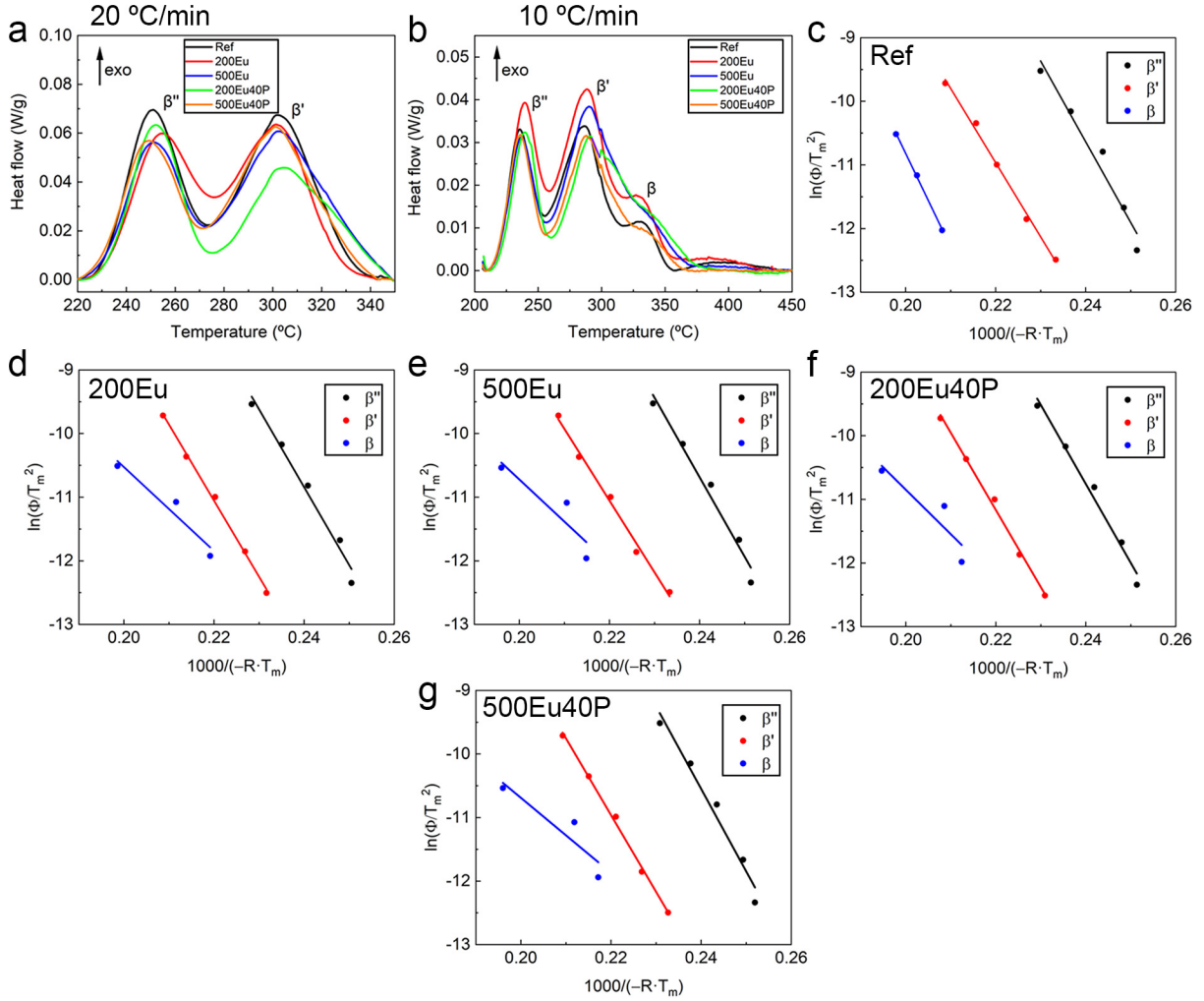
Figure 5.11: DSC thermographs of solution treated samples obtained for different heating rates: (a) 20 °C/min, (b) 10 °C/min. Kissinger plots of alloys (c) Ref, (d) 200Eu, (e) 500Eu, (f) 200Eu40P, and (g) 500Eu40P. Note that the temperature range in (b) is extended in order to clearly show the peak of β.

5.8 DFT-energetic of IIT and TPRE

Fig. 5.12 shows the colour map of substitutional energy (equation 3.10) of the most energetically preferred position at the TB. The next most energetically preferred positions are located along the Si{111} surface with the regular distance of approximately 3 atomic positions. Their energy preference decreases with increasing substitution energy and smaller differences between these preferred sites and the rest of the sites. Eu atoms are experimentally observed along the Si{111} interface in every second atomic position during the growth of eutectic Si in Eu-modified alloy [182], which resembles our theoretical calculation.

The surface of the TB (Fig. 3.22a) is not smooth after relaxation (Fig. 3.22b). Based on the 7x7 reconstruction of the Si{111} surface reported in the literature [240], the free

Table 5.5: Peak temperatures of Ta-refined and Eu-modified alloys extracted from the DSC cooling curve after T4.

		Heating rate				
		1 [ºC/min]	2 [ºC/min]	5 [ºC/min]	10 [ºC/min]	20 [ºC/min]
	Alloy	Maximum Peak temperature [ºC]				
β''	Ref	205.31	210.86	220.22	235.04	249.86
	200Eu	207.00	211.93	226.25	238.58	253.56
	500Eu	205.32	210.30	222.82	235.92	250.57
	200Eu40P	205.37	211.87	224.08	237.60	251.57
	500Eu40P	204.25	209.26	220.83	232.94	247.90
β'	Ref	242.25	257.05	272.94	284.54	302.88
	200Eu	246.09	256.98	272.90	289.26	303.25
	500Eu	242.27	259.15	272.90	290.92	303.25
	200Eu40P	247.75	260.78	274.23	290.44	305.92
	500Eu40P	243.81	257.08	270.90	286.11	301.58
β	Ref	-	304.80	320.71	334.74	-
	200Eu	-	275.72	295.33	332.58	-
	500Eu	-	286.63	298.17	340.42	-
	200Eu40P	-	293.08	303.57	344.77	-
	500Eu40P	-	280.67	294.58	340.42	-

Table 5.6: Activation energies of Ta-refined and Eu-modified alloys.

	Activation energy		
	β'' [kJ/mol]	β' [kJ/mol]	β [kJ/mol]
Ref	127	117	147
200Eu	122	120	66
500Eu	125	113	66
200Eu40P	124	121	70
500Eu40P	130	121	59

Si{111} surface is believed to undergo a surface reconstruction, where the atoms at the surface increase their distances from the surface and cause the puckering. Ab initio study by Sun [241] showed that Si{111} undergoes a surface reconstruction after an interaction with graphene monolayer within a distance of 4 Å from the free surface. Reconstructed surfaces exhibit a lower energy than the energy of perfectly flat configuration and therefore enhancing the thermodynamic driving force for this phenomenon. Substitutional energies of Eu atoms at different distances from TB are listed in Table B.1.

Substitutional energy of atoms far away from the TB corresponds to that of an infinite {111} Si surface as denoted in the puckered model in Fig. 3.22c. Values of ΔE_{sub} are in the range from 1.495 eV to 2.462 eV, as listed in Table B.2. Surprisingly, the most displaced surface site does not correspond to the lowest substitutional energy (Fig. 3.22c). It turns out, that
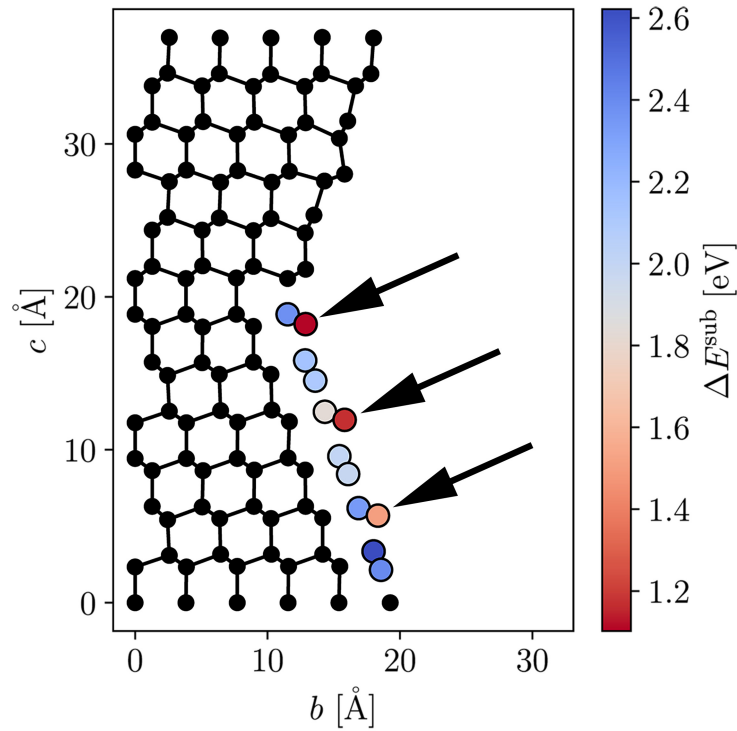
133

Figure 5.12: Substitutional energy of Si twin with an alloying element (Eu) at various distances from TB to model IIT mechanism and TPRE mechanism. For exact values please refer to Table B.1.

the other surface sites move out of the surface more than that site upon relaxation thus making these calculations consistent with the TB model.

5.9 Mechanical properties of Ta-refined and Eu-modified alloys

Fig. 5.13 shows the tensile properties of Ta-refined and Eu-modified alloys in T6 condition. The tensile and yield strength are comparable in Ref and 200Eu alloy. Surprisingly, increasing Eu up to 500 ppm results in a decrease of both the tensile and yield strength even compared with Ref alloy. Interestingly, Eu-modified alloys with additions of P exhibit a slight increase in tensile and yield strength. In terms of elongation, the most striking results are observed. Ref alloy exhibit elongation of $\sim$10 %, while the elongation gradually decreases with increasing Eu and/or P addition till $\sim$5 %. The detrimental effect of P on elongation is well-known. Decreasing elongation with increasing Eu concentration from 200 ppm to 500 ppm is due to formation of Al_2Si_2Eu phase.
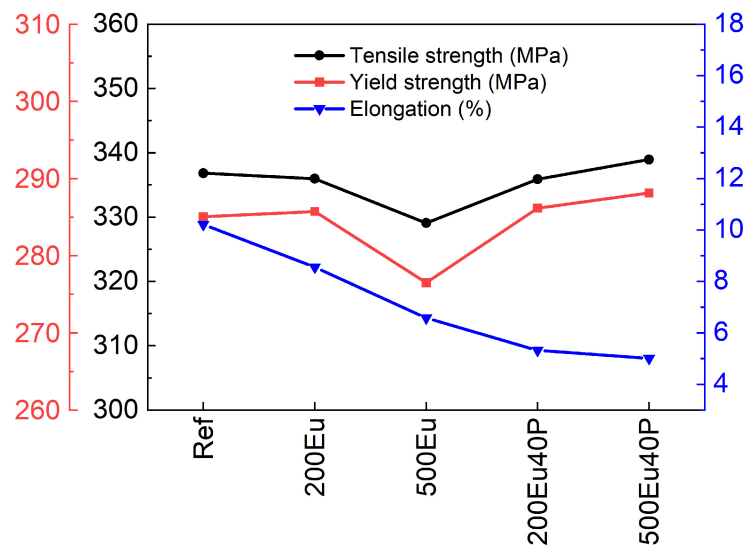
Figure 5.13: The mechanical properties of Ta-refined and Eu-modified alloys in T6 condition.
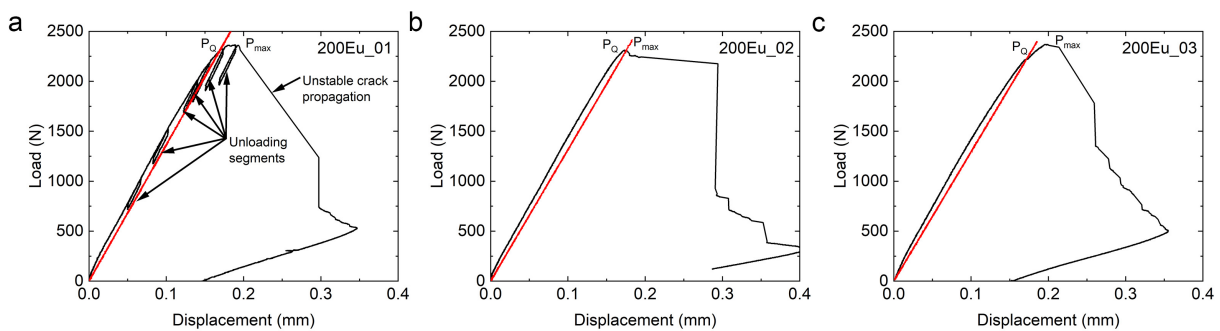

Figure 5.14: Test-records (black) of 200Eu alloy including the 95 % secant line (red) in conjunction with the provisional force, P_Q and the maximum force P_{max}.

5.10 Fracture toughness of Ta-refined and Eu-modified alloys

The fracture toughness assessment is performed in 200Eu alloy (Table 5.1) in T6 condition. In total three specimens of 200Eu alloy are measured (Fig. 5.14).

In the first series of experiments, the unloading sequences were applied (Fig. 5.14a). The same as in fracture toughness of Sr-modified alloy (section 4.14), the J-Integral approach is not applicable due to an unstable crack growth (Fig. 5.14a). Subsequent experiments revealed that the samples are only monotonically deformed. The fracture toughness is assessed according to ASTM E399.

It is evident from the Table 5.7 that the validity criteria (P_{max}/P_Q) is always fulfilled as the ratio is always smaller than 1.1. To qualify a plain strain fracture toughness the dimensions of

135

Table 5.7: Summary of important parameters and measures extracted from the fracture toughness testing of 200Eu alloy.

Alloy designation	B [mm]	a_{final} [mm]	$(W - a_{\text{final}})$ [mm]	P_{max}/P_Q [-]	K_Q [MPa·m$^{1/2}$]	K_{max} [MPa·m$^{1/2}$]	$2.5 \cdot (K_Q/\sigma_y)^2$ [MPa·m$^{1/2}$]
200Eu_01	8.9	9.60	8.40	1.01	23.7	23.9	12.5
200Eu_02	8.9	6.92	8.38	1.00	23.2	23.2	11.9
200Eu_03	8.9	10.09	7.91	1.07	22.9	24.5	11.6

the samples B, a_{final} and $(W - a_{\text{final}})$ must be larger than $2.5 \cdot (K_Q/\sigma_y)^2$. As the table and the nominal dimension show, this criterion could not be fulfilled. Nevertheless, the comparison of the obtained K_Q-values can be used to interpret the fracture resistance since as the sample dimensions are identical. The average K_Q of 200Eu alloy is 23.3±0.4 MPa·m$^{1/2}$.

5.11 Discussion about effect of Eu on modification, eutectic grain size and precipitation

5.11.1 Effect of Ta on grain refinement in Eu-modified alloys

Effective grain refinement using solute Ta and Al-2.2Ti-1B grain refiner is proved in Sr-modified alloys (Fig. 4.1). Here, the equally effective grain refinement (∼200 µm) using the same grain refined is obtained in Eu-modified alloys (Fig. 5.1). Interestingly, a slightly larger grain size is obtained in Eu-modified alloys. Thermal analysis (Table 5.2) shows a high T_{min} and no undercooling in Ta-refined alloys. The onset peak temperature of α-Al in the DSC curve (Fig. 5.10) is the highest for P-containing alloys (200Eu40P and 500Eu40P). Thermal analysis cannot be directly compared to DSC data since the T_{min} is significantly lower than the onset temperature detected using DSC. Effective grain refinement is maintained despite the various additions of Eu and/or P.

5.11.2 Effect of modification and heat treatment on eutectic Si

Fig. 5.5c and Fig. 5.6a show a plate-like morphology of eutectic Si in 200Eu40P alloy. Table 5.2 shows the highest T_N and the lowest ΔT_{eu}, which clearly indicates the easy heterogeneous nucleation and growth of eutectic Si. 200Eu40P contains 200 ppm Eu, which is insufficient in combination with increasing P additions. Eu is consumed to deplete all AlP and no free Eu is provided for modification during the growth. It is evident from the Si morphology that the plates are significantly larger than fine fibrous eutectic Si in fully modified alloys (200Eu, 500Eu and 500Eu40P). Increasing Eu additions up to 500 ppm provides the modified structure, therefore increasing Eu concentration can reduce the negative effect of increasing

P. This phenomenon is similar to other chemical modifiers (Sr [156], Eu [181]) to obtain a fibrous eutectic Si morphology.

5.11.3 Nucleation of eutectic Si and intermetallic phases

200Eu40P alloy exhibits an unmodified eutectic structure with the lowest ΔT_{eu} (Table 5.2), the lowest eutectic grain size (Fig. 5.2) and the lowest eutectic shape factor (Table 5.3) among Eu-modified alloys. These values are very similar to that of Ref alloy. It is clearly seen in the microstructure that the modification effect of Eu decreases with increasing P concentration due to increasing AlP. However, with increasing Eu the eutectic grain size and shape factor increases due to poisoning of AlP. EuP is believed to be a good nucleation site for eutectic Si [25] but less effective than AlP, while free Eu provides a modification effect.

Recently, Mao [183] observed the unmodified eutectic structure in Al-7Si alloy after the addition of 1000 ppm Eu. In Al-7Si-0.3Mg alloy, the modification effect of Eu is observed with the addition above 800 ppm Eu [184]. Here, a fully modified eutectic Si is achieved after the addition of 200 ppm Eu in Al-7Si-0.3Mg (Fig. 5.3). Note that Mao [183, 184] did not specify the P concentration. Li [25] investigated high purity Al-5Si alloy with the addition of Eu (up to 200 ppm) and P (up to 10 ppm) and found that Eu is effective in high purity alloys with low P concentration. However, a fully modified eutectic structure was not achieved with 200 ppm Eu and 10 ppm P. Bearing in mind that none of the mentioned studies did not introduce the grain refiner in their alloy systems.

The presence of Mg somehow reduces the amount of modifier. Studies of Mao [183, 184] support this statement. Joenoes [179] studied the effect of Sr in combination with Mg on the modification of Al-7Si alloy and found that the eutectic microstructure is less uniform with increasing Mg. The content of Mg is ∼0.3 wt. % in the present investigation (Table 5.1). SEM mapping in Fig. 5.7 shows the incorporation of Mg and P in the centre of the EuP phase, which is surrounded by Al-Si-Eu phase referred as Al_2Si_2Eu phase. Presence of Al_2Si_2Eu in Eu-modified alloys is in good agreement with literature [25, 183, 184]. Similar to SEM of Sr-modified alloy in Fig. 4.6, the Al_2Si_2Sr phase is found surrounding the Sr_3P_2 phase at the grain boundary in the vicinity of porosity. DSC of high purity Al-Si alloys produced by melt spinning shows Al_2Si_2Sr to be formed after the solidification of eutectic grain boundaries [175, 177]. The same result is observed in high purity Al-Si alloys modified with Eu [181]. It is not clear which phase (prior to the eutectic reaction) is involved in the nucleation of the Al_2Si_2Eu or Al_2Si_2Sr phase and therefore the nucleation sequence remains to be explored. Lattice mismatch (equation 2.26) is applied to elucidate the nucleation of Al_2Si_2Eu or Al_2Si_2Sr phases on proposed substrates. The result of equation 2.26 is the stretch or compression of the nucleating phase on the nucleant with the fixed size. The stretch or compression is interpreted in percentage (%).

Lattice mismatch of particular phases (Si, AlP, Al_2Si_2Eu, Al_2Si_2Sr, $EuMg_2$, EuP, MgO, Mg_2O, Mg_2P, Mg_3P_2, Na_3P and Sr_3P_2) and predicted formation energies are shown in Table 5.8. The effective lattice parameter a_{ef} of the (111) orientated cubic phases corresponds to $\frac{\sqrt{2}}{2} \cdot a_c$ (i.e. $\frac{1}{2}[110] \cdot a_c$, where a_c is the conventional cubic lattice parameter). In terms of hexagonal phases oriented in (0001), the lattice parameter is extracted as shown in Fig. B.4.

Firstly, it is clearly shown in Table 5.8 that Si can be easily nucleated on AlP. This result is consistent with the literature [141]. Note that the lattice mismatch of Si with Mg_2P and Sr_3P_2 phase is low. EDS measurement in Fig. 5.7h shows that according to atomic ratio (Mg:P=2:1) in the centre of EuP phase the Mg_2P phase may be present. Although, the Sr_3P_2 phase is believed to reduce the amount of AlP [175, 177], while it is not a good nucleation site for eutectic Si because of its large lattice parameter [25], the present lattice mismatch calculation shows a different trend. The difference is caused due to the measurement of atomic distances of Sr instead of P in a close-packed (111) plane. The lattice mismatch of Si with EuP and Sr_3P_2 is 7.99 % and 3.99 %, respectively. A significantly larger lattice mismatch of EuP indicates that the EuP is not likely to nucleate the eutectic Si compared to Sr_3P_2.

Secondly, P content and therefore the amount of AlP, is notoriously known to be present in CP Al alloys and its content increases with recycling. Thermodynamic calculation of Al-7Si of Liang [150] shows that the AlP can precipitate before eutectic Si even for low P additions ($\sim$4 ppm), while P additions above 15 ppm caused the AlP to precipitate before α-Al in Al-7Si alloys. The lattice mismatch of 0.17 % between Al_2Si_2Eu and EuP indicates that the EuP is a very good nucleation site for Al_2Si_2Eu. This calculation is fully consistent with EDS measurement of the EuP phase surrounded by Al_2Si_2Eu, as shown in Fig. 5.7. Cho [154] proposed that AlP could be the nucleation site for Al_2Si_2Sr in alloys modified with Sr. Nevertheless, as reported by Li [141], the free formation enthalpy of Na_3P and Sr_3P_2 are significantly lower than that of AlP. The lattice mismatch between AlP and Al_2Si_2Eu is 7.91 %, therefore there is a high (elastic) energy penalty for Al_2Si_2Eu to be nucleated on AlP. An even larger penalty applies for Al_2Si_2Sr, where the lattice mismatch with AlP equals to 8.69 %. For high P alloys modified with Eu, the Eu is expected to poison AlP and to from EuP. Subsequently, the Al_2Si_2Eu is then nucleated on EuP after the solidification of α-Al, while free Eu produces the modified eutectic structure.

Thirdly, the lattice mismatch of 4.91 % between the Al_2Si_2Sr and Sr_3P_2 indicates that Sr_3P_2 is not crystallographically favourable to nucleate Al_2Si_2Sr. On the other hand, the lattice mismatch of only 1.26 % between the Al_2Si_2Sr and Mg_3P_2 phase indicates that Mg_3P_2 may nucleate the Al_2Si_2Sr phase. Lee [135] predicted the formation of the Mg_3P_2 phase using Scheil simulation and even observed the Mg_3P_2 particle within the Al_2Si_2Sr phase in the Al-7Si-0.35Mg alloy system. However, Scheil simulation predicted the formation of Mg_3P_2

Table 5.8: Lattice parameters and calculated mismatch in % of the defined orientation relationship. Parameters of phases are taken from the Materials Project database [134]. Energy above hull and Predicted formation energy values refer to PBE exchange correlation potential.

Phase	Materials project number	Crystal structure	Orientation	Energy above Hull [eV/at.]	Predicted formation energy [eV/at.]	Lattice parameter in oriented plane [Å]	δ on Si (111)	δ on Al$_2$Si$_2$Eu (0001)	δ on Al$_2$Si$_2$Sr (0001)	δ on EuP (111)	δ on Sr$_3$P$_2$ (111)	δ on Mg$_2$P (111)	δ on Mg$_3$P$_2$ (111)
Si	mp-149	Cubic	(111)	0.000	0.000	3.8493	-	8.49	9.28	8.68	4.16	4.10	10.67
AlP	mp-1550	Cubic	(111)	0.000	-0.610	3.8700	0.53	**7.91**	**8.69**	8.10	3.60	3.54	10.08
Al$_2$Si$_2$Eu	mp-20595	Hexagonal	(0001)	0.000	-0.326	4.1761	7.83	-	0.72	0.17	3.99	4.05	2.01
Al$_2$Si$_2$Sr	mp-6931	Hexagonal	(0001)	0.000	-0.267	4.2063	8.49	0.72	-	0.55	4.68	4.74	1.27
EuMg$_2$	mp-1184321	Cubic	(111)	0.000	-0.115	6.2841	38.75	33.54	33.06	33.43	36.20	36.24	32.21
EuMg$_2$	mp-1101792	Hexagonal	(0001)	0.001	-0.114	6.3131	39.03	33.85	33.37	33.74	36.49	36.53	32.52
EuP	mp-20300	Cubic	(111)	0.000	-1.039	4.1834	**7.99**	**0.17**	0.55	-	4.16	4.22	1.83
MgO	mp-1265	Cubic	(111)	0.000	-3.054	2.9656	29.80	40.82	41.84	41.06	35.19	35.11	43.64
MgO$_2$	mp-2589	Cubic	(111)	0.014	-2.022	3.4143	12.74	22.31	23.20	22.52	17.43	17.36	24.77
Mg$_2$P	mp-1210592	Cubic	(111)	0.599	0.041	4.0070	3.94	4.22	4.98	4.40	0.06	-	6.31
Mg$_3$P$_2$	mp-8085	Cubic	(111)	0.187	-0.480	4.2599	9.64	1.97	**1.26**	1.80	5.88	5.94	-
Na$_3$P	mp-1598	Hexagonal	(0001)	0.000	-0.332	4.9712	22.57	15.99	15.39	15.85	19.35	19.40	14.31
Sr$_3$P$_2$	mp-1013552	Cubic	(111)	0.403	-0.638	4.0093	**3.99**	4.16	**4.91**	4.34	-	0.06	6.25

*Bold values are referenced in the main text.

after the Al_2Si_2Sr, which is different from that observed in their and our SEM results (Fig. 4.6), where the presumably Mg_3P_2 is found at the centre and surrounded by Al_2Si_2Sr. Based on the experimental results, it is highly unlikely, that the Al_2Si_2Sr is formed prior Mg_3P_2 phase. Mg_3P_2 was concluded by Lee [135] to be just a partial transformation of AlP. Our lattice mismatch calculation indicates an easier nucleation of Al_2Si_2Sr on Mg_3P_2 compared to Sr_3P_2.

Based on the obtained experimental results, lattice mismatch calculation and previous literature results, we propose the possible nucleation sequences: $Sr_3P_2 \rightarrow Mg_2P \rightarrow Al_2Si_2Sr$ and $Mg_3P_2 \rightarrow EuP \rightarrow Al_2Si_2Eu$ for Sr and Eu-modified alloys, respectively. Neither Al_2Si_2Sr [187] nor Al_2Si_2Eu (Table 5.8) are favourable to nucleate eutectic Si. Mg_2P has a smaller lattice parameter than Mg_3P_2 and therefore a smaller lattice mismatch with eutectic Si. However, predicted formation energies of Mg_2P and Mg_3P_2 phases are calculated to be 0.041 eV/at. and -0.480 eV/at, respectively [134]. This indicates that Mg_2P is less stable than Mg_3P_2. Furthermore, the energy above hull 0.599 eV/at. and 0.187 eV/at. are calculated for Mg_2P and Mg_3P_2 phase, respectively [134]. Hence, the predicted formation energies and the energies above hull strongly indicate that the observed Mg-P phase is more likely to be Mg_3P_2 rather than Mg_2P. The predicted formation energies of AlP (-0.610 eV/at.), EuP (-1.039 eV/at.) and Mg_3P_2 (-0.480 eV/at.) provide a strong support that EuP is formed prior to Mg_3P_2. However, the parallel formation of EuP and Mg_3P_2 cannot be ruled out. Overall, chemical modifiers are expected to form intermetallic phases with P that does not nucleate eutectic Si. Literature [135] and obtained experimental results suggest Mg_3P_2 can nucleate Al_2Si_2Sr (Fig. 4.6) and Al_2Si_2Eu (Fig. 5.7) in Sr and Eu-modified alloys. Mg_3P_2 may form on EuP by a mechanism similar to the duplex nucleation theory [17, 115]. Nevertheless, atomic scale investigations are required to confirm this mechanism.

Lastly, Na_3P, Eu-Mg or Mg-O are unlikely to nucleate eutectic Si, Al_2Si_2Sr or Al_2Si_2Eu intermetallic phases (Table 5.8). Hence, O present in EDS measurement in Fig. 5.7 is consistent with P-distribution caused by the oxidation of the P-rich particles [154] during SEM sample preparation rather than Mg-O phase.

High Eu and high P alloys (500Eu and 200Eu40P and 500Eu40P) show Al_2Si_2Eu (peak 3) in DSC thermographs (Fig. 5.10). Ref and 200Eu alloys do not show the peak 3 because the Eu interacts with the AlP and forms EuP and then free Eu provides a modification effect of eutectic Si. As discussed, the Al_2Si_2Eu phase may be nucleated on EuP, therefore free Eu is not available to form Al_2Si_2Eu with the addition of only 200 ppm Eu. Increasing Eu addition (500Eu alloy) causes eutectic grain size to increase (Fig. 5.2) and the Al_2Si_2Eu peak is observed (Fig. 5.10), therefore all AlP is consumed by reaction with Eu. Furthermore, the shape factor increases with increased Eu addition (Fig. 5.3). The peak temperatures of Al_2Si_2Eu peak in (Table 5.4) are not affected by Eu or P addition once the Eu addition is

enough to form Al_2Si_2Eu.

5.11.4 Effect of Eu and P on precipitation kinetics β-type precipitates

On one hand, the activation energy calculation shows negligible differences in β'' and β' precipitates in Eu-modified alloys (Table 5.6). On the other hand, precipitation of β exhibits significantly lower activation energies (60-70 kJ/mol) compared to Ref alloy (147 kJ/mol). These results give a strong experimental support that with increasing Eu and/or P, less energy is required for the precipitation of β precipitate than that in the Ref alloy, which is beneficial for applications at elevated temperatures, where the full precipitation into stable β precipitate is required. Differences in activation energies of β precipitate are negligible in Sr-modified alloys (Table 4.6). As noted in section 4.9, the activation energies cannot be directly compared with literature due to different heat treatments and chemical compositions of investigated alloy systems.

Phase preference energy of β precipitate is calculated using DFT (Fig. 4.21) shows nearly identical values for Sr and Eu, hence the effect of chemical modifiers on the precipitation of β can be assumed to be comparable. Although the activation energies in 0.01Ti alloy modified with 200 ppm Sr (Table 4.6) and 200 ppm Eu alloy (Table 5.6) exhibit large discrepancies, the different stoichiometry of intermetallic phases (Sr_3P_2, EuP) may consume more solutes and therefore the discrepancies in activation energies may occur.

Nucleation kinetics of HP Al-Si alloy in droplet with Ta, Eu, P

This chapter is based on one publication submitted to *Journal of Alloys and Compounds* with the title: *Revealing nucleation kinetics of entrained eutectic Si droplets in high purity melt spun Al-5Si based alloys with additions of Ta, TiB$_2$, Eu and P.*

The chemical composition of HP Al-5Si alloys produced by arc melting and melt spinning is listed in Table 6.1. The effect of Ta, Eu and P in combination with TiB$_2$ on nucleation and growth of entrained eutectic Si droplets in HP Al-5Si alloys is investigated using entrained droplet technique (section 2.6).

6.1 Melt-spun microstructure

Fig. 6.1 shows very fine α-Al grains. Different contrasts (bright) indicate intermetallic phases along the grain boundaries and within the α-Al. The less intermetallic phases are observed in alloys without Eu (Fig. 6.1a-g). On the other hand, the intermetallic phases are clearly observed in the melt-spun microstructure of Eu-modified alloys without the addition of P (Fig. 6.1h-k). The intermetallics are presumably identified as Al$_2$Si$_2$Eu phase using EDS (Fig. C.1). These intermetallic phases form in the pre-eutectic state. The Al$_2$Si$_2$Eu is entrained within α-Al grains due to the high cooling rate developed by melt spinning, which supports that Al$_2$Si$_2$Eu phase form in a pre-eutectic state or liquid. This type of Al$_2$Si$_2$Eu is further in this work referred as primary Al$_2$Si$_2$Eu. The relative amount of intermetallic phases is observed to decrease in Eu-modified alloys with increasing P addition, as shown in Fig. 6.1l-o. Low magnification SEM BS images are shown in Fig. C.2.
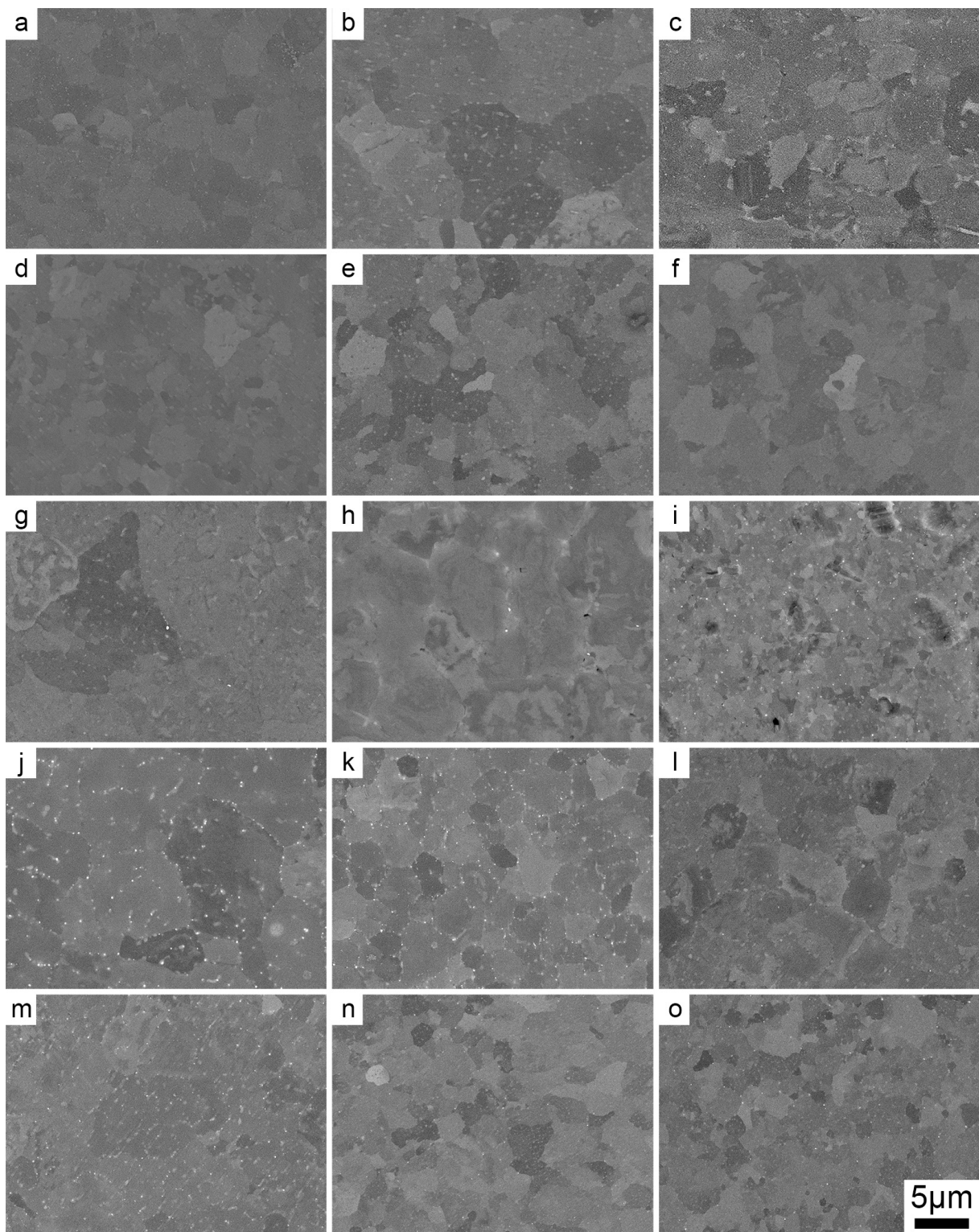
Figure 6.1: SEM backscattered (BS) images of melt-spun ribbons: (a) Ref, (b) TiB_2, (c) 0.05Ta, (d) 0.05-TiB_2, (e) 0.12Ta-TiB_2, (f) 0.30Ta-TiB_2, (g) 0.50Ta-TiB_2, (h) 0.02Eu, (i) 0.02Eu-TiB_2, (j) 0.05Eu, (k) 0.05Eu-TiB_2, (l) 0.02Eu-30P, (m) 0.05Eu-5P, (n) 0.05Eu-20P and (o) 0.05Eu-30P.

Table 6.1: Nominal compositions of Al–5Si based alloys with additions of different solutes.

	Elements					
Alloy designation	Si [wt. %]	Eu [wt. %]	P [wt. %]	Ta [wt. %]	TiB$_2$* [wt. %]	Al [wt. %]
Ref	5	-	-	-	-	Bal.
TiB$_2$	5	-	-	-	0.2	Bal.
0.05Ta	5	-	-	0.05	-	Bal.
0.05Ta-TiB$_2$	5	-	-	0.05	0.2	Bal.
0.12Ta-TiB$_2$	5	-	-	0.12	0.2	Bal.
0.30Ta-TiB$_2$	5	-	-	0.30	0.2	Bal.
0.50Ta-TiB$_2$	5	-	-	0.50	0.2	Bal.
0.02Eu	5	0.02	-	-	-	Bal.
0.02Eu-TiB$_2$	5	0.02	-	-	0.2	Bal.
0.05Eu	5	0.05	-	-	-	Bal.
0.05Eu-TiB$_2$	5	0.05	-	-	0.2	Bal.
0.02Eu-30P	5	0.02	0.0030	-	-	Bal.
0.05Eu-5P	5	0.05	0.0005	-	-	Bal.
0.05Eu-20P	5	0.05	0.0020	-	-	Bal.
0.05Eu-30P	5	0.05	0.0030	-	-	Bal.

*CP Al-2.2Ti-1B grain refiner is used to add TiB$_2$.

6.2 EBSD of melt-spun microstructure

The α-Al grain size is too fine to be evaluated using OM or SEM, thus the grain size is investigated using EBSD. The grain size measured using EBSD reveals a very fine grain size of α-Al (around $\sim$5 µm), as shown in Fig. 6.2. It is also evident from the EBSD image that the standard deviation is very high (usually close to 50 %). Nevertheless, the melt-spun microstructure exhibits a very fine grain size. The addition of grain refiner to CP Al-Si based alloy produced by gravity die casting exhibits a significant decrease in grain size, as shown in Fig. 4.1, Fig. 5.1 and in the literature [104, 130, 229, 239]. The addition of Al-2.2Ti-1B grain refiner has an insignificant effect on grain size due to the high cooling rate from melt spinning. Ref and TiB$_2$ alloys exhibit a comparable grain size. This further support that the TiB$_2$ alone cannot refine Al grains [14, 107]. Solely addition of Ta (0.05Ta) results in a lower grain size compared to that of Ref alloy, which further highlights the importance of solutes to provide growth restriction effect necessary for grain refinement [65, 66]. As demonstrated in Table 2.1, the Ti is the strongest growth restrictor, however, the Ta is the second highest growth restricting element [1]. Increasing Ta additions up to hyperperitectic concentration show no influence on the grain size of α-Al despite the presence of TiB$_2$ particles, solute Ta and pre-peritectic Al$_3$Ta (Fig 6.2c-g). Since the Ta-refined alloys show an inconsistent behaviour in terms of grain refinement, the melt temperature during melt spinning is believed to be an important factor in the determination of final grain size in melt-spun samples. The melt temperature is about 800 °C, but in an uncontrolled manner due to the limitation of

the melt spinning facility.

Interestingly, the Eu-modified alloys with low P addition (0.02Eu, 0.05Eu, 0.05Eu-5P) exhibit a larger grain size (Fig. 6.2h, j and m) than those with TiB_2 addition (0.02Eu-TiB_2, 0.05Eu-TiB_2), as shown in Fig. 6.2i, k. Surprisingly, the increasing additions of P results in decreasing grain size in Eu-modified alloys (Fig. 6.2l, n, o).

Signals of Al and Si are very close to each other, hence the EBSD indexed all the particles as Al. Therefore, particles smaller than 0.9 µm were excluded from grain size measurement because particles smaller than 0.9 µm are more likely to be Si particles than Al grains. Misorientation using Kernel average misorientation (KAM) analysis of melt-spun microstructure is provided in Fig. C.3. Overall, the strain is present in all investigated samples. The strain can be produced by a high cooling rate or sample preparation for SEM.

6.3   TEM of melt-spun microstructure

0.05Eu-5P alloy was chosen to investigate the possible entrained Si droplet in melt-spun sample. BF TEM image (Fig. 6.3a) shows the boundary of α-Al and entrained eutectic Si droplet. Enlarged Fig. 6.3b from Fig. 6.3a shows one layer to be present between eutectic Si and Al matrix. It should be noted that a clear observation of entrained eutectic Si droplet grain boundary with Al matrix is very challenging due to rarely distributed impurities (such as P) and a large size.

6.4   DSC

A controlled heating and cooling of melt-spun ribbons exhibits two stages. Firstly, the solidification of eutectic Si along the grain boundary is detected and denoted as exotherm A. Secondly, the solidification of entrained eutectic Si droplets within α-Al grains is detected and denoted as exotherm B. Exotherms are shown in Fig. 6.4. The undercooling (ΔT) is defined as the difference between the onset temperature of exotherm A and the onset temperature of exotherm B. The same extraction of ΔT can be found in the literature [176, 181]. Extracted undercooling from DSC thermographs is listed in Table 6.2.

The onset temperatures of exotherms A and B in Ref alloy are 573.65 $^{\circ}$C and 531.23 $^{\circ}$C, respectively. With increasing Ta or TiB_2 additions the onset temperatures of both exotherms are shifted to higher temperatures. Surprisingly, the combined effect of TiB_2 with hypoeutectic Ta concentrations leads to a decrease of exotherm B, as shown in Fig. 6.4a. It indicates that the combined effect of TiB_2 and Ta affects the nucleation of entrained eutectic Si droplets. Note that increasing onset temperature is attributed to an easier nucleation of entrained eutectic Si droplets. The main impurity to affect the onset temperature is the P.
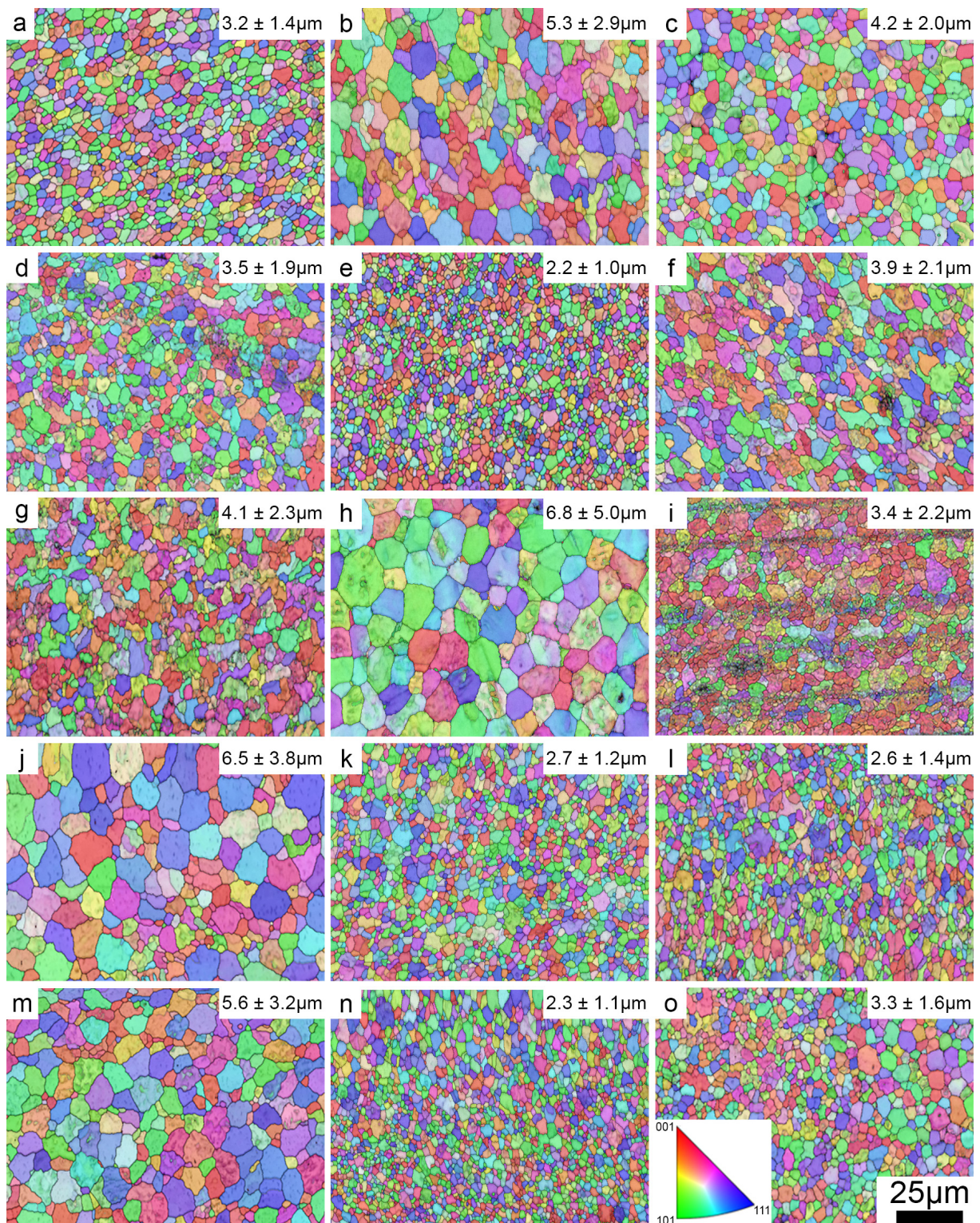
146

Figure 6.2: EBSD IPF images with measured grain size in melt-spun ribbons: (a) Ref, (b) TiB$_2$, (c) 0.05Ta, (d) 0.05-TiB$_2$, (e) 0.12Ta-TiB$_2$, (f) 0.30Ta-TiB$_2$, (g) 0.50Ta-TiB$_2$, (h) 0.02Eu, (i) 0.02Eu-TiB$_2$, (j) 0.05Eu, (k) 0.05Eu-TiB$_2$, (l) 0.02Eu-30P, (m) 0.05Eu-5P, (n) 0.05Eu-20P, and (o) 0.05Eu-30P.
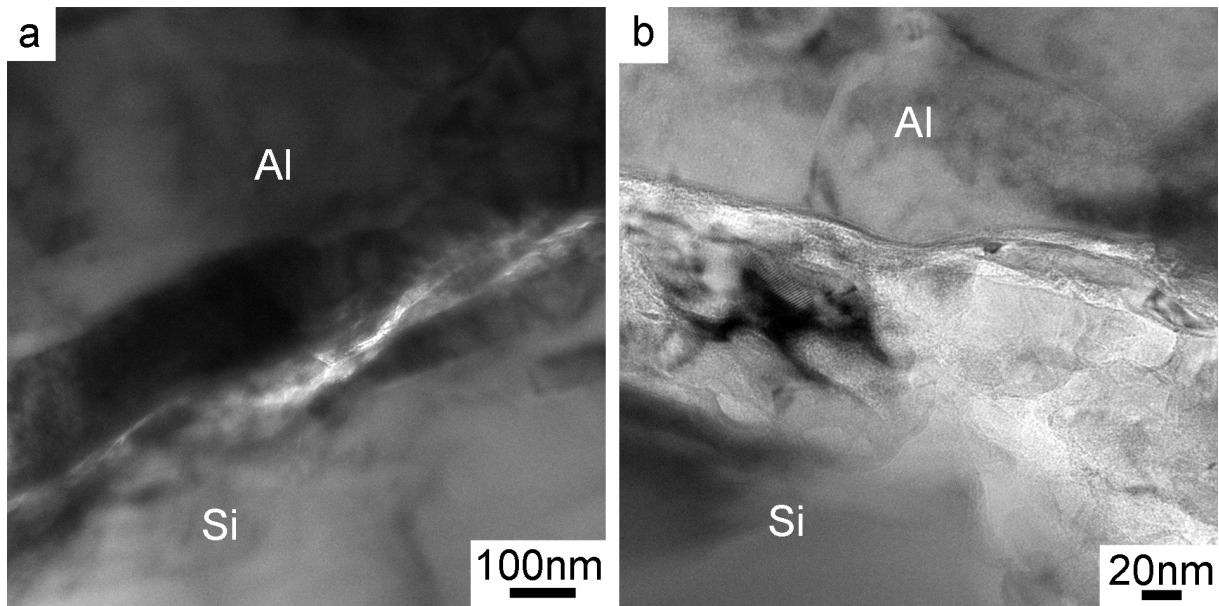
Figure 6.3: Bright field (BF) TEM images of the boundary between entrained eutectic Si droplets and Al matrix at (a) a low magnification and (b) a high magnification in alloy 0.05Eu-5P.

In our work, the base material (HP Al-5Si) was reported by Zarif [175] to contain only 0.4 ppm P.

As shown in Fig. 6.4b, peritectic and hyperperitectic concentrations of Ta combined with TiB_2 result in an increase of onset temperatures of both exotherms. A sharp onset temperature of exotherm B is observed at a peritectic concentration of Ta ($0.12Ta-TiB_2$), while the heat flow increases gradually in hyperperitectic Ta additions compared to peritectic Ta addition. The addition of Ta and TiB_2 using CP master alloys leads to an unintentional impurity addition (namely P), which facilitates the nucleation [158, 177] and therefore, decreases the measured undercooling compared to Ref alloy. None of the Ta, TiB_2 additions or their combinations increases the undercooling. This indicates that the Ta and TiB_2 have no significant effect on nucleation of eutectic Si.

The addition of TiB_2 and P into Eu-modified alloys is shown in Fig. 6.5a. Comparable onset temperatures of exotherm A are detected in 0.02Eu and Ref alloy, however, the onset temperature of exotherm B decreases $\sim$7.5 $^{\text{o}}$C in 0.02Eu alloy. A decrease in the onset temperature of exotherm A is detected with increasing Eu concentration up to 500 ppm (0.05Eu alloy). Hence, to initiate the growth of eutectic Si at the grain boundaries, a higher driving force is required. Furthermore, the onset temperature of exotherm B increases around $\sim$2 $^{\text{o}}$C in 0.05Eu alloy. This gives a strong experimental evidence that the EuP may be a potent nucleation site for eutectic. On the other hand, the lower addition of Eu results in a higher undercooling than the higher addition of Eu. Overall, the highest undercooling of
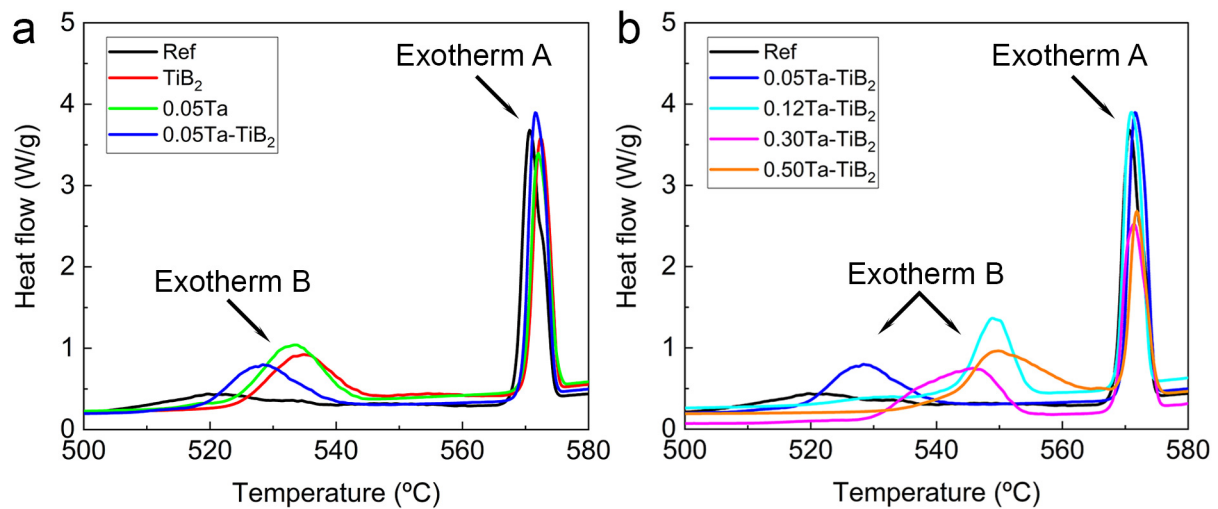
Figure 6.4: DSC cooling curves at a cooling rate of 10 ^{o}C/min of HP Al-5Si alloys with additions of (a) TiB$_2$, 0.05 wt. % Ta and their combination and (b) TiB$_2$ in combinations with hypoperitectic and hyperperitectic Ta additions.

Table 6.2: Measured undercooling of HP Al-5Si based alloys.

Alloy designation	Onset exotherm A [^{o}C]	Onset exotherm B [^{o}C]	ΔT [^{o}C]	Droplet diameter [µm]
Ref	573.65	531.23	42.42	17.81±8.5
TiB$_2$	575.09	543.32	31.77	14.41±6.1
0.05Ta	575.06	541.25	33.81	19.25±7.8
0.05Ta-TiB$_2$	574.52	536.40	38.12	27.03±12.5
0.12Ta-TiB$_2$	573.91	554.28	19.63	17.95±10.9
0.30Ta-TiB$_2$	575.22	552.97	22.25	20.41±8.6
0.50Ta-TiB$_2$	574.76	562.21	12.55	17.09±6.4
0.02Eu	573.55	523.76	49.79	16.08±6.7
0.02Eu-TiB$_2$	572.76	527.17	45.59	17.00±9.6
0.05Eu	572.24	525.93	46.31	14.99±7.4
0.05Eu-TiB$_2$	575.52	525.64	49.88	27.81±13.9
0.02Eu-30P	576.98	-	-	17.92±7.1
0.05Eu-5P	573.17	526.59	46.58	15.98±6.6
0.05Eu-20P	575.65	571.04	4.61	25.71±13.3
0.05Eu-30P	575.68	570.34	5.34	14.53±11.3
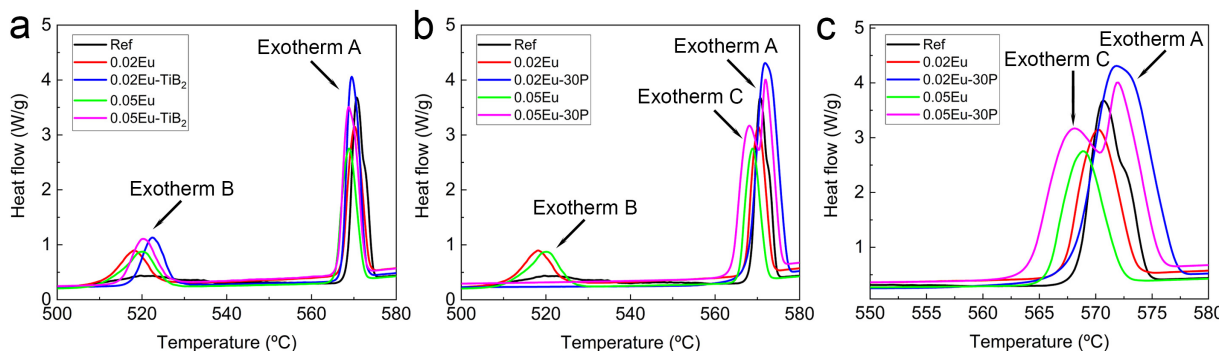
Figure 6.5: DSC cooling curves at a cooling rate of 10 $^{\circ}$C/min of HP Al-5Si alloys with additions of (a) Eu and TiB$_2$ and (b) Eu and P. (c) is an enlarged area of exotherm A from (b).

49.88 $^{\circ}$C and 49.79 $^{\circ}$C are detected in 0.05Eu-TiB$_2$ and 0.02Eu alloys, respectively.

With increasing P concentration up to 30 ppm, the onset temperature of exotherm A is shifted to higher temperatures in 0.02Eu-30P and 0.05Eu-30P alloys. 0.02Eu-30P alloys exhibit the onset temperature of exotherm A of 576.98 $^{\circ}$C, which is very close to the equilibrium eutectic temperature according to Al-Si diagram [97]. Alloys without the addition of P (0.02Eu and 0.05Eu) exhibit a lower onset temperature of exotherm A compared to alloys with a high addition of P (0.02Eu-30P and 0.05Eu-30P), as shown in Fig. 6.5c. Surprisingly, 0.02Eu-30P alloy exhibit no exotherm B, while only exotherm A is observed. Interestingly, 0.05Eu-30P alloy exhibits also no exotherm B, but right after the exotherm A, the new exotherm C is detected. This exotherm C is believed to be due to the formation of Al$_2$Si$_2$Eu phase as reported by Li [181]. The onset temperature of Al$_2$Si$_2$Eu phase was reported to be 560 $^{\circ}$C, which is significantly lower than the $\sim$567.5 $^{\circ}$C, as shown in Fig. 6.5c. The exact onset temperature can be extracted using the deconvolution of the peaks, however, in order to maintain reproducible and comparable results with the literature, only the onset temperature is used for comparison.

A lower addition of P (0.05Eu-5P and 0.05Eu-20P) is alloyed to investigate the exotherm C (Fig. 6.6). Exotherm B shows a higher onset temperature in 0.05Eu-5P than that in 0.05Eu, which clearly shows that the nucleation of eutectic Si droplets is easier with increasing P. Comparable onset temperatures of exotherm A in 0.05Eu-20P and 0.05Eu-30P alloys are observed. Even though the exotherm peak of exotherm C is shifted, the estimated onset temperature of exotherm C is not significantly changed. Exotherm C is close to exotherm A, therefore the exotherm C is attributed to the simultaneous precipitation of entrained eutectic Si droplet, as exotherm B, and precipitation of Al$_2$Si$_2$Eu. Surprisingly, there is a peak connected to exotherm A in 0.05Eu-5P alloy. This peak is denoted as exotherm D and was already observed in HP Al-Si alloy with the addition of 3 ppm P [177]. Exotherm D is believed to be only shifted from exotherm B, as reported by Li [177].
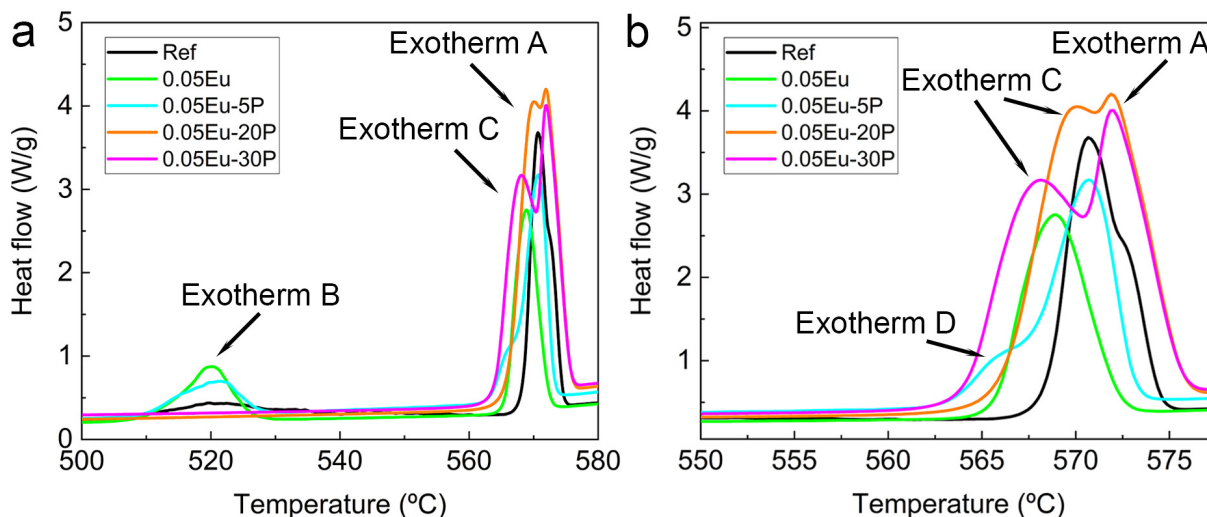
Figure 6.6: DSC cooling curves at a cooling rate of 10 °C/min of HP Al-5Si alloys with additions of (a) 0.05Eu and various P concentrations. (b) is an enlarged area of (a).

6.5 SEM (EDS) after DSC

High magnification SEM BS images of investigated alloys after DSC are shown in Fig. 6.7. Eutectic Si can be observed at the grain boundaries and within the α-Al grains, which gives a direct evidence that the entrained eutectic Si droplets are nucleated within α-Al grains. Ref alloy exhibits entrained eutectic Si droplets even though the DSC detects a very low height of exotherm B (Fig. 6.4). The entrained eutectic Si droplets are evaluated using their average diameter (Table 6.2) and size distribution (Fig. C.4). The average diameter and size distribution are measured from low magnification SEM BS images, which are shown in Fig. C.5. The diameter of entrained eutectic Si droplets is lower in TiB$_2$ alloy than in Ref alloy. Ta or Ta in combination with TiB$_2$ shows the increasing diameter of entrained eutectic Si droplets. The diameter is believed to increase with increasing additions of modifier due to a lower amount of nucleation sites. Surprisingly, the diameter size of entrained eutectic Si droplets shows a non-conclusive trend in investigated alloys alloyed with various separate and combined additions of Ta, TiB$_2$, Eu or P. It should be noted that approximately 100 droplets are investigated for the diameter measurement.

SEM BS image (Fig. 6.7f-g) shows intermetallic phases at the grain boundaries of entrained eutectic Si droplets. Fe-rich intermetallics are observed at the grain boundaries of entrained eutectic Si droplets in hypoperitectic 0.05Ta alloy (Fig. C.6). The detected Co and Fe are introduced via the addition of CP master alloy. Ta-rich particles are observed at the boundary of entrained eutectic Si droplets and also within α-Al matrix in hyperperitectic 0.50Ta-TiB$_2$, as shown in Fig. 6.7g. Presumably Al$_3$Ta phase is identified in the same alloy using EDS in Fig. C.7. The Al$_3$Ta phase is also visible in the vicinity of the plate-like Fe-rich
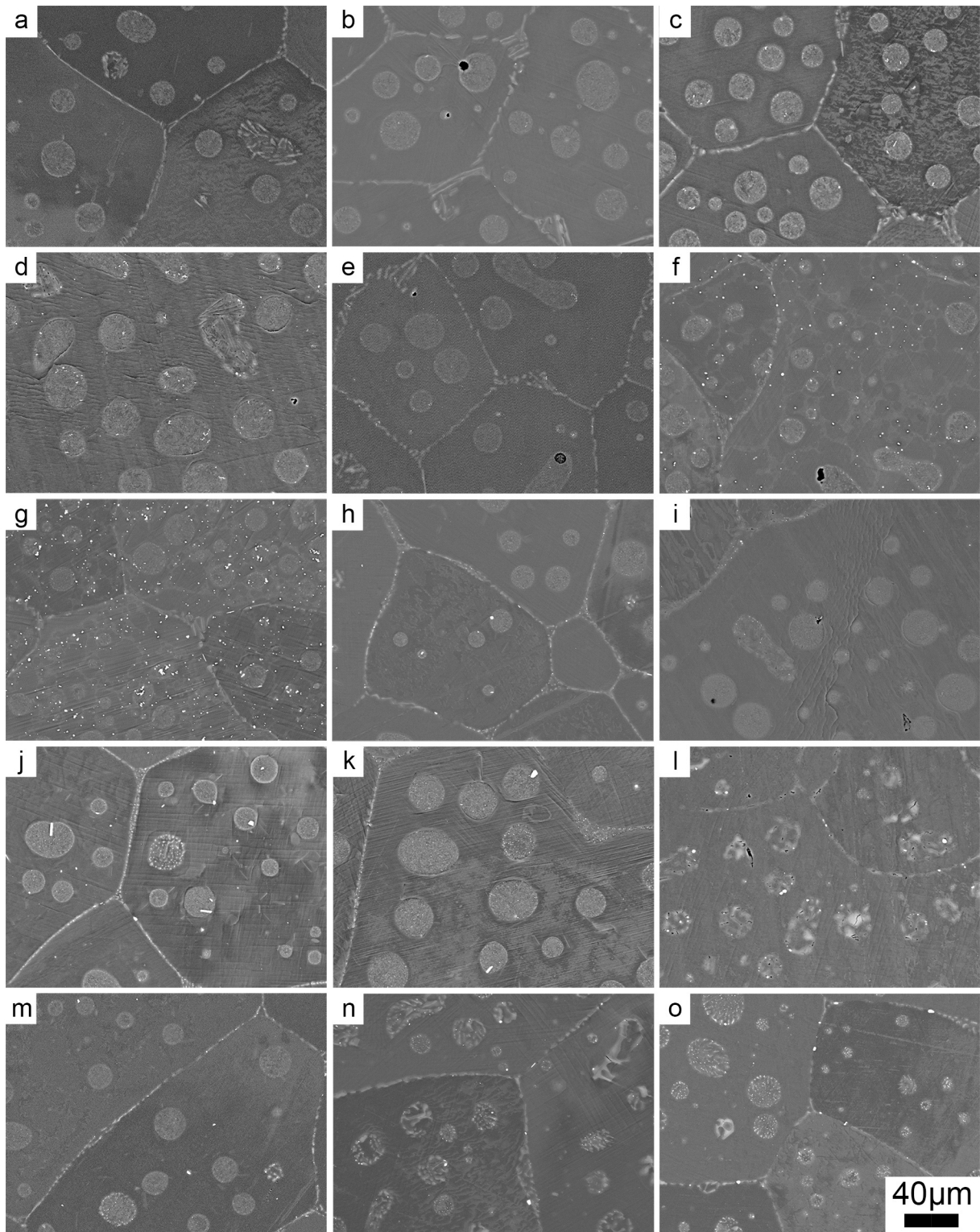
Figure 6.7: High magnification SEM BS images of entrained eutectic Si droplets after DSC: (a) Ref, (b) TiB_2, (c) 0.05Ta, (d) 0.05-TiB_2, (e) 0.12Ta-TiB_2, (f) 0.30Ta-TiB_2, (g) 0.50Ta-TiB_2, (h) 0.02Eu, (i) 0.02Eu-TiB_2, (j) 0.05Eu, (k) 0.05Eu-TiB_2, (l) 0.02Eu-30P, (m) 0.05Eu-5P, (n) 0.05Eu-20P, and (o) 0.05Eu-30P.
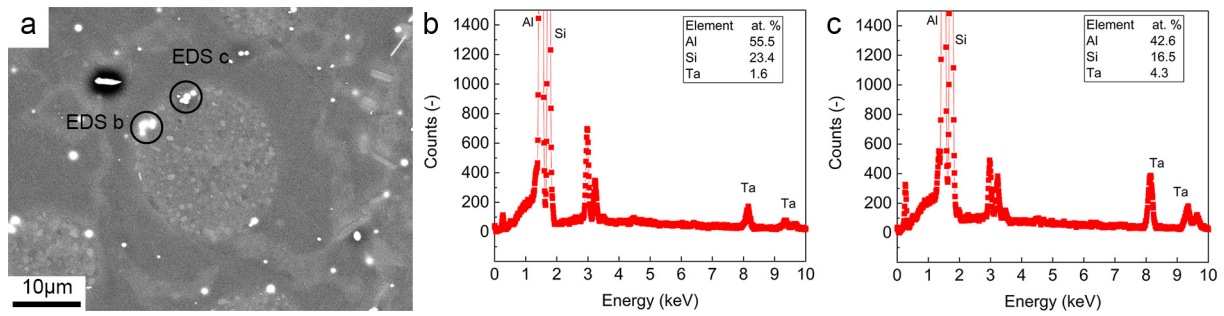
Figure 6.8: (a) SEM BS image of microstructure after DSC heating of alloy 0.50Ta-TiB$_2$. (b, c) EDS point analysis of intermetallic phase at the boundary of entrained eutectic Si droplet, taken from the areas as marked in (a).
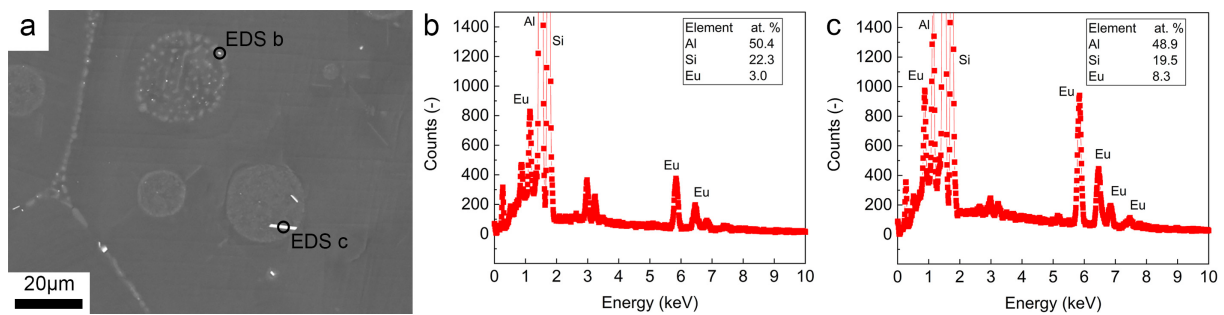
Figure 6.9: (a) SEM BS image of entrained eutectic Si droplet in 0.05Eu alloy. (b) and (c) are EDS analyses of the intermetallic phase present at the entrained eutectic Si droplet boundary and within the droplet, taken from the areas as marked in (a).

intermetallic phase. 0.50 wt. % Ta is a hyperperitectic concentration, therefore the Al$_3$Ta phase is formed in liquid prior to α-Al.

Bright intermetallic phases are observed within the entrained eutectic Si droplets in Eu-modified alloys, as shown in Fig. 6.7h, j and k. In 0.05Eu alloy, the EDS analysis identify those phases to be Al$_2$Si$_2$Eu phase (Fig. 6.9). Two morphologies of Al$_2$Si$_2$Eu are observed within the entrained eutectic Si droplets: the plate-like (EDS b) and the round-like (EDS c) particles. Different morphologies indicate different nucleation stages of the Al$_2$Si$_2$Eu phase. The amount of bright Al$_2$Si$_2$Eu phase is reduced with increasing addition of P or TiB$_2$ particles. Significantly coarser entrained eutectic Si droplets compared to Ref alloy are observed in Fig. 6.7l, n. It seems that modifier (Eu) is consumed with increasing P additions, hence the entrained eutectic Si droplets grow coarser.

EDS maps of the intermetallic particle at the grain boundaries in 0.02Eu-30P alloys show a P-rich phase completely surrounded by Al$_2$Si$_2$Eu phase (Fig. 6.10). The P-rich phase in the centre is believed to be AlP due to a strong Al signal. The shape of AlP as well as Al$_2$Si$_2$Eu is round, therefore, the formation of Al$_2$Si$_2$Eu is believed to occur in the pre-eutectic state or in the liquid state. Even larger Al$_2$Si$_2$Eu are found along the grain boundaries, as shown
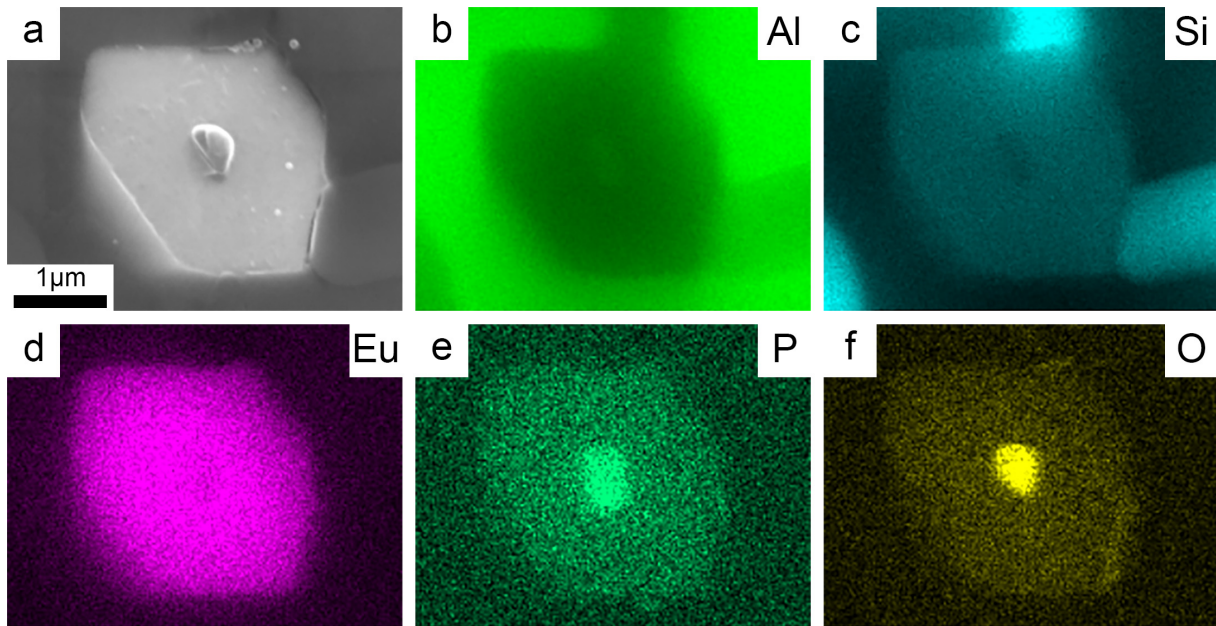
153

Figure 6.10: (a) SEM BS image and (b-f) EDS maps of intermetallic phase in 0.02Eu-30P alloy along grain boundaries: (b) Al, (c) Si, (d) Eu, (e) P, (f) O.

in Fig. 6.11. Due to the size of the phase, it is assumed that the particles are formed in the pre-eutectic state or in the liquid state and then pushed to grain boundaries as the growth of α-Al progresses.

Interestingly, the Al$_2$Si$_2$Eu phase is seen within the entrained eutectic Si droplet in 0.05Eu-30P alloy with high P additions (Fig. 6.12). The Al$_2$Si$_2$Eu phase is detected within the eutectic droplets, which is in contrast to Fig. 6.9, where the Al$_2$Si$_2$Eu phase is observed in the form of plates or small round particles mostly along the boundaries of eutectic droplets. The amount of ternary Al$_2$Si$_2$Eu increases with increasing P addition. Nevertheless, the round shape of Al$_2$Si$_2$Eu phase and DSC exotherm C (Fig. 6.6b) indicates that the ternary phase is formed during the solidification of entrained Si droplet from supersaturated solid solution.

6.6 EBSD after DSC

EBSD of microstructure after DSC heating is studied with a special focus on entrained eutectic Si droplets and grain boundaries (Fig. 6.13). Ref alloy exhibits fine randomly oriented eutectic Si within the droplets. The addition of Ta and/or TiB$_2$ shows a comparable microstructure after heating as Ref alloy, indicating that neither Ta nor TiB$_2$ affect the nucleation of entrained eutectic Si droplets. The addition of Eu (0.02Eu alloy) shows a similar microstructure as Ref alloy, although, the DSC shows a higher undercooling and a larger height of exotherm B (Fig. 6.5). Nevertheless, the addition of P from CP Al-2.2Ti-1B master
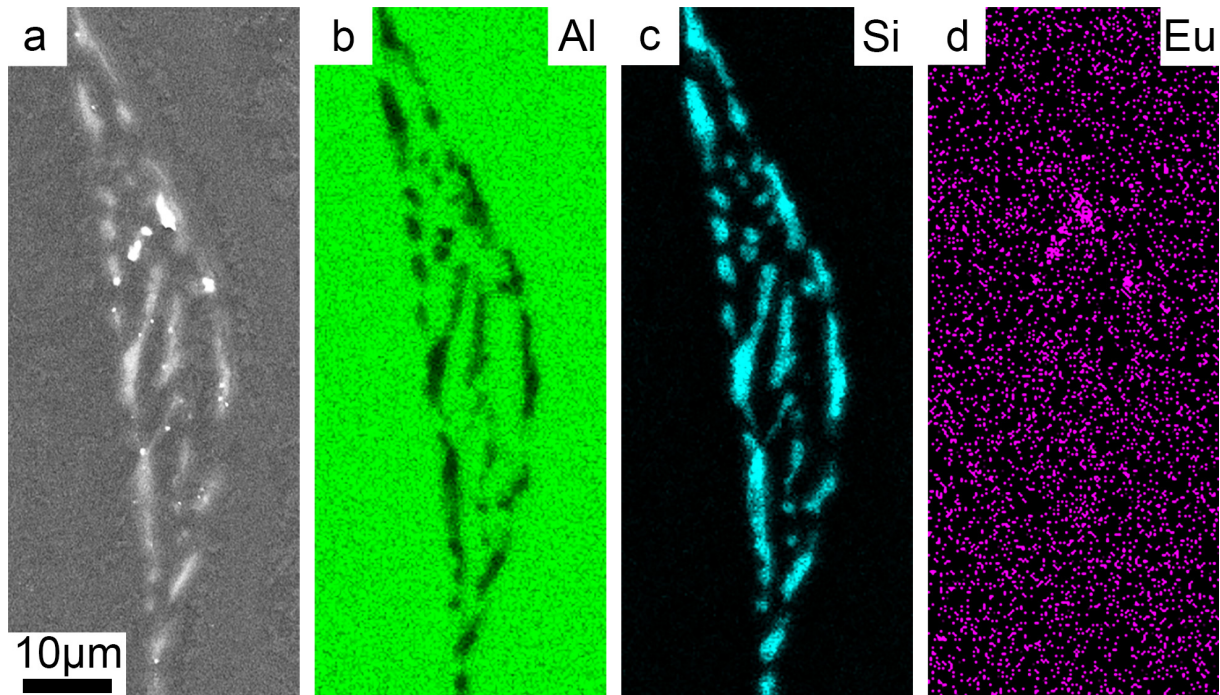
Figure 6.11: (a) SEM BS image and (b-d) EDS maps of grain boundary containing intermetallic phase in 0.05Eu-5P alloy: (b) Al, (c) Si, (d) Eu.
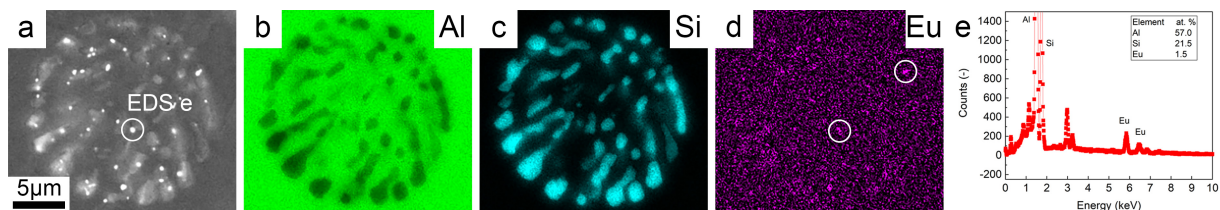

Figure 6.12: (a) SEM BS image and (b-d) EDS maps of entrained eutectic Si droplet in 0.05Eu-30P alloy: (b) Al, (c) Si, (d) Eu. (e) is EDS point analysis of the intermetallic phase taken from the areas as marked in (a).

alloy exhibits a coarsening of entrained eutectic Si droplets with less randomly oriented Si particles within the droplets. The coarsening is clearly observed in 0.02Eu-30P alloy, where the large Si particles are interconnected and single oriented (Fig. 6.13l). Therefore, it is evident that increasing P provides more AlP, which then facilities the nucleation and growth of entrained eutectic Si droplets and the droplets grow in a very coarse single oriented Si plate. KAM analysis after DSC heating is shown in Fig. C.8. Similar to KAM of melt-spun microstructure (Fig. C.3), the strain distribution is uniform, while the main strain centre is found within the eutectic Si droplets. However, strains within the microstructure are formed during sample preparation of thin ribbon for EBSD.

Fig. 6.14 shows the EBSD of entrained eutectic Si droplets. Ref alloy shows a very fine and randomly oriented eutectic Si within entrained eutectic Si droplets. The same result is
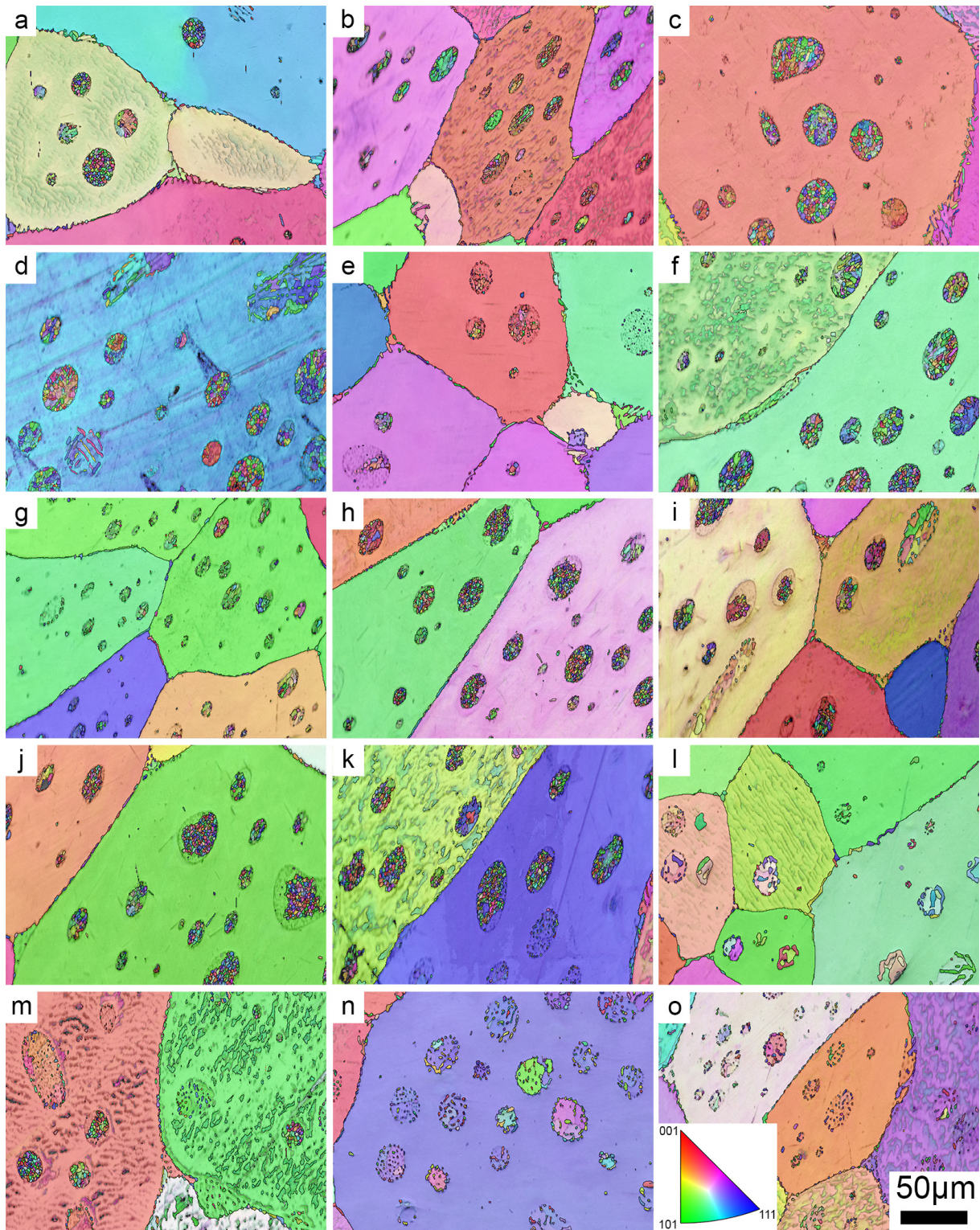
155

Figure 6.13: EBSD IPF images of entrained eutectic Si droplets after DSC: (a) Ref, (b) TiB$_2$, (c) 0.05Ta, (d) 0.05-TiB$_2$, (e) 0.12Ta-TiB$_2$, (f) 0.30Ta-TiB$_2$, (g) 0.50Ta-TiB$_2$, (h) 0.02Eu, (i) 0.02Eu-TiB$_2$, (j) 0.05Eu, (k) 0.05Eu-TiB$_2$, (l) 0.02Eu-30P, (m) 0.05Eu-5P, (n) 0.05Eu-20P, and (o) 0.05Eu-30P.
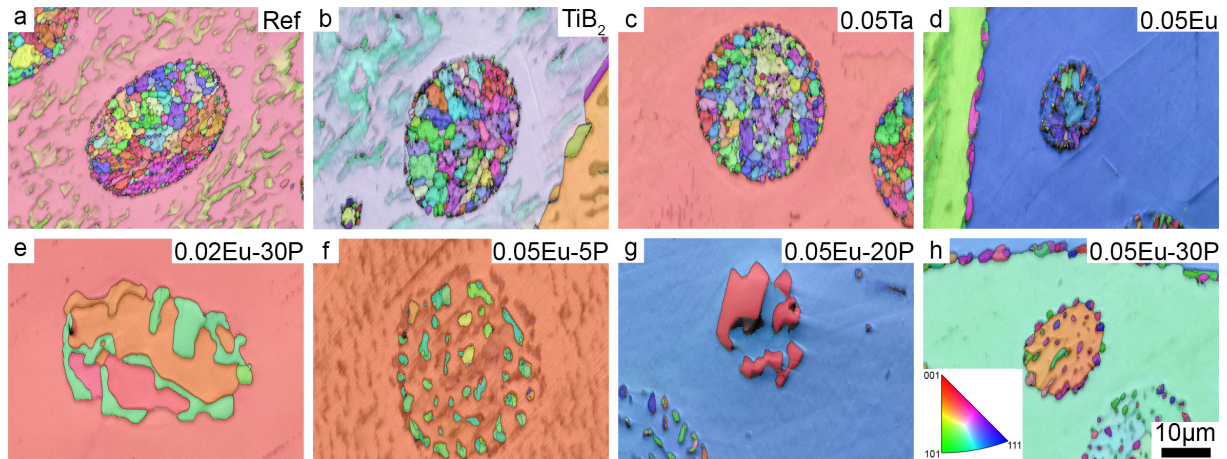
Figure 6.14: EBSD IPF images of entrained eutectic Si droplets in alloys: (a) Ref, (b) TiB_2, (c) 0.05Ta, (d) 0.05Eu, (e) 0.02Eu-30P, (f) 0.05Eu-5P, (g) 0.05Eu-20P and (h) 0.05Eu-30P.

observed in TiB_2, 0.05Ta and 0.02Eu alloys. On the other hand, as shown in Fig. 6.14e-h, with increasing P, the entrained eutectic Si droplets become coarser. Single oriented and interconnected coarse eutectic Si droplet is observed in 0.05Eu-20P alloy. P-rich alloys exhibit enhanced the nucleation and growth of eutectic Si. The eutectic Si prefers to grow in a rapid propagation direction, which exhibits a fast growth. The 0.05Eu-5P alloy shows a transition structure, where the orientation of eutectic Si particles within the droplet is more uniform compared to Ref alloy, however, the size of eutectic Si particles and the interparticle spacing increase significantly. Interestingly, the transition structure (Fig. 6.14f) contains a lower amount of eutectic phase compared to P-free alloys. The additions of 5 ppm and 30 ppm P cause a coarsening of entrained eutectic Si droplets, even though a sufficient amount of modifier is provided (500 ppm Eu). Surprisingly, different orientations of eutectic Al within one entrained eutectic Si droplet in 0.05Eu-30P alloys is observed in Fig. 6.14h, where the entrained eutectic Si droplets are not completely covered by randomly oriented eutectic Si. Note that the single droplet does not represent the whole microstructure.

6.7   TEM after DSC

BF TEM image (Fig. 6.15a) shows the boundary of Al and eutectic Si. An enlarged image (Fig. 6.15b) from Fig. 6.15a shows one layer to be present between eutectic Si and α-Al matrix, which is similar to BF TEM image of 0.05Eu-5P in melt-spun condition (Fig. 6.3). Unfortunately, entrained eutectic Si droplets become larger in size after DSC, therefore it is very challenging to observe the entrained eutectic Si droplet within the TEM sample produced by dimpling and PIPS. AlP is reported [177] to form a continuous layer around the eutectic Si droplets at a high P concentration, while the AlP patches are responsible for the nucleation of eutectic Si droplets at a low P concentration. A detailed investigation in
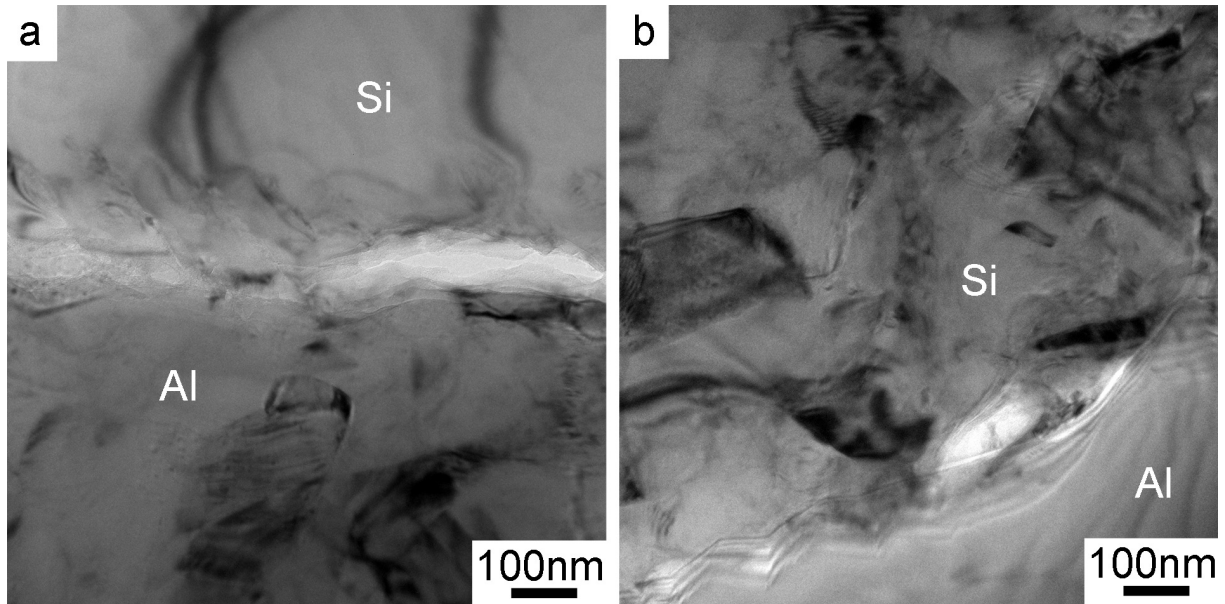
Figure 6.15: BF TEM images of the boundary between entrained eutectic Si droplet grain and α-Al matrix in alloy 0.05Eu-30P after DSC.

P distribution within the eutectic Si droplets and at its boundaries is still needed.

6.8 Discussion

6.8.1 Effect of Ta

Metallic glass experiments [17, 115] showed Al$_3$Ti exhibits a very close lattice parameter with Al$_3$Ta. Recently [229], ab initio calculation showed a nearly identical interface energy of Al$_3$Ti and Al$_3$Ta at the TiB$_2$ interface. The gravity die casting experiments of Al-7Si-Mg based alloys in the same study showed that grain refinement of α-Al using Ta is more effective than using Ti. In the present study, the cooling rate during melt spinning is too high to elaborate on the effect of Ta on grain refinement. The measured grain size using EBSD in Fig. 6.2 shows that the grain size varies with the various additions of Ta in combination with TiB$_2$. These results indicate that the grain refiner is less efficient with a high cooling rate. However, the melt temperature is believed to be the main reason for discrepancies in grain size.

Hypoperitectic concentration of Ta shows an increase in the onset temperature of exotherm B and a decrease in ΔT (Table. 6.2), which is due to the unintentional addition of impurities via the CP master alloy. Hyperperitectic concentrations of Ta also decrease in ΔT. Overall, Ta addition shows a slight increase in the onset temperature of exotherm A compared to the Ref alloy. At hyperperitectic concentrations of Ta, the Ta-rich particles, identified as Al$_3$Ta using EDS (Fig. 6.8), are found at the boundaries and within the entrained eutectic

droplet. Droplets investigated using EBSD (Fig. 6.14) show no significant difference in morphology or density of randomly oriented eutectic Si particles within the droplet. Based on the microscopy and DSC results, the Ta and TiB_2 have no significant effect on nucleation kinetics and morphology of entrained eutectic Si droplets.

Fe-rich intermetallic particles are found at the boundaries of eutectic droplets in 0.05Ta alloy (Fig. C.6). Significantly larger Fe-rich particles are found 0.50Ta-TiB_2 (Fig. C.7). It was reported by Li [177] that the addition of 25 ppm Fe increases the undercooling, however, further addition up to 2000 ppm Fe exhibits no change in the nucleation of eutectic Si. Cho [154] investigated 1100 ppm Fe in Al-10Si alloy via quenching experiment and found that eutectic grains are finer presumably due to pre-eutectic β-AlFeSi. Rapid solidification conditions produced by melt spinning and the reduced amount of impurities due to high purity material result in a significantly smaller β-AlFeSi intermetallic phase than that observed by Cho [154].

6.8.2 Effect of Eu and P

The onset temperatures of exotherm A in 0.02Eu and 0.05Eu alloys are 573.55 °C and 572.24 °C, respectively (Table 6.2). Therefore, the onset temperature of eutectic Si along the grain boundaries decreases with increasing Eu due to the consumption of AlP and the formation of EuP. In terms of exotherm B, the onset temperatures of entrained eutectic Si droplets in 0.02Eu and 0.05Eu alloy are detected at 523.76 °C and 525.93 °C, respectively. Also, the undercooling in 0.02Eu (49.79 °C) is higher than that in 0.05Eu (46.31 °C), which decreases with increasing Eu. Since the EuP is assumed to be a good nucleation site for eutectic Si due to its low lattice mismatch with Si and cube-to-cube orientation [25], these results confirm that the EuP nucleates the entrained eutectic Si droplets. The onset temperature of exotherm A increases, while the onset temperature of exotherm B decreases with increasing Eu. Displacement of exotherms A and B is detected with the addition of TiB_2 in Eu-modified alloy. The reason for this behaviour of TiB_2 particles is the unintentional addition of impurities via the addition of CP master alloy.

As shown in Fig. 6.5b, the addition of 30 ppm P in 0.02Eu and 0.05Eu alloys show no exotherm B, which indicates that the entrained eutectic Si nucleates at a negligible undercooling with increasing P. The same results were reported by Ludwig [94]. Interestingly, the 0.05Eu-30P alloy exhibits the exotherm C, as seen in Fig. 6.5c. Previously, the peak close to the exotherm C was reported to be Al_2Si_2Sr [177, 242], Al_2Si_2Ca [94] or Al_2Si_2Eu [181]. However, the reported peaks in previous reports were detected after the solidification of exotherm A. In the present alloy system, exotherm C is shifted to higher temperatures within exotherm A. This result indicates a complex interaction among AlP, EuP and Al_2Si_2Eu within the exotherm C. Note that in the previous studies [94, 165, 177, 181, 242],

the DSC was not performed in alloys with a high concentration of P.

SEM reveals bright intermetallic phases within the α-Al matrix and entrained eutectic Si droplets in 0.05Eu alloy (Fig. 6.7j). EDS measurement in Fig. 6.9 identified those particles to be Al_2Si_2Eu phase with two different morphologies. EDS B shows the round-like particle, which is assumed to be formed from supersaturated solution (SSSS) produced by rapid solidification during melt spinning and is assumed to be formed simultaneously with the solidification of entrained eutectic Si droplets, as shown in Fig. 6.6. On the other hand, EDS C shows plate-like particles, which are assumed to be formed in the liquid. Very fine Al_2Si_2Eu particles are observed within entrained eutectic Si droplets in 0.05Eu-30P in Fig. 6.12. Similar to round-like particles, the Al_2Si_2Eu is presumably formed from Al, Si and Eu from SSSS. Al_2Si_2Eu found at the grain boundaries is believed to form on the AlP phase due to a stronger Al signal in the centre of the Al_2Si_2Eu phase in 0.02Eu-30P (Fig. 6.10). The particle in the centre is assumed to be partly transformed to EuP, which then nucleates the Al_2Si_2Eu [25].

Coarse and single-oriented plates of eutectic Si are detected using EBSD in 0.02Eu-30P alloy (Fig. 6.13l). Coarse platelets of eutectic Si within the entrained eutectic droplets were observed on the etched surface by Ludwig [94]. Ludwig also proposed that the entrained eutectic Si droplet contains a low number of non-faceted Si crystals and a fewer number of coarse faceted Si crystals. The transition from non-faceted to faceted crystals is shown in Fig. 6.14. The addition of TiB_2, Ta and Eu shows that the large number of randomly oriented eutectic Si are formed within entrained eutectic Si droplet (Figs 6.14a-d). Significant coarsening of entrained eutectic Si droplets is observed with increasing P in Eu-modified alloys. The transition between fine multi-oriented to single oriented entrained eutectic Si droplets is shown in Figs 6.14f and h, where coarser eutectic Si particles with more uniform orientations are detected. The interparticle spacing increases significantly in P-rich alloys compared to Ref alloy. One interconnected and single oriented eutectic Si particle is observed in Fig. 6.14e and g. Keeping in mind that a single entrained eutectic Si droplet does not represent the whole microstructure. For example, a transition of eutectic Si structure is observed next to the investigated coarse eutectic Si particle in Fig. 6.14g.

The Jackson factor (α_J) is used to distinguish between the non-faceted ($\alpha_J < 2$) and faceted ($\alpha_J > 2$) morphology [84, 85]. The α_J is described in the equation 2.45. The calculation of α_J is shown in Table C.1. Without consideration of $\frac{CN_S}{CN_I}$, the α_J for Al and Si are ~1.38 and 3.58, respectively. This means that Al grows in a non-faceted manner and Si grows in a faceted manner. In terms of diamond Si structure, the Si{111} and Si{100} surfaces contain 2 and 3 nearest-neighbour sites, respectively. Hence Si{111} surface exhibit α_J of 2.68, therefore the faceted growth can be expected. While Si{100} surface exhibits α_J of 1.79. This indicates that the eutectic Si within the entrained droplets can grow non-

faceted. It was reported by Kurz [38] that the atomic interface can become rough at a high undercooling. Nevertheless, it is unlikely that Si grows in non-faceted growth preference in TPRE mechanism and high ΔS_F. The slow growth rate is usually accompanied by a large entropy of fusion [85]. Without the addition of P, the fine multi-oriented eutectic Si particles within entrained eutectic Si droplets exhibit a high ΔT, while more uniformly oriented eutectic Si particles within entrained eutectic Si droplets require a low ΔT in P-rich alloys. The multi-oriented eutectic Si particles are assumed to be formed due to a lack of nucleation sites (AlP) and a slower growth rate compared to the large single oriented Si crystal. However, no atomic scale data are provided to verify this assumption yet, the sample preparation using FIB is required due to the large size of entrained eutectic Si droplet.

Sand casting of investigated alloys

The aim of this section is to compare two alloy systems in sand casting experiments with different cooling rates from die-casting. The main focus is on the modification effect and porosity distribution in the sand casting part (Fig. 3.24).

7.1 Cooling curve comparison with ingot

Fig. 7.1a, c shows that the region of α-Al exhibits a very small constitutional undercooling ΔT. Interestingly, T_{min} and T_G in 200Eu alloy are suppressed at about 1 ºC compared to Sr-modified alloy. It should be noted that grain refiners added to 0.01Ti and 200Eu alloys are Al-5Ti1-B and Al-3Ti-1B, respectively. The amount of added grain refiner is the same and therefore the amount of TiB$_2$ particles is assumed to be the same. The eutectic region (Fig. 7.1b, d) of Sr-modified alloy shows ΔT of 6.1 ºC, while Eu modified alloy shows ΔT of 3.1 ºC. The nucleation temperature of eutectic Si (T_N) is observed to be about 5 ºC higher in Eu-modified alloy. Overall all the characteristic solidification temperatures are higher in Eu-modified alloys. These results indicate a facilitated nucleation and growth compared to Sr-modified alloys. Therefore, the eutectic grain size is assumed to be smaller in Eu-modified alloys.

7.2 Porosity distribution

It is evident from Fig. 7.2 that Sr (a, b) as well as Eu (d, e) show mostly modified eutectic structure in the sand casting part. It can be concluded that Sr as well as Eu are strong modifiers (like Na) and therefore are convenient for solidification technologies with low cooling rates (such as sand casting). However, MIA (section 3.4.2) from the middle of the sample clearly shows that Sr-modified (Fig. 7.2c) exhibits significantly larger porosity compared to Eu-modified alloy (Fig. 7.2f). Porosity distribution is more evident from Fig. 7.3, where
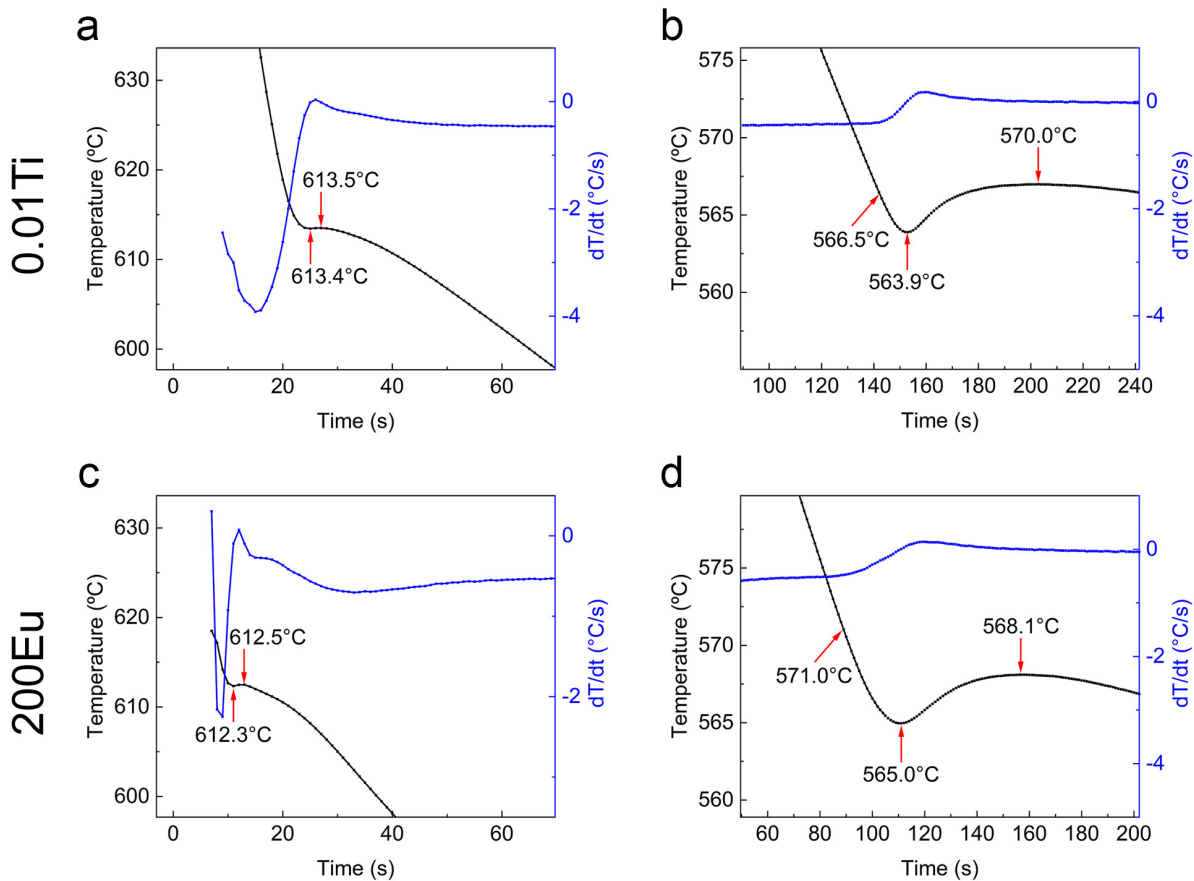
Figure 7.1: Comparison of cooling curves of two alloys; (a, b) 0.01Ti modified with 0.02 wt. % Sr and (c, d) 200Eu modified with 0.02 wt. % Eu.

the porosity is uniformly distributed in Sr-modified alloy. However, in Eu-modified alloy the porosity is mostly located at the centre of the sand casting sample (white spots at the centre are capillary residuals of OPS). The amount of porosity cannot be quantitatively defined by the naked eye, however, this result provides a useful insight into the feeding of Eu-modified Al-Si based alloys compared to conventionally Sr-modified alloys.

7.3 Shape factor of eutectic Si

Shape factor analysis of as-cast Sr and Eu-modified alloys shows its value below 0.3 (Fig. 7.4). It is generally accepted that solidification rates have an effect on the morphology of eutectic Si via so-called quench modification. However, in green sand casting the cooling rate is generally lower than in die casting. Therefore, a low shape factor is obtained due to the low cooling rate of sand mould, rather than inappropriate modification treatment.
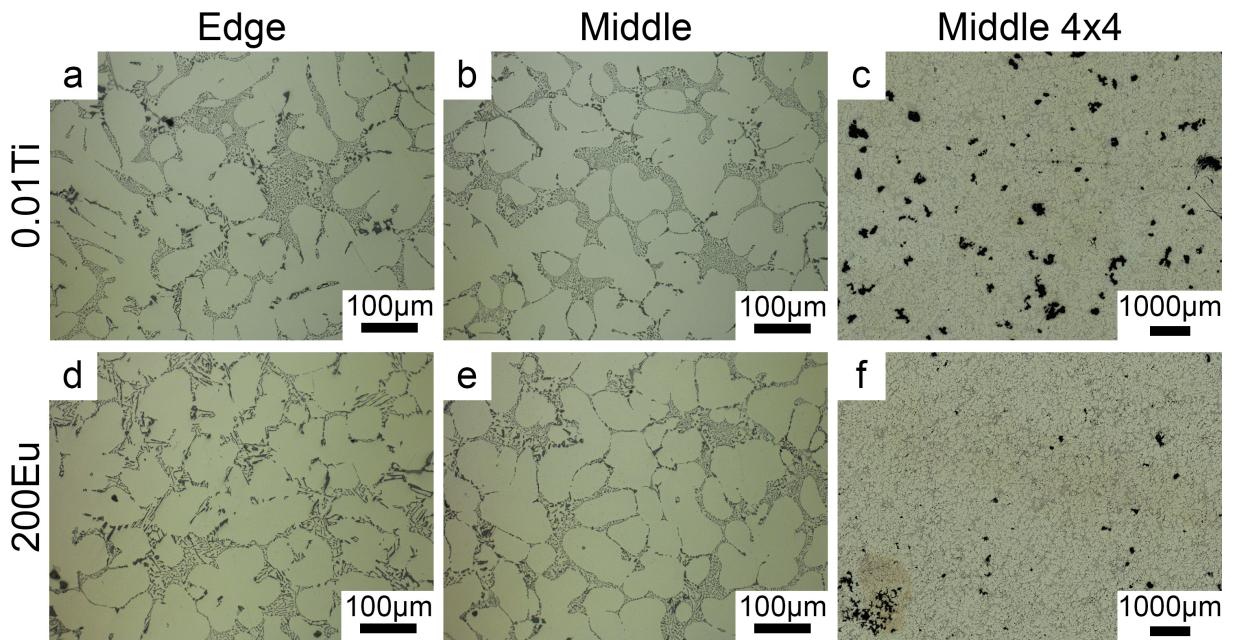
Figure 7.2: Comparison of modification effect and porosity in (a-c) 0.01Ti (Sr-modified) and (d-f) 200Eu (Eu-modified) alloys produced by sand casting.
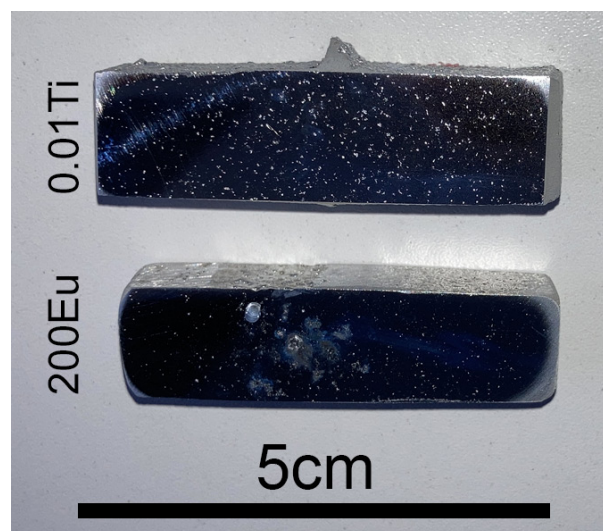

Figure 7.3: Macroporosity in 0.01Ti and 200Eu modified alloys. Samples are produced by sand casting using green sand mould.
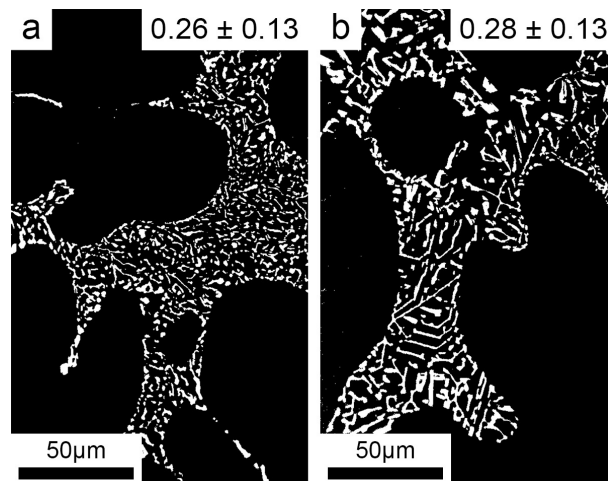
Figure 7.4: Shape factor of (a) 0.01Ti and (b) 200Eu alloys produced by green sand casting. Si particles smaller than 10 µm^2 were excluded from analysis.

Discussion

In this chapter, obtained results of this work are discussed in five different topics.

8.1   Grain refinement using solute Ta and TiB$_2$ particles

The conventional grain refinement of Al-Si-Mg based alloys is achieved via the addition of Al-5Ti-1B grain refiner, which contains TiB$_2$, Al$_3$Ti and free Ti. Ti is reported to have the highest growth restriction effect. TiB$_2$ particles alone are reported not to be efficient in grain refinement of pure Al. A combination of TiB$_2$ and free Ti results in the formation of 2DC Al$_3$Ti at the interface of TiB$_2$, which promotes the grain refining effect. However, the addition of free Ti into Al-Si based alloys results in a so-called Si-poisoning, where the grain size of α-Al increases with increasing Si content in the presence of free Ti.

In the chapter 4, the solute Ta in combination with stoichiometric Al-2.2Ti-1B grain refiner is introduced to Al-7Si-0.3Mg alloys (Table 4.1) in order to investigate the effectiveness of solute Ta as a grain refiner. Solute Ta is believed to form 2DC Al$_3$Ta on the TiB$_2$, however, Al$_3$Ta is believed not to interact with Si.

Thermal analysis (Table 4.2) clearly shows a low ΔT in Ti-refined and Ta-refined alloys, which is an indication of an easy nucleation of α-Al grains. Microstructure analysis using OM (Fig. 4.1) shows the grain size of $\sim$220 µm in 0.01Ti and 0.07Ta alloys. However, the grain size is further decreased up to $\sim$140 µm with increasing solute Ta (0.12Ta alloy). These results confirm that the Ta can be used as grain refiner and therefore, can replace the Ti in Al-7Si-0.3Mg alloys. SEM EDS maps of Fig. 4.7 and Fig. 4.8 show Ta-rich layer on the interface of TiB$_2$ particle. The Ta-rich layer is presumably identified as Al$_3$Ta layer, which is believed to promote grain refinement. However, Fig. 4.8 shows overlap of Ta and Si signal. The Ta-Si layer indicates the Si-poisoning in the presence of Ta. On the other hand, the increasing solute Ta up to 0.12 wt. % shows a decrease, in α-Al grain size, which indicates that Ta-Si layer has no negative effect on grain refinement. EDS analysis (Fig. 4.8i)

of Ta-Si layer detects the layer to be mainly Si and Al-rich, while only ∼5 at. % of Ta is detected. HAADF-STEM image (Fig. 4.11) shows the Ta-rich layer at the interface of TiB_2 particle. As shown in Fig. 4.11h, the EDS line scan across the interface identified the layer as $(Ta, Ti)B_2$ with Ta monolayer on top of this complex particle. The interface is modelled using interface energy calculation of $TiB_2(0001)$ with aluminides (Fig. 4.18). The interface energy calculation clearly showed the energetic preference of TiB_2 particle ending with Ti plane (Ti-terminated). Ti and Ta in the form of Al_3Ti and Al_3Ta layer are calculated to be energetically comparable, which shows the possible replacement of Ti by Ta. However, the aluminides in the interface are not supposed to change or interact with the particle, which is in contrast with the HAADF-STEM image (Fig. 4.11), where the chemically complex interface is detected.

DSC analysis of Ta-refined as-cast samples shows the onset temperature of α-Al peak comparable for Ti-refined alloys (Table 4.4). The onset temperature of α-Al peak increases with increasing Ta up to 615.41 ºC. DSC analysis of Ta-refined and Eu-modified as-cast samples (Table 5.4) shows the onset temperature of α-Al peak at ∼613 ºC. Only with further addition of P in Eu-modified alloys, the onset temperature of α-Al peak increases to ∼615 ºC.

In terms of conventional alloy grain refined with Al-Ti-B grain refiner and Sr as a modifier, the grain refinement and modification are well-known to have no mutual effect [16, 104]. The same result is obtained for Ta-refined and Sr or Eu-modified alloys. In terms of grain size, no interaction of Ta with Sr or Eu is detected in the microstructure. The microstructure is improved with increasing solute Ta. In Eu-modified alloys, the thermal analysis (Table 5.2) and α-Al grain size (Fig. 5.1) show comparable results with Sr-modified alloys. However, as-cast DSC thermographs of 0.01Ti alloy show the Peak 3a at the peak temperature of 551.75 ºC (Fig. 4.13b), which is identified as the precipitation of Ti-rich intermetallic phase. Unfortunately, no Ti-rich intermetallic phase is observed within the microstructure. The nucleation of eutectic Si investigated using entrained droplet technique, showed no significant effect of TiB_2 and/or hypoperitectic or hyperperitectic Ta additions.

Based on microstructure and ab initio investigations, the Ta is concluded to be a suitable element to avoid Si-poisoning and the grain refining effect is even increased with increasing Ta content. Also, Ta does not interact with solutes present in the liquid (Sr and Eu), which enables more solutes to contribute to growth restriction. No intermetallic phases are formed in the presence of Ta, therefore the solutes are contributing to growth restriction.

8.2   Sr and Eu-modified eutectic Si

Al-Si-Mg alloys are modified using Na or Sr. The goal of modification is to modify the morphology of eutectic Si from plate-like to fine fibrous morphology, which is accompanied

by an increase in mechanical properties, mainly elongation. Although the addition of Sr is reported to be the source of porosity in the casting parts, the benefit of morphological change of eutectic Si overrides the negative effect of porosity.

Thermal analysis of Ref alloy shows ΔT_{eu} of 0.5 $^{\circ}$C (Table 4.2), while with the addition of 0.02 wt. % Sr, the ΔT_{eu} increases to ~3.4 $^{\circ}$C in Ta-refined alloys (0.07Ta and 0.12Ta). Sr-modified and Ti-refined alloy (0.01Ti) shows the highest ΔT_{eu} of 6.1 $^{\circ}$C. This indicates that the Sr modification is stronger in Ti-refined alloys, however, the measured chemical composition (Table 4.1) reveals that the 0.01Ti alloy contains 225 ppm Sr, while Ta-refined alloys contain ~190 ppm Sr. This discrepancy in the addition of modifier is believed to result of such a large difference in ΔT_{eu}. On the other hand, thermal analysis of Eu-modified alloys shows ΔT_{eu} of 3.9 $^{\circ}$C and 1.2 $^{\circ}$C in 200Eu and 500Eu alloys, respectively (Table 5.2). ΔT_{eu} decreases with increasing Eu. Microstructure analysis of as-cast microstructure using SF reveals that both Sr (Table 4.3) and Eu-modified (Table 5.3) alloys have higher SF values compared to Ref alloy. Also, the SF value increases with implementing the heat treatment. 0.12Ta alloy shows the highest SF value, while the same addition of Eu as Sr (0.02 wt. %) shows a comparable SF of 0.73. 500Eu alloy shows the highest SF value of 0.87 in Eu-modified alloys. In contrast to ΔT_{eu}, the SF shows nearly equal SF values for the equal addition of different chemical modifiers and the SF further increases with increasing Eu additions.

DSC of as-cast Sr (Table 4.4) and Eu-modified (Table 5.4) samples exhibits comparable peak temperatures of eutectic peak (Peak 2 in Figs. 4.13 and 5.10) within the difference level of ~1 $^{\circ}$C. The highest peak temperature is measured in 200Eu alloy. More interestingly, both DSC cooling thermographs of as-cast samples exhibit the Peak 3, which is identified as the precipitation of Al_2Si_2Sr and Al_2Si_2Eu in Sr and Eu-modified alloys, respectively. In Sr-modified alloys, the Al_2Si_2Sr is formed at ~548.2 $^{\circ}$C, while the Al_2Si_2Eu in Eu-modified alloys is formed at ~550.6 $^{\circ}$C, which is about 2 $^{\circ}$C higher. The peak temperature of Al_2Si_2Eu (560.2 $^{\circ}$C) was reported [181] even higher in HP Al-Si alloy modified with Eu. Although this difference is not significant, the author believes that the earlier precipitation of Al_2Si_2Eu in Eu-modified alloys is due to its low lattice mismatch of Al_2Si_2Eu with EuP phase (Table 5.8). The lattice mismatch of Al_2Si_2Eu with EuP and Al_2Si_2Sr with Sr_3P_2 is 0.17 % and 4.91 %, respectively.

Both Al_2Si_2Sr and Al_2Si_2Eu intermetallic phases are observed in SEM images (Fig. 4.6 and Fig. 5.7). Interestingly, both of these intermetallic phases are containing P, O and Mg-rich centre of the particle. The O was reported by Cho [154] to be present due to the oxidation of P during sample preparation. Based on the lattice mismatch calculation (Table 5.8) the Mg_2O and MgO phases are ruled out in terms of any type of nucleation in the alloy system in the present work. The Mg_2P phase is found with a very low lattice mismatch with Sr_3P_2 of

only 0.06 %. Similarly, the Mg_3P_2 phase has a very low lattice mismatch with EuP of 1.83 %. Mg_3P_2 phase was experimentally observed in the centre of Al_2Si_2Sr by Lee [135], however, it was assumed that Mg_3P_2 is only the partial transformation of AlP phase, which is reported [154] to be responsible for the nucleation of Al_2Si_2Sr intermetallic phase. However, the energy above hull and the predicted formation energies indicate that Mg_3P_2 is more stable than the Mg_2P phase. EDS in the centre of the Al_2Si_2Eu phase (Fig. 5.7h) detects 19 at. % of Mg, 13 at. % of Eu and 9 at. % of P. Due to the close atomic ratio of Eu and Mg the lattice mismatch of hexagonal and cubic $EuMg_2$ phases is calculated and it reveals that none of the $EuMg_2$ phases exhibits a low lattice mismatch. Therefore, the $EuMg_2$ is not believed to be responsible for the nucleation of any Eu-rich intermetallic and Mg is expected to bond with P. Based on the microstructure observation, the lattice mismatch calculation and reported literature results, the new possible nucleation sequences are proposed: $Sr_3P_2 \rightarrow Mg_2P \rightarrow Al_2Si_2Sr$ and $Mg_3P_2 \rightarrow EuP \rightarrow Al_2Si_2Eu$ in Sr and Eu-modified alloys, respectively. The sequences are not strict due to the fact that Al_2Si_2Sr and EuP phases are reported without the presence of Mg. However, the enhancing effect of Mg on the nucleation cannot be ruled out and is indeed in the present work.

The Al_2Si_2Eu phase is found in various sizes and morphologies after DSC heating in HP Al-5Si alloys produced by melt-spinning. Fig. 6.9 shows 0.05Eu alloys containing round-like and plate-like intermetallic phases, presumably identified as Al_2Si_2Eu using EDS. Round-like Al_2Si_2Eu phase is believed to be formed from SSSS produced by melt spinning. Al_2Si_2Eu phase is also believed to be formed on EuP, due to the large amount of round-like Al_2Si_2Eu phase within the entrained eutectic Si droplet of 0.05Eu-30P alloy (Fig. 6.12). Plate-like morphology of the Al_2Si_2Eu phase is believed to be formed from a single nucleation site also from SSSS, however, assuming the growth of droplets from the outer shell to inner, all the solutes are incorporated in the growth of the Al_2Si_2Eu phase. Due to a lack of nucleation sites (EuP), the solutes of Al, Si and Eu are attached to a growing Al_2Si_2Eu in the lowest energy configuration, possibly the plate morphology. Note that the density of eutectic Si particles within the droplets is changed. Round-like Al_2Si_2Eu is found in coarser entrained eutectic Si droplets, while plate-like Al_2Si_2Eu is found in very fine entrained eutectic Si droplets. These results give a strong argument that P affects the size and density of eutectic Si particles and the amount and morphology of the Al_2Si_2Eu phase within the entrained eutectic Sidroplet.

8.3   Eutectic grain size in Sr and Eu-modified alloys

Eutectic Si is nucleated on AlP, however, the addition of the modifier results in a lower amount of AlP. Therefore, the nucleation requires a larger undercooling to be initiated. AlP is depleted and Sr_3P_2 and EuP phases are formed in Sr and Eu-modified alloys. Sr_3P_2 is not

believed to be a good nucleation site for eutectic Si, however, EuP is expected to be a good nucleation site based on the crystallography and predicted formation energies (Table 5.8).

Thermal analysis of Sr-modified alloys (Table 4.2) shows that with addition of 200 ppm Sr (0.01Ti, 0.07Ta and 0.12Ta alloys), the nucleation undercooling of eutectic Si ($T_{eq} - T_{N,eu}$) decreases on in about 10 ^{o}C average, while with addition of 200 ppm Eu (200Eu alloy), the $T_{eq} - T_{N,eu}$ is only 5.6 ^{o}C (Table 5.2). The $T_{N,eu}$ in Ref alloy is the highest (576.2 ^{o}C), which is due to the presence of a large amount of AlP phase. Sr-modified alloys show the average $T_{N,eu}$ of ~566.9 ^{o}C. Interestingly, Eu-modified 200Eu alloy shows the $T_{N,eu}$ of 571.4 ^{o}C, which is more than 4 ^{o}C higher compared to Sr-modified alloys. This clearly supports the hypothesis that EuP can nucleate eutectic Si grains, when a lower $T_{eq} - T_{N,eu}$ and a higher $T_{N,eu}$ are detected with the presence of Eu. Although the ΔT_{eu} of 200Eu alloy is comparable with 0.07Ta and 0.12Ta alloy, a large difference in nucleation area is detected. Further addition of Eu up to 500 ppm (500Eu alloy) shows comparable $T_{N,eu}$ and $T_{eq} - T_{N,eu}$ with 200Eu alloy. The addition of 40 ppm P to 200Eu alloy results in an increase of $T_{N,eu}$, while $T_{eq} - T_{N,eu}$ is not extracted from TA cooling curve, due to a larger $T_{N,eu}$ (579.9 ^{o}C) than T_{eq} (577 ^{o}C). Such a large $T_{N,eu}$ due to a high P addition indicates that the nucleation of eutectic Si is initiated before the T_{eq}. According to thermodynamic calculation by Liang [150] the AlP is precipitated before α-Al and eutectic Si, when the P concentration is higher than ~15 ppm in Al-7Si alloy. Although, the calculation was performed assuming impurity-free alloy, the presence of AlP before the eutectic reaction is seen in 200Eu40P alloy and not seen in Ref alloy or Sr and Eu-modified alloys with lower P additions. A simultaneous increase of Eu and P (up to 500 ppm Eu and 40 ppm P) results in a comparable $T_{N,eu}$, $T_{eq} - T_{N,eu}$ and ΔT_{eu} with Eu-modified alloys with low P. SEM images of Eu-modified alloys after deep etching (Fig. 5.5) clearly show that 200 ppm Eu with 40 ppm P is insufficient to obtain a fully modified structure while increasing Eu up to 500 ppm can compensate the high P addition. Therefore with the presence of P, the more Eu is required to compensate the poisoning effect of P on modification.

Eutectic grain size of Sr-modified alloys (Fig. 4.3) after MMR etching shows low eutectic grain size in Ref alloy of ~600 µm. However, a significant increase in eutectic grain size is detected in 0.01Ti and 0.07Ta alloys after the addition of 200 ppm Sr (~2000 µm). Interestingly, eutectic grain size of ~1500 µm is measured in 0.12Ta alloy, which indicates that Ta can refine the eutectic grains. No SEM investigation revealed a Ta-rich phase, which could have been used to verify lattice mismatch calculation. However, HP experiments using entrained droplet technique are performed in the present work. Undercooling (Table 6.2) shows a decrease in the presence of Ta, but it is caused due to unintentional addition of impurity (e.g., P) from commercial purity Al-Ta master alloy. Ta is therefore not believed to refine eutectic grains in Al-Si alloys. Eutectic grain size of 200Eu alloy (Fig. 5.2) shows a slightly lower eutectic grain size than 0.01Ti and 0.07Ta alloys in Sr-modified alloys. Increasing the

addition of Eu results in an increase in eutectic grain size. Introducing the 40 ppm P in 200Eu alloy exhibits an unmodified eutectic Si morphology, which is related to a significant decrease in eutectic grain size close to 1000 µm. On the other hand, a high P amount compensated with a high Eu addition (500 ppm) results in a modified eutectic structure (Fig. 5.6) compared with 200Eu40P alloy and the eutectic grain size increases up to ∼1500 µm. Even though the eutectic grain size of Eu-modified ranges between 1500 and 1800 µm, it is still lower than in Sr-modified alloys. Therefore, eutectic grain refinement using a combined addition of Eu and P is achieved, while the modification effect is maintained.

DSC curves of Sr (Fig. 4.13) and Eu-modified (Fig. 5.10) alloys exhibit comparable eutectic peak temperatures (Peak 2). However, increasing the addition of P up to 40 ppm in Eu-modified alloys increases the eutectic peak temperature similar to that of Ref alloy. This indicates that the P increases the nucleation temperature. Although, the 500Eu40P alloy exhibits the behaviour of unmodified alloy according to DSC data, the microstructure investigations revealed that Eu is a suitable element to combine with P to achieve a fully modified eutectic structure, while simultaneously refining eutectic grain size. The exact ratio of Eu and P for optimum microstructure and therefore mechanical properties still remains to be explored.

The decrease of ΔT_{eu} with increasing Eu addition is measured using thermal analysis (Table 5.2) and DSC of entrained eutectic Si droplets (Table 6.2). These results support the hypothesis that EuP is not as effective as AlP, therefore the ΔT_{eu} is lower in Eu-modified alloys, but it is not small as in Ref alloy. Sr [175, 176] and Eu shift the nucleation of entrained eutectic Si droplets to a high ΔT_{eu}. A very low ΔT_{eu} is measured with increasing P additions up to 30 ppm in HP Eu-modified alloys produced by melt spinning. With increasing P, the exotherm B is displaced to a lower ΔT_{eu} due to an easier nucleation of entrained eutectic Si droplets (Fig. 6.6). Displacement of exotherm B to exotherm A results in very coarse eutectic Si particles within the entrained eutectic Si droplet that exhibit a large size and, subjectively, interparticle spacing. Ludwig [94] observed coarse eutectic Si particles within the entrained eutectic Si droplets on the etched surface, however, no orientation data were provided. EBSD of entrained eutectic Si droplets with various solutes additions is done here (Fig. 6.14). Alloys without P (Ref, TiB$_2$, 0.05Ta, 0.05Eu) show very fine and randomly oriented eutectic Si particles. On the other hand, coarse interconnected Si particles with a much uniform distribution are observed with increasing P. The transition from fine multi oriented to coarse single oriented eutectic particles is for the first time reported here using EBSD.

8.4 Mechanical properties

The mechanical properties such as hardness, tensile properties and fracture toughness are mainly influenced by the size, morphology and number density of β-type precipitates and eutectic Si. Modification is applied to improve the morphology of eutectic Si from large platelets to fine fibrous particles [141] and therefore, improve strength and elongation [23, 99, 105].

The strengthening of Al-Si-Mg alloys is given by the number, size, size distribution, and volume fraction of β-type precipitates. In the present work, hardness is investigated only in Ta-refined and Sr-modified alloys (Table 4.1). The hardness curve (Fig. 4.14) shows that hardness slightly increases with increasing Ta content up to 0.12 wt. %. However, the peak hardness in Ref, 0.01Ti and 0.07Ta alloys is achieved after 3 h of ageing at 180 °C, while 0.12Ta alloy shows the peak hardness after 4 h of ageing at 180 °C. The lowest hardness is measured in 0.01Ti alloy. After reaching the peak hardness, the hardness decreases with increasing ageing time. Fig. 4.16 shows the rod shape β'' precipitate with a size of 5 nm in length and 1 nm in width. The number density of β'' precipitate increases with increasing ageing time up to 4 h (Fig. 4.15), therefore the peak hardness is obtained (Fig. 4.14). DFT thermodynamic stability calculation (Fig. 4.21a) shows that both Ta and Ti are preferred to remain in SSSS. Ti and Ta-doped interface of Al(001)$\|\beta''(010)$ (Fig. 4.19) shows lower interface energies with the presence of Ta. The minimum energy required for the reaction is termed as activation energy (E_a), thus the lower the minimum energy with the presence of solutes, the higher catalytic effect of solute. E_a of Sr-modified alloys (Table 4.6) shows no significant differences among β-type precipitates. Ti increases the E_a, which indicates that Ti increases the amount of required driving force. E_a of Eu-modified alloys (Table 5.6) shows comparable activation energies of β'' and β' precipitates with Sr-modified alloys. However, E_a of β precipitate changes significantly with the addition of Eu. Sr-modified alloys exhibit E_a of 135-162 kJ/mol, while Eu-modified alloys exhibit E_a of 59-70 kJ/mol for β precipitate. Therefore, modification using Eu is beneficial for applications at elevated temperatures, where the full precipitation into stable β precipitate is required.

Tensile properties of investigated alloys in T6 condition are shown in Fig. 8.1. The results of tensile testing are summarised in Table 8.1. It is evident that no significant improvement is achieved in tensile and yield strength. Surprisingly, a significant decrease in tensile and yield is measured in 0.12Ta. Although, the grain size (Fig. 4.1), shape factor (Fig. 4.4) and eutectic grain size (Fig. 4.3) show an improvement in microstructure, the strength is not significantly increased. On the other hand, the highest elongation is measured in 0.01Ti alloy, which is modified with 200 ppm Sr, while 200Eu alloy, which is modified with an equal concentration of Eu as Sr, shows a lower elongation. Further addition of Eu and/or P results in a decrease in elongation. The possible explanation of the phenomena may be
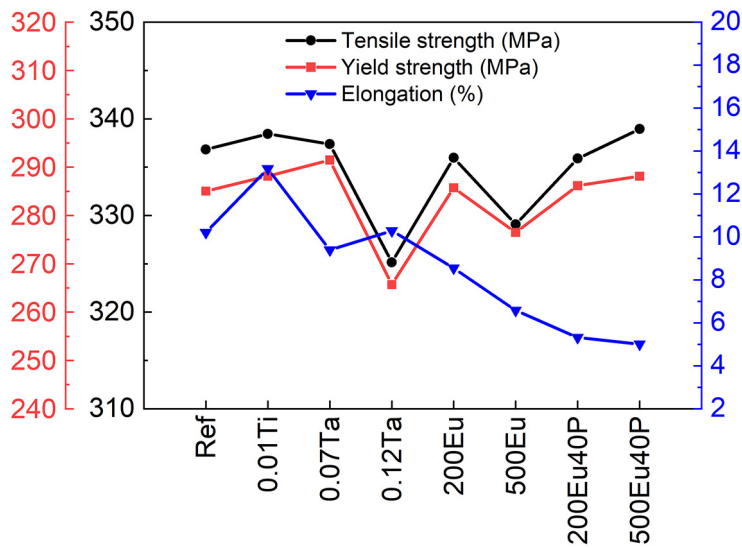
Figure 8.1: Tensile properties of investigated alloys. Measurement is performed in T6 condition.

due to the increased nucleation potency of Al_2Si_2Eu phase on EuP with increasing Eu and P additions, as supported by lattice mismatch calculation (Table 5.8) and SEM of entrained eutectic droplets (Fig. 6.12). Porosity distribution in sand casting experiment of 0.01Ti and 200Eu alloy is shown in Fig. 7.3. It is clear that with the addition of Sr, the porosity is uniformly distributed throughout the sand casting sample. On the other hand, the addition of Eu shows a large porosity in the centre and a low porosity at the edges of the sample. The porosity distribution is crucial for mechanical properties, therefore, using computed tomography (CT) is required for further assessment. However, the uniformly distributed porosity of 0.01Ti alloy modified with Sr shows significantly improved mechanical properties compared to 200Eu alloy modified with Eu. The porosity with the addition of Eu needs to be compensated using a different feeding system from Sr-modified alloys. Even though the cooling rate is higher in die casting samples produced using Diez mould, the differences in porosity formation and distribution are believed to be the main source of discrepancies in mechanical properties testing. The SF of investigated alloys is comparable (Fig. 7.4), therefore, both Sr and Eu show well modification effects even at low cooling rates.

The tensile properties of Eu-modified alloys are not performed in T4 condition, while Sr-modified 0.12Ta alloy (Fig. 4.22a) shows the highest elongation of ∼24 %. Very high elongation is attributed to the lowest grain size (Fig. 4.1a) and the lowest eutectic grain size (Fig. 4.3) in as-cast microstructure.

The fracture toughness assessment is performed in 0.01Ti (Table 4.1) and 200Eu (Table 5.1) alloys. The measured parameters of both alloys are summarised in Table 8.2. The comparison of the obtained K_Q values can be used to interpret the fracture resistance since

Table 8.1: Summary of tensile properties of investigated alloys in T6 condition.

Alloy designation	$R_{p0.2}$ [MPa]	R_m [MPa]	A_5 [%]
Ref	336.8	285.1	10.2
0.01Ti	338.4	288.0	13.2
0.07Ta	337.4	291.5	9.4
0.12Ta	325.2	265.7	10.3
200Eu	336.0	285.8	8.6
500Eu	329.1	276.5	6.6
200Eu40P	335.9	286.2	5.4
500Eu40P	338.9	288.1	5.0

Table 8.2: Summary of important parameters and measures extracted from the experiments.

Alloy designation	B [mm]	a_{final} [mm]	$(W - a_{\text{final}})$ [mm]	$P_{\max}/P_Q$ [-]	K_Q [MPa·m$^{1/2}$]	$K_{\max}$ [MPa·m$^{1/2}$]	$2.5 \cdot (K_Q/\sigma_y)^2$ [MPa·m$^{1/2}$]
0.01Ti_01	8.9	9.73	8.27	1.04	21.5	22.3	10.1
0.01Ti_02	8.9	9.43	8.57	1.07	21.3	22.7	9.9
0.01Ti_03	8.9	9.87	8.13	1.02	22.7	23.2	11.2
200Eu_01	8.9	9.60	8.40	1.01	23.7	23.9	12.5
200Eu_02	8.9	6.92	8.38	1.00	23.2	23.2	11.9
200Eu_03	8.9	10.09	7.91	1.07	22.9	24.5	11.6

the sample dimensions are identical. Evaluation of the single and the average values shows that 200Eu alloy does show a significant improvement in fracture toughness in terms of K_Q. The average value of K_Q increases from 21.8±0.7 MPa·m$^{1/2}$ in 0.01Ti alloy to 23.3±0.4 MPa·m$^{1/2}$ in 200Eu alloy. The fracture surface of investigated alloys does not show any significant differences. Dimples observed in SEM (Fig. 8.3) are typical for ductile fracture of the material. The fracture behaviour of the investigated alloys is very similar. The fracture is characterised as a microductile fracture, where the voids are initiated at second phase particles (Fig. 8.3e and f). After initiation, the formed voids subsequently join (coalescence) the main crack. Fracture surfaces exhibit a non-decisive difference, therefore the reason why Eu increases the fracture toughness still remains to be explored. The interparticle spacing between second particles (eutectic Si) or the distance to the crack tip may play a role in fracture toughness.
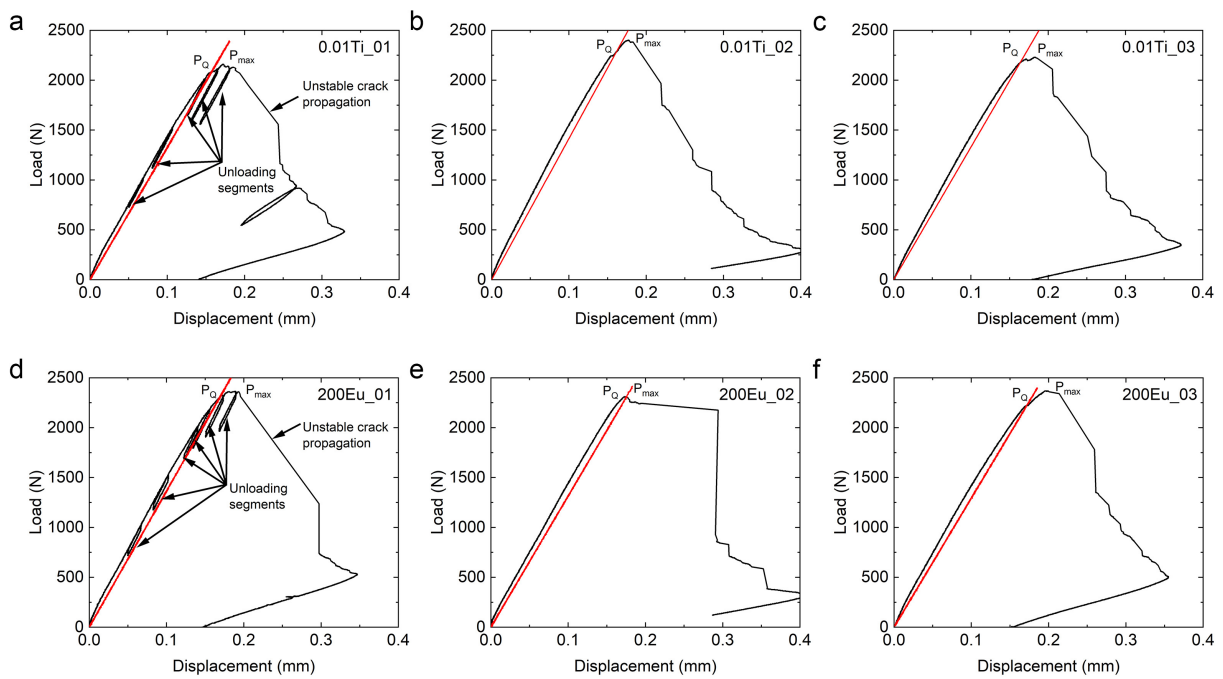
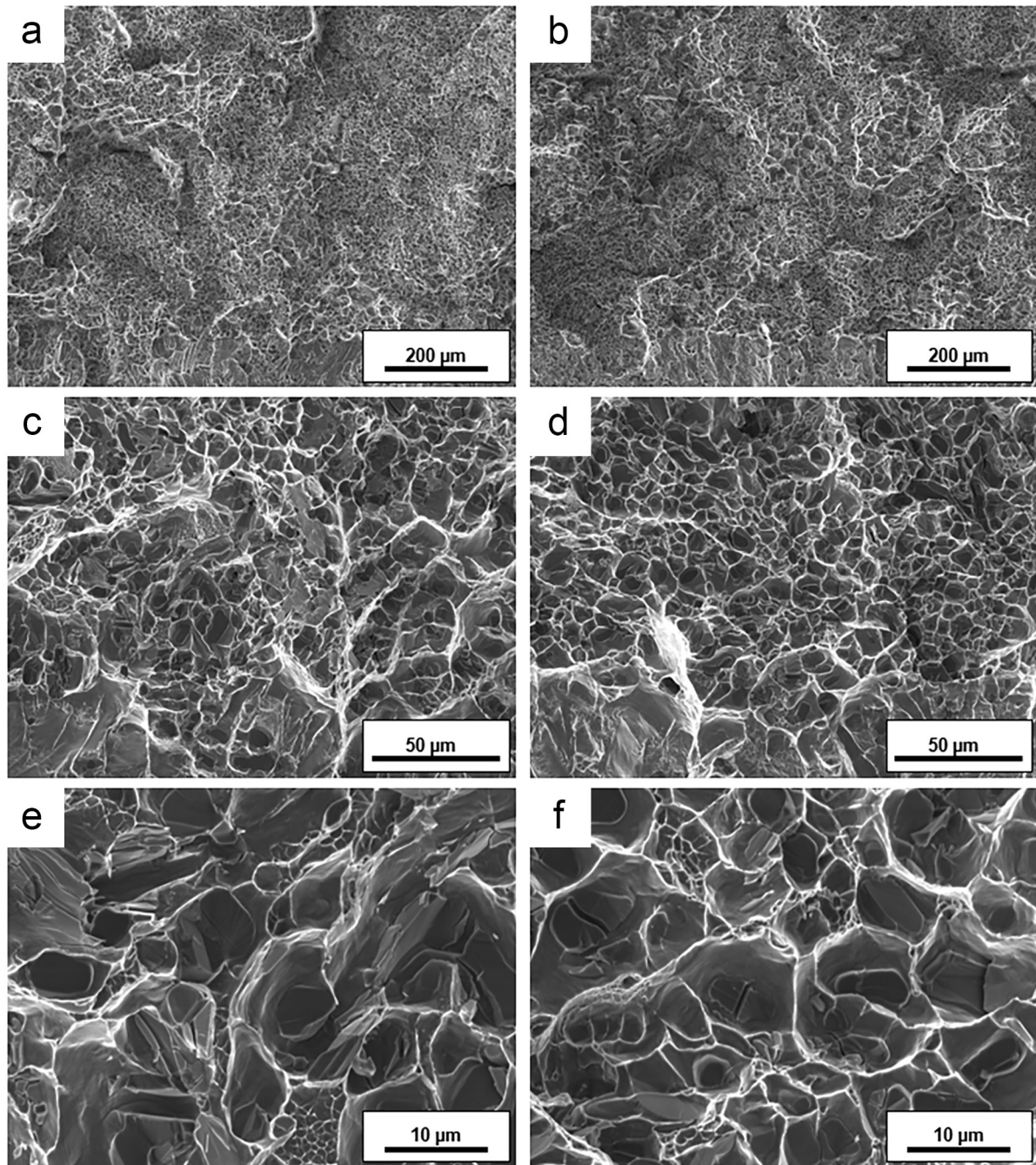Figure 8.2: Records of the test samples of alloys (a-c) 0.01Ti and (d-f) 200Eu.

Figure 8.3: SEM fracture surface of (a,c,e) 0.01Ti alloy and (b,d,f) 200Eu alloy taken at different magnifications.

CHAPTER $\mathbf{9}$

Conclusions

The effect of solute Ti, Ta, Sr, Eu and P on the grain refinement of α-Al grains, modification of eutectic Si and refinement of eutectic grains is investigated using multi-scale characterisation techniques, DSC, DFT, entrained droplet technique, mechanical properties testing and casting experiments. Main conclusions can be drawn as follows.

9.1 Grain refinement

- Solute Ta in combination with Al-2.2Ti-1B grain refiner exhibits a lower α-Al grain size than conventional Al-5Ti-1B grain refiner.

- The addition of Ta shifts the nucleation to higher temperatures, therefore, the Ta in combination with TiB_2 enhances the nucleation while exhibiting a negligible under-cooling.

- DSC showed the peak of Ti-rich intermetallic after the solidification of eutectic Si, however, this peak is not detected in Ta-refined alloys. No Ta-rich intermetallic phases are observed in the microstructure.

- SEM and TEM reveal a Ta-rich layer at the interface of TiB_2 particle, which is believed to enhance grain refinement.

- Interface energy calculation proved that Ti-terminated TiB_2 particle is more favourable than B-terminated. Further, Al_3Ta at the interface of TiB_2 shows the same interface energy as the Al_3Ti layer. Close to identical values are calculated for the sandwich structure of $TiB_2||(Al_3Ta$ or $Al_3Ti)||Al$.

- No increase in grain size via Si-poisoning is observed using Ta. No interaction with Sr or Eu and/or P is observed. Ta is proved theoretically (DFT) and experimentally to overcome Si poisoning.

9.2 Modification of eutectic Si

- Sr and Eu change the morphology of eutectic Si from large platelets to fine fibrous Si particles.

- Shape factor increases with increasing addition of Eu. The highest shape factor is measured with the addition of 500 ppm Eu. Addition of 40 ppm P in combination with 200 ppm Eu shows an unmodified eutectic structure, while increasing 500 ppm Eu and 40 ppm P results in a modified structure. P addition needs to be compensated with an increased addition of modifier.

- The formation of Al_2Si_2Sr and Al_2Si_2Eu is found in Sr and Eu-modified alloys using SEM. Entrained droplet technique shows a higher amount of Al_2Si_2Eu phase with the presence of high P additions.

- DSC showed that the peak temperature of Al_2Si_2Eu is a few degrees higher than that of the Al_2Si_2Sr phase, which confirms that EuP is the nucleation site for the Al_2Si_2Eu phase.

- The new nucleation sequence in Eu-modified alloys is proposed: $EuP \rightarrow Mg_3P_2 \rightarrow Al_2Si_2Eu$.

- DFT calculation revealed a slight energetical preference for the TPRE mechanism. Eu solute is preferably located along the TB of eutectic Si.

- A simultaneous grain refinement and modification effect can be obtained with the addition of solute Ta and Eu. No interaction of Ta and Eu is found.

9.3 Eutectic grain size

- The eutectic grain size increases with increasing Eu addition. On the other hand, P reduces the eutectic grain size due to the presence of the AlP phase. The addition of P to Eu-modified alloy shows a refinement of eutectic grains, while the modified structure of eutectic Si is maintained.

- Increasing Ta from 0.07 wt. % to 0.12 wt. % shows a decrease in eutectic grain size, while maintaining a modified structure. No Ta-rich intermetallics are found in the microstructure. Entrained droplet technique proved that neither Ta nor TiB_2 has an effect on the nucleation of eutectic Si.

- The entrained eutectic Si droplets are coarser with increasing P. The transition from a high number of randomly oriented fine fibrous Si to a fewer number of single oriented

coarser faceted plate Si is observed with high P additions. The addition of P displaces the nucleation of entrained eutectic Si droplets to a lower undercooling.

- EuP is not as effective as AlP, however, EuP is a good nucleation site for intermetallic particles (e.g., Al_2Si_2Eu).

9.4 Precipitation of β-type precipitates

- TEM reveals that β'' is formed already after solution treatment (T4) and its number density increases with artificial ageing. The time required to obtain peak hardness is shifted from 3 h to 4 h with increasing solute Ta from 0.07 wt. % to 0.12 wt. %. The highest peak hardness is obtained in the high Ta alloy.

- The interface of Al and β'' precipitate doped with Ti and Ta shows a lower interface energy for the Ta-doped interface.

- Solute Eu significantly reduces the activation energy of β precipitate, therefore the complete precipitation may take less time and hence the economic costs can be reduced.

9.5 Mechanical properties

- The highest elongation of 24 % is measured in Ta-refined and Sr-modified alloy in T4 condition.

- The highest elongation in T6 condition is measured in conventional Ti-refined and Sr-modified alloy. Modification using Eu in combination with P decreases the elongation due to the large amount of Al_2Si_2Eu phase at the grain boundaries.

- Fracture toughness is slightly improved in Ta-refined and Eu-modified alloys compared to conventional Ti-refined and Sr-modified alloys.

- Modification using Eu results in a large porosity located in the centre of the sand casting sample, while Sr shows homogeneous porosity distribution. Eu-modified alloys require an improved feeding to improve the soundness of the casting part and therefore improve the mechanical properties.

Future works

Based on the present investigations, future works can be recommended.

- The experimental work can be repeated for Ti-refined and Eu-modified alloys to examine, whether possible Ti and Eu interaction influences the microstructure, precipitation and therefore tensile properties and hardness.

- Fracture toughness testing can be repeated for high Eu alloy with or without P to verify, whether the refinement of eutectic grains using Eu and P could improve the fracture toughness.

- The optimum ratio of Eu and P can be further investigated to obtain the best modification effect and the lowest eutectic grain size.

- Dynamical fatigue testing of Ta-refined and Eu-modified alloys is strongly recommended in order to examine the effect of solutes on fatigue since the static mechanical properties testing does not show significant changes.

- Impact toughness testing is the non-expensive method to verify the ability of energy adsorbed before fracture. This testing may highlight the importance of refinement of eutectic grains in Eu-modified alloys.

- DFT calculation of eutectic Si TB can be performed for different solutes such as Sr, Na, Ta and Ti.

- Interface energy calculation of sandwich structure and $Al||\beta''$ can be calculated for different solutes such as Ag, Cu, Eu, Sr, V and Zr.

- The hardness curve can be repeated for Ta-refined and Eu-modified alloys to reveal the strengthening effect of Eu in combination with P.

- TEM of the Mg_3P_2 phase at the interface of the Al_2Si_2Eu phase can be performed to confirm the established orientation relationship and proposed nucleation sequence. The sample preparation using FIB is highly recommended.

- TEM of entrained eutectic Si droplets to observe the interface of entrained eutectic Si droplets with α-Al matrix to precisely determine the P distribution and to measure the amount of modifier in this area. The sample preparation using FIB is highly recommended due to the large size of entrained eutectic Si droplets.

- Atom probe tomography (APT) is proposed to clearly establish the 3D distribution and chemical composition of Ta and other solutes at the basal plane of TiB_2.

- Computed tomography (CT) of large sand casting parts would provide a useful insight into the 3D porosity distribution of Sr-modified and Eu-modified alloys.

List of publications

First author

1. **I. Spacil**, J. Li: "Revealing nucleation kinetics of entrained eutectic Si droplets in high purity melt spun Al-5Si based alloys with additions of Ta, TiB_2, Eu and P". submitted to *Journal of Alloys and Compounds* – under review

2. **I. Spacil**, D. Gehringer, D. Holec, M. Albu, J. Li: "Elucidating effects of Eu and P on solidification and precipitation of Al-7Si-0.3Mg based alloys refined by Ta and stochiometric Al-Ti-B". submitted to *Journal of Alloys and Compounds* – under review

3. **I. Spacil**, D. Holec, M. Albu, J. Li: "Revealing effects of solute Ta on solidification and precipitation of Al-7Si-0.3Mg based alloys". *Materialia*, **30**, 101846 (2023), DOI: `10.1016/j.mtla.2023.101846`.

4. **I. Spacil**, P. Schumacher, J. Li: "Effect of Eu and P additions with Ta grain refiner on the solidification microstructure of Al-7Si-0.3Mg alloys". *IOP Conference Series: Materials Science and Engineering*, **1274**, 012006 (2023), DOI: `10.1088/1757-899X/1274/1/012006`.

5. **I. Spacil**, D. Holec, P. Schumacher, J. Li: "Effect of Solute Ta on Grain Refinement of Al-7Si-0.3Mg Based Alloys". *Solid State Phenomena*, **327**, 54 (2022), DOI: `10.4028/www.scientific.net/SSP.327.54`.

Co-authored

1. J. Li, **I. Spacil**, J. Winklhofer, Fabian Hofstätter, S. Griesebner : "A Comparasion of Microstructure and Casting Defects of Rheocasting and Thixocasting Al-Si-Mg Based Alloy". *Solid State Phenomena*, **347**, 61 (2023), DOI: `10.4028/p-M4FKyR`.

   Contribution: I have contributed, the heat treatment, preparation of metallography samples, microstructure analysis and editing the paper.

2. J. Li, **I. Spacil**, J. Winklhofer, Fabian Hofstätter, S. Griesebner: "Effect of Mn Addition on Microstructure, Mechanical Properties and Die Soldering of Rheocasting Al-7Si-0.3Mg Based Alloys", **347**, 67 (2023), DOI: `10.4028/p-U4O8Pv`.

   Contribution: I have contributed, the heat treatment, preparation of metallography samples, microstructure analysis and editing the paper.

3. M. Zarif, **I. Spacil**, T. Pabel, P. Schumacher, J. Li: "Effect of Ca and P on the Size and Morphology of Eutectic Mg_2Si in High-Purity Al-Mg-Si Alloys". *Metals*, **13**, 784 (2023), DOI: `10.3390/met13040784`.

   Contribution: I have contributed, the casting experiments, preparation of TEM samples and editing the paper.

Appendix
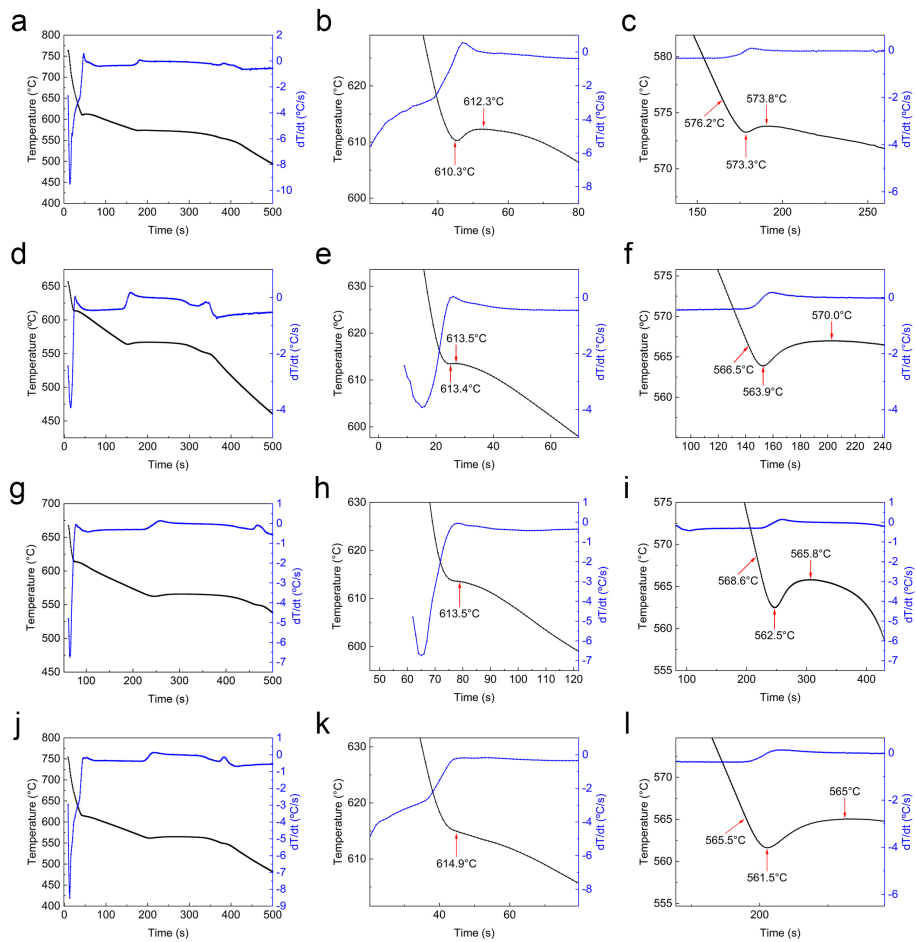
Figure A.1: Cooling curve of alloys; (a-c) Ref, (d-f) 0.01Ti, (g-i) 0.07Ta, and (j-l) 0.12Ta.
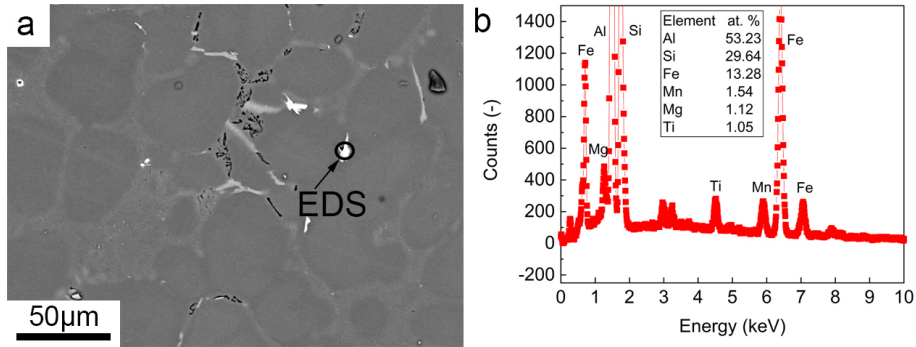
Figure A.2: (a) SEM BS image and (b) EDS analysis of Fe-rich phase at the grain boundaries in 0.12Ta alloy [232].
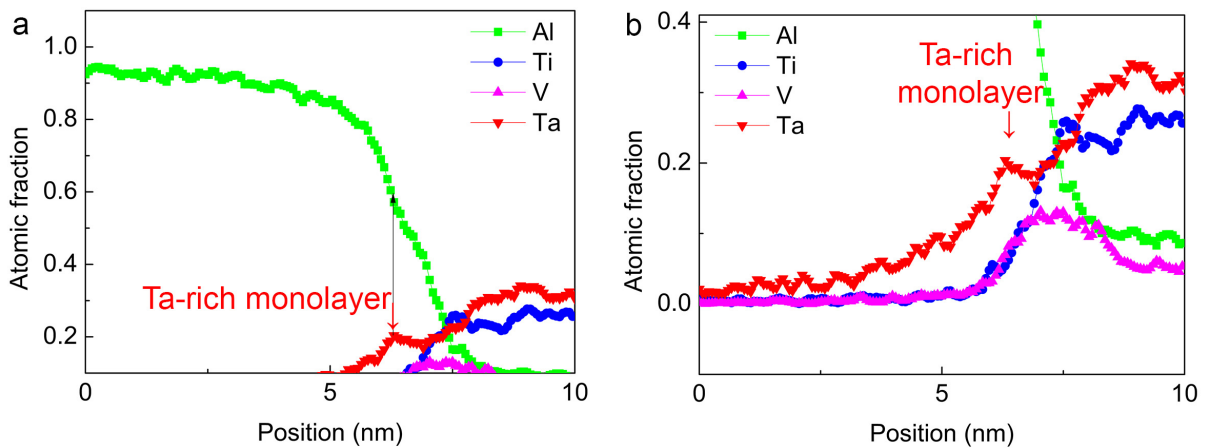

Figure A.3: (a) and (b) two EDS line scannings enlarged from Fig. 4.11 [232].

Appendix

Table B.1: Substitution energies of 12 non-equivalent positions at the various distances from TB.

Number of positions	Distance [Å]	Total energy of the TB [eV]	ΔE_{sub} [eV]
0*	0**	-1152.923	-
1	1.012	-1150.557	2.373
2	1.327	-1151.820	1.100
3	3.625	-1150.782	2.138
4	5.867	-1150.665	2.255
5	7.359	-1150.754	1.166
6	9.012	-1150.096	1.824
7	10.359	-1150.921	1.999
8	11.823	-1150.901	2.010
9	14.233	-1151.405	1.515
10	15.390	-1150.591	2.329
11	16.946	-1150.300	2.620
12	17.758	-1150.492	2.428

*Position 0 equals to the reference point at the intersection of TB.
**Total energy of TB without Eu.
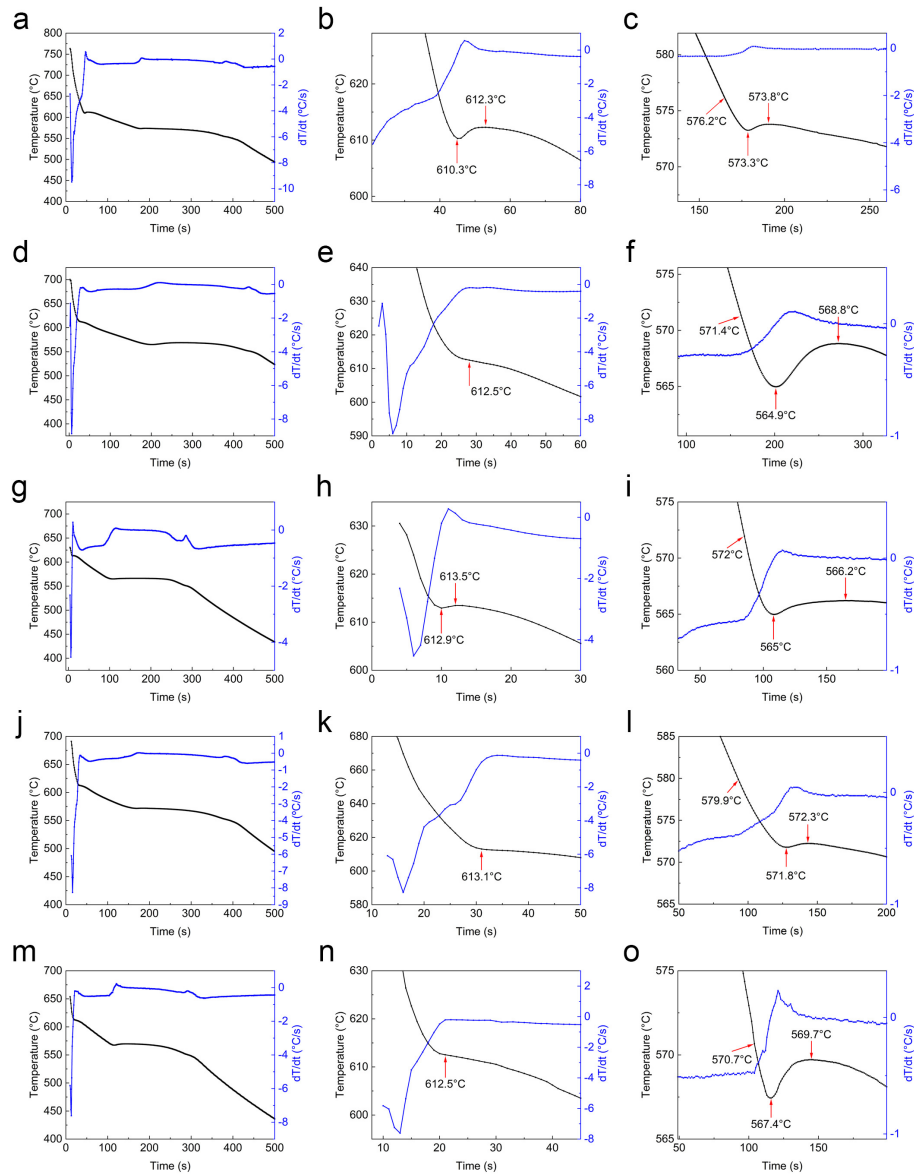
Figure B.1: Cooling curve of alloys; (a-c) Ref, (d-f) 200Eu, (g-i) 500Eu, (j-l) 200Eu40P, and (m-o) 500Eu40P.
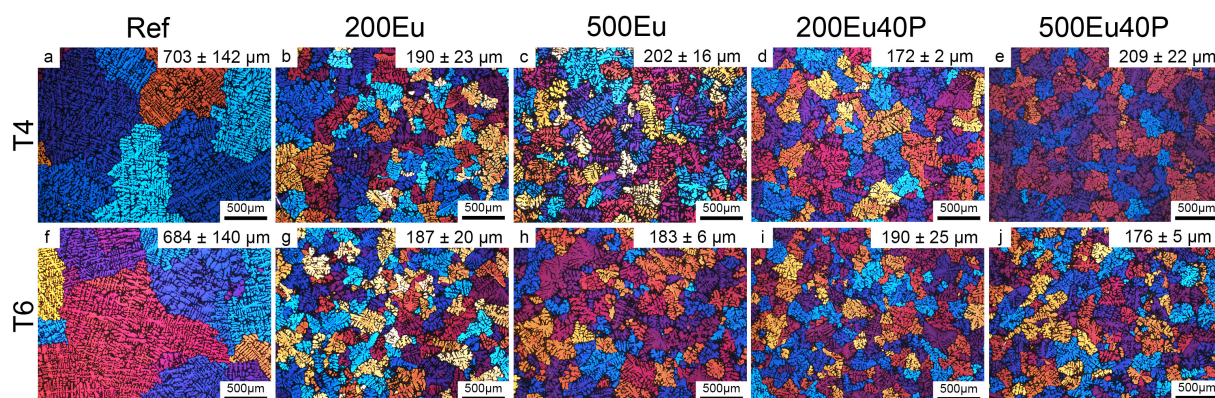
Figure B.2: Optical micrographs of T4 (a-e) and T6 (f-j) treated alloys: (a,f) Ref, (b,g) 200Eu, (c,h) 500Eu, (d,i) 200Eu40P and (e,j) 500Eu40P, including measured grain size of α-Al after Barkers etching.
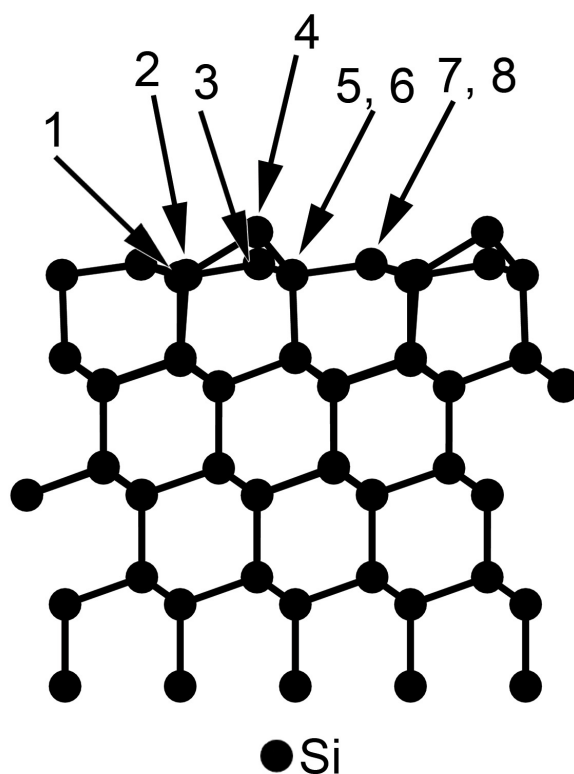

Figure B.3: Modelled free surface of Si{111} with denoted 8 substituted atoms. Model (c) represents a free surface located far from the TB.

Table B.2: Substitution energy of Eu atoms at free Si{111} interface.

Number of positions	Total energy of the TB [eV]	ΔE_{sub} [eV]
0*	-181.629	-
1	-179.167	2.462
2	-179.166	2.463
3	-180.134	1.495
4	-179.738	1.891
5	-179.166	2.463
6	-179.166	2.463
7	-180.134	1.495
8	-180.134	1.495

*Position 0 equals to pure Si{111} flat surface
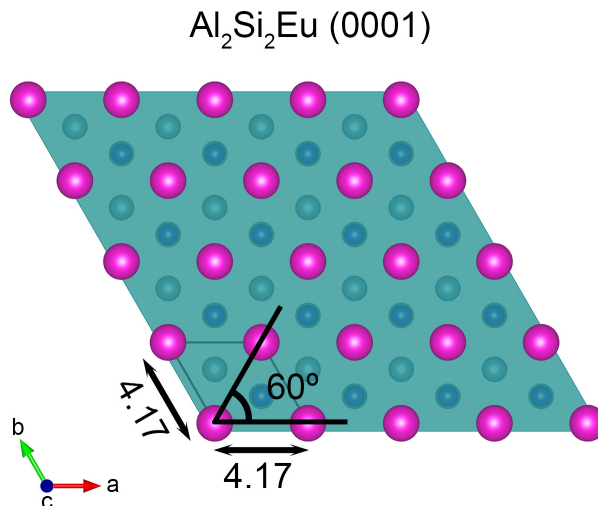
Figure B.4: Extracted lattice parameter a of hexagonal phases for the lattice mismatch calculation.
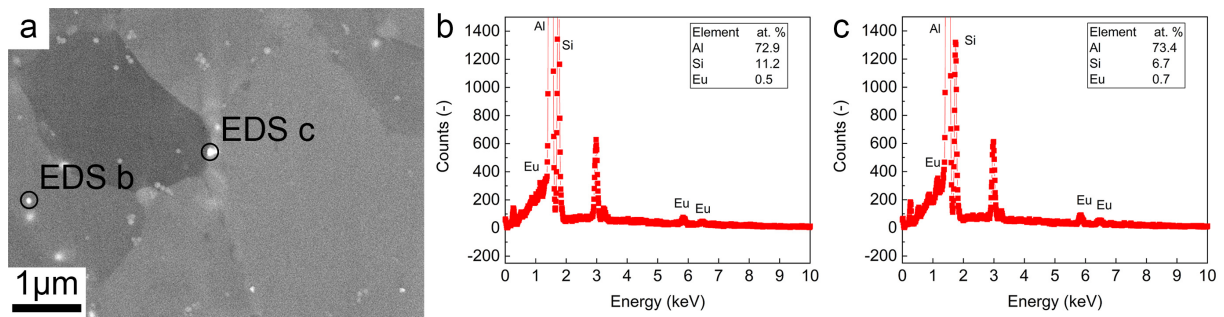
Appendix

Figure C.1: (a) SEM backscattered (BS) image of melt-spun microstructure of alloy 0.05Eu-TiB$_2$. (b) EDS point analysis of intermetallic phase within the α-Al grain and (c) at the grain boundary of α-Al.
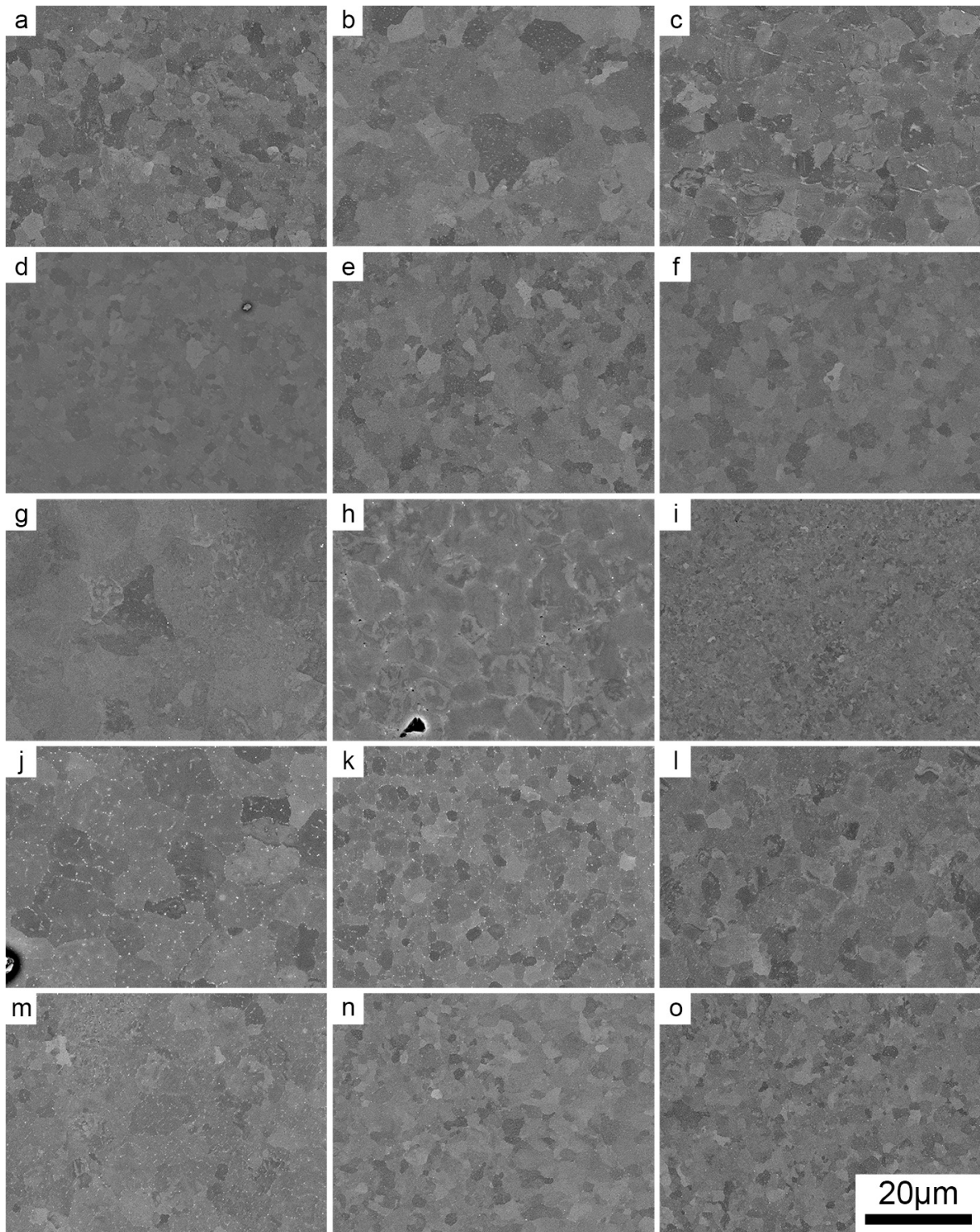
Figure C.2: SEM BS low magnification images of melt-spun ribbons: (a) Ref, (b) TiB$_2$, (c) 0.05Ta, (d) 0.05-TiB$_2$, (e) 0.12Ta-TiB$_2$, (f) 0.30Ta-TiB$_2$, (g) 0.50Ta-TiB$_2$, (h) 0.02Eu, (i) 0.02Eu-TiB$_2$, (j) 0.05Eu, (k) 0.05Eu-TiB$_2$, (l) 0.02Eu-30P, (m) 0.05Eu-5P, (n) 0.05Eu-20P, and (o) 0.05Eu-30P.
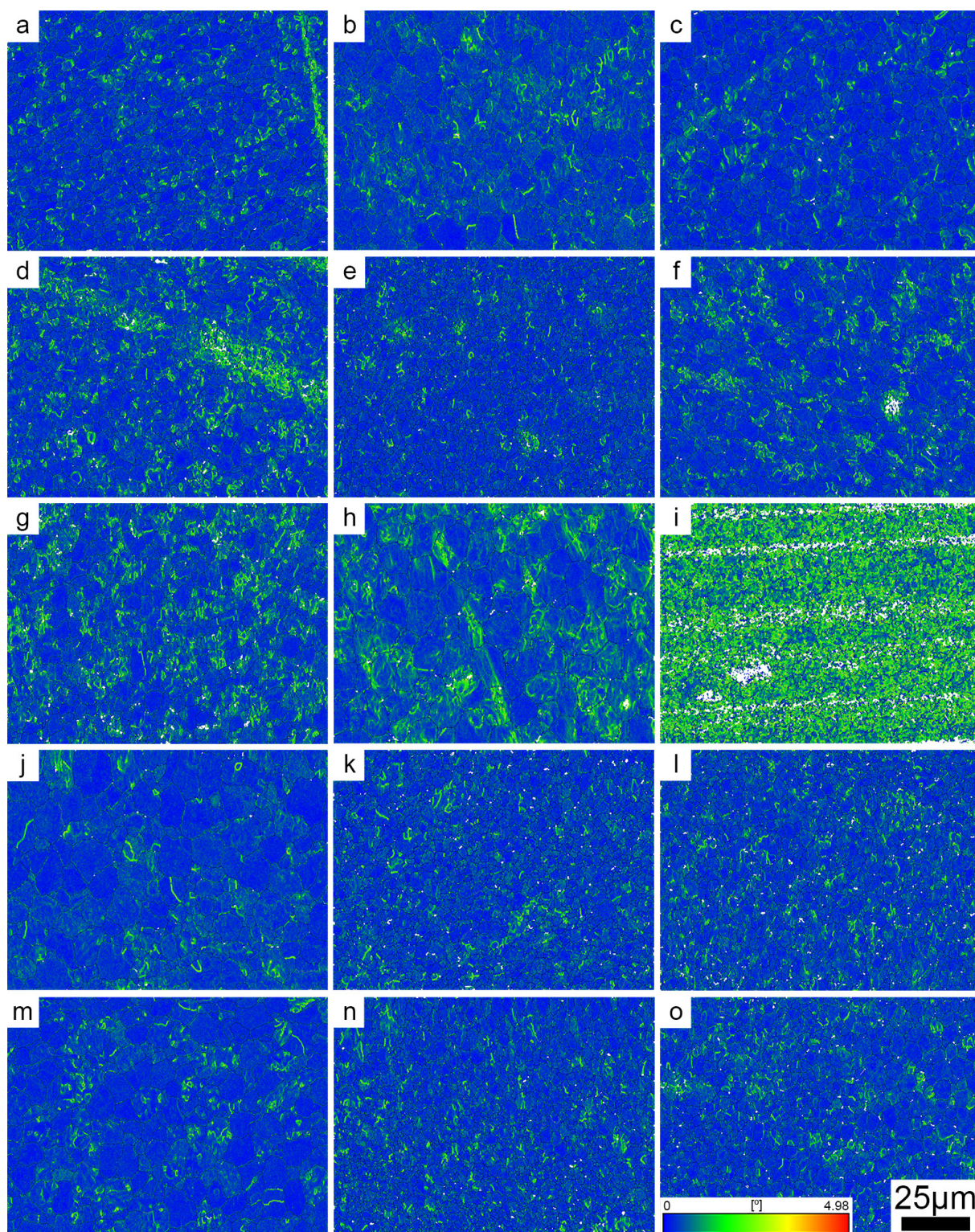
Figure C.3: KAM analysis of melt-spun ribbons: (a) Ref, (b) TiB_2, (c) 0.05Ta, (d) 0.05-TiB_2, (e) 0.12Ta-TiB_2, (f) 0.30Ta-TiB_2, (g) 0.50Ta-TiB_2, (h) 0.02Eu, (i) 0.02Eu-TiB_2, (j) 0.05Eu, (k) 0.05Eu-TiB_2, (l) 0.02Eu-30P, (m) 0.05Eu-5P, (n) 0.05Eu-20P, and (o) 0.05Eu-30P.
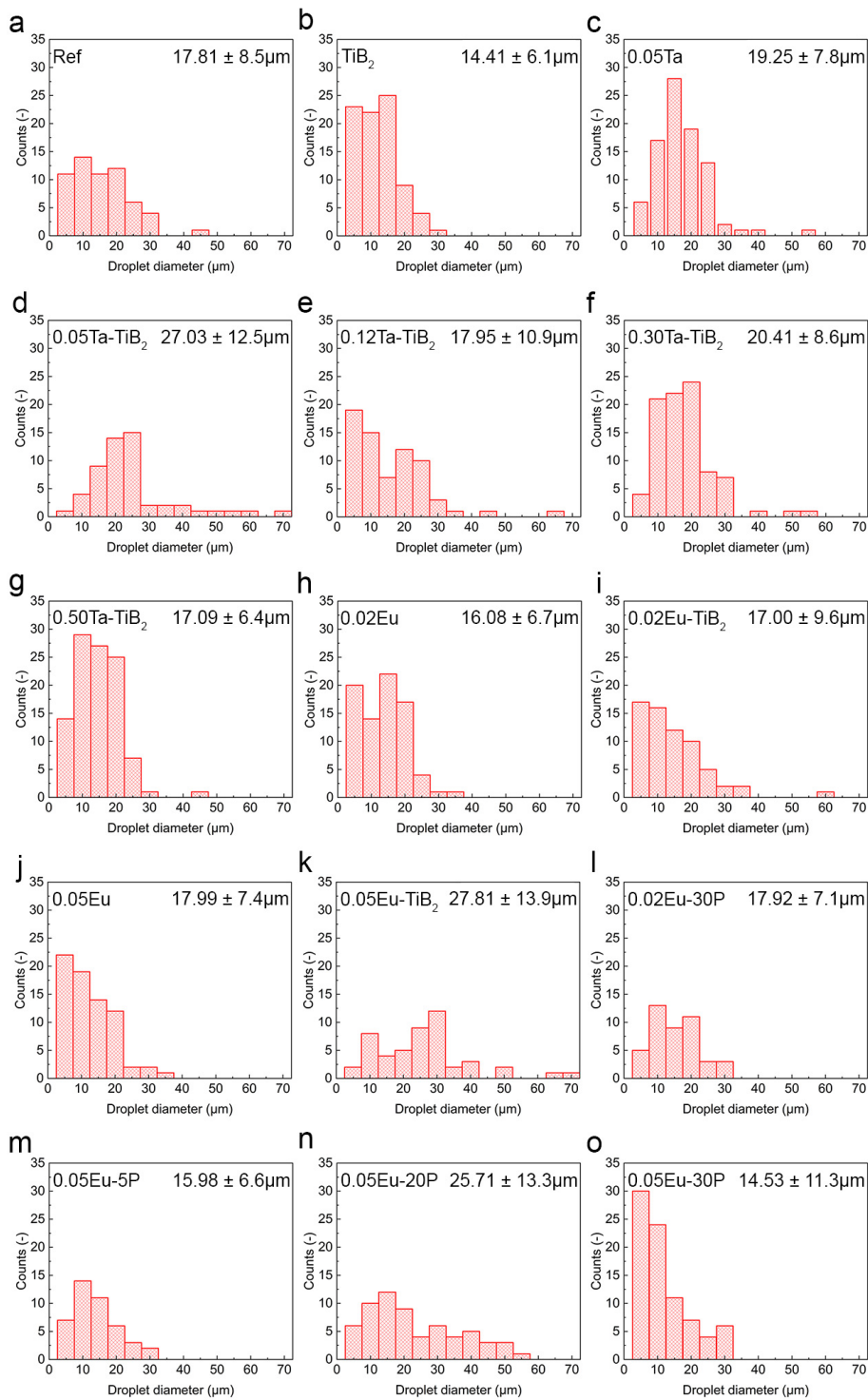
Figure C.4: Size distribution of entrained eutectic Si droplets of alloys: (a) Ref, (b) TiB$_2$, (c) 0.05Ta, (d) 0.05-TiB$_2$, (e) 0.12Ta-TiB$_2$, (f) 0.30Ta-TiB$_2$, (g) 0.50Ta-TiB$_2$, (h) 0.02Eu, (i) 0.02Eu-TiB$_2$, (j) 0.05Eu, (k) 0.05Eu-TiB$_2$, (l) 0.02Eu-30P, (m) 0.05Eu-5P, (n) 0.05Eu-20P, and (o) 0.05Eu-30P. Note that the entrained eutectic Si droplets with a diameter size below 5 µm were excluded.
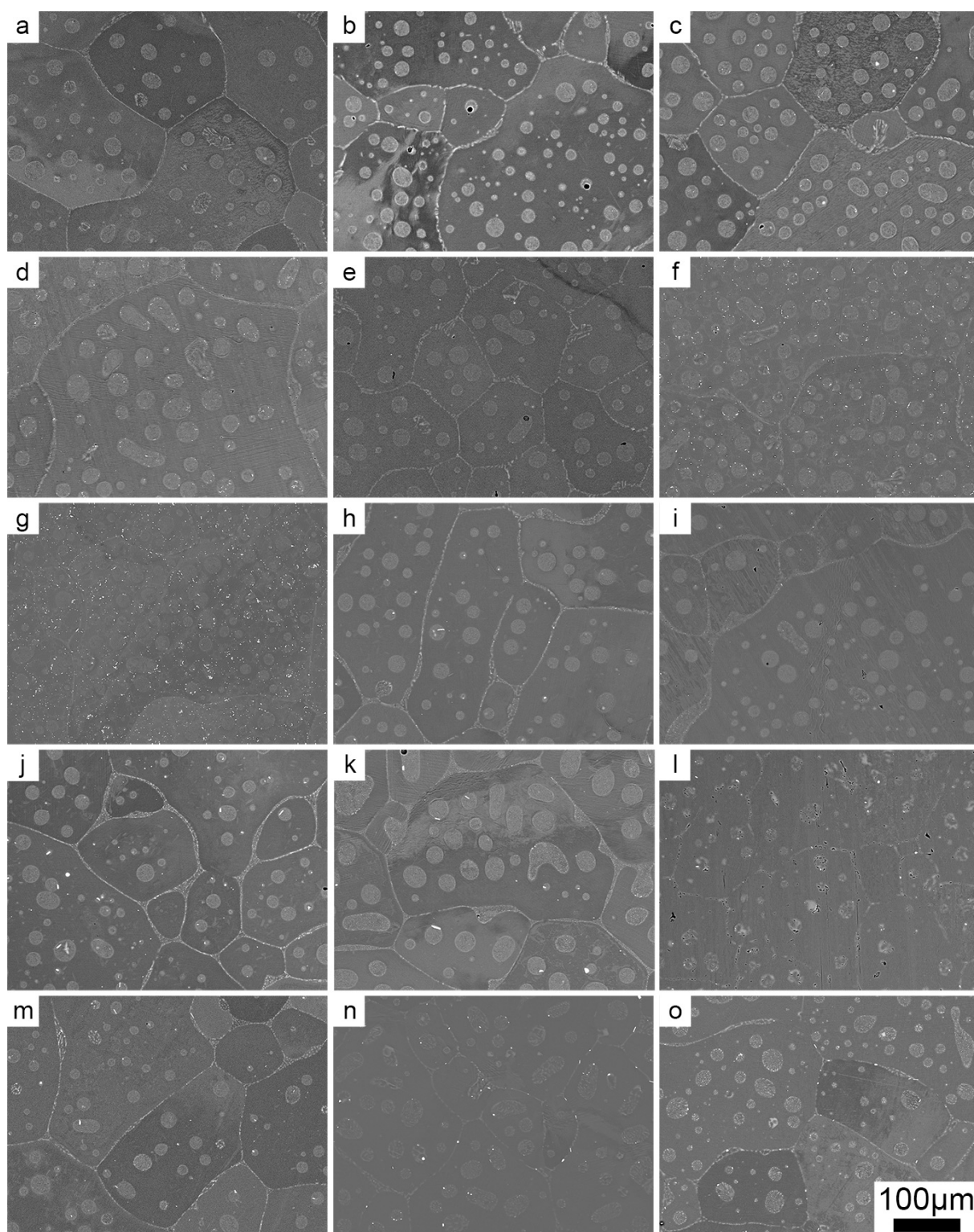
Figure C.5: SEM BS low magnification images of entrained eutectic Si droplets after DSC: (a) Ref, (b) TiB$_2$, (c) 0.05Ta, (d) 0.05-TiB$_2$, (e) 0.12Ta-TiB$_2$, (f) 0.30Ta-TiB$_2$, (g) 0.50Ta-TiB$_2$, (h) 0.02Eu, (i) 0.02Eu-TiB$_2$, (j) 0.05Eu, (k) 0.05Eu-TiB$_2$, (l) 0.02Eu-30P, (m) 0.05Eu-5P, (n) 0.05Eu-20P, and (o) 0.05Eu-30P.
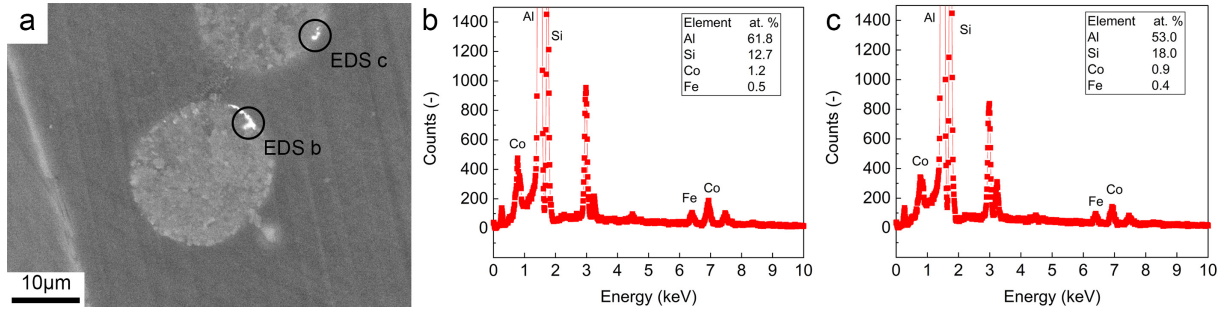
Figure C.6: (a) SEM backscattered image (BS) image of alloy 0.05Ta after DSC. (b, c) EDS point analysis of the Fe-intermetallic phase at the boundary of entrained eutectic Si droplets.
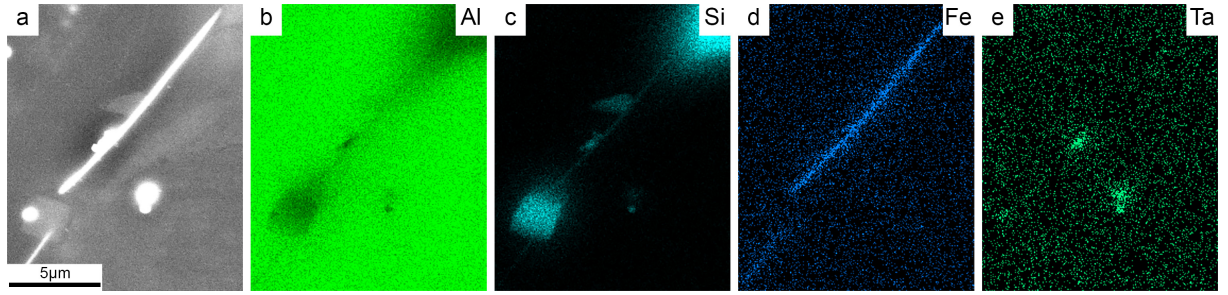

Figure C.7: (a) SEM BS image and (b-d) EDS maps of entrained eutectic Si droplet in 0.50Ta-TiB2 alloy: (b) Al, (c) Si, (d) Fe, and (e) Ta.

Table C.1: Calculation of Jackson factor α_J for Al and Si. L_m is the latent heat of fusion, T_m is the melting point, $S_F = \frac{L_m}{T_m}$ is the entropy of fusion, R_{gas} is the gas constant, $\alpha_J = \frac{S_F}{R_{\text{gas}}}$ is the Jackson factor (equation 2.27), CN_I is the total number of nearest-neighbour sites in the crystal, $CN_S\{XXX\}$ is the number of nearest-neighbour sites in a layer parallel to the $\{XXX\}$ surface and $\alpha_J\{XXX\}$ is the Jackson factor with respect to $\{XXX\}$ surface.

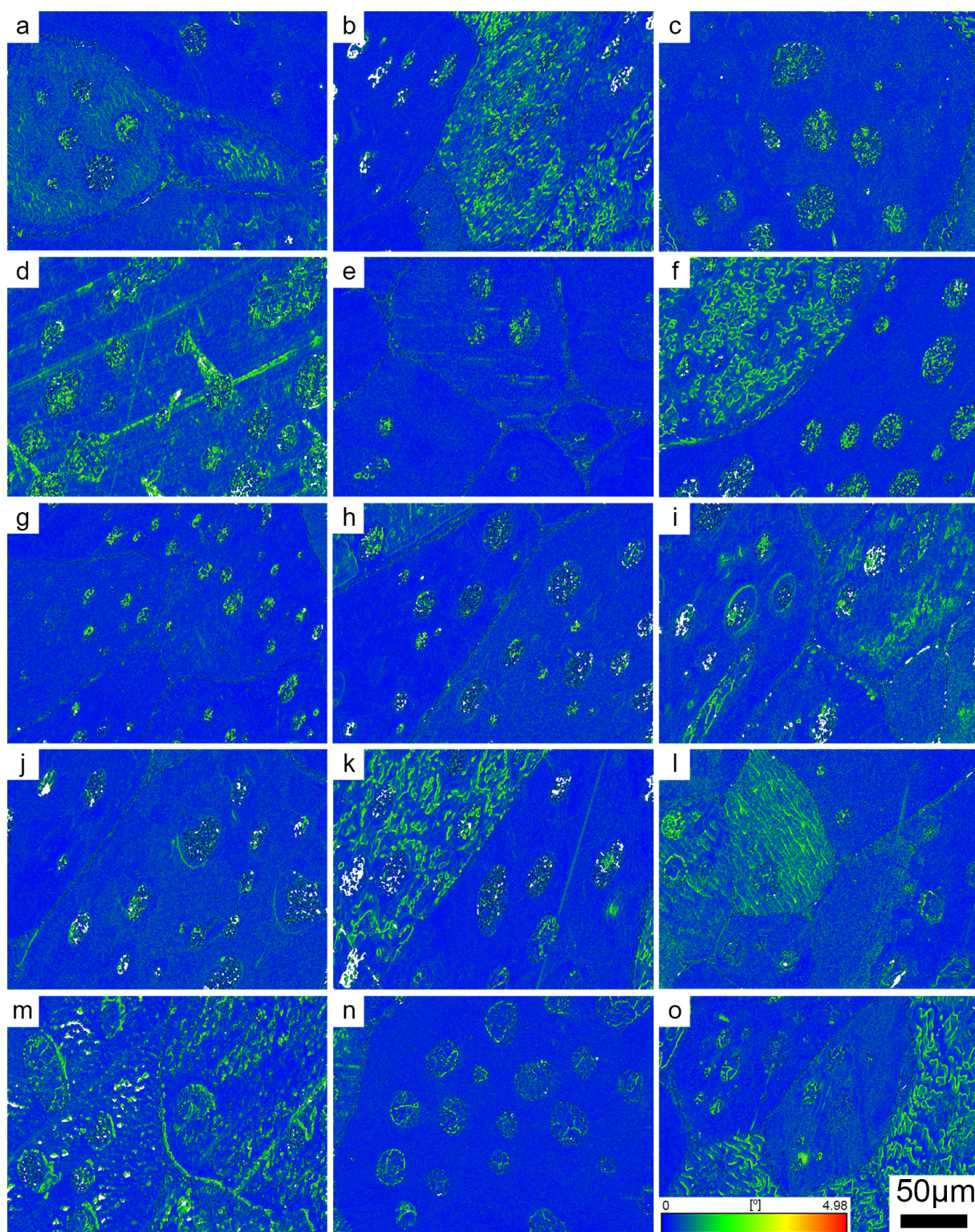|	Al	Si
L_m [J/mol]	10.71x10 3	50.21x10 3
T_m [K]	933	1687
S_F [J/mol·K]	11.48	29.76
R_{gas} [J/mol·K]	8.314	8.314
α_J [-]	1.38	3.58
CN_I [-]	12	4
CN_S {111} [-]	9	3
CN_S {100} [-]	8	2
$\frac{CN_S}{CN_I}$ {111} [-]	0.75	0.75
$\frac{CN_S}{CN_I}$ {100} [-]	0.66	0.5
α_J {111}$=\frac{S_F}{R_{\text{gas}}} \cdot \frac{CN_S}{CN_I}$ [-]	1.04	2.68
α_J {100}$=\frac{S_F}{R_{\text{gas}}} \cdot \frac{CN_S}{CN_I}$ [-]	0.91	1.79

Figure C.8: KAM analysis of melt-spun ribbons after DSC heating: (a) Ref, (b) TiB$_2$, (c) 0.05Ta, (d) 0.05-TiB$_2$, (e) 0.12Ta-TiB$_2$, (f) 0.30Ta-TiB$_2$, (g) 0.50Ta-TiB$_2$, (h) 0.02Eu, (i) 0.02Eu-TiB$_2$, (j) 0.05Eu, (k) 0.05Eu-TiB$_2$, (l) 0.02Eu-30P, (m) 0.05Eu-5P, (n) 0.05Eu-20P, and (o) 0.05Eu-30P.

Bibliography

[1]   M. Johnsson and L. Bäckerud, International Journal of Materials Research **87**, 216 (1996).

[2]   Y. Birol, Materials Science and Technology **28**, 385 (2012).

[3]   P. Schumacher, A. L. Greer, J. Worth, P. V. Evans, M. A. Kearns, P. Fisher, and A. H. Green, Materials Science and Technology **14**, 394 (1998).

[4]   J. Gröbner, D. Mirković, and R. Schmid-Fetzer, Materials Science and Engineering: A **395**, 10 (2005).

[5]   Y. Li, Q.-F. Gu, Q. Luo, Y. Pang, S.-L. Chen, K.-C. Chou, X.-L. Wang, and Q. Li, Materials & Design **102**, 78 (2016).

[6]   T. Wang, Z. Chen, H. Fu, J. Xu, Y. Fu, and T. Li, Scripta Materialia **64**, 1121 (2011).

[7]   S. Kori, B. Murty, and M. Chakraborty, Materials Science and Technology **15**, 986 (1999).

[8]   J. A. Spittle, International Journal of Cast Metals Research **19**, 210 (2006).

[9]   J. Li, G. Yang, F. S. Hage, Z. Chen, T. Wang, Q. M. Ramasse, and P. Schumacher, Materials Characterization **128**, 7 (2017).

[10]   X. Wang, Journal of Alloys and Compounds **403**, 283 (2005), publisher: Elsevier BV.

[11]   Y. Li, B. Hu, Q. Gu, B. Liu, and Q. Li, Scripta Materialia **160**, 75 (2019).

[12]   Y. Li, Y. Jiang, B. Hu, and Q. Li, Scripta Materialia **187**, 262 (2020).

[13]   J. Xu, Y. Li, K. Ma, Y. Fu, E. Guo, Z. Chen, Q. Gu, Y. Han, T. Wang, and Q. Li, Scripta Materialia **187**, 142 (2020).

[14]   P. S. Mohanty and J. E. Gruzleski, Acta Materialia **44**, 3749 (1996).

[15]   A. Banerji and W. Reif, Metallurgical Transactions A **17**, 2127 (1986).

[16] S. A. Kori, B. S. Murty, and M. Chakraborty, Materials Science and Engineering: A **283**, 94 (2000).

[17] P. Schumacher and A. L. Greer, Materials Science and Engineering: A **178**, 309 (1994).

[18] A. Pacz, "Aluminum-Silicon Alloy," (1921).

[19] J. H. Li, J. Barrirero, M. Engstler, H. Aboulfadl, F. Mücklich, and P. Schumacher, Metallurgical and Materials Transactions A **46**, 1300 (2015).

[20] M. Timpel, N. Wanderka, R. Schlesiger, T. Yamamoto, N. Lazarev, D. Isheim, G. Schmitz, S. Matsumura, and J. Banhart, Acta Materialia **60**, 3920 (2012).

[21] A. K. Dahle, K. Nogita, S. D. McDonald, C. Dinnis, and L. Lu, Materials Science and Engineering: A International Conference on Advances in Solidification Processes, **413-414**, 243 (2005).

[22] K. Nogita, S. D. McDonald, K. Tsujimoto, K. Yasuda, and A. K. Dahle, Journal of Electron Microscopy **53**, 361 (2004).

[23] G. K. Sigworth, International Journal of Metalcasting **2**, 19 (2008).

[24] K. Nogita, S. D. McDonald, and A. K. Dahle, Materials Transactions **45**, 323 (2004).

[25] J. H. Li, T. H. Ludwig, B. Oberdorfer, and P. Schumacher, International Journal of Cast Metals Research **31**, 319 (2018).

[26] C. R. Ho and B. Cantor, Acta Metallurgica et Materialia **43**, 3231 (1995).

[27] C. R. Ho and B. Cantor, Journal of Materials Science **30**, 1912 (1995).

[28] T. Ludwig, *Trace Elements in Al-Si Foundry Alloys*, Ph.D. thesis, Norwegian University of Science and Technology (2013).

[29] D. M. Stefanescu, *Science and engineering of casting solidification* (Kluwer Academic/Plenum Publishers, New York, 2002).

[30] K. F. Kelton and A. L. Greer, *Nucleation in condensed matter: Applications in Materials and Biology*, 1st ed., Elsevier Science, Vol. 15 (Pergamon, Oxford, 2010).

[31] H. Fredriksson and U. Åkerlind, *Solidification and crystallization processing in metals and alloys* (Wiley, Chichester, 2012).

[32] J. A. Dantzig and M. Rappaz, *Solidification*, Engineering sciences (EPFL press CRC press, Lausanne (Suisse) Boca Raton (Fla.), 2009).

[33] D. A. Porter, K. E. Easterling, and M. Y. Sherif, *Phase transformations in metals and alloys*, 3rd ed. (CRC Press, Boca Raton, FL, 2009).

[34] M. Johnsson, Thermochimica Acta Thermal Analysis and Calorimetry, **256**, 107 (1995).

[35] D. M. Stefanescu and R. Ruxanda, in *Metallography and Microstructures*, Vol. 9 (ASM International, 2004) pp. 1–24.

[36] D. G. Eskin, *Physical metallurgy of direct chill casting of aluminum alloys*, Advances in metallic alloys, Vol. 6 (CRC Press/Taylor & Francis, Boca Raton, 2008).

[37] D. H. StJohn, M. Qian, M. A. Easton, and P. Cao, Acta Materialia **59**, 4907 (2011).

[38] W. Kurz and D. J. Fisher, *Fundamentals of solidification*, 4th ed. (Trans Tech Publications, Uetikon-Zuerich, Switzerland ; Enfield, N.H, 1998).

[39] M. C. Flemings, Metallurgical transactions **5**, 2121 (1974).

[40] D. G. McCartney, International Materials Reviews **34**, 247 (1989).

[41] D. Turnbull, The Journal of Chemical Physics **18**, 198 (1950).

[42] D. Turnbull and B. Vonnegut, Industrial & Engineering Chemistry **44**, 1292 (1952).

[43] D. Turnbull, Journal of Applied Physics **20**, 817 (1949).

[44] B. S. Murty, S. A. Kori, and M. Chakraborty, International materials reviews **47**, 3 (2002).

[45] T. Young, Philosophical Transactions of the Royal Society of London **95**, 65 (1805).

[46] J. H. Perepezko and M. J. Uttormark, Metallurgical and Materials Transactions A **27**, 533 (1996).

[47] M. Z. Zarif, *Modification of Al-Si and Al-Mg2Si Eutectic*, Ph.D. thesis, University of Leoben, Austria (2011).

[48] N. H. Fletcher, The Journal of Chemical Physics **29**, 572 (1958).

[49] A. Hellawell, Progress in Materials Science **15**, 3 (1970).

[50] D. R. Hamilton and R. G. Seidensticker, Journal of Applied Physics **31**, 1165 (1960).

[51] R. Trivedi and W. Kurz, International Materials Reviews **39**, 49 (1994).

[52] A. Cziegler, *Revealing grain refinement mechanisms in copper alloys*, Ph.D. thesis, University of Leoben, Austria (2019).

[53] L. M. Hogan, in *Encyclopedia of Materials: Science and Technology* (Elsevier, Oxford, 2001) pp. 1913–1918.

[54] W. Tiller, K. Jackson, J. Rutter, and B. Chalmers, Acta Metallurgica **1**, 428 (1953).

[55] J. Campbell, ed., *Complete casting handbook* (Butterworth-Heinemann, Oxford, 2011).

[56] K. A. Jackson, Progress in Solid State Chemistry **4**, 53 (1967).

[57] W. Kurz, C. Bezençon, and M. Gäumann, Science and Technology of Advanced Materials **2**, 185 (2001).

[58] U. K. Mohanty and H. Sarangi, *Solidification of Metals and Alloys* (IntechOpen, 2020).

[59] M. C. Flemings, *Solidification processing*, Materials Science and Engineering (McGraw-Hill, 1974).

[60] R. Trivedi and K. Somboonsuk, Materials Science and Engineering Solidification Microstructure: 30 Years after Constitutional Supercooling, **65**, 65 (1984).

[61] M. A. Chopra, M. E. Glicksman, and N. B. Singh, Metallurgical Transactions A **19**, 3087 (1988).

[62] J. Campbell, *Castings*, 2nd ed. (Butterworth-Heinemann, Oxford, 2003).

[63] R. K. Yajjala, N. M. Inampudi, and B. R. Jinugu, Journal of Materials Research and Technology **9**, 6257 (2020).

[64] E. Vandersluis and C. Ravindran, Metallography, Microstructure, and Analysis **6**, 89 (2017).

[65] M. Easton and D. StJohn, Metallurgical and Materials Transactions A **30**, 1613 (1999).

[66] M. Easton and D. StJohn, Metallurgical and Materials Transactions A **30**, 1625 (1999).

[67] L. A. Tarshis, J. L. Walker, and J. W. Rutter, Metallurgical Transactions **2**, 2589 (1971).

[68] J. A. Spittle and S. Sadli, Materials Science and Technology **11**, 533 (1995).

[69] I. Maxwell and A. Hellawell, Acta Metallurgica **23**, 229 (1975).

[70] R. Schmid-Fetzer and A. Kozlov, Acta Materialia **59**, 6133 (2011).

[71] A. Greer, A. Bunn, A. Tronche, P. Evans, and D. Bristow, Acta Materialia **48**, 2823 (2000).

[72] A. Greer, P. Cooper, M. Meredith, W. Schneider, P. Schumacher, J. Spittle, and A. Tronche, Advanced Engineering Materials **5**, 81 (2003).

[73] M. A. Easton and D. H. StJohn, Acta Materialia **49**, 1867 (2001).

[74] T. E. Quested, Materials Science and Technology **20**, 1357 (2004).

[75] A. L. Greer, Philosophical Transactions of the Royal Society of London. Series A: Mathematical, Physical and Engineering Sciences **361**, 479 (2003).

[76] A. M. Bunn, P. V. Evans, D. J. Bristow, and A. L. Greer, in *Essential Readings in Light Metals: Volume 3 Cast Shop for Aluminum Production* (Springer International Publishing, Cham, 2016) pp. 387–392.

[77] M. Easton and D. StJohn, Metallurgical and Materials Transactions A **36**, 1911 (2005).

[78] M. Qian, P. Cao, M. A. Easton, S. D. McDonald, and D. H. StJohn, Acta Materialia **58**, 3262 (2010).

[79] M. A. Easton and D. H. StJohn, Materials Science and Engineering: A **486**, 8 (2008).

[80] K. A. Jackson and J. D. Hunt, in *Dynamics of Curved Fronts* (Academic Press, San Diego, 1988) pp. 363–376.

[81] P. Magnin and R. Trivedi, Acta Metallurgica et Materialia **39**, 453 (1991).

[82] M. M. Makhlouf and H. V. Guthy, Journal of Light Metals **1**, 199 (2001).

[83] D. J. Fisher and W. Kurz, Acta Metallurgica **28**, 777 (1980).

[84] K. A. Jackson, D. R. Uhlmann, and J. D. Hunt, Journal of Crystal Growth **1**, 1 (1967).

[85] K. A. Jackson, in *Changes of State*, Treatise on Solid State Chemistry, edited by N. B. Hannay (Springer US, Boston, MA, 1975) pp. 233–282.

[86] B. Cantor and K. A. O'Reilly, Current Opinion in Solid State and Materials Science **2**, 318 (1997).

[87] K. A. Q. O'Reilly and B. Cantor, Acta Metallurgica et Materialia **43**, 405 (1995).

[88] D. Turnbull, Journal of Applied Physics **21**, 1022 (1950).

[89] C.-C. Wang and C. S. Smith, JOM **2**, 136 (1950).

[90] K. I. Moore, D. L. Zhang, and B. Cantor, Acta Metallurgica et Materialia **38**, 1327 (1990).

[91] D. L. Zhang and B. Cantor, Metallurgical Transactions A **24**, 1195 (1993).

[92] B. Cantor, Philosophical Transactions of the Royal Society of London. Series A: Mathematical, Physical and Engineering Sciences **361**, 409 (2003).

[93] W. T. Kim, D. L. Zhang, and B. Cantor, Metallurgical Transactions A **22**, 2487 (1991).

[94] T. H. Ludwig, J. Li, P. L. Schaffer, P. Schumacher, and L. Arnberg, Metallurgical and Materials Transactions A **46**, 362 (2015).

[95] W. T. Kim and B. Cantor, Acta Metallurgica et Materialia **40**, 3339 (1992).

[96] F. Paray and J. E. Gruzleski, Cast Metals **5**, 187 (1992).

[97] J. L. Murray and A. J. McAlister, Bulletin of Alloy Phase Diagrams **5**, 74 (1984).

[98] A. Kaye and A. Street, *Die casting metallurgy* (Butterworth, London, 1982).

[99] A. C. Street, ed., *The Diecasting Book*, 2nd ed. (Portcullis Pr, Redhill, Surrey, 1986).

[100] B. Closset and J. E. Gruzleski, Metallurgical and Materials Transactions A **13**, 945 (1982).

[101] I. Spacil, *Degassing of small amounts of aluminum alloy melt*, Master's thesis, Brno University of Technology, Faculty of Mechanical Engineering (2020).

[102] S. Hegde and K. N. Prabhu, Journal of Materials Science **43**, 3009 (2008).

[103] B. Closset and J. Gruzleski, Transactions of the American Foundrymen's Society **89**, 801 (1981).

[104] S. Kori, B. Murty, and M. Chakraborty, Materials Science and Engineering: A **280**, 58 (2000).

[105] L. Wang, M. Makhlouf, and D. Apelian, International Materials Reviews **40**, 221 (1995).

[106] G. K. Sigworth and T. A. Kuhn, International Journal of Metalcasting **1**, 31 (2007).

[107] P. S. Mohanty and J. E. Gruzleski, Acta Metallurgica et Materialia **43**, 2001 (1995).

[108] I. G. Davies, J. M. Dennis, and A. Hellawell, Metallurgical Transactions **1**, 275 (1970).

[109] M. Johnsson, L. Backerud, and G. K. Sigworth, Metallurgical Transactions A **24**, 481 (1993).

[110] G. P. Jones and J. Pearson, Metallurgical Transactions B **7**, 223 (1976).

[111] G. Sigworth and M. Guzowski, AFS Transactions **93**, 907 (1985).

[112] L. Arnberg, L. Bäckerud, and H. Klang, Metals Technology **9**, 7 (1982).

[113] A. M. Bunn, P. Schumacher, M. A. Kearns, C. B. Boothroyd, and A. L. Greer, Materials Science and Technology **15**, 1115 (1999).

[114] G. K. Sigworth, Metallurgical Transactions A **15**, 277 (1984).

[115] P. Schumacher and A. L. Greer, Materials Science and Engineering: A **181-182**, 1335 (1994).

[116] T. Quested and A. Greer, Acta Materialia **52**, 3859 (2004).

[117] T. E. Quested and A. L. Greer, Acta Materialia **53**, 4643 (2005).

[118] T. E. Quested, A. T. Dinsdale, and A. L. Greer, Acta Materialia **53**, 1323 (2005).

[119] T. E. Quested and A. L. Greer, Acta Materialia **53**, 2683 (2005).

[120] D. Shu, B. Sun, J. Mi, and P. S. Grant, Acta Materialia **59**, 2135 (2011).

[121] Z. Fan, Metallurgical and Materials Transactions A **44**, 1409 (2013).

[122] Z. Fan, F. Gao, L. Zhou, and S. Z. Lu, Acta Materialia **152**, 248 (2018).

[123] K. T. Kashyap and T. Chandrashekar, Bulletin of Materials Science **24**, 345 (2001).

[124] A. K. Dahle, P. A. Tøndel, C. J. Paradies, and L. Arnberg, Metallurgical and Materials Transactions A **27**, 2305 (1996).

[125] Y. C. Lee, A. K. Dahle, D. H. StJohn, and J. E. C. Hutt, Materials Science and Engineering: A **259**, 43 (1999).

[126] T. E. Quested, A. T. Dinsdale, and A. L. Greer, Materials Science and Technology **22**, 1126 (2006).

[127] P. Schumacher and B. J. McKay, Journal of Non-Crystalline Solids Advances in Metallic Glasses, **317**, 123 (2003).

[128] D. Qiu, J. A. Taylor, M.-X. Zhang, and P. M. Kelly, Acta Materialia **55**, 1447 (2007).

[129] Y. Li, B. Hu, B. Liu, A. Nie, Q. Gu, J. Wang, and Q. Li, Acta Materialia **187**, 51 (2020).

[130] J. Li, F. S. Hage, Q. M. Ramasse, and P. Schumacher, Acta Materialia **206**, 116652 (2021).

[131] Z. Chen, H. Kang, G. Fan, J. Li, Y. Lu, J. Jie, Y. Zhang, T. Li, X. Jian, and T. Wang, Acta Materialia **120**, 168 (2016).

[132] A. M. Samuel, H. W. Doty, S. Valtierra, and F. H. Samuel, International Journal of Metalcasting **11**, 305 (2017).

[133] L. Lu and A. K. Dahle, Materials Science and Engineering: A **435-436**, 288 (2006).

[134] A. Jain, S. P. Ong, G. Hautier, W. Chen, W. D. Richards, S. Dacek, S. Cholia, D. Gunter, D. Skinner, G. Ceder, and K. A. Persson, APL Materials **1**, 011002 (2013).

[135] J.-Y. Lee, J.-M. Lee, K.-S. Son, J.-i. Jang, and Y.-H. Cho, Journal of Alloys and Compounds **938**, 168598 (2023).

[136] D. Wu, S. Ma, T. Jing, Y. Wang, L. Wang, J. Kang, Q. Wang, W. Wang, T. Li, and R. Su, Acta Materialia **219**, 117265 (2021).

[137] J. Xu, Y. Li, B. Hu, Y. Jiang, and Q. Li, Journal of Materials Science **54**, 14561 (2019).

[138] M. E. Pammer, *Silicon poisoning and the influence of tantalum on grain refinement of AlSi alloys.*, Master's thesis, University of Leoben, Austria (2022).

[139] E. A. Brandes, G. B. Brook, and C. J. Smithells, eds., *Smithells metals reference book*, 7th ed. (Butterworth-Heinemann, Oxford , Boston, 1998).

[140] A. A. Abdel-Hamid and A. I. O. Zaid, in *Current Advances in Mechanical Design and Production VII* (Pergamon, Oxford, 2000) pp. 331–338.

[141] J. H. Li, S. Suetsugu, Y. Tsunekawa, and P. Schumacher, Metallurgical and Materials Transactions A **44**, 669 (2013).

[142] S. C. Flood and J. D. Hunt, Metal Science **15**, 287 (1981).

[143] A. C. of Canada, *Casting aluminium*, 1st ed. (Alcan, 1949).

[144] M. D. Hanna, S.-Z. Lu, and A. Hellawell, Metallurgical Transactions A **15**, 459 (1984).

[145] J. Barrirero, M. Engstler, N. Ghafoor, N. Jonge, M. Odén, and F. Mücklich, Journal of Alloys and Compounds **611**, 410 (2014).

[146] T. H. Ludwig, P. L. Schaffer, and L. Arnberg, Metallurgical and Materials Transactions A **44**, 5796 (2013).

[147] S. D. McDonald, K. Nogita, and A. K. Dahle, Acta Materialia **52**, 4273 (2004).

[148] S. D. McDonald, K. Nogita, and A. K. Dahle, Journal of Alloys and Compounds **422**, 184 (2006).

[149] T. H. Ludwig, E. Schonhovd Dæhlen, P. L. Schaffer, and L. Arnberg, Journal of Alloys and Compounds **586**, 180 (2014).

[150] S.-M. Liang and R. Schmid-Fetzer, Acta Materialia **72**, 41 (2014).

[151] A. K. Dahle, L. Lu, K. Nogita, and S. D. McDonald, "Aluminium casting alloy," (2012).

[152] J. Li, F. S. Hage, X. Liu, Q. Ramasse, and P. Schumacher, Scientific Reports **6**, 25244 (2016).

[153] S. Shankar, Y. W. Riddle, and M. M. Makhlouf, Acta Materialia **52**, 4447 (2004).

[154] Y. Cho, H.-C. Lee, K. Oh, and A. Dahle, Metallurgical and Materials Transactions A **39**, 2435 (2008).

[155] T. H. Ludwig, P. L. Schaffer, and L. Arnberg, Metallurgical and Materials Transactions A **44**, 3783 (2013).

[156] A. K. Dahle, K. Nogita, S. D. McDonald, J. W. Zindel, and L. M. Hogan, Metallurgical and Materials Transactions A **32**, 949 (2001).

[157] S. D. McDonald, A. K. Dahle, J. A. Taylor, and D. H. StJohn, Metallurgical and Materials Transactions A **35**, 1829 (2004).

[158] J. H. Li, Y. G. Yang, S. Sömmez, J. A. Taylor, B. Oberdorfer, D. Habe, S. Heugenhauser, and P. Schumacher, International Journal of Cast Metals Research **29**, 158 (2016).

[159] R. S. Wagner, Acta Metallurgica **8**, 57 (1960).

[160] S.-Z. Lu and A. Hellawell, Journal of Crystal Growth **73**, 316 (1985).

[161] M. G. Day and A. Hellawell, Proceedings of the Royal Society of London. Series A. Mathematical and Physical Sciences **305**, 473 (1968).

[162] K. F. Kobayashi and L. M. Hogan, Journal of Materials Science **20**, 1961 (1985).

[163] S.-Z. Lu and A. Hellawell, Metallurgical and Materials Transactions A **18**, 1721 (1987).

[164] A. Knuutinen, K. Nogita, S. D. McDonald, and A. K. Dahle, Journal of Light Metals **1**, 229 (2001).

[165] J. H. Li, M. Albu, T. Ludwig, Y. Matsubara, F. Hofer, L. Arnberg, Y. Tsunekawa, and P. Schumacher, Materials Science Forum **794-796**, 130 (2014).

[166] J. Barrirero, C. Pauly, M. Engstler, J. Ghanbaja, N. Ghafoor, J. Li, P. Schumacher, M. Odén, and F. Mücklich, Scientific Reports **9**, 5506 (2019).

[167] K. Nogita, H. Yasuda, M. Yoshiya, S. D. McDonald, K. Uesugi, A. Takeuchi, and Y. Suzuki, Journal of Alloys and Compounds **489**, 415 (2010).

[168] J. Barrirero, J. Li, M. Engstler, N. Ghafoor, P. Schumacher, M. Odén, and F. Mücklich, Scripta Materialia **117**, 16 (2016).

[169] L. Qiyang, L. Qingchun, and L. Qifu, Acta Metallurgica et Materialia **39**, 2497 (1991).

[170] Z. Dong, Z. Hu, H. Yan, H. Xie, and X. Li, Advances in Materials Science and Engineering **2019**, 9750526 (2019).

[171] C. Xu, W. Xiao, S. Hanada, H. Yamagata, and C. Ma, Materials Characterization **110**, 160 (2015).

[172] O. Gursoy and G. Timelli, Journal of Materials Research and Technology **9**, 8652 (2020).

[173] Y. Gyursoy, *Effects of lanthanide microalloying additions on the microstructure and mechanical properties of Al-Si-Cu-Mg cast alloys*, Ph.D. thesis, Università degli Studi di Padova, Italy (2023).

[174] J. L. Murray, Bulletin of Alloy Phase Diagrams **4**, 407 (1983).

[175] M. Zarif, B. McKay, J. Li, and P. Schumacher, Berg- und Hüttenmännische Monatshefte **155**, 506 (2010).

[176] M. Zarif, B. Mckay, and P. Schumacher, Metallurgical and Materials Transactions A **42**, 1684 (2011).

[177] J. H. Li, M. Z. Zarif, M. Albu, B. J. McKay, F. Hofer, and P. Schumacher, Acta Materialia **72**, 80 (2014).

[178] S. Shivkumar, L. Wang, and C. Keller, Journal of Materials Engineering and Performance **3**, 83 (1994).

[179] A. T. Joenoes and J. E. Gruzleski, Cast Metals **4**, 62 (1991).

[180] J. R. Denton and J. A. Spittle, Materials Science and Technology **1**, 305 (1985).

[181] J. H. Li, X. D. Wang, T. H. Ludwig, Y. Tsunekawa, L. Arnberg, J. Z. Jiang, and P. Schumacher, Acta Materialia **84**, 153 (2015).

[182] J. Li, F. Hage, M. Wiessner, L. Romaner, D. Scheiber, B. Sartory, Q. Ramasse, and P. Schumacher, Scientific Reports **5**, 13802 (2015).

[183] F. Mao, Y. Qiao, P. Zhang, L. Ou, C. Chen, C. Zhang, and Y. Wang, International Journal of Metalcasting **16**, 634 (2022).

[184] F. Mao, G. Yan, Z. Xuan, Z. Cao, and T. Wang, Journal of Alloys and Compounds **650**, 896 (2015).

[185] A. Mazahery and M. O. Shabani, JOM **66**, 726 (2014).

[186] F. Mao, S. Wei, C. Chen, C. Zhang, X. Wang, and Z. Cao, Materials & Design **186**, 108268 (2020).

[187] J. H. Li, M. Albu, F. Hofer, and P. Schumacher, Acta Materialia **83**, 187 (2015).

[188] E. Sjölander and S. Seifeddine, Journal of Materials Processing Technology **210**, 1249 (2010).

[189] X. Sauvage, E. V. Bobruk, M. Y. Murashkin, Y. Nasedkina, N. A. Enikeev, and R. Z. Valiev, Acta Materialia **98**, 355 (2015).

[190] Aluminium Company of America, *Alcoa Aluminium and Its Alloys*, 1st ed. (Aluminum Co. of America, Pittsburgh, 1950).

[191] E. Sjölander, *Heat treatment of Al-Si-Cu-Mg casting alloys*, Ph.D. thesis, Jönköping University (2011).

[192] A. M. A. Mohamed, F. H. Samuel, A. M. A. Mohamed, and F. H. Samuel, *A Review on the Heat Treatment of Al-Si-Cu/Mg Casting Alloys* (IntechOpen, 2012).

[193] R. I. Mackay and J. E. Gruzleski, International Journal of Cast Metals Research **10**, 255 (1998).

[194] A. L. Dons, G. Heiberg, J. Voje, J. S. Mæland, J. O. Løland, and A. Prestmo, Materials Science and Engineering: A International Conference on Advances in Solidification Processes, **413-414**, 561 (2005).

[195] H. W. Zandbergen, S. J. Andersen, and J. Jansen, Science **277**, 1221 (1997).

[196] ASM-International, *Heat Treating of Aluminum Alloys*, Vol. 4 (ASM handbook Committee, 1991).

[197] R. Vissers, M. A. van Huis, J. Jansen, H. W. Zandbergen, C. D. Marioara, and S. J. Andersen, Acta Materialia **55**, 3815 (2007).

[198] D. Zhang, L. Zheng, and D. StJohn, Journal of Light Metals **2**, 27 (2002).

[199] C. H. Caceres, C. J. Davidson, J. R. Griffiths, and Q. G. Wang, Metallurgical and Materials Transactions A **30**, 2611 (1999).

[200] Q. G. Wang and C. J. Davidson, Journal of Materials Science **36**, 739 (2001).

[201] W. S. Ebhota, T.-C. Jen, W. S. Ebhota, and T.-C. Jen, *Intermetallics Formation and Their Effect on Mechanical Properties of Al-Si-X Alloys* (IntechOpen, 2018).

[202] P. I. Sarafoglou and G. N. Haidemenopoulos, International Journal of Materials Research **105**, 1202 (2014).

[203] H. S. Hasting, A. G. Frøseth, S. J. Andersen, R. Vissers, J. C. Walmsley, C. D. Marioara, F. Danoix, W. Lefebvre, and R. Holmestad, Journal of Applied Physics **106**, 123527 (2009).

[204] C. D. Marioara, S. J. Andersen, J. Jansen, and H. W. Zandbergen, Acta Materialia **49**, 321 (2001).

[205] M. Takeda, F. Ohkubo, T. Shirai, and K. Fukui, Journal of Materials Science **33**, 2385 (1998).

[206] S. J. Andersen, H. W. Zandbergen, J. Jansen, C. TrÆholt, U. Tundal, and O. Reiso, Acta Materialia **46**, 3283 (1998).

[207] G. A. Edwards, K. Stiller, G. L. Dunlop, and M. J. Couper, Acta Materialia **46**, 3893 (1998).

[208] S. Cottenier, *Density Functional Theory and the family of (L)APW-methods: a step-by-step introduction*, 2nd ed. (2013).

[209] D. Holec, *Multi-scale modelling of III-nitrides: from dislocations to the electronic structure*, Ph.D. thesis, Cambridge, Selwyn College (2008).

[210] J. G. Lee, *Computational materials science* (Taylor & Francis, Boca Raton, Fla., 2011).

[211] W. Kohn and L. J. Sham, Physical Review **140**, A1133 (1965).

[212] J. P. Perdew, K. Burke, and M. Ernzerhof, Physical Review Letters **77**, 3865 (1996).

[213] G. Kresse and J. Furthmüller, Physical review. B **54**, 11169 (1996).

[214] H. S. Jang, H. J. Kang, J. Y. Park, Y. S. Choi, and S. Shin, Metals **10**, 1422 (2020).

[215] G. Gyarmati, G. Fegyverneki, T. Mende, and M. Tokár, Materials Characterization **157**, 109925 (2019).

[216] E04 Committee, "ASTM E112-13 Test Methods for Determining Average Grain Size," (2021).

[217] E. Ogris, H. Lüchinger, and P. J. Uggowitzer, Materials Science Forum **396-402**, 149 (2002).

[218] G. B. Thompson, M. K. Miller, and H. L. Fraser, Ultramicroscopy **100**, 25 (2004).

[219] M. Schaffer, B. Schaffer, and Q. Ramasse, Ultramicroscopy **114**, 62 (2012).

[220] "FEI Helios 600i Dual Beam SEM/FIB," ().

[221] M. Watanabe and D. B. Williams, Journal of Microscopy **221**, 89 (2006).

[222] "ZFE - Zentrum für Elektronenmikroskopie ASTEM," ().

[223] M. Starink, International Materials Reviews **49**, 191 (2004).

[224] D. Chen, X. Gao, and D. Dollimore, Thermochimica Acta **215**, 109 (1993).

[225] H. E. Kissinger, Journal of Research of the National Bureau of Standards **57**, 217 (1956).

[226] H. E. Kissinger, Analytical Chemistry **29**, 1702 (1957).

[227] M. I. Daoudi, A. Triki, A. Redjaimia, and C. Yamina, Thermochimica Acta **577**, 5 (2014).

[228] M. Liu, Z. Wu, R. Yang, J. Wei, Y. Yu, P. C. Skaret, and H. J. Roven, Progress in Natural Science: Materials International **25**, 153 (2015).

[229] I. Spacil, D. Holec, P. Schumacher, and J. Li, Solid State Phenomena **327**, 54 (2022).

[230] D. Wearing, A. P. Horsfield, W. Xu, and P. D. Lee, Journal of Alloys and Compounds **664**, 460 (2016).

[231] P. Norby, A. N. Christensen, E. Pedersen, R. Zingales, I. Vikholm, F. Urso, J. Weidlein, and R. A. Zingaro, Acta Chemica Scandinavica **40a**, 157 (1986).

[232] I. Spacil, D. Holec, M. Albu, and J. Li, Materialia **30**, 101846 (2023).

[233] A. H. Geisler and J. K. Hill, Acta Crystallographica **1**, 238 (1948).

[234] G. Kresse and D. Joubert, Physical Review B **59**, 1758 (1999).

[235] V. N. Yeremenko, Y. V. Natanzon, and V. I. Dybkov, Journal of the Less Common Metals **50**, 29 (1976).

[236] V. T. Witusiewicz, A. A. Bondar, U. Hecht, J. Zollinger, V. M. Petyukh, O. S. Fomichov, V. M. Voblikov, and S. Rex, Intermetallics **18**, 92 (2010).

[237] T. H. Ludwig, P. L. Schaffer, and L. Arnberg, in *Light Metals 2013*, The Minerals, Metals & Materials Series (Springer International Publishing, Cham, 2016) pp. 1023–1028.

[238] Y. Meng, J. Cui, Z. Zhao, and Y. Zuo, Journal of Alloys and Compounds **573**, 102 (2013).

[239] I. Spacil, P. Schumacher, and J. Li, IOP Conference Series: Materials Science and Engineering **1274**, 012006 (2023).

[240] K. D. Brommer, M. Needels, B. Larson, and J. D. Joannopoulos, Physical Review Letters **68**, 1355 (1992).

[241] Y. W. Sun, D. Holec, D. Gehringer, L. Li, O. Fenwick, D. J. Dunstan, and C. J. Humphreys, Physical Review B **105**, 165416 (2022).

[242] J. H. Li, M. Albu, T. H. Ludwig, F. Hofer, L. Arnberg, and P. Schumacher, IOP Conference Series: Materials Science and Engineering **117**, 012006 (2016).